



1995

Research and Technology
NASA Ames Research Center

Research and Technology

1995

Ames Research Center

National Aeronautics
and Space Administration

Ames Research Center
Moffett Field, California

NASA TM-110419

Aeronautics and Space Transportation Technology Enterprise

Overview	1
Advanced Vehicles / Rotorcraft	
Short Haul Civil Tiltrotor Mission and Configuration Baseline	5
<i>Karen Studebaker, Michael Fletcher, James Phillips, David Schleicher, Richard Peyran, Henry Lee</i>	
Noise-Abatement Flight Tests	5
<i>Robert T. N. Chen, William S. Hindson</i>	
Civil Tiltrotor One Engine Inoperative Terminal Area Operations	7
<i>William A. Decker, Rickey C. Simmons</i>	
Pilot Aids to Minimize the Impact of Engine Failures on Rotorcraft Operations	9
<i>Laura E. Iseler, Robert T. N. Chen, William S. Hindson</i>	
Optimal Trajectories for Category-A Helicopters	10
<i>Robert T. N. Chen, Yiyuan Zhao</i>	
Pilot-Directed Automated Guidance System	12
<i>Richard A. Coppenbarger, Chima E. Niaka</i>	
Real-Time Image-Based Obstacle Detection and Ranging System	14
<i>Phillip Smith, Banavar Sridhar</i>	
Stall Control of Helicopter Blades	15
<i>Khanh Nguyen</i>	
UH-60A Airloads Program	17
<i>Robert M. Kufeld, William G. Bousman</i>	
Rotor Data Correlation	18
<i>Randall Peterson</i>	
Identification of Hub Loads Using Neural Networks	19
<i>Sesi Kottapalli, Anita Abrego, Stephen Jacklin</i>	
Comparison of Computational and Experimental Rotor Blade-Vortex Interactions	20
<i>Megan McCluer</i>	
Numerical Simulation of Tiltrotor Aerodynamics in Hover	22
<i>Robert L. Meakin, William J. McCroskey</i>	
Wing Download Analysis	23
<i>Paul Stremel</i>	
Flow Field Analysis of a Model Proprotor in Hover	24
<i>Gloria K. Yamauchi, Wayne Johnson</i>	
Tiltrotor Aeroacoustic Model Isolated Rotor Checkout	25
<i>Larry Young, Jeff Johnson</i>	
High-Speed Proprotor Design with Optimum Performance and Weight	27
<i>Sesi Kottapalli, Thomas R. McCarthy, Aditi Chattopadhyay, Sen Zhang</i>	

Aeronautics and Space Transportation Technology Enterprise (continued)

Advanced Vehicles / Subsonic Fixed-Wing Aircraft

Propulsion Controlled Aircraft	28
<i>John Bull, Robert Mah</i>	
Advanced Navigation Display System: Initial B-747 Simulation Evaluation	29
<i>Vernol Battiste</i>	
Hazard Posed by Lift-Generated Wakes	30
<i>Vernon J. Rossow</i>	
The Final Approach Spacing Tool	31
<i>Tom Davis</i>	
Descent Advisor Field Evaluation	32
<i>Steven Green, Everett Palmer, Robert Vivona</i>	
Scene-Linked Symbolology for Low-Visibility Taxi	34
<i>David Foyle, Robert S. McCann</i>	
DC-10 Airframe Noise Source Location with Ames' Phased-Array Microphone Antenna	36
<i>Julie Hayes, M. Watts</i>	
Aerodynamics and Noise Associated with Flap Tips	37
<i>Bruce Storms, James C. Ross, Clif Horne, Julie Hayes</i>	
Flight Demonstration of Airframe-Noise Reduction Using Flap-Tip Fences	38
<i>James C. Ross, Bruce Storms, Hiro Kumagai</i>	
Investigation of Lift-Enhancing Tabs on a Multielement Airfoil	39
<i>Dale Ashby</i>	

Advanced Vehicles / High-Performance Aircraft

Intelligent Aircraft Control System	40
<i>Charles Jorgensen, James Urness</i>	
Joint Strike Fighter Large-Scale Powered Model Thrust Calibration and Hover Performance	41
<i>C. Hange, T. Naumowicz, D. Wardwell, T. Arledge</i>	
Large-Scale Test of Lift and Control Enhancement for Advanced Fighter Aircraft	42
<i>Jeffrey Samuels, Larry Meyn</i>	
Integrated Control Design Guidelines for STOVL Aircraft	44
<i>James A. Franklin, William W. Y. Chung</i>	
V/STOL Systems Research Aircraft Flight Research Program	45
<i>James A. Franklin, Delamar M. Watson, Ernesto Morales III</i>	
Computational Maneuver Aerodynamics	46
<i>Neal M. Chaderjian, Lewis B. Schiff</i>	
Time-Accurate Navier-Stokes Simulation of a Canard-Wing-Body Configuration with Moving Canards	48
<i>Eugene L. Tu</i>	

Aeronautics and Space Transportation Technology Enterprise (continued)

Advanced Vehicles / High-Speed Civil Transport

Applications of Nonlinear Design Optimization and Validation Wind Tunnel Testing	50
<i>Susan Cliff, Ray Hicks, Mina Cappuccio, James Reuther, Dan Bencze</i>	
Aeroacoustic Interactions Between the Noise Suppressor Nozzle and Airframe of the High-Speed Civil Transport	51
<i>Chris Allen, Paul Soderman, Brian Smith, Fanny Zuniga</i>	
High-Speed Research Guidance and Flight Control	53
<i>Jeffery A. Schroeder, Chima Njaka, Shawn A. Engelland, Charles S. Hynes, Karl Bilimoria, Robert W. Gardner</i>	
Obstacle Detection Systems to Augment a Windowless Cockpit	54
<i>Phillip Smith</i>	

Advanced Vehicles / Aerospace Vehicles

Computational Fluid Dynamics Analysis in Support of the X-33 Program	55
<i>William Henline, Grant Palmer</i>	
Thermal Protection Information System	55
<i>Ann Patterson-Hine</i>	
Fiber Optic Strain and Pressure Sensors	56
<i>Charles Gary, Meriç Özcan</i>	

Advances in Physics and Tools / Physical Understanding and Theoretical Tools

Human Motion Perception: Performance Measures and Computational Models	57
<i>Leland S. Stone, Preeti Verghese, Brent R. Beutter</i>	
Fatigue Countermeasures Program	58
<i>Mark Rosekind, Kevin Gregory, Donna Miller, Lissa Webbon, Ray Oyung, Julie Johnson</i>	
Boundary Layer Transition Induced by Convected Vorticity	59
<i>Anthony Dietz</i>	
The Structure of Stable and Unstable Waves in a Blasius Boundary Layer	61
<i>Sanford S. Davis</i>	
Measurement of Attachment Line Transition in a Supersonic Quiet Tunnel	64
<i>Colin Coleman</i>	
A Particle Representation Method for the Distortion of Homogeneous Turbulence	65
<i>W. C. Reynolds, S. C. Kassinos</i>	
A One-Point, Structure-Based Turbulence Model for Engineering Use	67
<i>S. C. Kassinos, W. C. Reynolds</i>	
Three-Dimensional Separating Flow Study for Turbulence Modeling	69
<i>David M. Driver</i>	
Analysis of Three-Dimensional, Separated Flows Using Topological Concepts	70
<i>Murray Tobak</i>	

Aeronautics and Space Transportation Technology Enterprise (continued)

Advances in Physics and Tools / Computational Tools

Computational Fluid Dynamics Design of NASA/DeBaKey Ventricular Assist Device	72
<i>Cetin Kiris, Dochan Kwak</i>	
Progress in Computational Fluid Dynamics for High-Lift Aerodynamics	73
<i>Stuart E. Rogers</i>	
Three-Dimensional Cartesian Computational Fluid Dynamics Technology: Improvements and Applications	75
<i>John E. Melton, Michael J. Aftosmis</i>	
Wing-Body-Control Aeroelastic Computations on IBM SP2	76
<i>Guru P. Guruswamy, Chansup Byun</i>	
Automated Computational Fluid Dynamics for Subsonic Transports	76
<i>Steven M. Nash, William M. Chan, Jin J. Chou, Pieter G. Buning</i>	
Validation of ENSAERO for an Elastic Supercritical Wing	77
<i>Guru P. Guruswamy, Mehrdad Farhangnia</i>	
The Unsteady Flow Analysis Toolkit	77
<i>David L. Kao</i>	
Recent Enhancement to the Navier–Stokes Code OVERFLOW	78
<i>Dennis Jespersen, Thomas Pulliam</i>	
Improved Numerical Methods for Large-Eddy Simulation of Complex Turbulent Flows	80
<i>Parviz Moin, Thomas Lund, Sandip Ghosal, Kenneth Jansen, Youhei Morinishi</i>	
An Improved Grid Generator	81
<i>Reese L. Sorenson</i>	
Surface Movement Advisor	82
<i>Brian Glass</i>	
An Automated Instrumentation and Monitoring System	83
<i>Jerry Yan, Melisa Schmidt</i>	
The Numerical Aerodynamics Simulation Trace Visualizer	83
<i>Louis Lopez</i>	
An Emerging Standard for File Access on Parallel Systems	85
<i>Sam Fineberg, Bill Nitzberg, Parkson Wong</i>	

Advances in Physics and Tools / Experimental Tools

Monitoring Human Motion Perception by Measuring Eye Movements	86
<i>Leland S. Stone, Brent R. Beutter, Philippe Stassart</i>	
Three-Dimensional Sound Synthesis: Measuring Personalized Head-Related Transfer Functions	87
<i>Durand R. Begault, Elizabeth M. Wenzel</i>	
Head-Mounted Displays of Virtual Objects for Assembly and Maintenance	88
<i>Stephen R. Ellis, B. D. Adelstein</i>	
Ames Spatial Auditory Display	90
<i>Durand R. Begault, Elizabeth M. Wenzel</i>	

Aeronautics and Space Transportation Technology Enterprise (continued)

Advances in Physics and Tools / Experimental Tools (continued)

Coordinated Haptic-Visual Virtual Environments	91
<i>Bernard D. Adelstein, Stephen R. Ellis</i>	
Skin-Friction Measurements on a Commercial Transport Configuration	92
<i>David M. Driver, George Mateer</i>	
Surface Imaging Skin Friction Instrument Package	94
<i>James L. Brown, Jon Naughton</i>	
Interferometric Fringe Analysis Software Development	95
<i>Gregory G. Zilliac</i>	
A New Method for Obtaining Full-Surface Measurements of Shear-Stress Vector Distributions Using Liquid Crystal Coatings	96
<i>Daniel C. Reda, Michael C. Wilder, John R. Lehman</i>	
Atmospheric Gas-Sampling Probe	97
<i>Kevin D. James, James C. Ross, Gerald M. Vogel</i>	
Wind Tunnel Flow Quality and Boundary Layer Transition	98
<i>Jonathan H. Watmuff</i>	
Multielement Acoustic Array Calibration	100
<i>Stephen Jaeger, Srba Jovic, Marianne Mosher</i>	
Software Acoustics Project	101
<i>Kevin McCabe</i>	
Adaptive-Grid Wake Survey System	101
<i>Timothy T. Takahashi</i>	

Developments and Improvements of Facilities

Surface Development and Test Facility	103
<i>Stanton Harke</i>	
Ames Research Center 12-Foot Pressure Wind Tunnel	104
<i>Thomas N. Aiken</i>	
DARWIN Remote Access Systems	105
<i>David Korsmeyer</i>	
Qualification Testing of the Laminar Flow Supersonic Wind Tunnel	107
<i>James A. Laub, Stephen W. D. Wolf</i>	
Separation Control in a Wind Tunnel Diffuser System	110
<i>David Yaste, Rabindra Mehta, Jonathan Watmuff</i>	
Arc Jet Characterization	112
<i>D. G. Fletcher, T. Gökçen, M. E. Newfield, C.-S. Park</i>	
Spectroscopic Study of the Arc Column in an Arc-Jet Wind Tunnel	114
<i>Imelda Terrazas-Salinas, Chul Park, Anthony W. Strawa, Jaswinder S. Taunk, Nigel K. J. M. Gopaul</i>	

Aeronautics and Space Transportation Technology Enterprise (continued)

Developments and Improvements of Facilities (continued)

Portable Batch System Project	117
<i>David Tweten</i>	
Super Home File System Offers Increased User Productivity	118
<i>Alan Powers</i>	
Asynchronous Remote Copy Program	119
<i>Jude A. George</i>	

Space Science Enterprise

Overview	121
----------------	-----

Progress in Exobiology

Development of CHEMIN, an Instrument for In Situ Determination of the Mineralogy of Soil and Rocks on Mars	124
<i>David Blake, Philippe Sarrazin, Friedemann Freund</i>	
Dynamics of Microbial Mats, the Oldest Ecosystem	126
<i>David J. Des Marais</i>	
Rock-Made Organics	127
<i>Friedemann Freund, Alka Gupta, Devendra Kumar</i>	
The Crystallization of Water Ice in the Solar System	130
<i>David Blake, Peter Jenniskens</i>	
Formation of Simple Biomolecules in Interstellar Clouds	131
<i>Steven B. Charnley</i>	
Dissolved Gases in Perennially Ice-Covered Lakes of Antarctica	134
<i>Dale T. Andersen, Christopher P. McKay</i>	
Cyanobacterial Biomarkers as Clues to the Nature of Ancient Ecosystems	135
<i>Linda L. Jahnke</i>	
On the Identification of a Chimeric ATPase in the Bacterium <i>Paracoccus Halodenitrificans</i>	136
<i>Lawrence I. Hochstein</i>	
The Isolation of a Gene that Codes for the F ₀ F ₁ -ATP Synthase (F-ATPase) in the Extremely Halophilic Bacteria	137
<i>Roberto Bogolmolini, Lawrence I. Hochstein</i>	
Investigation into the Nature of the ATP Synthase in <i>Halorubrum Saccharovorum</i>	138
<i>David Faguy, Lawrence I. Hochstein</i>	
New Prebiotic Synthesis of Amino Acids	139
<i>Arthur L. Weber</i>	
Bonded Porous Layer Open Tubular Columns	140
<i>Thomas C. Shen, Cindy X. Zhou</i>	
Ion Mobility Spectra of Unresolved Gas Chromatographic Peaks	141
<i>Daniel R. Kojiro, Norishige Takeuchi, Maxine R. Shao</i>	

Space Science Enterprise (continued)

Progress in Astrophysics

The Infrared Telescope in Space Experiment	143
<i>Thomas L. Roellig</i>	
Excitation of the Arched Filaments near the Galactic Center	144
<i>Sean W. J. Colgan, Edwin F. Erickson, Janet P. Simpson, Michael R. Haas, Mark Morris</i>	
Studies of Interstellar Matter and Gaseous Nebulae	146
<i>Robert H. Rubin</i>	
Molecular Opacity Databases for Titanium Oxide and Water	147
<i>Stephen Langhoff, David Schwenke, Harry Partridge</i>	
Water as an Opacity in Stellar Spectra	148
<i>Duane F. Carbon, David Goorvitch</i>	
Spectral Flux Standards for Infrared Astronomy	149
<i>Fred C. Witteborn, Martin Cohen, Diane H. Wooden</i>	
Radiation-Environment Testing of Focal-Plane Sensor Arrays	150
<i>Mark E. McKelvey, Robert E. McMurray, Jr., Craig R. McCreight</i>	
Stratospheric Observatory for Infrared Astronomy Simulated in Cruise Flight	151
<i>Karlin Roth, G. R. Srinivasan</i>	
Organic Signatures in the Interstellar Medium	152
<i>Yvonne Pendleton</i>	
Identifying Stardust—Interstellar Nitrogen and Oxygen	153
<i>Lou Allamandola, Scott Sandford, Max Bernstein, Robert Walker, Jamie Elsila</i>	
Gas-Phase Reactions in the Interstellar Medium	154
<i>David E. Woon, Gilda H. Loew</i>	
Complex Organics and the 3.4 μm Emission of The Orion Bar	156
<i>Max Bernstein, Scott Sandford, Louis Allamandola, Robert Walker, Greg Sloan</i>	
Ultraviolet-Near Infrared Spectroscopy of Organic Dust Analogs	157
<i>Farid Salama, Louis Allamandola, Christine Joblin, Robert Walker</i>	
On the Central Regions of Galaxies	159
<i>Bruce F. Smith</i>	
Abundance Variations in the Galaxy	160
<i>Janet P. Simpson, Sean W. J. Colgan, Robert H. Rubin, Edwin F. Erickson, Michael R. Haas</i>	
Investigating the Evolution of Circumstellar Photodissociation Regions	162
<i>William B. Latter, A. G. G. M. Tielens</i>	

Progress in Planetology

Planetary Surface Rover Mission Simulation	164
<i>Carol Stoker, Michael Sims</i>	
A Micro-Meteorological Network Mission for Atmospheric Circulation Studies on Mars	165
<i>Robert M. Haberle, Steven C. Merrihew, David C. Catling, Lawrence G. Lemke</i>	

Space Science Enterprise (continued)

Progress in Planetology (continued)

Martian Mountain Waves	166
<i>Julio A. Magalhães</i>	
Water Adsorption on Mars	167
<i>Aaron P. Zent</i>	
Oxidants in the Martian Regolith	168
<i>Aaron P. Zent, Richard C. Quinn</i>	
Environmental Perturbations by Large Asteroid and Cometary Impacts	168
<i>Owen B. Toon, Kevin Zahnle, David Morrison</i>	
Ejecta Plumes from the Collisions of Comet Shoemaker-Levy 9 with Jupiter	170
<i>Kevin Zahnle</i>	
Planetesimal Formation in the Protoplanetary Nebula	171
<i>Jeffrey Cuzzi</i>	
Interstellar Grains in the Solar System	173
<i>Patrick Cassen</i>	
Theoretical and Empirical Studies of Planetary Surface Analogs	175
<i>Ted Roush</i>	

Progress in Space Technologies

New Millennium Autonomous Spacecraft Architecture	176
<i>B. Pell, D. E. Bernard, S. A. Chien, E. Gat, N. Muscettola, P. Nayak, M. D. Wagner, B. Williams</i>	
Model-Based Autonomous Systems	177
<i>Brian C. Williams, P. Pandurang Nayak</i>	
Spacecraft Task Planning: New Millennium, Extreme Ultra-Violet Explorer, and Cassini	178
<i>Nicola Muscettola, Sunil Mohan, Charles Fry, Kanna Rajan</i>	
A Fuzzy/Genetic Diagnostic System	179
<i>Silvano Colombano</i>	
Galileo Probe Vaporization Data Reduction	180
<i>Frank Milos</i>	
Mars Aerocapture Entry	182
<i>Paul F. Wercinski</i>	
Computer Model of a Pulse Tube Cooler	183
<i>Pat R. Roach, Jeffrey M. Lee, Peter Kittel, Ali Kashani</i>	
Bacteriorhodopsin Films for Optical Data Storage and Processing	185
<i>John D. Downie, Dogan A. Timucin</i>	
Simulations to Determine Polymer Electrolyte Properties	186
<i>Richard L. Jaffe, Grant Smith</i>	
New Millennium Electronic Collaboration and Document Sharing	187
<i>Michael Compton, Helen Stewart, Vinod Baya, Bob Kanefsky, Martha DeAlto</i>	

Human Exploration and Development of Space Enterprise

Overview	189
Powered Linear Sled for Research on Mammalian Gravity-Sensors	191
<i>Dan Kalcic, David Tomko, Tom Wynn</i>	
Hypergravity Facility for Cell Culture	192
<i>Alexandre C. L. Malouvier, Emily Morey-Holton</i>	
Pilot Study for Human Research Experiments Planned for the Life and Microgravity Sciences Spacelab Mission	194
<i>Sara B. Arnaud, D. O'Hara</i>	
Cycle-Powered Short Radius (1.9 m) Centrifuge: Exercise versus Passive Acceleration	196
<i>J. E. Greenleaf, D. P. Gundo, D. E. Watenpaugh, G. M. Mulenburg, N. Marchman, R. Looft-Wilson, A. R. Hargens, S. M. Bowley</i>	
Exercise Prevents Bed-Rest Deconditioning	198
<i>Donald E. Watenpaugh, Richard E. Ballard, Jacqueline M. William, Andrew C. Ertl, Suzanne M. Fortney, Stuart M. C. Lee, Wanda L. Boda, Alan R. Hargens</i>	
Finite Volume Simulation of Neuron Activity	199
<i>Muriel D. Ross, Samuel W. Linton</i>	
A Pentium-Based System for Physiological Monitoring and Displays	201
<i>Patricia S. Cowings</i>	
CD ROMS Archive Human Biomedical Data From Space	203
<i>Patricia S. Cowings</i>	
Center for Health Applications of Aerospace Related Technologies	204
<i>Byron Wood, Louisa Beck, Sheri Dister</i>	
Global Monitoring and Human Health	205
<i>Louisa Beck, Sheri Dister, Mike Spanner</i>	
Patented Training Process Enables Technology Transfer—Ames Autogenic-Feedback Training System	206
<i>Patricia Cowings</i>	
Portable Computer Technology Project	207
<i>Richard Alena, Kim Hubbard</i>	
Just-In-Time-Training	209
<i>Nicolas Groleau, Leo Yu, Kim Hubbard</i>	
Biological System Dynamics	210
<i>Harry Jones</i>	
Systems Control	211
<i>Charles C. Blackwell</i>	

Mission to Planet Earth Enterprise

Overview	213
Airborne Southern Hemisphere Ozone Experiment/Measurements for Assessing the Effects of Stratospheric Aircraft	215
<i>Steve Hipskind, Duane Allen, Quincy Allison, Stu Bowen, Paul Bui, Roland Chan, Estelle Condon, Michael Craig, Guy Ferry, Steve Gaines, Jeff Grose, Patti Hathaway, Max Loewenstein, Jim Podolske, Rudi Pueschel, Tony Trias</i>	
Ecosystem Trace Gas Fluxes	216
<i>Christopher S. Potter, Steven A. Klooster</i>	
The Arizona Program	217
<i>Peter Pilewskie, Warren J. Gore</i>	
Remote Sensing of Phytoplankton Dynamics Using AVIRIS Derived Spectral and Image Data	218
<i>Vincent G. Ambrosia, Laurie L. Richardson</i>	
Convectively Generated Gravity Waves	219
<i>Leonhard Pfister</i>	
BOREAS Modeling	220
<i>Joseph Coughlan</i>	
Trace Gas Flux Measurements	221
<i>Gerald P. Livingston, Gordon L. Hutchinson, William H. Anthony, James Podolske, Leslie A. Morrissey, David J. DesMarais, Richard W. Healy, Rob G. Striegl</i>	
Spatial and Temporal Distribution of Biomass Combustion and Pyrogenic Trace Gas Emissions	222
<i>James Brass, Christine Hlavka, Robert Chatfield, Pamela Matson, Liane Guild, Vincent Ambrosia</i>	
Mapping Northern Ecosystems Using Synthetic Aperture Radar	223
<i>Leslie A. Morrissey, Gerald P. Livingston, Joel Stearn, Stephen Durden</i>	
Non-Methane Hydrocarbon Emissions	224
<i>Susan E. Alexander, Christopher S. Potter, Steven A. Klooster, Joseph C. Coughlan, Robert B. Chatfield</i>	
Paleoenvironmental Studies	225
<i>Hector D'Antoni</i>	
Radiation Measurement System for Atmospheric Research	226
<i>Warren J. Gore, Francisco P. J. Valero, Larry Pezzolo, Neil Heather</i>	
A New Within-Leaf Radiative Transfer Model	226
<i>David Peterson, Barry Ganapol, Lee Johnson, Christine Hlavka, Phillip Hammer</i>	
Impact of Land Use and Land Surface Aggregation on Estimating Temperate Coniferous Forest Net Primary Productivity, Dry Matter Yield, and Carbon Budgets	227
<i>Joseph Coughlan, Jennifer Dungan</i>	

Mission to Planet Earth Enterprise (continued)

Monitoring and Enforcement of Fisheries Aided by Synthetic Aperture Radar	228
<i>Robert Wrigley, Don Sullivan</i>	
The Reliable Multicasting Protocol	229
<i>John Callahan</i>	
Web Integrated Software Environment	230
<i>John Callahan</i>	

Appendix

Color Plates (1–23)	232
---------------------------	-----

Aeronautics and Space Transportation Technology Enterprise



Overview

NASA's mission for the Aeronautics and Space Transportation Technology Enterprise is to pioneer the identification, development, verification, transfer, application, and commercialization of high-payoff aeronautics technologies and to provide a program of leading-edge exploratory and focused technology to ensure continued U.S. preeminence in space transportation at substantially reduced costs. Ames' scientists and engineers support this mission by pursuing a triad of objectives.

One objective of this triad is to excel in modeling and simulation using computers, in aerodynamics and aerothermodynamics developments using wind tunnels and arc-jet and hypervelocity facilities, in virtual reality using flight simulators, and in the synergistic integration of these powerful and distinct capabilities. Another objective is to develop, validate, and verify enabling, cutting-edge, high-payoff technologies and prepare them for advanced vehicles—rotorcraft, fixed-wing subsonic aircraft, high-performance aircraft, and aerospace vehicles—by probing previously unexplored configurations and flight regimes. Finally, the third objective is to develop aerospace information systems (including airspace operation systems), integrating information technology, modeling and simulation, operations research, human factors, guidance and control, artificial intelligence, and computer science.

Ames addresses this triad, in part, by focusing on developments that lead to advanced vehicles, by further understanding the physics, by enhancing design and analysis tools, and by improving and developing facilities. Ames' scientists and engineers also participate in jointly funded partnerships with industrial entities having a direct interest in using Ames expertise or technologies. During FY95, numerous such efforts were accomplished to achieve the following Enterprise goals:

- Develop high-payoff technologies for a new generation of environmentally compatible, economic rotorcraft and subsonic, fixed-wing aircraft, and a safe, highly productive global air transportation system.
- Prepare the technology options for new capabilities in high-performance aircraft.

- Prepare the technology base for an economically viable and environmentally friendly high-speed civil transport (HSCT).
- Reduce the cost of access to space.
- Build capability in the space industry through focused space technology efforts.
- Develop advanced concepts, physical understanding, and theoretical, experimental, and computational tools, including high-performance computing and information technology, to enable advanced aerospace systems.
- Develop, maintain, and operate critical national facilities for research and for the support of industry, the Federal Aviation Administration (FAA), the Department of Defense (DOD), and NASA programs.

Ames is the primary Center for Aviation Operations Systems and for Information Systems. In addition, Ames is the Program Lead Center for the Research and Technology Base Program in Rotorcraft, for the Numerical Aerodynamic Simulation (NAS) Program, for the High Performance Computing and Communications Program, and for supercomputing; Ames leads the Competency Group Area for vertical/short takeoff and landing technology; and Ames maintains competencies in airborne systems, aerodynamics, hypersonics and hypervelocity flight, mission/system analysis, crew station design and integration, turbomachinery and combustion, experimental aircraft flight research, testbed aircraft research and operation, and flight test techniques and instrumentation. Ames is being established as NASA's Center of Excellence for Information Technology to enable the creation of a new NASA. Application of this new technology will revolutionize NASA's ability to accomplish its mission.

Vehicles

Ames made significant contributions to the Enterprise goal for rotorcraft, which led to accomplishments in defining the civilian tiltrotor mission and baseline configuration, helicopter noise abatement, engine-out operations, very-low-altitude operations, noise reduction and blade control, rotorcraft airloads, and flow-field analyses.

The guidance and control of transport aircraft to land automatically using only engine power was successfully demonstrated by an information system, called the Propulsion Controlled Aircraft System, on board a jumbo transport aircraft. An advanced navigation display system was also evaluated for the simulated operation of a jumbo transport aircraft. In addition, research was conducted in wake vortex hazard and its avoidance, pilot taxiing aids, head-up display design, airframe noise, wing flap-edge noise, and lift-enhancing devices.

Several Ames projects contributed to the Enterprise goals for high-performance aircraft. One of the technology-options development efforts for new capabilities in high-performance aircraft describes the first flight test involving a neural network placed in the onboard flight processor of a fighter aircraft. The neural network, an information system, performed adaptive real-time control for the reconfiguration of the aircraft in response to off-nominal or unforeseen flight conditions. The other such efforts include: tests of one variant in the Joint Aircraft Strike Technologies (now the Joint Strike Fighter) Program; wind tunnel tests of a highly maneuverable fighter design; powered-lift aircraft control concept testing in simulations and in flight; and computer simulations of high-angle-of-attack aerodynamic performance and of a canard/wing/body configuration.

The efforts for HSCT include the vehicle shape optimization for increased performance and reduced sonic boom overpressure, the High-Lift Engine Aeroacoustics Tests, and the development of HSCT flight-control laws and of external vision technology for windowless cockpits.

The reduction in the life-cycle cost of access to space is principally addressed by developing lightweight, low-cost, thermal protection systems (TPSs). Using Ames' NASA-unique capability in TPS, new aerospace materials for reusable launch vehicles are being developed. Specifically, the industrial entities, conducting efforts for the X-33 and the X-34 programs, were assisted. Design concepts were analyzed using engineering tools and complex computer simulations of flow fields. Ames took the lead in defining requirements for new, lightweight, durable,

low-cost TPS to be incorporated in the X-33 vehicle. A by-product of this effort was the development of the Thermal Protection Information System, which provides easy access to material developers to vast amounts of data, reports, and images generated during the testing of candidate materials.

Another example of the Ames/industry partnership is the development of a health management system facilitating vehicle maintenance, a critical enabling technology for the reusable launch vehicles. A stress sensor based on fiber-optic technology was developed, as part of the X-33 Technology Program with Lockheed Martin. A prototype sensor system was built in the Photonics Laboratory at Ames, and successfully demonstrated at Lockheed Martin's test facility.

Physics and Tools

Developments for addressing the Enterprise goal of enabling advanced aeronautics and aerospace systems require, in part, advances in physics and tools. The accomplishments related to improved physical understanding and theoretical tools are described in reports on human motion perception, fatigue countermeasures, boundary layer transition, turbulence modeling, and flow-separation topology. Computational tools were developed for studying ventricular-assist devices for human blood flow and for analyzing the aerodynamics and aeroelasticity of subsonic transport planes. Improvements in tools were accomplished for Reynolds-averaged Navier-Stokes simulations, for simulations with Cartesian grids, and for large-eddy simulations.

Articles on advanced information tools include the Unsteady Flow Analysis Toolkit to assist computational fluid dynamics scientists to understand fluid-flow phenomena; the Automated Instrumentation and Monitoring System to realize the full potential of the parallel computing platforms and to assist developers in the transition from vector-based supercomputing to these platforms; the Message Passing Interface (input/output interface) for parallel file operations that simultaneously provide both portability and performance; and the status of a joint NASA/FAA effort for developing an information system, the Surface Movement Advisor, to enhance the terminal-area productivity by facilitating unprecedented information sharing between user communities by electroni-

cally connecting the air traffic control, airline, and airport operations.

The accomplishments related to experimental tools for improving the performance of humans include reports on monitoring motion perception, sound synthesis, displays of virtual objects, spatial auditory display, and visual virtual environments. Tools are also discussed for fluid-flow measurements, such as skin friction, atmospheric samples, and acoustics.

Facilities

The most sophisticated flight simulators in the United States can be found at Ames, and the Crew-Vehicle Systems Research Facility is a unique national laboratory designed to study human factors in aviation safety. Ames operates a complex of wind tunnels (the National Full-Scale Aerodynamics Complex, the 12-Foot Pressure Wind Tunnel, and the Unitary Plan Facility) for aerodynamics research and development testing. In addition, advanced supercomputers and experimental, highly parallel computers are assembled at Ames in the NAS facility, also a national facility.

The Enterprise goal to develop, maintain, and operate critical national facilities is continuously addressed by developing and building new facilities at Ames, by improving existing facilities for enhancing user productivity, and by further developing them to provide new capabilities.

A progress report presents the status of a new simulation facility, the Surface Development and Test Facility, to validate future airport surface and air traffic control tower technologies prior to field deployment.

Efforts for significantly improving productivity of test operations include a description of the newly rebuilt 12-Foot Pressure Wind Tunnel—the only large scale, low-turbulence, variable-density subsonic tunnel in the United States; development of an information system called DARWIN to allow remote access to the Ames wind tunnel facilities from within Ames through a local fiber-optic intranet and from industry sites through the AEROnet nationwide network; qualification testing of the Laminar Supersonic Wind Tunnel for investigating transitions from laminar to turbulent flows; and arc-jet characterization studies in the Ames arc-jet wind tunnel and a

spectroscopic study of the arc column enhancing the value of data taken in this tunnel.

The NAS facility is continuously improved to enhance user productivity. For example, the Portable Batch System moves NASA closer to its goal of combining heterogeneous computing resources into a virtual computing facility targeted at solving a wide range of scientific and engineering problems. The

“super home” file system on the NAS Cray C90 (von Neumann) increases user productivity by increasing total user disk capacity and by reducing the complexity of the file system structure. And, the Asynchronous Remote Copy Program is designed to quickly and reliably transfer large scientific datasets from host to host, with minimal input from the supercomputer user to transfer files over the AEROnet.

Short Haul Civil Tiltrotor Mission and Configuration Baseline

Karen Studebaker, Michael Fletcher, James Phillips, David Schleicher, Richard Peyran, Henry Lee

A baseline mission and aircraft configuration were designed to meet an early requirement and milestone of the Short Haul Civil Tiltrotor (SHCT) Program. In this program, the baseline serves as a



Fig. 1. Civil Tiltrotor Baseline Design.

current technology design from which to measure the benefits of new technology. NASA incorporated the design inputs of U.S. rotorcraft airframe and engine manufacturers so that the baseline can now serve as a common reference for industry and government research programs, conducting rotor and engine design studies, simulations, and acoustic and economic analyses.

The baseline configuration (shown in the figure) is a forty-passenger, commercial aircraft intended for operation from city center vertiports, flying at 350 knots with a 600 nautical mile range. The three-bladed rotors are proven technology that are demonstrated in flight by the XV-15 and V-22 tiltrotors. This baseline design incorporates a high T-tail and fixed engines that are believed to be achievable with current technology. The aircraft was sized assuming an entry into the marketplace in the year 2005.

Point of Contact: K. Studebaker
(415) 604-4682

Noise-Abatement Flight Tests

Robert T. N. Chen, William S. Hindson

Community noise has been recognized as a major barrier to the full utilization of rotorcraft in an integrated air transportation system. One of the most significant sources of noise generated by a passing, overflying, or approaching helicopter occurs when a rotor blade encounters the vortices shed by preceding blades. The phenomenon is known as blade-vortex interaction (BVI), and is characterized by an impulsive noise, sometimes called blade slap, which can be particularly objectionable during the descent to landing.

Solutions to the BVI noise problem lie both in design improvements to the rotor system and in the use of special flight procedures that avoid operation in conditions that are particularly conducive to BVI. The noise reduction improvements in the rotor-system design include appropriate selection of blade-tip speed, number of blades, disc loading, blade loading, blade-tip geometry, and the use of active on-the-blade control schemes. The use of special flight procedures that are of primary interest in this

work are known to pilots, but they are difficult to fly with the necessary navigational precision, even in visual-flight conditions. The increasingly broad applications of the Local Differential Global Positioning System (LDGPS) to civilian aviation now makes this possible, thus opening the way to greater use of rotorcraft by the urban transportation infrastructure, as depicted schematically in the figure.

A specific, noise-abatement profile tailored to avoid the BVI-intensive region of the NASA/Army Rotorcraft Aircrew Systems Concepts Airborne Laboratory (RASCAL) research helicopter was designed based on acoustic data from wind-tunnel tests and from flight tests that were available for this type of helicopter. Acoustic tests were then conducted jointly by Ames and Langley Research Centers at Crows Landing Airfield, California, in January 1995. A precision, laser-tracking facility at the airfield was used to assess the navigational accuracy of the LDGPS. A laser-based, rotor-state measurement system on board the aircraft measured the main rotor, tip-path-plane, angle of attack. A microphone array similar to that used in the standard Federal Aviation Administration noise certification test assessed the noise reduction effectiveness of this specific noise-abatement profile. Generic approach

profiles recommended by the Helicopter Association International for light and medium helicopters were also tested for acoustic reduction effectiveness. Additionally, three conventional descending approaches, namely 9 degrees decelerating, 6 degrees decelerating, and 6 degrees constant speed at 80 knots, were also flown for the purpose of comparing the noise characteristics because of deceleration and flying single and multisegment approach profiles.

The test results indicate that over 4 dBA reductions from the standard, 6 degrees, constant-speed approach are realized at the certification measurement locations for those noise-abatement approach profiles. The effect of deceleration on descending approach flight was also found to increase the tip-path-plane angle of attack of the main rotor with an accompanying increase in the effective rate of descent. The effect can influence significantly the BVI noise characteristics; therefore, this effect should be considered in the design of a deceleration approach profile for BVI noise abatement.

**Point of Contact: R. Chen/W. Hindson
(415) 604-5008/1106**

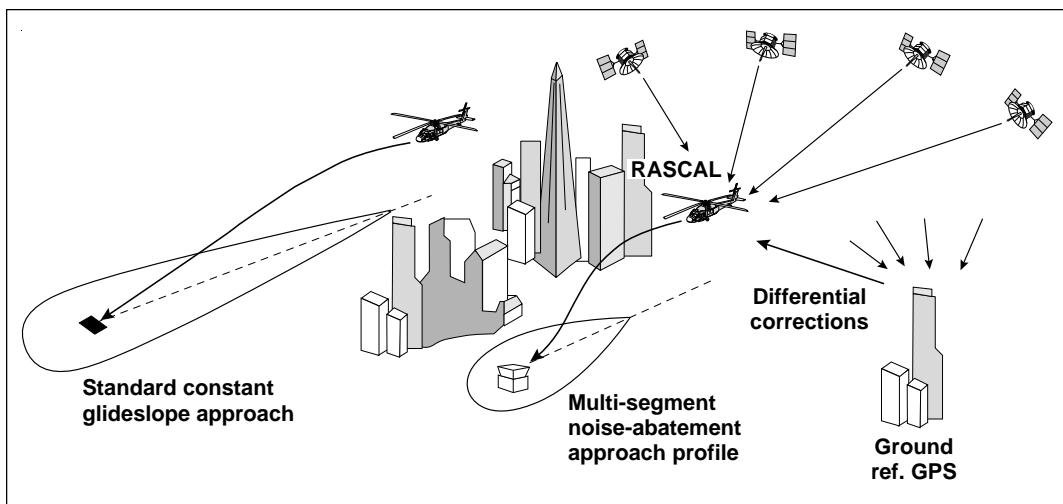


Fig. 1. Schematic diagram: LDGPS-guided noise-abatement approaches in an urban area.

Civil Tiltrotor One Engine Inoperative Terminal Area Operations

William A. Decker, Rickey C. Simmons

A civil tiltrotor regional transport operating from urban vertiports offers considerable potential for relieving current conventional airport runway congestion. A market-responsive, commercial tiltrotor must balance economic operation with initial acquisition cost and infrastructure costs such as vertiport size and location, while maintaining a commercial airline safety standard. Provision for continued safe flight in the event of a single engine failure is critical to the low-speed and vertical-flight operations needed at a small vertiport such as that illustrated in the first figure.

The fifth in a series of piloted simulation experiments investigating civil tiltrotor certification and operation issues focused on contingency power requirements for the remaining engine with one engine inoperative. As illustrated in the second figure, two engine sizes were defined in terms of the hover and low-speed performance requirements of a 40-passenger tiltrotor transport. The base engine power provided for sustained climb-out with one engine inoperative, but with insufficient power to hover. A 15%, short-time, contingency power augmentation, typical of today's rotorcraft design practice, provided only limited, low-speed operation. A 30% contingency power, considered for future tiltrotor designs, provided sufficient power to hover when close to the ground.

Engine failures during departure and approach and landing operations were investigated with the two, short-time, engine contingency ratings. The most critical operations occurred when engine failures were introduced shortly after a landing commitment at the landing decision point. These critical approach and landing operations must account for the effects of winds, turbulence, and approach-path tracking errors. The space required to safely recover and land the aircraft under adverse conditions exceeded the



Fig. 1. Civil tiltrotor transport landing at a conceptual urban vertiport located near downtown San Francisco.

space requirements for take-off under the same conditions.

Very short roll-on and roll-off operations were recommended for an aircraft engine with the base plus 15% contingency rating. The required vertiport "rollway" (paved operating surface) was at least 600 feet long, which is the length of a three- or four-gate vertiport terminal design. The larger contingency rating engine (30% above the base, continuous rating) supported operations from smaller facilities (200–300 feet long) and a lower landing decision height.

Thirteen evaluation pilots participated, representing the National Aeronautics and Space Administration, the Federal Aviation Administration, Department of Defense, British Civil Aeronautics Authority, United States rotorcraft industry, and

commercial helicopter operators. Evaluations were conducted in the Vertical Motion Simulator (VMS) at Ames Research Center. The unique, sustained-acceleration capabilities of the VMS helped pilots assess aircraft responses during critical recovery operations.

Results of this experiment will guide aircraft design, terminal area operations planning, aircraft certification, and vertiport design efforts.

Point of Contact: W. Decker
(415) 604-5362

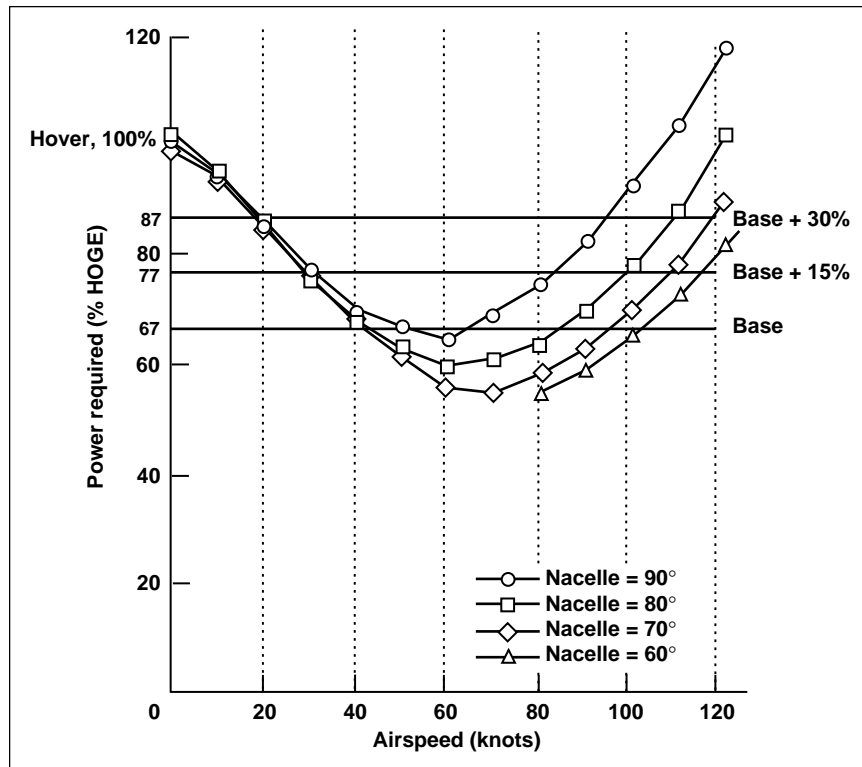


Fig. 2. Power required as a function of airspeed and nacelle tilt angle.

Pilot Aids to Minimize the Impact of Engine Failures on Rotorcraft Operations

Laura E. Iseler, Robert T. N. Chen, William S. Hindson

Operating from small urban vertiports, rotorcraft have the potential to increase the capacity and the efficiency of the urban transportation infrastructure, as well as to off-load the growing demand placed on already congested large airports. Coincident with any expanded use of multiengine, transport-category helicopters to serve public transportation will come the need for improved safety. Certification criteria for these operations require that the rotorcraft possess the performance capability for continued safe flight in the event of an engine failure. Takeoff and landing operations are critical since they involve low altitudes, low airspeeds, and high levels of power, and they frequently occur in densely populated areas.

The objective of this research is to develop technology to assure safe flight in engine failure situations, while still providing maximum payload capability to the operator. Two parallel but complementary approaches are being used. One approach involves analytical determination of optimal profiles and control strategies to assure maximum performance at maximum operating weight, and the other approach, described here, uses piloted simulations to investigate pilot aids that could assist the pilot in performing these difficult and demanding procedures.

A second simulation using the Ames Vertical Motion Simulator was conducted during FY95 to investigate the potential of advanced cockpit displays, and to assess to what degree aural and tactile cues could assist the pilot during recoveries from engine failures. The focus of the second simulation included short and vertical takeoffs and landings from confined areas with all engines operating (AEO), and one engine inoperative (OEI) flyouts, as shown in the first figure. The pilot was assisted during AEO approaches and OEI flyouts with the flightpath vector pathway-in-the-sky display concept shown in the second figure. For the vertical takeoff task from a confined helipad involving a short backup segment to an altitude of approximately 100 feet, an advanced display concept similar to that used in the Apache AH-64 for near-hover maneuvering was used.

The second simulation showed that the performance achieved in recovering (flying away) from an engine failure is highly dependent on pilot technique. Recoveries from engine failure are high workload tasks, requiring prompt action and close attention to the flightpath of the aircraft and its energy state (speed, altitude, rotor revolutions per minute (rpm)).

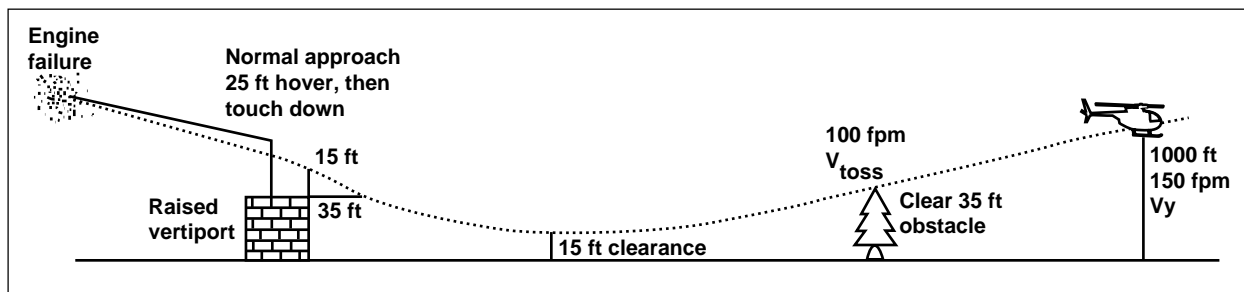


Fig. 1. Balked landing following engine failure.

The ability to exploit displays, especially at low airspeeds, is limited in the initial recovery portion near to the ground, where attention must be directed outside the cockpit. To assist the pilot with achieving maximum performance, a tactile cue was used on the pilot's collective lever to indicate when maximum power was being used from the operating engine. An additional cue, either tactile of a different character, or a display cue, was used to assist the pilot in setting optimum rotor rpm to maximize the climb performance during flyout maneuvers. The pilots considered the concepts effective and promising as aids to maximize performance.

Point of Contact: L. Iseler
(415) 604-0872

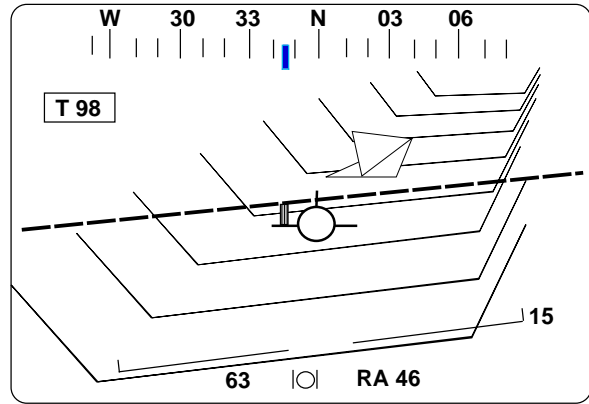


Fig. 2. Flightpath vector display.

Optimal Trajectories for Category-A Helicopters

Robert T. N. Chen, Yiyuan Zhao

A major safety concern to helicopter operations, especially in the critical flight phases of takeoff and landing from/to small, confined areas, is an engine failure. As a result, the Federal Aviation Administration (FAA) certifies a transport helicopter as either Category-A or Category-B, according to its ability to continue operations following engine failure. For the more stringent Category-A certification, a multiengine helicopter must be capable of continuing the flight with one engine inoperative (OEI). This and related requirements, while permitting operations from rooftops, oil rigs, or flight to areas where no emergency landing sites are available, significantly reduce the maximum payload of a Category-A transport helicopter. Typical Category-A helicopter vertical takeoff and landing procedures are shown in the figure.

Specifically, in a takeoff flight, the pilot must continue the takeoff (CTO) if an engine fails at or after passing the takeoff decision point (TDP), and should land or reject the takeoff (RTO), if an engine failure occurs at or before reaching the TDP. In a landing flight, the pilot must continue the landing

(CL) if an engine fails after the helicopter has passed the landing decision point (LDP). The pilot may either continue or balk the landing (BL) if an engine failure occurs at or before reaching the LDP. If no engine fails, the helicopter simply proceeds with the all-engine-operating (AEO) normal takeoff or landing.

The current certification process involves extensive flight tests that are potentially dangerous, costly, and time consuming. These tests require the pilot to simulate engine failures at increasingly critical conditions. Flight manuals based on these tests tend to provide very conservative recommendations with regard to maximum takeoff weight or required runway length. Usually, a single TDP or LDP is recommended for all flight conditions. As a result, the pilot cannot trade favorable ambient conditions or less takeoff weight for a shorter runway length. Analytical investigations into optimal takeoff and landing trajectories for OEI operations are needed to reduce the time and cost of flight testing and to enhance safety through appropriate cockpit display guidance.

Trajectory optimization studies have been conducted in FY95 to examine basic characteristics of a twin engine helicopter in Category-A, OEI takeoff and landing operations. These studies also investigated the associated heliport size requirements and the maximum gross weight capability of the helicopter. Using an augmented, point-mass model representative of the UH-60A helicopter, RTO, CTO, BL, and CL were investigated for both vertical takeoff and landing (VTOL) from/to a helipad and short takeoff and landing (STOL) from/to a clear heliport.

For VTOL operations, a linear backup procedure is assumed for normal AEO takeoff, and a straight-in procedure for normal landing. In RTO and CL, optimal trajectories were calculated to minimize the deviations of the touchdown point from the original takeoff point, subject to safe touchdown speed limits. For CTO and BL, two performance indices were considered: one minimizes the horizontal distance, and the other minimizes the maximum altitude loss. Both are subject to terminal constraints correspond-

ing to the steady OEI climb required by the FAA regulations.

In STOL operations, which use typical AEO takeoff and landing procedures, two trajectory optimization problems were formulated for OEI transitional flight: one to minimize the runway length requirements and another to maximize the takeoff weight. Both are subject to appropriately specified terminal conditions. Results indicate that in an OEI transitional flight, the optimal control strategies maneuver the helicopter to match the power required to the level of the OEI contingency power available, along the way trading among the helicopter's potential, kinetic, and rotor rotational energy sources. Other key results were documented and presented at 1995 conferences of the American Helicopter Society and the American Institute of Aeronautics and Astronautics.

Point of Contact: R. Chen
(415) 604-5008

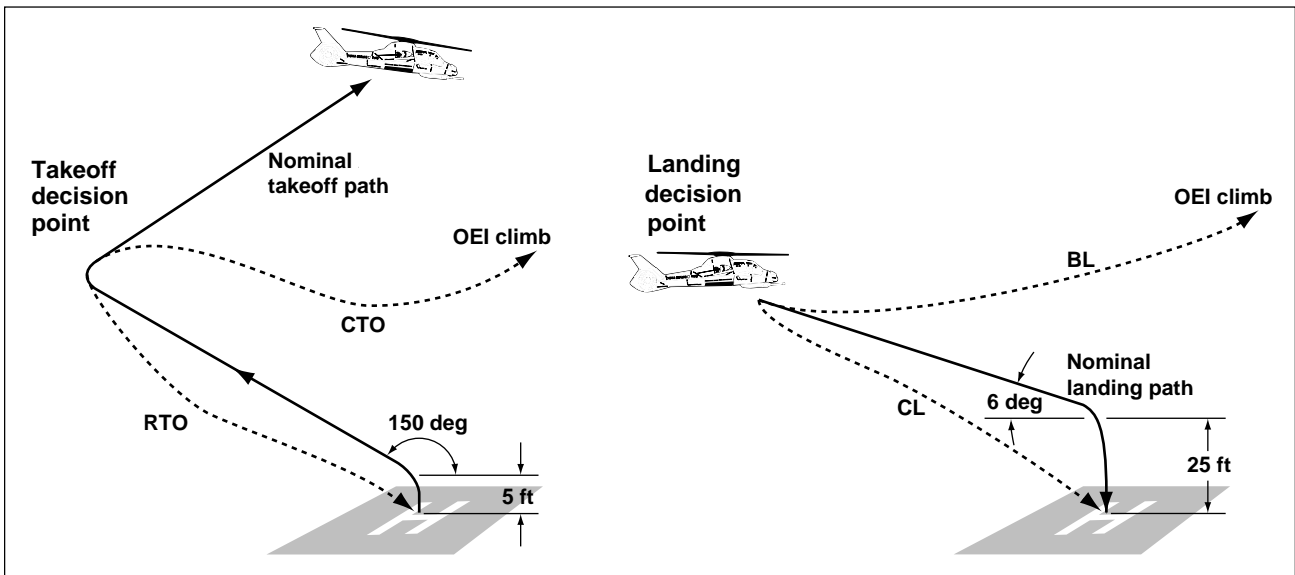


Fig. 1. Typical VTOL Category-A operation: backup takeoff and landing.

Pilot-Directed Automated Guidance System

Richard A. Coppenbarger, Chima E. Niaka

Pilots flying rotorcraft close to the ground in nap-of-the Earth (NOE) flight are confronted with unique guidance and control tasks that require a high degree of concentration. These flight tasks, which can be intensified by low visibility and high auxiliary workload conditions, include long-range mission planning as well as real-time piloting for obstacle avoidance. Although commonly associated with military operations, high workload missions requiring intensive guidance and control tasks are also encountered by civilian rotorcraft pilots involved with Emergency Medical Service and fire-fighting operations.

The Pilot-Directed Guidance (PDG) automation system, shown schematically in the first figure, assists pilots flying NOE by providing for (1) automated obstacle detection and avoidance; (2) terrain-following altitude control; and (3) airspeed control. PDG relies on real-time, forward-looking, sensor information to provide the system with knowledge of

obstacles and terrain in the vicinity of the rotorcraft. When the PDG system determines that an obstacle or terrain collision is imminent, the necessary avoidance control activity is provided automatically for the pilot. The PDG guidance logic is designed to favor lateral maneuvers over vertical maneuvers to provide greater concealment of the vehicle under hostile conditions. To provide a mechanism by which the pilot can override or modify automatic system commands, the cyclic and collective control inceptors are back-driven in the cockpit. With this implementation, the pilot is able to override the PDG system at any time by providing a sufficient force input to the control inceptors. To improve situational awareness and PDG system monitoring, a Helmet-Mounted Display (HMD) is also provided for the pilot. Along with rotorcraft and system-state information, the HMD displays inertially referenced, course-following symbology that resembles a pathway on the ground.

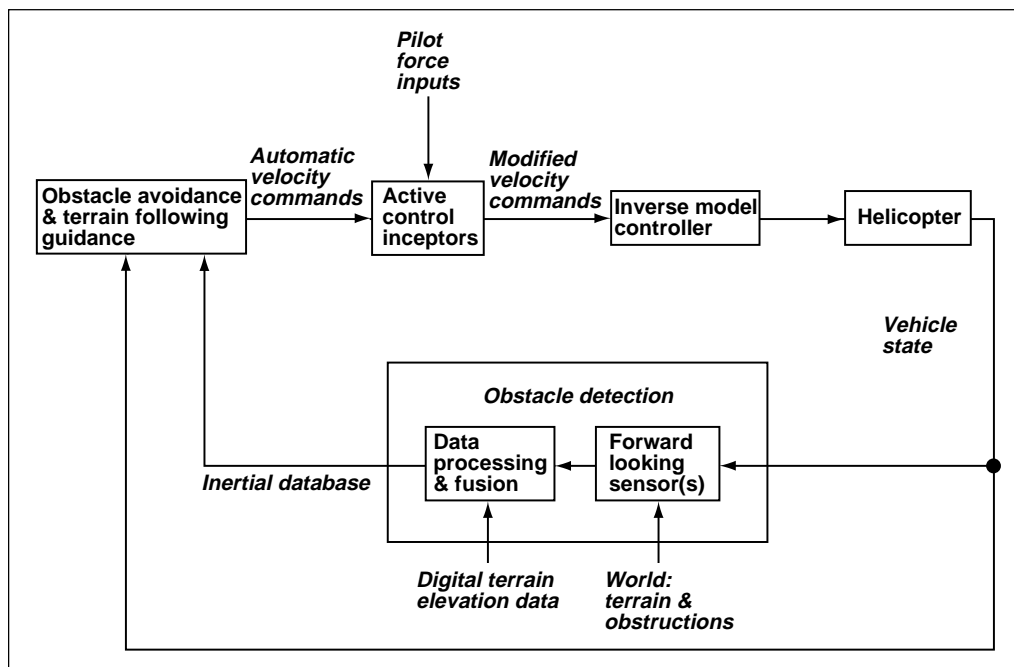


Fig. 1. Automated PDG system diagram.



Fig. 2. Cockpit view during VMS evaluation of PDG system.

The PDG controller is based on a novel, nonlinear design technique that facilitates its use over the entire flight envelope of the vehicle. The technique transforms the input-output map of the original nonlinear system into a much more tractable, linear, time-invariant form. The transformed system is then easily controlled using any well-known, linear-control, design technique. This technique was incorporated in the design of a nonlinear autopilot that was synthesized for a comprehensive, flight-test-validated, engineering model of the UH-60A Black Hawk helicopter for the PDG application. A simple, time-invariant, proportional-derivative type control law design is used and remains valid throughout the helicopter's operational flight envelope.

Simulation evaluation of the PDG system was conducted on the Ames Vertical Motion Simulator

(VMS). NASA research pilots, along with pilots from the rotorcraft industry, participated in this initial simulation study focused on concept validation and system refinement. A cockpit view of the simulation imagery is shown in the second figure. Pilots were given the opportunity to fly NOE missions, requiring intensive terrain and obstacle avoidance, with and without PDG automation. The results indicate that use of the PDG system greatly improves altitude, airspeed, and collision-avoidance performance, and provides a substantial reduction in pilot workload, especially under poor visibility conditions.

**Point of Contact: R. Coppenbarger
(415) 604-6440**

Real-Time Image-Based Obstacle Detection and Ranging System

Phillip Smith, Banavar Sridhar

Military and civilian rotorcraft are required to operate at low altitudes for emergency rescue, fire-fighting, and military missions in spite of the severe pilot workload requirements imposed by obstacle detection and avoidance tasks. Improved safety and reduced workload can be achieved by assisting pilots in detecting potential obstacles and in selecting obstacle-free flightpaths. Systems based on digital terrain maps have led to improved effectiveness for some missions but are limited by map resolution and the presence of unmapped, man-made, and natural obstacles. Further improvements in safety and effectiveness can be achieved through the use of onboard sensors to confirm terrain maps and detect unmapped obstacles.

The U.S. Army has taken the lead in developing active sensors, while requesting NASA to investigate complementary, low-observable, passive sensor technologies. The NASA effort has focused on techniques for obstacle detection and range estimation based on processing of images from two onboard cameras. This vision-based approach has the advantage of using inexpensive sensors and the ability to range to objects within a large field-of-view. In addition, the general approach applies unmodified to low-light-level television and infrared images to allow operations at night and in the presence of smoke. Similar techniques are applicable to images provided by other sensors (such as radars), potentially allowing for operations under poor weather conditions.

NASA has developed algorithms to detect, track, and range to potential obstacles based on input from two onboard cameras and an inertial navigation system. The processing of data collected from flight experiments has demonstrated the ability to estimate an obstacle's range with less than 10% error for obstacles up to a distance of 1000 feet. The general approach is to (1) identify regions of interest (called features) in an image from the master camera, (2) determine the location of each feature in the corresponding image from the slave camera, and (3) based on these measurements and the relative position of the cameras, estimate the three-

dimensional (3-D) position of the object giving rise to the feature. Using information from the helicopter's inertial navigation system, the feature's location in the next set of images can be predicted. When the next set of images becomes available, the feature's actual location is measured and compared with the predicted location to refine the 3-D position estimate. The first figure (see Color Plate 1 in the Appendix) shows a sample input image and the same image overlaid with the identified features color-coded to indicate the range between 0 and 1000 feet (red features indicate near range; green, middle range; and blue, far range).

A real-time implementation of the NASA algorithm was achieved through a Small Business Innovative Research effort with Innovative Configurations, Inc., in which a parallel computer system was developed to match the requirements of the passive ranging algorithm. Relying largely on commercial off-the-shelf products, the computer system consists of a 32-processor parallel computer delivering a peak performance of 2 GFlops (2 billion floating-point operations per second), two image digitizers, and an output display generator. The resulting three-board computer system (shown in the second figure with



Fig. 2. Real-time image-processing system.

two cameras and a display monitor) is compact enough for installation on board a helicopter. The parallel computer system has demonstrated the capability of acquiring image-pairs from two cameras, detecting and ranging to 300 simultaneous

features, and generating a pilot display at a sustained rate of 15 hertz.

Point of Contact: P. Smith
(415) 604-1747

Stall Control of Helicopter Blades

Khanh Nguyen

A numerical analysis was developed to evaluate the effectiveness of an automatic stall suppression system for helicopters. The analysis employed a finite element method and included unsteady aerodynamic effects (dynamic stall) and a nonuniform inflow model. The stall suppression system, based on a transfer matrix approach, employed a stall index as a measure of stall and blade-root actuation. The results showed that stall could effectively be suppressed

using higher harmonic, blade-root actuation at both cruise- and high-speed flight conditions. The effectiveness of the stall suppression system is shown in the two figures that compare the stall regions of the uncontrolled (first figure) and controlled (second figure) cases at a high-thrust, high-speed flight condition. The control amplitude was small, less than 1 degree. In a high-thrust, low-speed flight condition, stall was fairly insensitive to higher harmonic inputs.

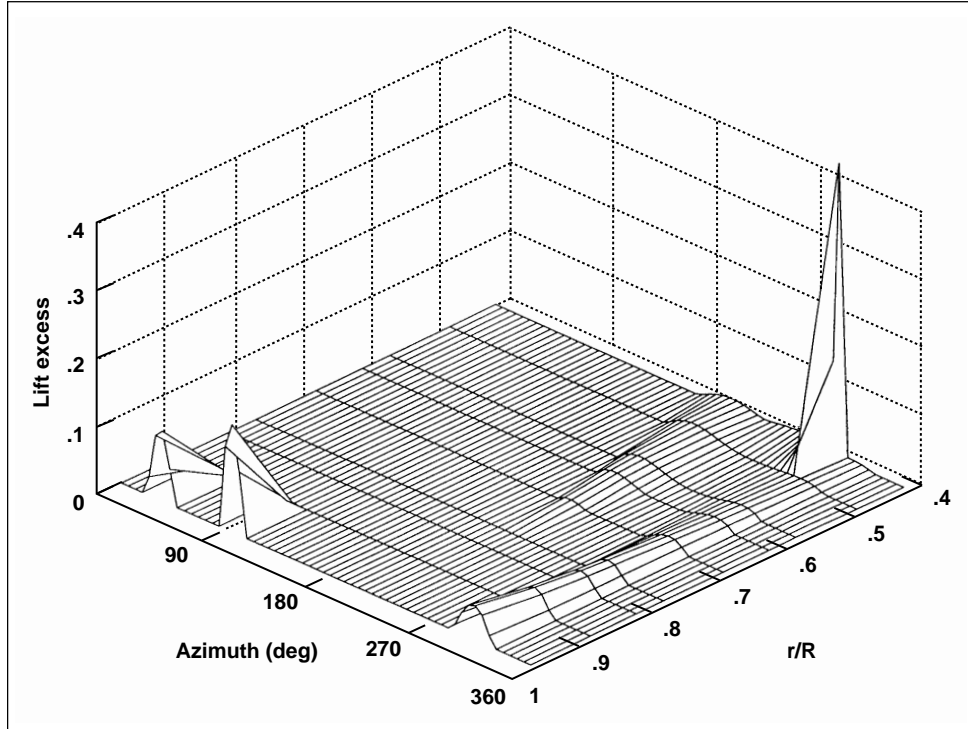


Fig. 1. Uncontrolled stall regions over rotor disk.

In general, stall suppression did not guarantee performance improvements. The results also showed the distinction between stall suppression and performance improvement with active control. When the controller aimed to reduce the shaft torque, rotor

performance improvement could be achieved with a small degradation in stall behavior.

Point of Contact: K. Nguyen
(415) 604-5043

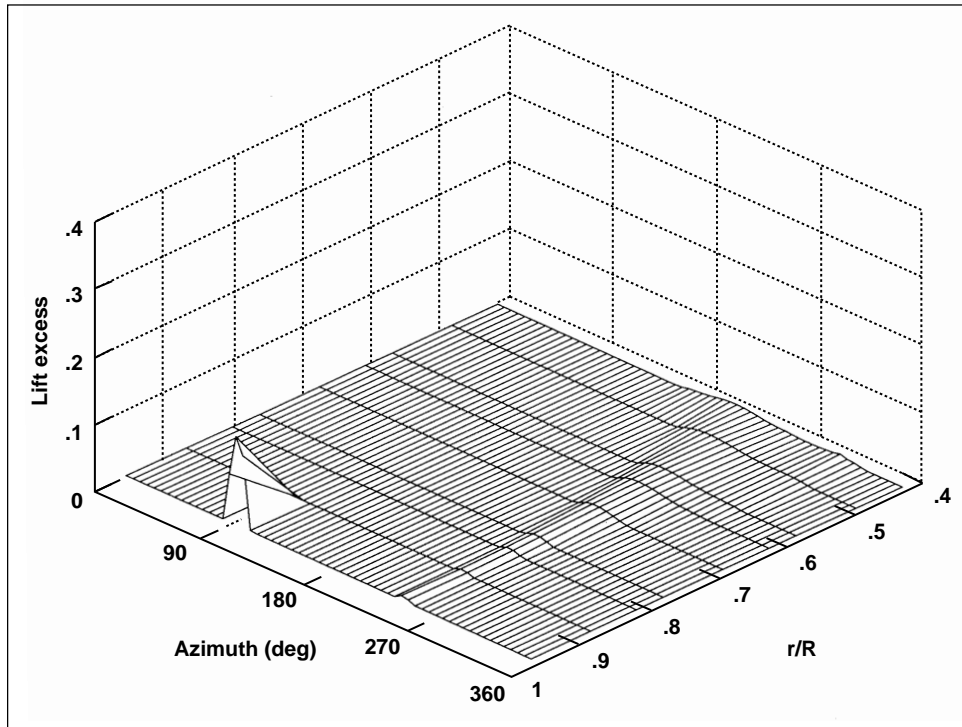


Fig. 2. Controlled stall regions over rotor disk.

UH-60A Airloads Program

Robert M. Kufeld, William G. Bousman

The UH-60A Airloads Program has collected high-quality pressure measurements from a UH-60A rotor system for over 800 flight conditions. A total of 221 pressure transducers were installed on one blade at nine radial and another 21 transducers were located near the blade leading edge between the radial arrays to provide information of the aerodynamic phenomenon of the rotor system in various flight conditions. This data is used to validate design codes, enabling faster and better design of helicopters.

The figure shows an example of the type of data available within this database. Here, the data from one leading edge pressure transducer located at $r/R = 0.865$ (where r is the arbitrary radius along the leading edge and R is the blade radius) is displayed for eight different descent rates ranging from 200 to 900 feet per minute, while the thrust of the rotor system and advanced ratio are maintained at a constant level. The interaction of the preceding blade's trailing vortex and pressure transducer blade is affected by the descent rate. The changes can be seen near the 270-degrees azimuth position as the down/up pressure pulse at a descent rate of 200 feet per minute transitions into three separate pressure pulses at 900 feet per minute.

This year, significant accomplishments were centered on improving the use of the data and the validation of the database. Utility was increased by adding calculations of normal force, chord force, pitching moment, and blade thrust from integrated pressure measurements to the database for selected flight conditions. These integrated values had been requested by numerous users.

Part of the validation effort (the search for unacceptable pressure transducers) has been going through a number of phases. This effort is, of course, required prior to integrating the pressures as noted above. Work is continuing in this area with a focus on a few transducers with marginal bias defects.

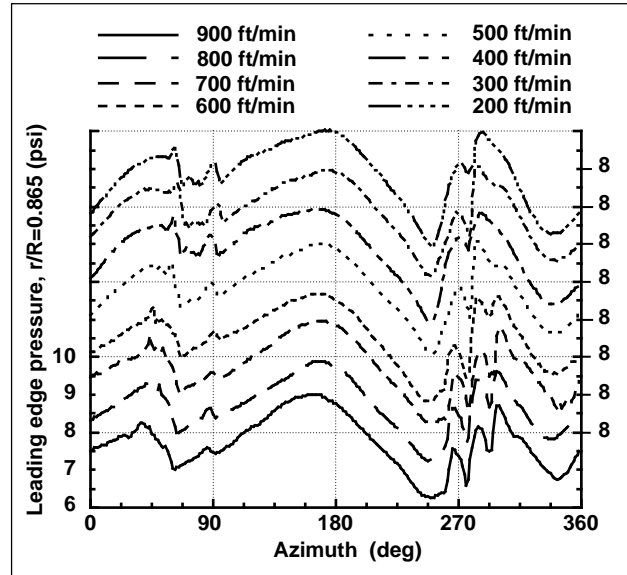


Fig. 1. Leading edge pressure at $r/R = 0.865$ versus rotor azimuth for different descent rates at constant rotor thrust and advance ratio.

In addition, comparisons between the flight test and wind tunnel data have been reported. Discrepancies in thrust, blade airloads, and disk angle of attack were noted. With respect to the airloads, further efforts indicate that most of the discrepancy is in the elastic motion of the blade, which, in flight, is poorly known. The very stiff swashplate of the tunnel model compared to the relatively soft swashplate for the flight vehicle result in different elastic deformation and, hence, airloads.

Point of Contact: R. Kufeld
(415) 604-5664

Rotor Data Correlation

Randall Peterson

The use of wind-tunnel test measurements, flight-test measurements, and analytical prediction plays a key role in the development of new rotor systems. Such tests are typically performed using a range of rotor system sizes and wind-tunnel test facilities. To assure the accuracy of wind-tunnel testing methodologies, a validation study is in progress using test results from model- and full-scale tests in comparison with flight-test data. This study is being conducted under the auspices of the U.S. Army/German Memorandum of Understanding on Cooperative Research in the field of helicopter aeromechanics. This comparison will determine the ability to accurately predict helicopter flight behavior from wind-tunnel experiments and the influence of the test facility on these results. Experimental data from a series of wind-tunnel tests, including both model- and full-scale experiments, are being studied.

Results of a recently completed model-scale test of a BO-105 hingeless rotor in the Deutsch-Niederlandischer Windkanal (DNW) are being studied. A 40% scale model BO-105 rotor was tested in five different test sections of the DNW wind tunnel with the intent to evaluate and identify the influence

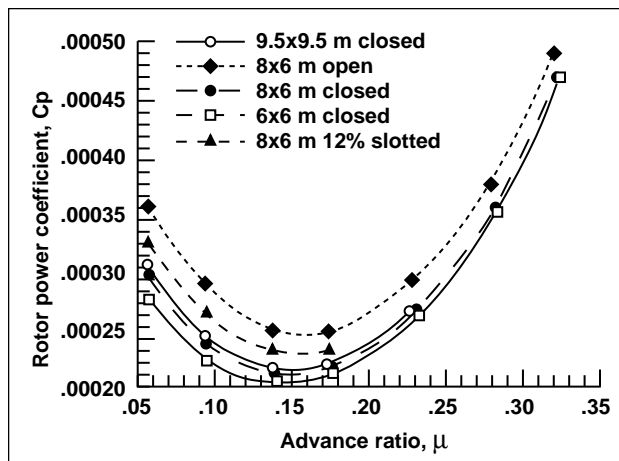


Fig. 1. Comparison of rotor power as a function of advance ratio without wall corrections for five different DNW test sections with identical rotor trim conditions.

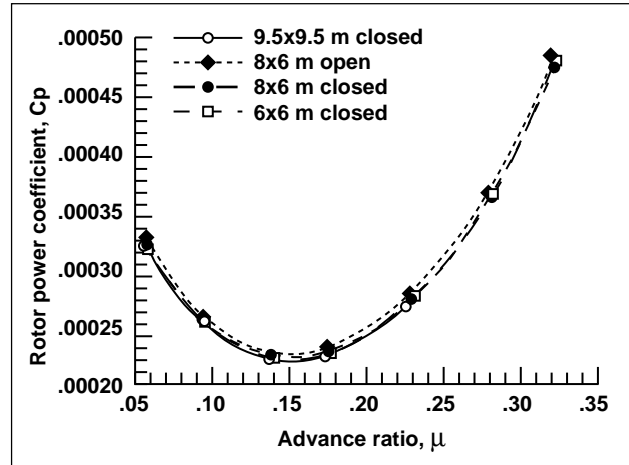


Fig. 2. Comparison of corrected rotor power as a function of advance ratio with wall corrections for four different DNW test sections with identical rotor trim conditions.

of the wind-tunnel walls on measured rotor performance. The influence of wind-tunnel walls has been reported by many researchers over the years. From these studies, numerous methods have been developed to account for the tunnel wall-induced effects in order to approximate free-flight conditions in the wind tunnel. Results from the DNW model-scale test are being used to evaluate the applicability of these methods for rotorcraft testing.

Results from the recently completed DNW test are shown. The influence of the wall-induced effects on rotor power as a function of tunnel speed are clearly seen in the first figure. This figure shows rotor power as a function of tunnel speed with rotor thrust and hub moments adjusted to match flight-test measurements. Data is presented for five different test section configurations. The influence of the tunnel walls clearly reduces as the tunnel speed increases. This trend is consistent with existing wall correction theories. The data presented in this figure has not been corrected for the wall-induced effects.

The second figure shows a comparison of model-scale rotor power as a function of tunnel speed with corrections for wall-induced effects applied. Angle-of-attack corrections as a function of rotor thrust and tunnel speed were determined based on existing wall correction theories. Application of the wall corrections to both the open and closed test section data does an excellent job of collapsing the data for all the tunnel speeds tested. The data for the 8 × 6 meter

slotted test section are not shown in this figure, as existing wall correction methodologies do not account for slotted test sections. These results indicate that existing wall correction theories are indeed valid for correcting or accounting for the tunnel wall-induced effects on rotors in a wind tunnel.

Point of Contact: R. Peterson
(415) 604-5044

Identification of Hub Loads Using Neural Networks

Sesi Kottapalli, Anita Abrego, Stephen Jacklin

The development and implementation of a robust, active-control system for helicopter dynamics must include an accurate representation of how the control inputs influence the measured outputs (in the present context, vibratory hub loads). These hub loads almost always behave nonlinearly with respect to the phase of a higher harmonic or individual blade pitch control input.

In the present study, neural networks are applied to model and predict experimentally measured vibratory hub loads. Data from a wind tunnel test of a four-bladed, hingeless rotor in forward flight (with individual blade control (IBC)) were used to provide 2-per-revolution and 3-per-revolution control amplitude, control phase, and vibratory hub loads.

In the *multiple-input, single-output* application case, a metric consisting of an equally weighted combination of five 4-per-revolution vibratory hub loads was used to characterize the hub loads. Using the control phase and/or amplitude as inputs and the vibratory hub loads metric as output, the radial-basis function (RBF) and back-propagation types of networks were trained. The RBF network is robust for interpolative purposes, including significant nonlinearities. The RBF network also works well when there are multiple inputs and a single output (prediction of nonlinear, nonbaseline metrics and accompanying baseline metrics). The back-propagation neural network is robust for interpolation, and with some guidance, produces acceptable extrapolations.

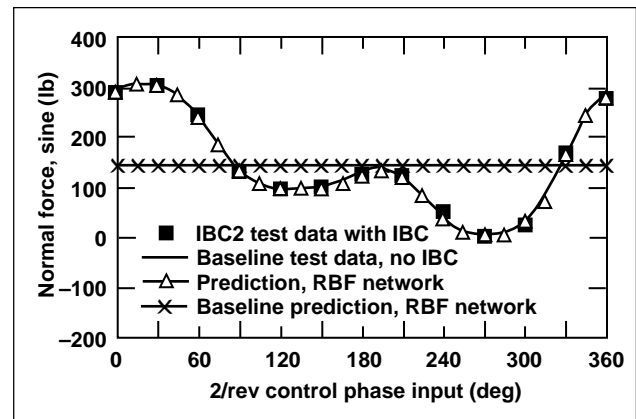


Fig. 1. Six-output application: RBF neural network modeling and prediction of sine component of normal force (includes baseline prediction).

In the second phase of this study, the multiple-input, multiple-output application was considered; modeling and prediction of cosine and sine components of measured rotorcraft hub loads were undertaken. Present results show that the RBF type of neural network accurately models these experimental data. This type of network works well for the present interpolative type of prediction involving significant nonlinearities. Consider the following multiple-input, multiple-output neural network application case:

four inputs (control amplitudes and phases at 2 per revolution and 3 per revolution) and six outputs (cosine and sine components of the normal force, pitching, and rolling moments). The figure shows a typical result from the present four-input, six-output neural networks application; in the figure, “IBC2 test”

refers to a particular wind tunnel test—the second United States/German IBC test.

Point of Contact: S. Kottapalli
(415) 604-3092

Comparison of Computational and Experimental Rotor Blade-Vortex Interactions

Megan McCluer

Computational predictions were compared to experimental acoustics data for a helicopter rotor blade interacting with a vortex. Acoustic measurements were acquired from an experiment performed in the Ames Research Center 80- by 120-Foot Wind Tunnel. The experiment was designed to examine the

aerodynamics and acoustics of parallel blade-vortex interaction (BVI).

The first figure is an illustration of the experimental setup in the wind tunnel. An independently generated vortex interacted with a small-scale, nonlifting helicopter rotor at the 180-degree azimuth

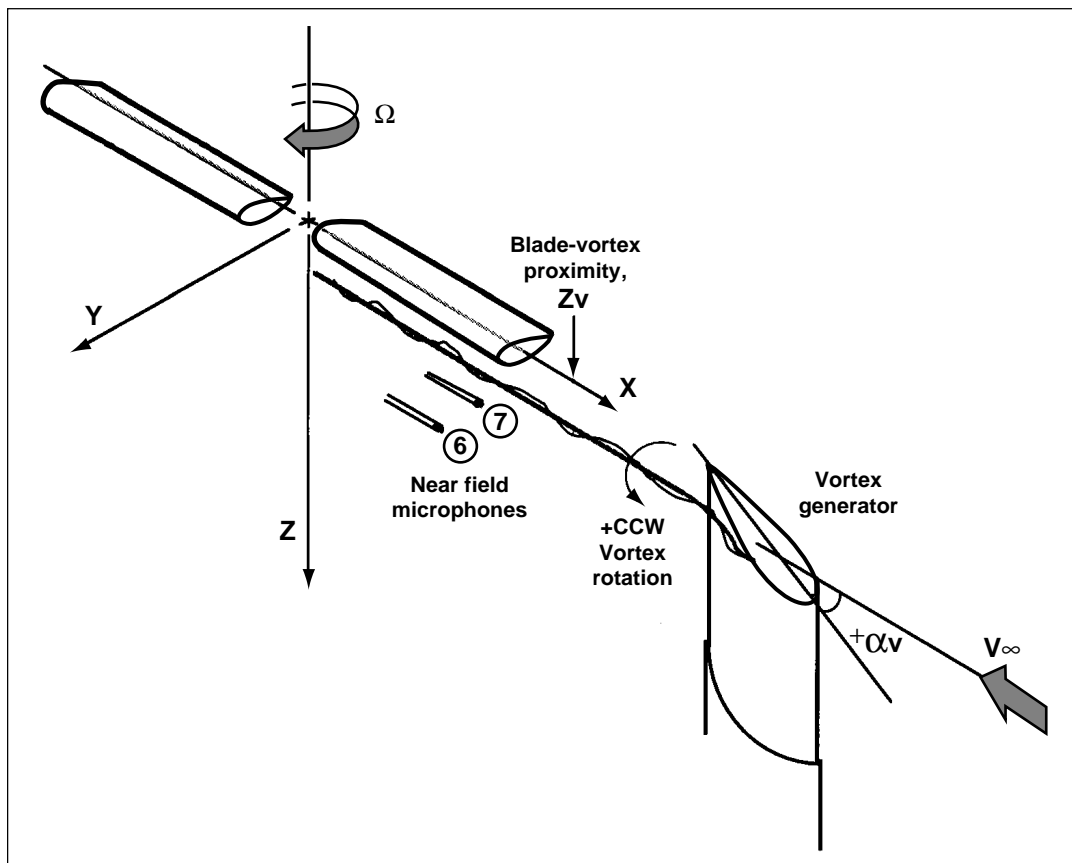


Fig. 1. Schematic of experimental setup in the wind tunnel test section.

angle to create the interaction in a controlled environment. Near-field pressure time histories were calculated using computational fluid dynamics (CFD). The Transonic Unsteady Rotor Navier-Stokes (TURNS) code was used to make comparisons with the acoustic pressure measurements at two microphone locations, with several test conditions. The test conditions that were examined included hover tip Mach numbers of 0.6 and 0.7, advance ratio of 0.2, positive and negative vortex rotation, and the vortex passing above and below the rotor blade by 0.25 rotor chords.

The second figure illustrates one example of computational and experimental data plotted

together. The results show that the CFD qualitatively predict the acoustic characteristics very well, but quantitatively overpredict the peak-to-peak sound pressure level by 15% in most cases. Additional calculations were performed to examine the effects of vortex strength, thickness, time accuracy, and directionality. This study validates the TURNS code for qualitative prediction of near-field acoustic pressures of controlled parallel blade-vortex interactions when interaction parameters are known.

Point of Contact: M. McCluer
(415) 604-0010

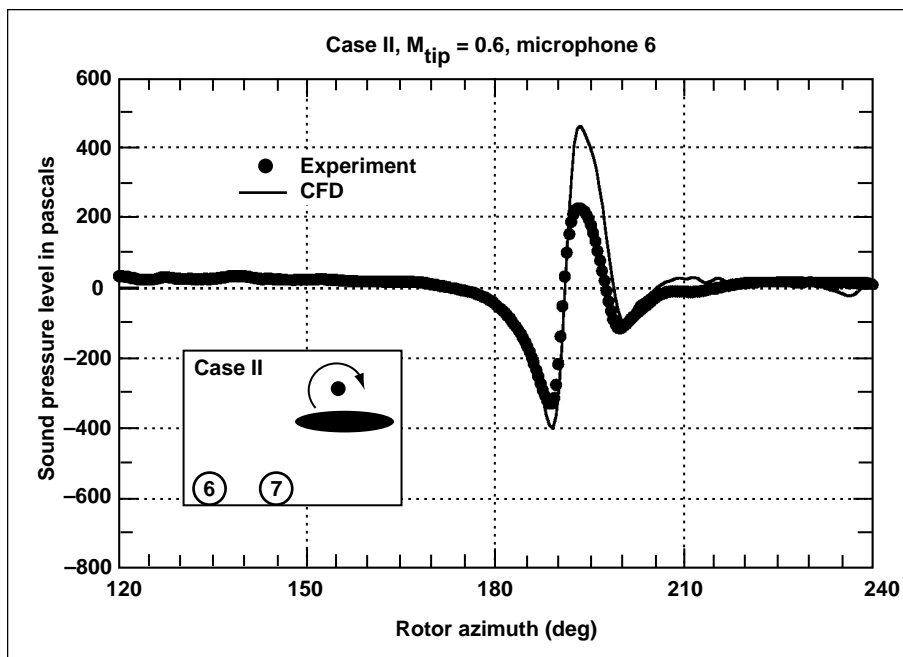


Fig. 2. Comparison of computational and experimental results.

Numerical Simulation of Tiltrotor Aerodynamics in Hover

Robert L. Meakin, William J. McCroskey

The aerodynamic “fountain effect” and wing “download” of the V-22 Osprey tiltrotor aircraft in hover have been simulated numerically. A detailed knowledge of these phenomena is important to the efficiency and noise control of tiltrotor aircraft. Vortical wakes of tiltrotors interact with the wings to form a recirculating flow condition over the fuselage/wing junction, known as the tiltrotor “fountain.” The rotor downwash over the wings results in massive regions of separated, turbulent flow on and beneath the wing, and the resultant download reduces the lifting capacity of the aircraft. Blade interactions with tip-vortices and the fountain are primary sources of noise.

This investigation, a pioneering, unsteady, Navier-Stokes simulation of a 0.658-scale, V-22 Osprey rotor and flapped-wing configuration, had the dual purpose of validating the computational fluid dynamics code and studying the fluid physics of tiltrotor download and fountain effects. The first figure shows the layout of the components and surface grids used in this simulation. The flow

visualizations in the second figure (see Color Plate 2 in the Appendix) mimic the hydrogen-bubble, flow-visualization technique of physical experiments; they show the development of the fountain flow field. The simulated conditions were derived from an experimental configuration tested in the Ames 40-by 80-Foot Wind Tunnel. The simulation includes accurate modeling of all geometric components of the test rig, including the rotating blades, wing, flaps, and support structure. The computed pressure distributions agree well with the experimentally measured values. The difference between computed and measured wing download is less than 1% of the rotor thrust.

The present simulation confirms previous heuristic descriptions of the aerodynamics of a tiltrotor in hover, except that the actual case appears to be more three-dimensional and unsteady than is usually assumed. Three-dimensional effects are especially important near the wing/fuselage junction and under the wings. The simulation has produced a very large

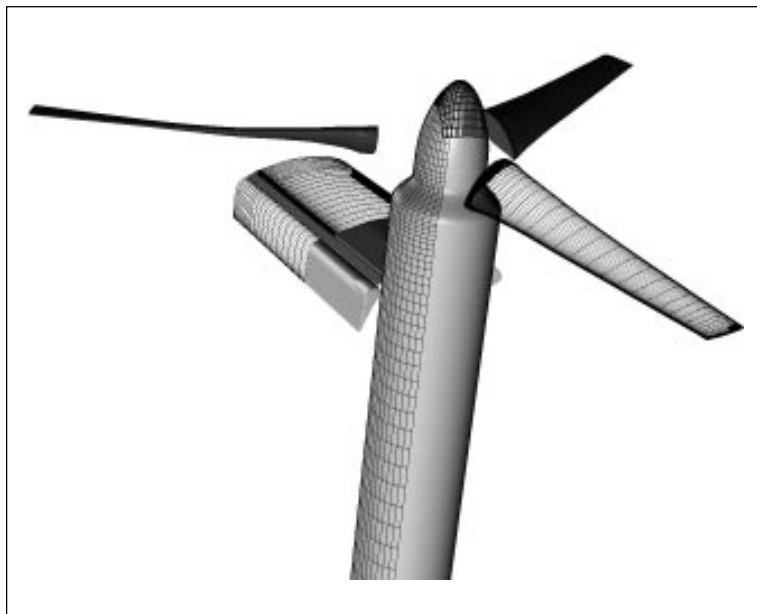


Fig. 1. Selected surface grid components used in the unsteady simulation of a V-22 Osprey rotor and wing configuration.

data set for a complex, unsteady problem. The complete geometry and solution files have been saved every 5 degrees of rotor rotation for 17 revolutions. The database is now available for further study of the V-22 Osprey in hover conditions, for coupling with acoustics models to study tiltrotor acoustics in

hover, and for testing post-process analysis software, such as graphical tools for flow visualization of unsteady problems.

Point of Contact: R. Meakin
(415) 604-3969

Wing Download Analysis

Paul Stremel

Wing download is a significant and limiting factor in the development of efficient tiltrotor aircraft, especially in hover where download limits payload. In recent years, numerous experimental and numerical investigations have been conducted to understand the aerodynamics associated with download and to identify ways to reduce it. These investigations included the experimental evaluations of “devices” for download reduction in the wind tunnel and in flight and the numerical prediction of download in two-dimensions to the full-vehicle simulation of the V-22 aircraft. While the experimental results will provide the overall variations in download, the aerodynamic mechanisms that increase, decrease, or contribute to download cannot be separated from the results.

While numerical analysis in two-dimensions is limited in that the three-dimensional flow field is not modeled, previous two-dimensional analysis on airfoil drag reduction with the use of fences has provided valuable insight into the flow mechanisms that contribute to download. However, three-dimensional flow must be modeled to analyze the flow about a wing under the influence of download. The full-vehicle simulations have provided an excellent representation of the flow-field aerodynamics, but are computationally prohibitive to address parametric studies to identify mechanisms for download reduction. A simplified model is needed to address wing download and to identify mechanisms for download reduction.

The simplified model for download consists of an isolated wing coupled with an actuator disk to model the rotor. The flow field surrounding the wing and actuator disk is computed by a numerical method

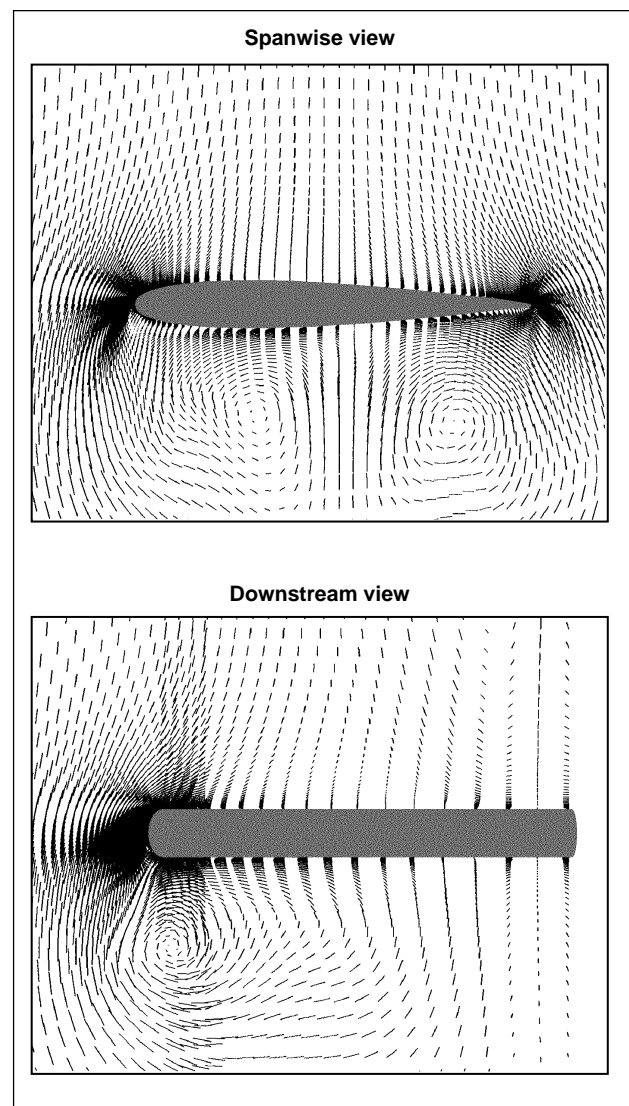


Fig. 1. Flow-field velocity vectors. (a) Spanwise view, (b) downstream view.

that combines the OVERFLOW computational fluid dynamics code and the PEGSUS domain connectivity program. In the present computations, an isolated wing of aspect ratio equal to 4 with a NACA 0012 section is considered. The wing is normal to the free-stream flow, and the actuator disk is not modeled. In the figure, the flow-field velocity vectors for the computed flow are shown for a spanwise view,

looking from the wing root toward the wing tip, and a view looking downstream. Near the wing tip, a pair of separated vortices are shown in the spanwise view. These vortices merge into the single separated vortex shown in the downstream view.

Point of Contact: P. Stremel
(415) 604-4563

Flow Field Analysis of a Model Proprotor in Hover

Gloria K. Yamauchi, Wayne Johnson

The objective of this work was to assess the ability of a state-of-the-art, thin-layer, Navier–Stokes analysis to predict general flow features of a highly twisted proprotor in hover. The Transonic Unsteady Rotor Navier–Stokes (TURNs) analysis developed by Dr. Srinivasan (Sterling Software) was used as a starting point for the study. Modifications to the blade root and far-field boundary conditions in the analysis were implemented. Data from two experiments using a model proprotor and a tip Mach number (M_{tip}) of 0.33 were used to validate the modified analysis.

The collective pitch in the analysis was adjusted to match the measured thrust. Calculations were then compared with measured hover performance, surface pressures, and wake geometry. Differences in calculated and measured figure of merit (FM) ranged from less than 1% at low thrust to 7% at high thrust coefficients (C_T) (see first figure). This level of difference is comparable to results from previous helicopter rotor performance validation studies. For both low- and high-thrust levels, differences between calculated and measured section normal force coefficient and surface pressures decreased with increasing radial station, with good agreement at

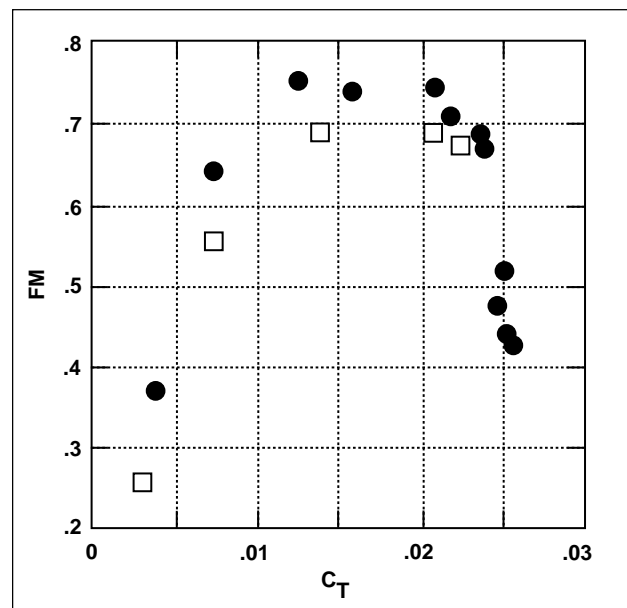


Fig. 1. Figures of merit (FM) at various thrust coefficients for comparison of proprotor performance for $M_{tip} = 0.33$ (data—solid symbols; analysis—open symbols).

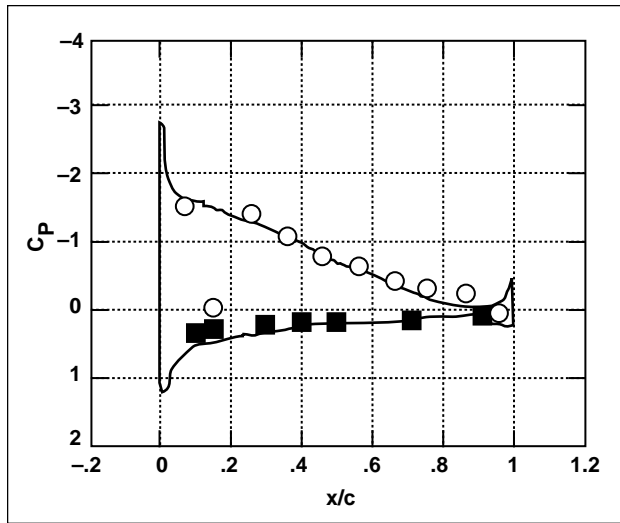


Fig. 2. Pressure coefficients (C_p) at $0.75R$ for $C_T = 0.02$ and $M_{tip} = 0.33$ (data—solid symbols; analysis—curve).

the most outboard measured station, namely, at the three-fourth blade radius (R) location (see second figure). The study also showed fair correlation with measured wake geometry, although calculated tip vortex descent rate and contraction rate were initially less than the measured rates. Based on these results, the analysis was determined to be sufficient for investigating highly-twisted rotors.

Point of Contact: G. Yamauchi
(415) 604-6719

Tiltrotor Aeroacoustic Model Isolated Rotor Checkout

Larry Young, Jeff Johnson

Assembly and checkout of the isolated rotor portion of the Tiltrotor Aeroacoustics Model (TRAM) was conducted in the Ames Research Center 80- by 120-Foot Wind Tunnel during the summer of 1995. TRAM is a small-scale, tiltrotor, test stand and is being developed under the Short Haul (Civil Tiltrotor) program to study the acoustics of tiltrotor aircraft. The isolated rotor model features a pressure-instrumented, 1/4 scale, V-22 proprotor, a rotating amplifier system,

a five-component rotor balance, and a series of drive train components that are interchangeable with the full-span model. The figure shows the TRAM in helicopter mode installed in the 80- by 120-foot wind tunnel.

Assembly of the model included installation of the rotor balance, static mast, rotor control system, and model utility systems. All model instrumentation



Fig. 1. TRAM isolated rotor in the Ames 80- by 120-Foot Wind Tunnel.

was installed and checked out during this entry. Gearbox lubrication and cooling systems were functionally checked and performed well. The drive train was run up to partial power and speeds and operated over the range of nacelle tilt angles. The pressure instrumented rotor was installed and checked out, and limited hover data was acquired.

TRAM is continuing checkout activities that include new drive motors, upgraded model utilities, and a new rotor control console.

Point of Contact: L. Young
(415) 604-4022

High-Speed Proprotor Design with Optimum Performance and Weight

Sesi Kottapalli, Thomas R. McCarthy, Aditi Chattopadhyay, Sen Zhang

The goal of this research is to develop a composite tailoring procedure for investigating aeroelastic stability of proprotors. A multilevel, multidisciplinary, design-optimization procedure is being developed. The design trade-offs associated with improvement in aeroelastic stability and aerodynamic performance are to be validated using rotorcraft codes that comprehensively include aerodynamic and aeroelastic effects.

Currently, the optimization procedure includes aerodynamic performance and structural design for both high-speed cruise and hover flight conditions. The aerodynamic objective functions to be maximized include the hover figure of merit (FM) and the high-speed cruise propulsive efficiency (η). The structural objective function to be minimized is taken as the wing weight (W_{wing}).

Details of the conditions under which optimization has been performed are as follows. Using the

XV-15 gimballed, three-bladed rotor as a reference rotor, optimization was performed for an airspeed of 300 knots and a rotor speed of 421 revolutions per minute (rpm); a lift/drag ratio of 5.3 was assumed for the aircraft. The hover rpm was 570. The vehicle weight was taken as 13,000 pounds. The aircraft was assumed to be operating at sea level during hover and at an altitude of 25,000 feet during cruise.

The figure shows the present, predicted improvements in aerodynamic performance and weight obtained using the multidisciplinary optimization procedure. Note that the blade weight (W_{blade}) is included only as a constraint in the optimization procedure, and the total weight, W_{total} , is defined as ($W_{\text{wing}} + 3 W_{\text{blade}}$).

Point of Contact: S. Kottapalli
(415) 604-3092

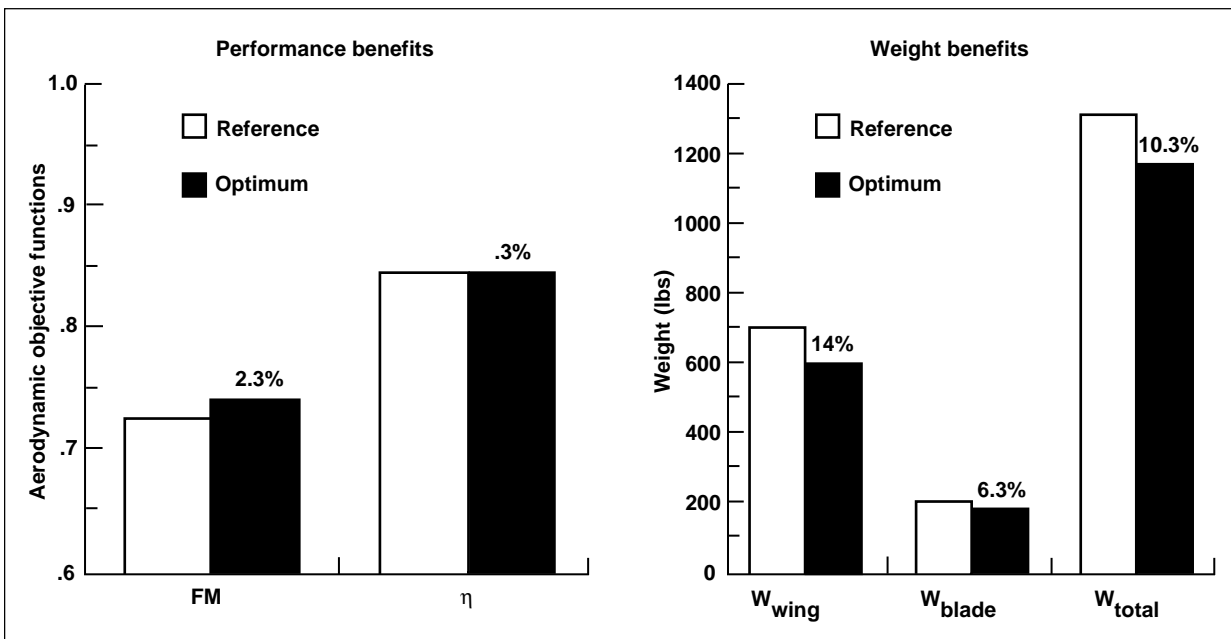


Fig. 1. Optimum aerodynamic and structural results.

Propulsion-Controlled Aircraft

John Bull, Robert Mah

Engineers and pilots from Ames Research Center played a key role in the first propulsion-controlled landing of a jet transport aircraft. The flight milestone occurred on August 29, 1995, with the successful flight-test landing of a McDonnell Douglas MD-11 at Dryden Flight Research Center, using only the aircraft's engine to control the landing. The successful flight was part of a NASA project to develop a computer-assisted engine control system that enables a pilot to land a plane safely when its normal control surfaces are disabled.

Following several incidents of hydraulic failures that resulted in loss of part or all of the aircraft's flight controls (most notably the 1989 crash of a DC-10 at Sioux City, Iowa), Dryden and Ames initiated development of a propulsion-controlled aircraft (PCA) system in which engine thrust provides the control needed to land an aircraft safely.

The PCA system uses standard autopilot controls already present in the cockpit, along with new programming in the aircraft's flight control computers. The PCA concept is simple—for pitch control, the program increases thrust to climb and reduces thrust to descend. To turn right, the PCA system increases the left engine thrust while decreasing the right engine thrust, and conversely to turn left. Since flight control in this mode is not normally a pilot task, extensive practice and intense concentration are required to perform this task manually with the engine throttles. Using computer-controlled thrust greatly improves flight precision and reduces pilot workload, making safe landings possible.

In piloted simulations in April-May 1995, Ames and Dryden pilots flew a large matrix of options, including several different PCA control modes in many different failure conditions and vehicle configurations. Transport pilots from several airlines, including the Airline Pilots Association Safety Committee, Air Transport Association, Boeing, McDonnell Douglas, and NASA-Federal Aviation Administration program managers also participated in the flight simulations.

In all, 30 pilots completed 500 landings using the Advanced Concepts Flight Simulator in the Crew Vehicle Systems Research Facility at Ames. Their work resulted in important pilot interface recommendations and validation of PCA system concepts for the successful MD-11 flight tests.

Extremely good acceptance by air transport pilots was demonstrated in the simulation tests using the PCA system. In addition to validating the control concepts in an expanded operational environment, the piloted simulation experiment highlighted and resolved several issues with regard to operational modes and displays.

This research will contribute to the design and development of an independent, emergency-backup flight control system for advanced multiengine jet transports using only thrust modulation for flightpath control.

Point of Contact: R. Mah
(415) 604-6044

Advanced Navigation Display System: Initial B-747 Simulation Evaluation

Vernol Battiste

The efficient movement of airport traffic under all weather conditions is critical to improving the overall efficiency of the National Airspace System. As weather conditions deteriorate and visibility is reduced, advanced cockpit aids are needed to support geographical orientation and navigation. In support of ground-taxi navigation research, this project (1) developed a prototype Advanced Navigation Display System (ANDS), as shown in the first figure (see Color Plate 3 in the Appendix); (2) developed a highly accurate database of the Chicago O'Hare airport; (3) developed two map configurations and the simulator visual scenes; and (4) performed a Crew Vehicle Systems Research Facility B-747 simulation to evaluate three map configurations (paper map, basic electronic map, and ANDS during simulated landing and surface operations at Chicago O'Hare under three visibility conditions: Visual Flight Rules, 600 Runway Visual Range (RVR), and 300 RVR).

Comparisons of taxi performance, workload, and user feedback showed that taxi time, during 300 feet visibility for the ANDS group, was reduced by 17% over the paper map group. Crews in the ANDS group made significantly fewer navigation errors and were able to recover from errors faster than crews in the paper and basic map groups. Crew head-down time was increased with both electronic maps; however, head-down duration was reduced with ANDS.

Additionally, crew workload was lower with either electronic map, but crews in the ANDS group experienced higher workload than crews in the basic map group. The questionnaire data showed that B-747 flightcrews had very little simulation or real world experience conducting ground taxi operations in low-visibility conditions. Captains averaged 14 hours and First Officers averaged 12 hours, which may account for some of the maneuvering errors. Crews responded very favorably to the ANDS display design. On a 0 to 10 scale with 10 = positive response, rating of how ANDS presented the basic airport were 9.4 for Captains and 9.7 for First Officers. Captains ratings of the ANDS display utility during low-visibility navigation was 9.4, while First Officers rated 9.8. The second figure presents additional crew comments.

In conclusion, crews in the ANDS group performed ground-taxi navigation significantly better than crews in the paper or basic map groups. Crew workload was reduced with either electronic map compared to the map information currently being used by flightcrews (paper maps). Finally, crews responded favorably to the ANDS display design and were able to use the system to support the ground-taxi navigation task.

Point of Contact: V. Battiste
(415) 604-3666

Crew Post Simulation design comments:

- "Could you rotate the text so it is always right side up?"
- "Stop bars should be included on the display."
- "The display was inherently clear and useful. Location . . . was rarely in doubt."
- "I think it's just wonderful the way it is. Great Job, great invention that major airlines need, to facilitate/save time and money for them, not to mention safety."
- "I like it. When can I have it in my airplane? Thanks."

Fig. 2. Crew post-simulation comments.

Hazard Posed by Lift-Generated Wakes

Vernon J. Rossow

The wake-vortex program was undertaken because the current capacity of airports is limited by the hazard posed by vortices that are shed by the wings of subsonic transport aircraft, as shown in the first figure. Although the vortex wake of a lead aircraft induces lifting, yawing, and pitching motions on a following aircraft, the most hazardous feature of the wake occurs as an overpowering rolling moment near the center of a vortex. For this reason, research into the characteristics of vortex wakes produced by lift generation has concentrated on the structure of the wakes and, in particular, on the rolling moments induced by the wakes that are encountered by following aircraft. Information obtained during the program supports various endeavors within NASA and the Federal Aviation Administration to safely increase the rate at which aircraft can land and takeoff from a given runway.

Because it is now the largest NASA wind-tunnel facility, and, consequently, has the greatest downstream test distance, the Ames 80- by 120-Foot Wind Tunnel was chosen for the experimental part of the investigation of wake vortices. In the two tests conducted in this facility to date, a 0.03 scale model of the Boeing 747 and of the McDonnell Douglas DC-10 have been used as the wake-generating models. In order to assess the characteristics of

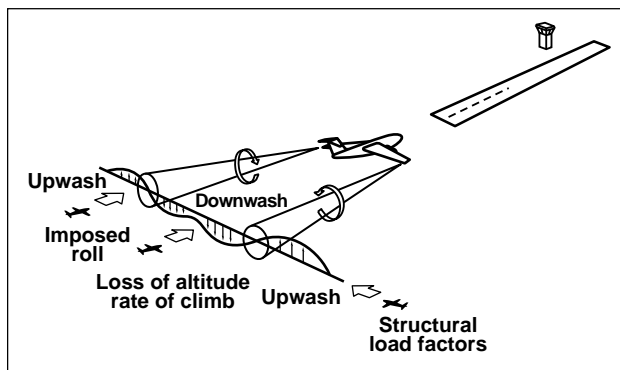


Fig. 1. Possible encounters with a lift-generated wake by a following aircraft.

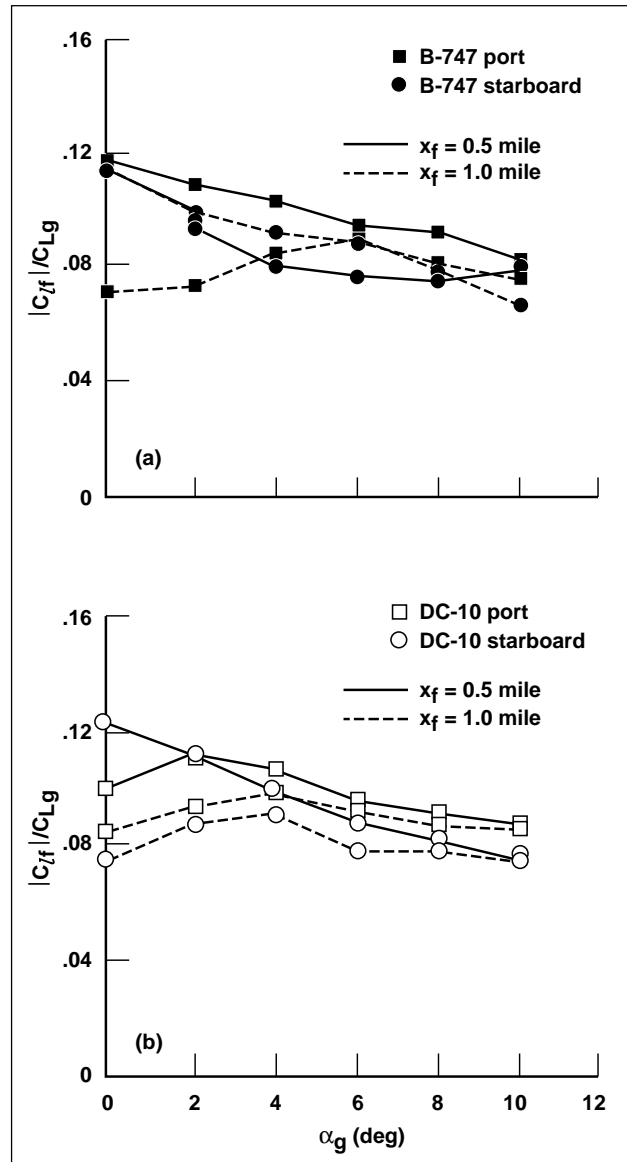


Fig. 2. Rolling moment induced on Lear Jet size following wing by wakes of the standard landing configurations of two wake-generating models as a function of angle of attack.

vortex wakes, following wings that range in size from 0.186 to 1.21 times the span of the wake-generating model were tested. Also, a two-component, hot-film anemometer probe is used to determine the up- and down-wash distributions in the wake at both the 81- and 162-foot downstream measuring stations (that is, simulations of full-scale distances of one-half and one mile). As an example of the data, measurements taken on the characteristics of the vortex wakes that trail from the models of the B-747 and the DC-10 are presented in the second figure as a

function of angle of attack. To improve the basis of comparison, the data are presented as the ratio of the wake-induced rolling moment on a following wing to the lift on the wake-generating models. It should be noted that the hazard characteristics of the two aircraft models are comparable. The current program continues to provide data and guidance for studies of the interaction of aircraft with vortex wakes.

Point of Contact: V. Rossow
(415) 604-4570

The Final Approach Spacing Tool

Tom Davis

Under development at Ames Research Center, the Center/TRACON Automation System is an air-traffic control automation system. The system is designed to support increasing demands for greater capacity and efficiency in the National Airspace System. The terminal area component of the system, the Final Approach Spacing Tool (FAST), is designed to assist terminal air-traffic controllers to efficiently manage and control arrival air traffic for the last 40 miles of flight down to the runway. The FAST system issues a series of sequencing, runway, heading, and speed advisories to the controllers to achieve an efficient flow of traffic that increases airport capacity, reduces delay, and reduces controller workload.

The objective of the research and development effort is to test the FAST system operationally in a series of phased functionality enhancements at the Dallas/Fort Worth TRACON. The operational field testing of the FAST system will allow researchers to further develop and assess the system with the end-users (the air-traffic controllers). The assessments include a series of observations with the FAST system operating in a shadow mode on live traffic data, real-time simulation evaluations of the FAST system at Ames and the Federal Aviation Administration (FAA)

Technical Center, and a limited operational assessment of the FAST system functionalities at Dallas/Fort Worth.

The development and field testing of the FAST system achieved a series of milestones during FY95. The "Passive" FAST functionality, which includes the sequence and runway advisories, has undergone extensive real-time simulations and shadow operations that resulted in the approval of the system for operational use in late 1995. The real-time simulations of the Dallas/Fort Worth airspace were conducted at the FAA Technical Center in cooperation with the FAA Air Traffic Requirements Division. These simulations established that the Passive FAST system met all interface, functionality, and performance requirements set by the FAA. The shadow tests validated the system's interfaces with FAA computers and performance with live air-traffic data. The shadow tests also allowed the observation of the system in an operational setting by a wider range of traffic management and controller personnel at the Dallas/Fort Worth TRACON.

Point of Contact: T. Davis
(415) 604-5438

Descent Advisor Field Evaluation

Steven Green, Everett Palmer, Robert Vivona

The Center/TRACON Automation System (CTAS) is designed to increase airspace capacity and flight efficiency in the extended terminal area by providing controllers with traffic management and clearance

advisories. The development and field evaluation of the Descent Advisor (DA) tool achieved a significant milestone with the completion of the Initial Descent Evaluation at the Denver Air Route Traffic Control Center in September 1995. The DA computes fuel-conservative descent trajectories and provides the Center controller with clearance advisories for efficient arrival sequencing and traffic separation.

The field-test objectives included analysis of DA trajectory prediction accuracy, human factors assessment of a prototype DA clearance procedure and phraseology, evaluation of a prototype DA auxiliary display and interface, and shadow evaluation of DA tools for conflict and spacing advisories.

A total of 185 commercial flights participated in the test under a wide variety of weather, traffic, and delay conditions. The flights comprised nine aircraft types, operated by three air carriers, including turboprops and jets (conventional and flight management system (FMS)-equipped). Preliminary results were good with an arrival time prediction accuracy within 20 seconds for a 15–20 minute trajectory prediction and a single descent advisory in cruise. An example flight is illustrated in the first figure.

Prototype DA procedures and phraseology were developed in collaboration with the Federal Aviation Administration (FAA) and the airlines, and were published in a Jeppesen chart. Based on standard phraseology, these procedures enabled pilots to take maximum advantage of their FMS capability while meeting air-traffic control constraints in a predictable manner. A “holistic” approach was taken to simultaneously evaluate the procedures from both the pilot and controller perspectives via subject interviews and observers at the sector and in the cockpit. Preliminary results are positive with nearly every pilot effectively executing the procedure with no prior formal training.

The DA auxiliary display (shown in part (a) of the second figure) effectively supported the test and demonstrated the feasibility of utilizing commercial-off-the-shelf hardware to provide controllers with CTAS advisories with minimum integration with FAA

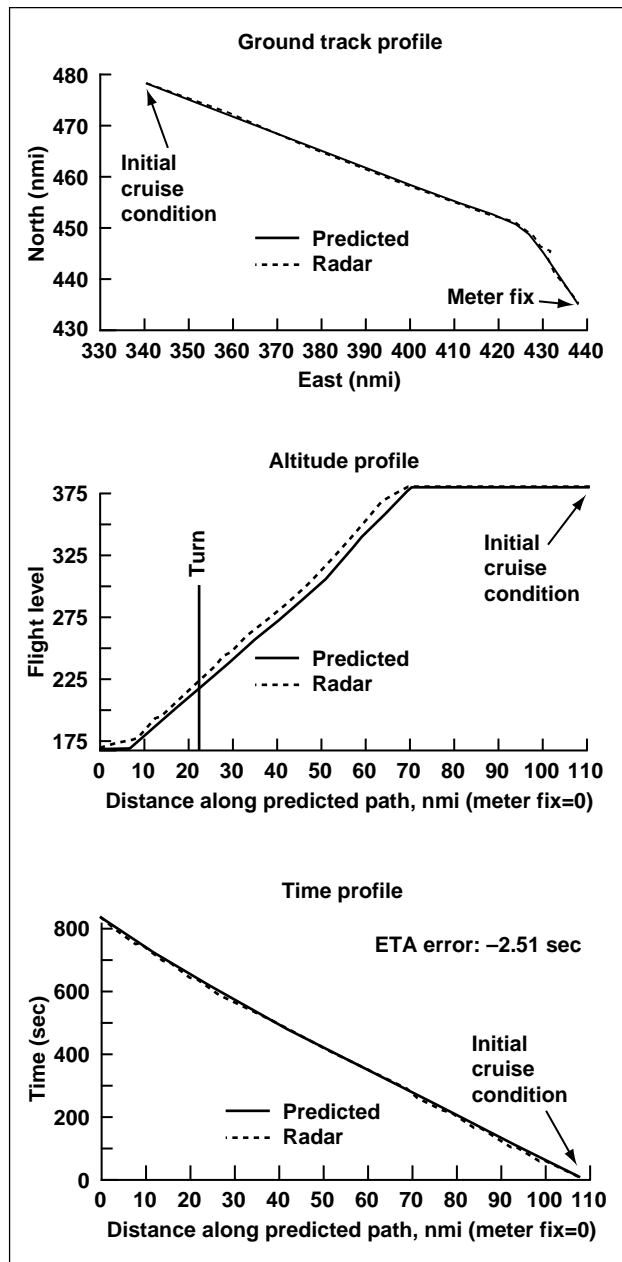


Fig. 1. Trajectory prediction accuracy for an FMS-equipped Boeing 757.



Fig. 2(a). DA auxiliary display and interface located directly behind the sectors participating in the evaluation.



Fig. 2(b). CTAS station, located in the Denver Center Traffic Management Unit, includes both the CTAS TMA (four Sun workstations) and the ACARS terminal (workstation on upper right).

systems. The CTAS Traffic Management Advisor (TMA) was operated during the test (shown in part (b) of the second figure) to provide the DA with scheduled arrival times for each flight. The conflict and spacing tools were not only effective in shadow evaluations, but were also found to be indispensable in setting up particular traffic scenarios for flights participating in the test.

In collaboration with United Airlines, an Airline Communications Addressing and Reporting System (ACARS) air/ground datalink terminal was installed at the Denver Center CTAS station and used to

exchange data between United flights and CTAS. Participating flights downlinked aircraft and atmospheric state in cruise for validating CTAS data, flight status for scheduling and delay preference, and aircraft weight for tuning CTAS predictions. For some FMS-equipped aircraft, CTAS wind profiles were uplinked to the aircraft to improve FMS accuracy and compatibility.

**Point of Contact: S. Green
(415) 604-5431**

Scene-Linked Symbology for Low-Visibility Taxi

David Foyle, Robert S. McCann

As part of NASA's Terminal Area Productivity (TAP) program, this project is focused on developing candidate cockpit display technology for the improvement of civil transport (airline) taxi performance for navigation and traffic avoidance under low-visibility conditions (fog or rain in which visibility is limited to about 300 feet). Specifically, this display technology involves displaying symbology on a head-up display (HUD). A HUD is a clear, glass display mounted in the aircraft that enables the pilot to see through the display to view the out-the-window taxiway and to see information that is reflected on the display itself. This allows for viewing of display information while still maintaining out-the-window viewing.

For this project, candidate HUD symbology that contains aircraft instrumentation information and current location displayed on a virtual "billboard," as well as pictorial augmentations to the scene, has been developed as shown in the figure. The symbology is projected virtually in a three-dimensional fashion so that the symbology objects move and change size as if they actually existed in the out-the-window scene. This is termed "scene-linked

symbology." The figure shows a virtual billboard that includes aircraft status information and ground location. The top line contains the aircraft's current ground speed (20 knots, "20 GS"). This is a dynamic readout and it changes, as appropriate. Similarly, the ground control radio frequency that is currently set is shown ("GND CTL 118.50"). The other two lines on the virtual billboard represent the aircraft's current airport location. The "Current, Last/Next" format represents current runway or taxiway segment ("Inner Taxiway"), the last intersection passed ("Alpha"), and the next intersection upcoming ("Bravo").

The pictorial scene augmentations include visual enhancements that aid the pilot in following the taxiway clearance and completing turns. Vertical cones on the side of the commanded taxiway path depict the cleared route on the HUD in superimposed symbology (as in "Pink 5" at Chicago O'Hare airport). These are conformal and represent a virtual representation of the cleared taxi route on the HUD. The side cones and the centerline markings are shown repeated every 50 feet down the taxiway. The vertical development and constant spacing should

yield increased capability for estimating ground speed, drift, and look-ahead capability for turns. Turn "countdown" warnings are shown in which each turn has countdown (4, 3, and 2) centerline lights that appear (300, 200, and 100 feet, respectively) before each turn and give added distance cues for the turn. Virtual turn signs (with the arrows) give another cue that there is a necessary turn. In addition, the angle of the arrow on the sign represents the true angle of the

turn (that is, 30 degrees right for a 30-degree right turn). All of the HUD symbology is scene-linked (virtually projected as if they were real objects in the world), allowing the pilot to process the symbology in parallel with other traffic, including possible incursions.

Point of Contact: D. Foyle
(415) 604-3053

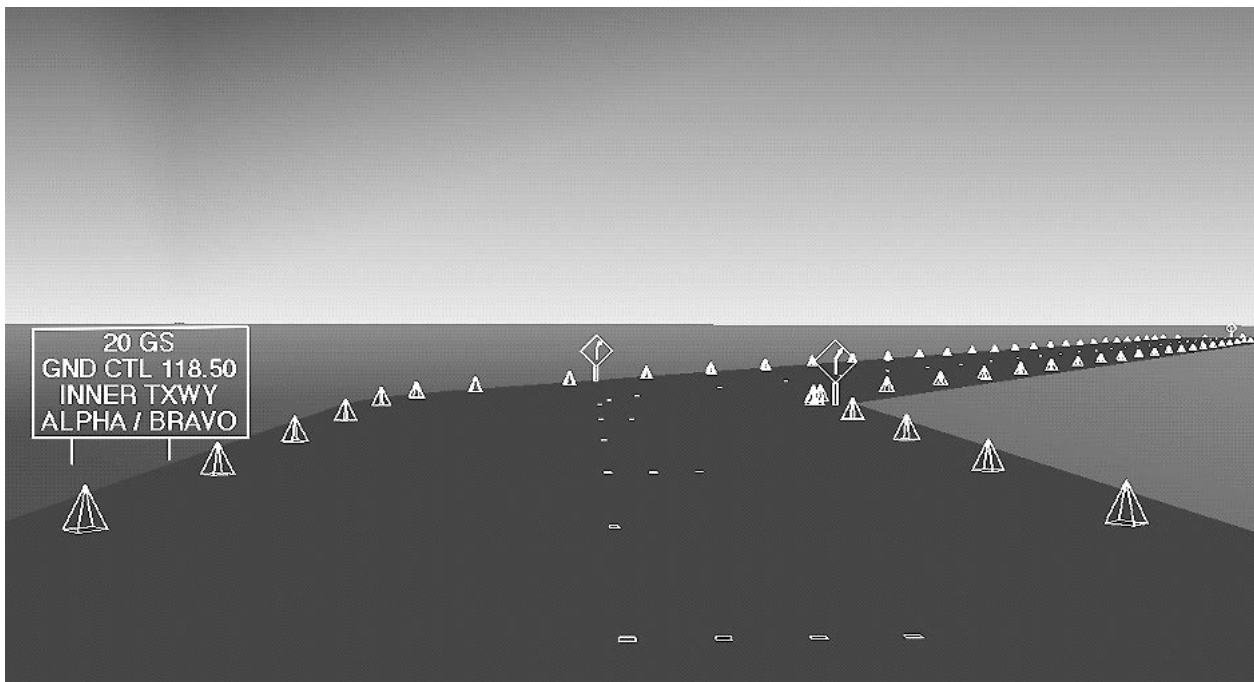


Fig. 1. Scene-linked symbology (in white) superimposed on runway scene.

DC-10 Airframe Noise Source Location with Ames' Phased-Array Microphone Antenna

Julie Hayes, M. Watts

To achieve NASA and industry goals of reduced airframe noise on commercial aircraft, an understanding of the character and interrelationships of airframe component noise sources must be developed. Tests like the Ames/McDonnell Douglas 4.7% DC-10 model Airframe Noise Test conducted in the Ames 40- by 80-Foot Wind Tunnel are important to the accomplishment of these objectives. For the first time, the use of the Ames phased-array microphone antenna as an interactive research tool was fully realized. The objectives of the airframe noise tests were to identify and characterize component noise sources and to measure the effectiveness of noise-reduction treatments such as flap-tip fences. Without the background noise reduction and the noise-source location technology of the Microphone Array Phased Processing System antenna, these objectives would not have been possible.

To contrast the ability of conventional microphone measurements with those of a phased-array antenna, the first figure shows the power spectrum of a typical single microphone located 10 feet from the DC-10 model with the response of the microphone array at the same position. The top two curves are the sound-pressure level measured by a single microphone within the array. The lower two curves are the maximum sound-pressure response for each frequency measured in the plane scanned by the antenna. The antenna curves are lower in amplitude than the single microphone curves because the noise from the wind-tunnel environment has been removed. Notice that by removing the background noise, interesting spectral features are revealed.

During the DC-10 test, the importance of the flap-side edge noise relative to other airframe components was measured for various configurations. For many configurations and over broad frequency ranges, the flap-side edge noise was the dominant

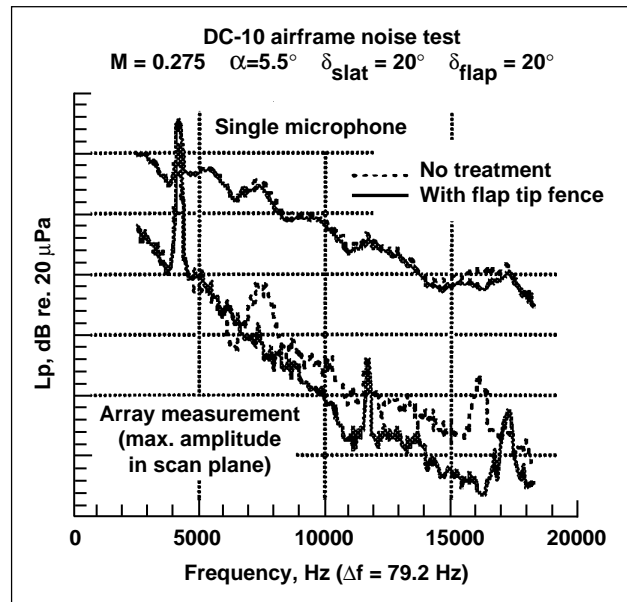


Fig. 1. Single microphone measurement versus antenna measurement. Measurements with and without noise-reduction treatment.

source by up to 10 decibels. The second figure (Color Plate 4 in the Appendix) shows the array map of the model with the relative noise-source strength shown with colored contours. The noise map represents the noise-source locations for a single frequency (10 kilohertz) for the configuration described in the first figure (no treatment). The dominant noise sources are the flap-side edges.

Point of Contact: J. Hayes/M. Watts
(415) 604-0807/6574

Aerodynamics and Noise Associated with Flap Tips

Bruce Storms, James C. Ross, Clif Horne, Julie Hayes

The current generation of commercial transport aircraft is substantially quieter than previous designs, largely due to the introduction of low-noise, high-bypass ratio turbofan engines. Increasingly stringent noise regulations will require further noise reductions, including the alleviation of airframe noise that is significant during approach and landing. For typical aircraft, the dominant airframe-noise sources are the flap tips, the leading-edge slats, and the landing gear.

As part of the Advanced Subsonic Technology Program, NASA is studying both the aerodynamics and noise associated with high-lift systems. A test was performed in the 7- by 10-Foot Wind Tunnel at Ames Research Center to study a high-lift system with a simplified wing geometry. The first figure shows the model installed in the test section. This installation is similar to a two-dimensional test arrangement with the wing main element spanning the wind tunnel.

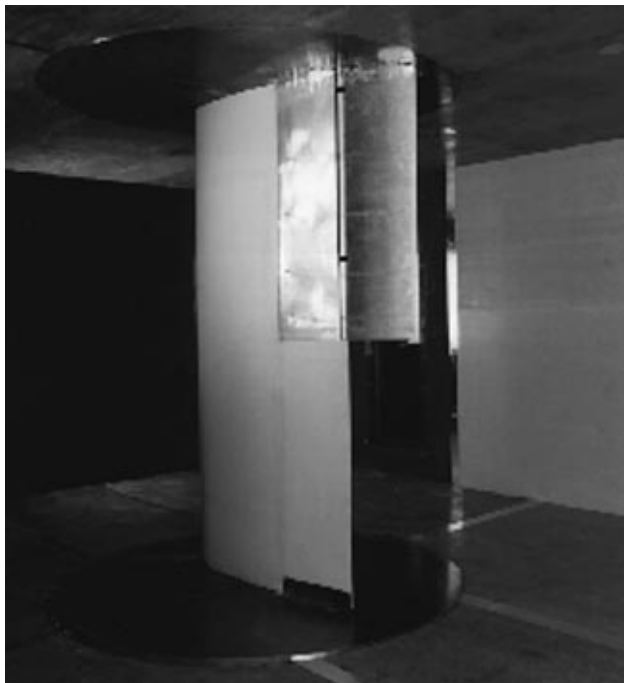


Fig. 1. Simple wing with part-span flap installed in the Ames 7- by 10-Foot Wind Tunnel.

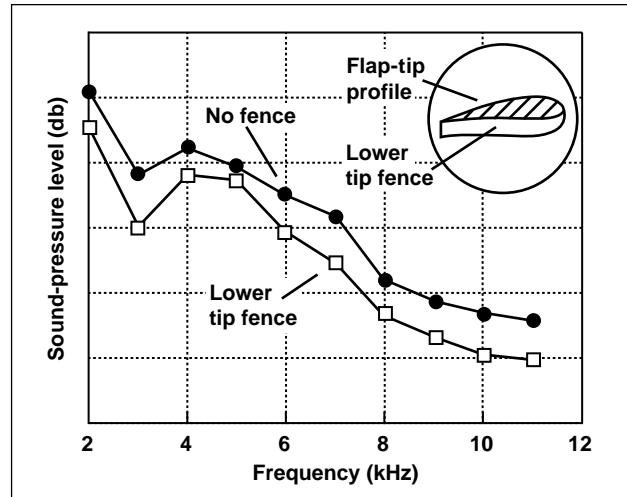


Fig. 2. Comparison of noise spectra with and without a lower tip fence.

However, the 30%-chord Fowler flap (and its associated cove region on the main element) only extends across half of the span to simulate the spanwise limitations of a typical high-lift system.

The test was a cooperative effort involving researchers from Ames, Boeing Commercial Airplane Group, and Stanford University. Ames researchers were responsible for the aerodynamic measurements that included steady and unsteady surface pressures, wake surveys, and flow visualization; Boeing researchers provided phased-array acoustic measurements for noise-source location; and Stanford researchers performed Navier-Stokes computations.

The acoustic measurements identified the flap-tip region as the dominant noise source for this simplified high-lift system. The associated aerodynamic measurements suggest that the noise is related to the formation of multiple vortices near the flap tip. The experimental results also confirmed the association of surface-pressure fluctuations with radiated noise as predicted by aeroacoustic theory. Several potential noise-reduction concepts were also evaluated during

the test. The greatest noise reduction was obtained using fences on the flap tip. The lower fence, in particular, provided significant noise reduction relative to the untreated flap as shown in the second figure. The noise-reduction levels measured in the

wind tunnel were later confirmed in a flight test of a general-aviation aircraft.

Point of Contact: B. Storms
(415) 604-1356

Flight Demonstration of Airframe-Noise Reduction Using Flap-Tip Fences

James C. Ross, Bruce Storms, Hiro Kumagai

Aerodynamic noise generated by the flow around the tips of trailing-edge flaps and leading-edge slats has been identified as a large component of the airframe noise produced by transport aircraft during approach and landing. As the engines for these airplanes become quieter, the need to reduce this lift-generated airframe noise will increase. The goal of the Advanced Subsonic Technology Noise Reduction Program is to reduce airframe noise by 4 decibels by 1997. A flight test was performed to demonstrate noise reduction using flap-tip fences on an airplane.

As a precursor to the flight test, wind-tunnel tests were carried out in the Ames 7- by 10-Foot Wind Tunnel to measure the noise reduction that could be achieved using a lower-surface fence at the tip of a Fowler flap. This fence extended below the flap lower surface by a distance approximately equal to the flap maximum thickness and resulted in significant noise reduction on a simple wing model.

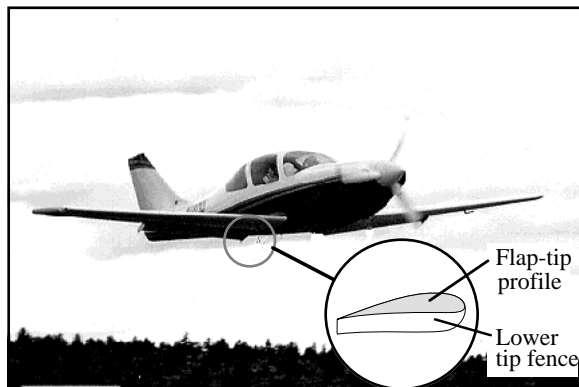


Fig. 1. Lancair IV in flight and details of the lower flap-tip fence.

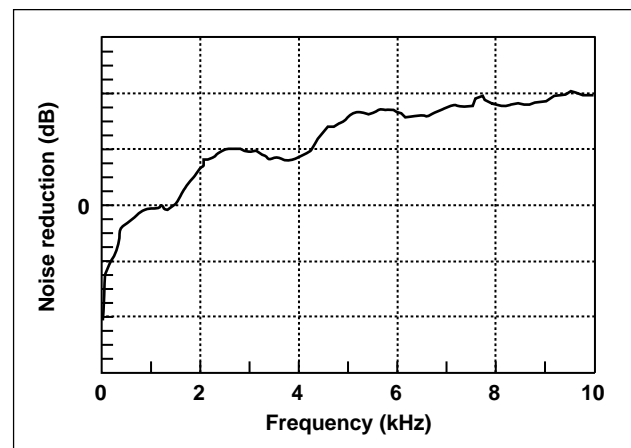


Fig. 2. Noise reduction versus frequency due to flap-tip fence on Lancair IV.

The flight test was conducted using a Lancair IV airplane which is shown in the first figure. This is a high-performance, four-seat kit plane that was chosen for its low drag and retractable landing gear. These features minimize extraneous noise and assure that the dominant airframe-noise sources are the flap tips. A total of 85 flyovers were performed at a nominal altitude of 64 feet above ground level during a three day period. The results of the flight test were nearly identical with those from the wind tunnel showing significant noise reduction for frequencies between 3 and 10 kilohertz as shown in the second figure.

Point of Contact: J. Ross
(415) 604-6722

Investigation of Lift-Enhancing Tabs on a Multielement Airfoil

Dale Ashby

The high-lift capability of an aircraft is an important parameter that affects takeoff and landing performance and low-speed maneuverability. The current trend in high-lift system design for transport aircraft is to return to simpler single-element, trailing-edge, flap systems and improve the performance of these systems to meet design requirements. Lift-enhancing tabs, shown in the first figure, are one of the more promising means of improving high-lift performance.

An experimental and computational investigation of the effect of lift-enhancing tabs on a two-element airfoil has been conducted. The objective of the study is to develop an understanding of the flow physics associated with lift-enhancing tabs on a multi-element airfoil. A NACA 63₂-215 ModB airfoil with a 30% chord Fowler flap was tested in the Ames 7- by 10-Foot Wind Tunnel. Lift-enhancing tabs of various heights were tested on both the main element and the flap for a variety of flap riggings. Computations of the flow over the two-element airfoil were performed using the two-dimensional, incompressible, Navier-Stokes code INS2D-UP. The computed results predicted all of the trends observed in the experimental data quite well.

When flow over the flap upper surface is attached, tabs mounted at the main element trailing edge (cove tabs) produce very little change in net airfoil lift. The lift of the main element is increased by the cove tab, but the increase is offset by a reduction in lift of the flap. At high flap deflections, however, the flow over the flap is separated, and cove tabs produce large increases in lift and corresponding reductions in drag by eliminating the separated flow. Cove tabs can achieve higher flap deflection angles

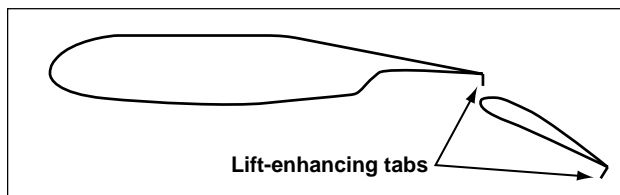


Fig. 1. Lift-enhancing tabs.

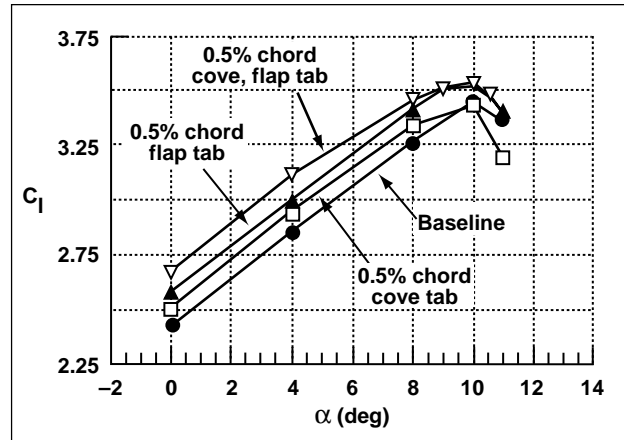


Fig. 2. Effect of lift-enhancing tabs on the lift coefficient of a two-element airfoil

and reduce the sensitivity of the airfoil lift to the size of the flap gap. Tabs attached to the flap trailing edge (flap tabs) effectively increase lift without significantly increasing drag. A combination of a cove tab and a flap tab increased the airfoil lift coefficient by 11% relative to the highest lift coefficient achieved by any baseline configuration at an angle of attack of 0 degrees, as shown in the second figure. Note that all configurations had a flap deflection angle of 39 degrees, but flap gap was varied to produce the highest lift coefficient for each configuration.

A simple, analytic model based on potential flow was developed to provide a more detailed understanding of how lift-enhancing tabs work. The tabs were modeled by a point vortex at the trailing edge. Sensitivity relationships were derived that provide a mathematical basis for explaining the effects of lift-enhancing tabs on a multielement airfoil. Results of the modeling effort indicate that the dominant effects of the tabs on the pressure distribution of each element of the airfoil can be captured with a potential flow model for cases with no flow separation.

Point of Contact: D. Ashby
(415) 604-5047

Intelligent Aircraft Control System

Charles Jorgensen, James Urness

The objective of this program is to develop and flight demonstrate a revolutionary aircraft control concept that can efficiently identify aircraft stability and control characteristics using neural networks. The work is being performed under a four-year, advanced concepts initiative involving two NASA centers (Ames Research Center and Dryden Flight Research Center), the McDonnell Douglas Aerospace Corporation, Washington University, and Tennessee Tech University. The program is developing adaptive, real-time control techniques for the reconfiguration of aircraft in response to off-nominal or unforeseen flight conditions. The program is intended to compensate for sudden major changes in stability and control behaviors that might result from failures in flight control actuation or damage to aircraft control surfaces.

In FY95, this program demonstrated that, through function learning and compression, neural networks are capable of significantly reducing the amount of tabular information an F-15 flight computer needs to provide control of the aircraft over the entire performance envelope. F-15 ACTIVE storage was reduced from 5.3 megabytes to 10.3 kilobytes using traditional methods. Code size requirements for software were reduced from 71,982 lines of code to 1823 lines, an approximate 39-to-1 increase in efficiency. This reduction was important because it permits the inclusion of new, advanced, adaptive learning software within the existing storage limitations of fielded aircraft designs.

Also during 1995, major improvements were made in the virtual-reality neural network simulator

of the Ames Neuro Engineering Laboratory. This simulator was designed to rapidly prototype and test new neural network control concepts by linking both software- and hardware-based neural controllers to high-fidelity aircraft simulation models, and then testing them in a piloted, virtual-reality environment using the same protocols that will be run in the 1996 flight tests of the real aircraft at Dryden. Several neural network designs were coded and demonstrated in the simulator in 1995, including the Leavenberg Marquardt network regenerating the compressed aerodynamic coefficients discussed previously.

New visualization software was implemented to facilitate the analysis of the phase II controller designs. This software allows controlled flight of a scaled image of the test aircraft, including its actuator dynamics. As test maneuvers are flown, the axis of the aircraft and its performance parameters such as exhaust pressure ratios are left in a graphic "contrail" hanging in the air behind the aircraft's flightpath. Each cross bar appearing on this contrail represents a one-second time slice. The slices are indexed in turn to dynamic strip charts showing detailed performance of the aircraft during the maneuver and under control of the neural networks. Such direct visual presentation permits more rapid identification of off-nominal control behavior points and dramatically increases the speed of neural controller evaluation.

Point of Contact: C. Jorgensen
(415)604-6725

Joint Strike Fighter Large-Scale Powered Model Thrust Calibration and Hover Performance

C. Hange, T. Naumowicz, D. Wardwell, T. Arledge

A Department of Defense program called Joint Advanced Strike Technology (JAST) was established in 1992, with joint participation between the Advanced Research Projects Agency, the National Aeronautics and Space Administration, U.S. Industry, and the United Kingdom's Ministry of Defense. This program investigates the technical feasibility of designing an affordable, lightweight, advanced-strike fighter aircraft. This concept has three variations—a Short Takeoff and Vertical Landing (STOVL)

attack aircraft for the U.S. Marine Corps, a U.S. Air Force Conventional Takeoff and Landing multirole fighter aircraft, and an aircraft carrier-capable fighter/attack aircraft for the U.S. Navy. The JAST program provides a unique opportunity to develop a truly common aircraft for expeditionary naval forces and fixed-base land use. The objective of the JAST program is to provide the technology that will make the next generation multiservice fighter aircraft affordable, flexible, and militarily viable.



Fig. 1. Lockheed Martin large-scale powered model at the Ames Outdoor Aerodynamics Research Facility.

Because the STOVL aircraft hovers, rather than taking off and landing like a conventional aircraft, it has a relatively complex propulsion system that generates complex jet-flow fields. The effects of these flow fields on the aircraft are critical to its performance and flightworthiness. Current mathematical predictions and small-scale testing cannot adequately predict these interactions, but large- to full-scale testing can. Since each STOVL concept will be using new technologies (mainly propulsive) to generate the vertical force required to hover, it is important to the overall program, in terms of risk reduction, that these new technologies be demonstrated. These technologies include the core propulsion system and associated nozzles, the propulsion control system, and large-scale to small-scale data scaling.

As shown in the figure, the Lockheed Martin large-scale powered model, utilizing a Pratt &

Whitney F100-229 engine, was tested at the Ames Outdoor Aerodynamic Research Facility. Thrust calibrations, jet plume pressure decay measurements, and hover tests were completed. Thrust calibration forces and digital engine control data were integrated so that each throttle setting gave a calibrated value for installed thrust. Hover testing included both a canard configuration and a horizontal tail configuration, and provided in and out-of-ground effect aerodynamic forces and moments. Since the model was powered by a real jet engine, critical large-scale STOVL propulsive technology was demonstrated. Preliminary comparisons show that previous small-scale results agree within expected norms with these large-scale results both in and out of ground effect.

**Point of Contact: D. Wardwell
(415) 604-6566**

Large-Scale Test of Lift and Control Enhancement for Advanced Fighter Aircraft

Jeffrey Samuels, Larry Meyn

Advanced, multirole aircraft will have low observables geometries and use control concepts that are fundamentally different than those of older aircraft. A joint National Aeronautics and Space Administration/U.S. Air Force research program was established to enhance the maneuver and control capability of these next-generation aircraft. For this program, a realistic, near-term technology, generic fighter concept was developed by the Innovative Concepts Branch at Wright-Patterson Air Force Base.

As part of this program, several small- and large-scale wind-tunnel models were built and tested with several mechanical and pneumatic lift augmentation and control concepts. Two wind-tunnel tests of the 55%-scale Subsonic High-Alpha Research Concepts (SHARC) model shown in the first figure were

conducted in the Ames 40- by 80-Foot Wind Tunnel. The objectives of these tests were to use mechanical and pneumatic devices to improve lift and control of the aircraft.

The controls portion of the tests included blowing slots on the forebody chine, forebody strakes, LE-extension spoilers, and asymmetric wing jet blowing (WJB) on the outboard wing panel. The size, shape, and location of the forebody strakes and LEX spoilers were based on previous small-scale results; test parameters included strake deflection angles and symmetric and asymmetric spoiler deployment. Test parameters for slot and WJB were location, exit direction, and mass flow.

Lift-enhancement concepts were used with numerous flap settings to improve maneuvering performance (that is, increase lift-to-drag ratio (L/D)) by energizing the boundary layer to prevent or delay flow separation. Concepts tested included co-rotating vane vortex generators (VGs), Gurney Flaps, wing slot blowing (WSB) at the leading-edge hinge line, and WJB. Test parameters for VGs were location, size, spacing, and orientation. WSB parameters were slot location, length, and mass flow. WJB parameters were mass flow (C_{μ}), nozzle height, and nozzle angle.

Nearly all high priority test objectives were met for WJB, asymmetric WJB, WSB, strakes, spoilers, VGs, and Gurney Flaps. Preliminary results indicate that forebody slot blowing was effective at generating control moments and side force, and compared well with 10%-scale model tests. Spoiler and strake data

generated additional control moments at high angle of attack and confirmed results from 10%-scale testing. Asymmetric WJB provided significant rolling moments.

WJB and WSB show beneficial aerodynamic effect and L/D for $C_{\mu} > 0.01$ (~2.8 pounds mass per second). However, VG configurations that improved high-lift performance in the 10%-scale tests failed to show similar improvements at large scale, and VG performance was insensitive to VG location, height, and spacing. Gurney Flaps increased lift coefficient but also generally increased drag. The second figure (see Color Plate 5 in the Appendix) shows an example of flow visualization studies conducted to characterize the flow field.

Point of Contact: J. Samuels
(415) 604-4235

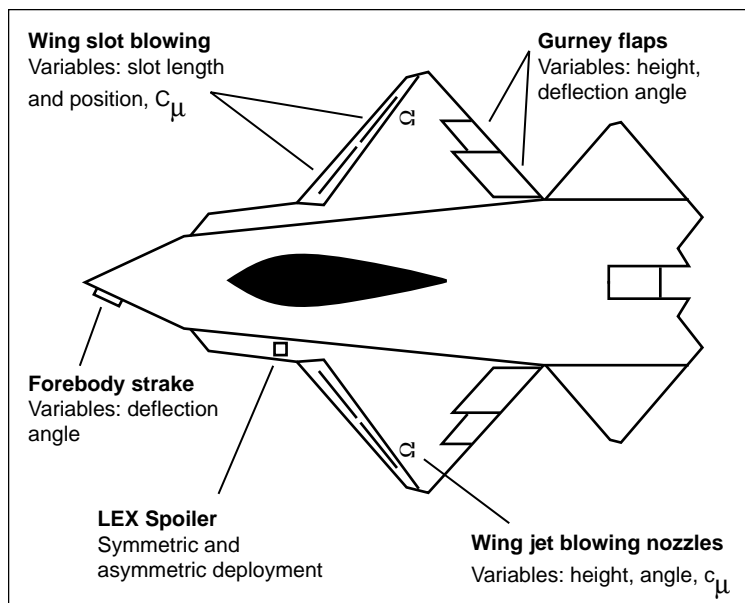


Fig. 1. SHARC test concepts.

Integrated Control Design Guidelines for STOVL Aircraft

James A. Franklin, William W. Y. Chung

Ames Research Center is participating in technology development for short takeoff vertical landing (STOVL) fighter aircraft as a member of the Joint Advanced Strike Technology program team. NASA's role in the program is to develop design guidelines for integrated flight/propulsion controls, support technology development for a demonstrator aircraft, and provide consultation on integrated control design to industry participants. The choice of control response types and pilot/vehicle interface strongly influences the operational capability for STOVL aircraft. Design criteria have not been developed for response characteristics for integrated control systems that offer the potential for significantly reducing pilot workload for STOVL operations. As part of NASA's effort, a simulation model of a lift fan configuration that represents a prospective STOVL concept was developed. This simulation has recently been used to evaluate design variations in integrated control systems, specifically translational-rate command system bandwidth and phase delay, to determine their influences on flying qualities for precision hover and for landing aboard an LPH amphibious assault ship.

Data indicate that the boundary for satisfactory/adequate flying qualities call for system bandwidths for translational-rate command of at least 0.3 radian per second for precision longitudinal control, 0.37 radian per second for lateral control, and 0.93 radian per second for height control. Recent flight data from the V/STOL Systems Research Aircraft at Ames support the longitudinal and lateral boundaries but indicate that a lower bandwidth of 0.6 radian per second could be accepted for the vertical axis. In addition, satisfactory/adequate boundaries are also indicated for bandwidths exceeding 1 radian per second for longitudinal and 0.7 radian per second for lateral control. Results of the simulation also show that satisfactory/adequate boundaries on phase delay fall at 0.6 second for longitudinal control, 0.7 second for lateral control, and 0.3 second for vertical control. In the figure, example results are shown for bandwidth and phase delay for the longitudinal translational-rate system.

Point of Contact: J. Franklin
(415) 604-6004

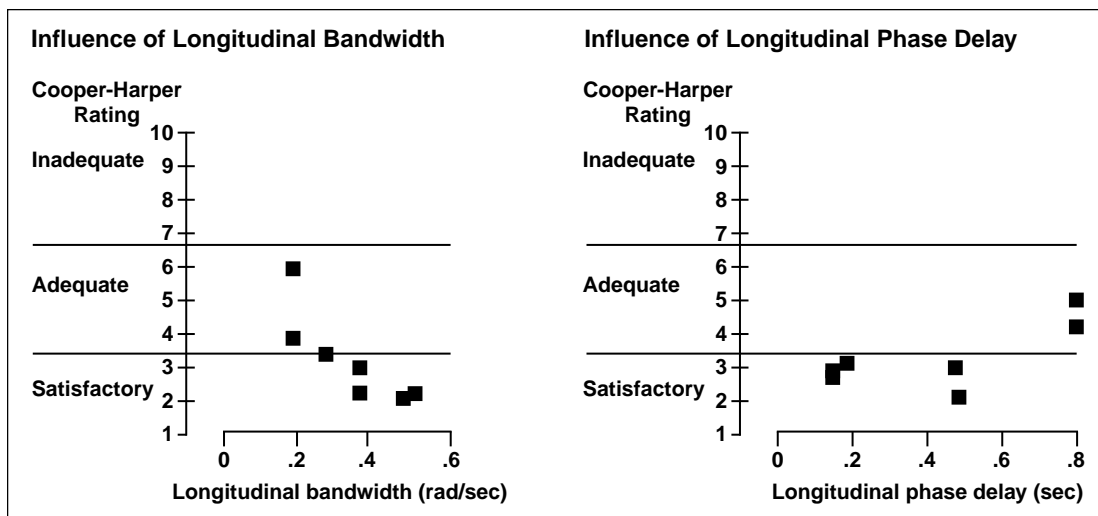


Fig. 1. Design criteria for translational-rate command systems for ASTOVL aircraft.

V/STOL Systems Research Aircraft Flight Research Program

James A. Franklin, Delamar M. Watson, Ernesto Morales III

Flight experiments were performed on Ames Research Center's vertical/short takeoff and landing (V/STOL) Systems Research Aircraft (shown in the figure) to obtain an assessment of the influence of advanced control modes and head-up displays on flying qualities for precision approach and landing operations. The principal contribution of results from these flight experiments is to the Advanced Research Project Agency's Advanced Short Takeoff and Landing aircraft technology program and to the U.S. industry participants in the Joint Advanced Strike Technology program. Results will also have broader applicability to other military and commercial V/STOL programs, particularly to the tiltrotor transport.

Evaluations were conducted for decelerating approaches to hover followed by a vertical landing and for slow landings for four control/display mode combinations. The control modes included (1) rate damping stability augmentation; (2) attitude command for pitch, roll, and yaw; (3) flightpath/acceleration command and translational-rate command; and (4) height damper with translational-rate command. Head-up displays that could be used in conjunction with these control modes provided flightpath tracking/pursuit guidance for the decelerating approach and a mixed horizontal and vertical presentation for precision hover and landing. Test pilot and engineer teams from the Naval Air Warfare Center, Boeing, Lockheed Martin, McDonnell Douglas, Northrop Grumman, Rolls-Royce, and the British Defence Research Agency participated in the program along with NASA research pilots from Ames and Lewis Research Centers.

Results of the pilots' evaluations indicated that satisfactory flying qualities could be achieved for the decelerating transition to hover with flightpath/longitudinal acceleration command systems and for precision hover and vertical landing with translational-rate command systems. These findings, in conjunction with related ground-based simulation

results, indicate that the flightpath/longitudinal acceleration command response type would be an essential part of a system to permit operation to instrument minimums significantly lower than those achieved today for the AV-8B Harrier II. It would also be a superior mode for performing slow landings to an austere landing area such as a narrow road where precise control is demanded. The translational-rate command system would reduce pilot workload for demanding, vertical-landing tasks aboard ship and in confined, land-based sites.

The head-up display offered excellent path guidance for the curved approach through the ghost aircraft as well as effective commands for the deceleration to hover. It could significantly reduce pilot workload and improve precision for night shipboard recovery for AV-8B operations or for operation to lower visibility minimums than permissible for the AV-8B. In combination with the translational-rate command control, the hover display enabled the pilot to achieve excellent hover and landing precision, with touchdowns consistently within a 5-foot radius circle.

Control utilization and frequency content were documented for the control effectors in all axes. The only significant effect of control response type on control activity was a reduction in pitch control used with the longitudinal acceleration command during the approach to hover in comparison to that used for the rate damping stability augmentation or the attitude command system. This is attributed to the absence of pitch maneuvering to control deceleration to hover for the longitudinal acceleration command. Similar results were observed for the translational-rate command system during hover and vertical landing; thrust deflection rather than pitch attitude was used to maneuver longitudinally. Otherwise, only minor differences in control activity or none at all were experienced for the different response types for pitch,

roll, yaw, and thrust control for the various tasks. Borderline satisfactory/adequate flying qualities associated with bandwidth of the translational-rate control were established for the hover and landing task: for longitudinal and lateral position and height

control. These bandwidths were 0.33, 0.25, and 0.6 radian per second, respectively.

Point of Contact: J. Franklin
(415) 604-6004



Fig. 1. Ames Research Center's V/STOL Systems Research Aircraft.

Computational Maneuver Aerodynamics

Neal M. Chaderjian, Lewis B. Schiff

Fighter aircraft can achieve improved maneuver and agility performance by flying at high angles of attack. This performance gain is a result of the nonlinear lift obtained from vortices that form on the leeward side of the aircraft. If the angle of attack is sufficiently large, vortex asymmetries can form and result in a sustained roll oscillation known as wing rock. This phenomenon can be further exacerbated by the presence of vortex breakdown. It is important to understand and accurately predict high angle-of-attack maneuver aerodynamics in order to insure pilot safety and extend the useful flight envelope of the aircraft to obtain tactical superiority.

The approach adopted here is to use the Navier-Stokes Simulation code to numerically integrate the time-dependent, three-dimensional, Reynolds-averaged, Navier-Stokes equations. The goal is to

provide an experimentally validated computational tool to compute wing rock and other aircraft motions. This work supports the NASA High-Alpha Technology Program and experimental investigations at Wright Aeronautical Laboratory.

This year's research utilized the Unsteady Flow Analysis Toolkit (UFAT) to visually analyze the dynamics of vortex breakdown and the resulting nonsteady surface-flow patterns. UFAT is a post-processing tool capable of reading stored, time-dependent, computational fluid dynamics (CFD) solution files and rendering nonsteady streaklines and surface properties such as pressure, density, temperature, vorticity, etc. The resultant animation is stored in a graphics file that can be viewed on a graphics workstation or ported to a video format for viewing on a video cassette recorder.

The first figure compares the experimental and computational mean surface-flow patterns. The flow is highly nonsteady due to vortex breakdown occurring at 40% of the root chord. The CFD, mean surface-flow patterns were obtained by time-averaging the nonsteady CFD results, and then releasing particles within, and constrained to, a surface one grid point above the wing surface. Both experiment and computation are in good agreement with each other and indicate a primary separation line at the wing leading edge, a secondary separation line (the one most inboard), and a tertiary separation line (between the secondary line and the wing leading edge).

The second figure (see Color Plate 6 in the Appendix) shows a snapshot from a video animation of the nonsteady surface pressures and surface-flow

patterns. Red corresponds to high pressure while blue corresponds to low pressure. The nonsteady separation lines are significantly different from the mean separation lines in the first figure. Moreover, a lambda-type separation line was found to periodically form and branch off from the secondary separation line and move downwind toward the wing trailing edge. This phenomenon is a result of the expanded vortex core, downwind of breakdown, which entrains the surface flow. This nonsteady phenomenon is entirely missed with the experimental and computed mean surface-flow patterns, thus emphasizing the importance of visualizing nonsteady flow.

Point of Contact: N. Chaderjian
(415) 604-4472

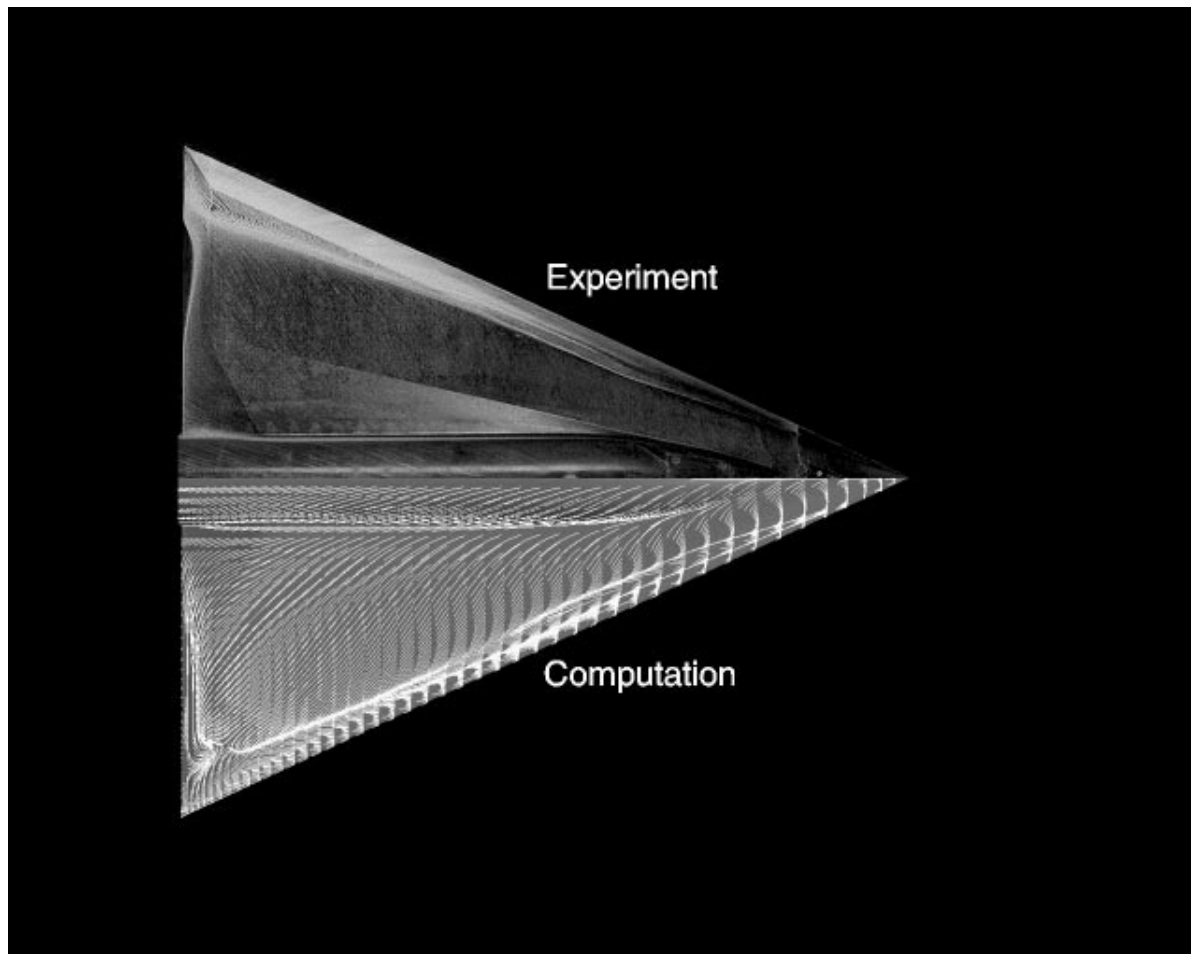


Fig. 1. Comparison of computed and experimental mean surface-flow patterns.

Time-Accurate Navier-Stokes Simulation of a Canard-Wing-Body Configuration with Moving Canards

Eugene L. Tu

The use of canards for control and improved aerodynamic performance in advanced aircraft is a topic of continued interest and research. In addition to trim, movable canards can provide advanced maneuver control. For close-coupled canards, the unsteady aerodynamic performance associated with moving canard interaction with the wing is of particular interest. In this study, time-accurate, Navier-Stokes simulations of the unsteady canard-wing-body flow fields are conducted. The selected configuration is schematically shown in the first figure, with the axis of canard rotation as indicated.

Simulations are performed for nonlinear flight regimes at transonic Mach numbers and for several moderate angles of attack. The analyses of the canard-wing-body flow field include the unsteady aerodynamics associated with canard pitch-up ramp and pitch oscillatory motions. The unsteady effects of the canard on surface pressures, integrated forces and moments, and canard-wing vortex interaction have been analyzed in detail.

The sample result given in the second figure illustrates the effect of the oscillating canard on the wing surface pressures at the 55% and 75% semispan

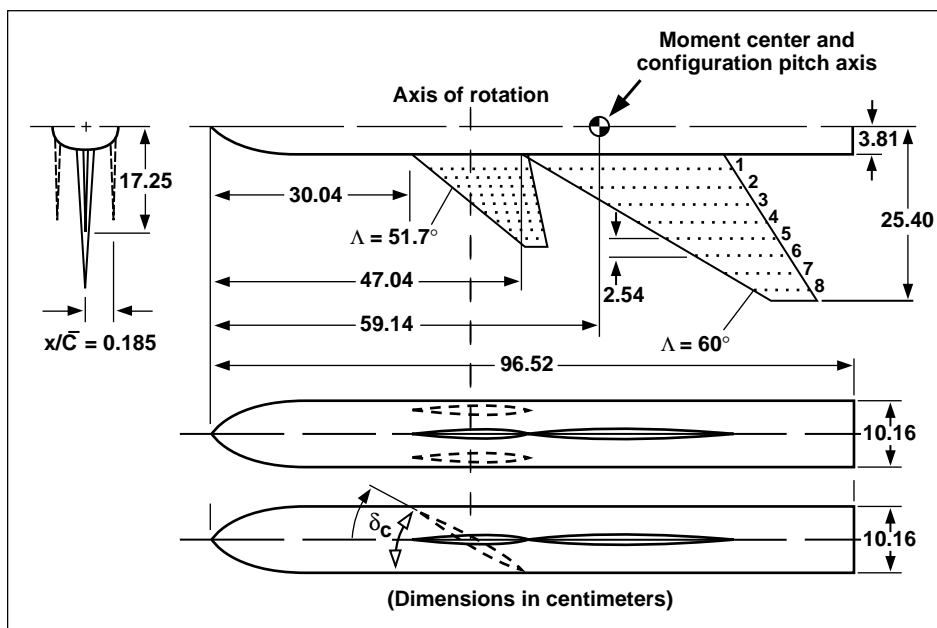


Fig. 1. Close-coupled, canard-wing-body geometry (canard axis of rotation shown).

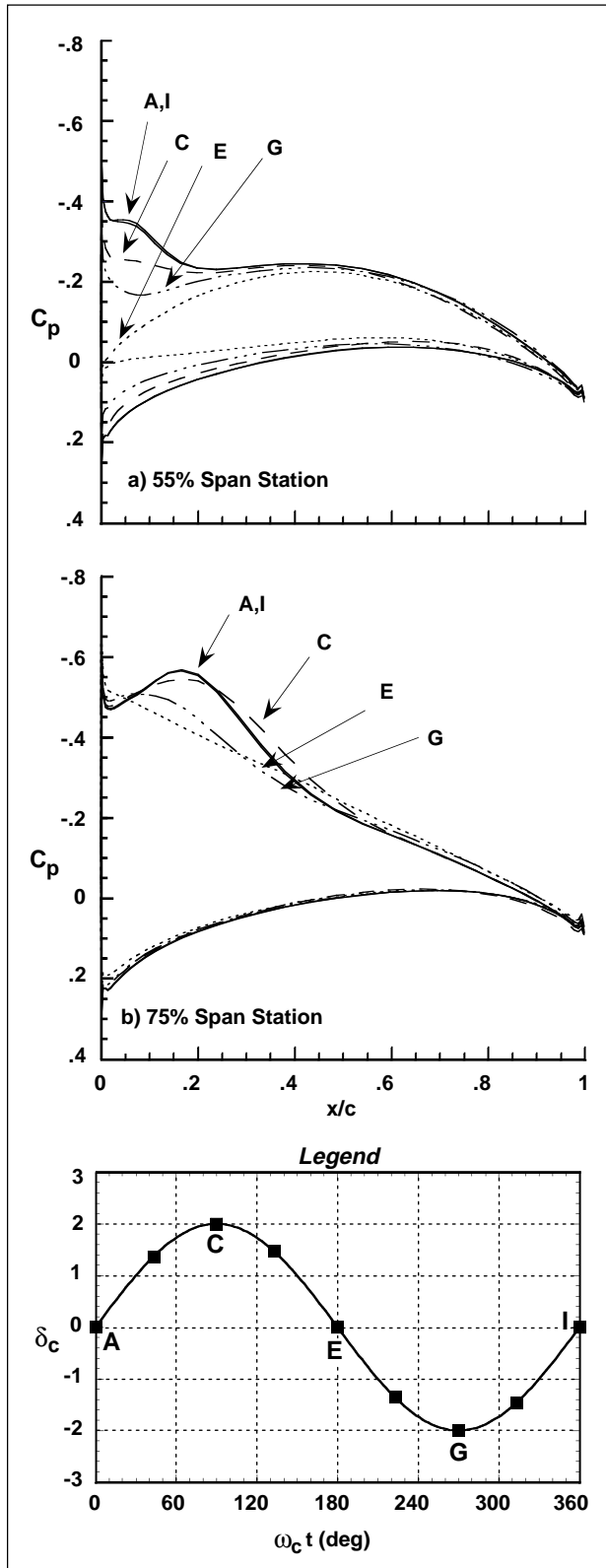


Fig. 2. Effect of canard pitch oscillation on wing-surface pressures at a free-stream Mach number of 0.85 and angle of attack of 4.27 degrees.

stations. In this case, the canard is oscillating at a reduced frequency of 1.0 and an amplitude of 2.0 degrees. Each streamwise pressure distribution curve represents the instantaneous pressure on the wing at a selected time instance (A, C, E, G, and I) during the canard oscillation. On the inboard portion of the wing, the canard oscillation clearly affects the formation of the wing leading-edge vortex. The changes on the lower-surface pressure distribution near the leading edge indicates that the local effective angle of attack of the wing is changing as well.

Further outboard, the second figure shows that there are significant changes in the upper-surface pressure peaks that are generated by the wing vortex. Starting from the beginning of the cycle, the suction peak weakens and appears to move aft (from A to C). Later in the same cycle, the peak moves forward towards the leading edge as suction again increases near the end of the cycle (E-I). Although the wing upper surface at 75% semispan shows considerable change, the local, effective, angle of attack at this station is observed to be relatively constant from the nearly constant lower-surface pressures. Therefore, there is very little effect of the oscillating canard on the local angle of attack of the outboard wing. Moreover, the significant influences observed on the outboard wing are primarily due to the canard effects on the development of the wing's vortex (inboard) and the presence of the canard vortex.

The computational technology presented here can be used to provide high-fidelity simulations of the moving, close-coupled canard. In addition to providing a detailed understanding of the complex canard-wing, flow-field interactions, the current technology can potentially provide dynamic stability predictions of moving canard control surfaces.

Point of Contact: E. Tu
(415) 604-4486

Applications of Nonlinear Design Optimization and Validation Wind Tunnel Testing

Susan Cliff, Ray Hicks, Mina Cappuccio, James Reuther, Dan Bencze

In the past, high-speed civil transport aircraft were designed using linear aerodynamic tools. Although these linear tools have been improved through the years, they still do not fully represent the aerodynamic flow fields about an aircraft, potentially missing areas for performance enhancements. Therefore, the NASA High Speed Research (HSR) Program is adapting and evaluating nonlinear, aerodynamic, design optimization tools and methods to take advantage of potential nonlinear benefits. Within a teaming environment, Boeing, McDonnell Douglas, and NASA's Langley and Ames Research Centers are each working on design tools in a coordinated effort to improve the various tools. Lessons learned by each of the organizations, as well as the computer codes themselves, are shared among the teammates with the overall goal of providing the U.S. airframe industry with the most advanced aircraft design capability in the world.

As an initial part of this effort, the HSR teammates applied their nonlinear, aerodynamic,

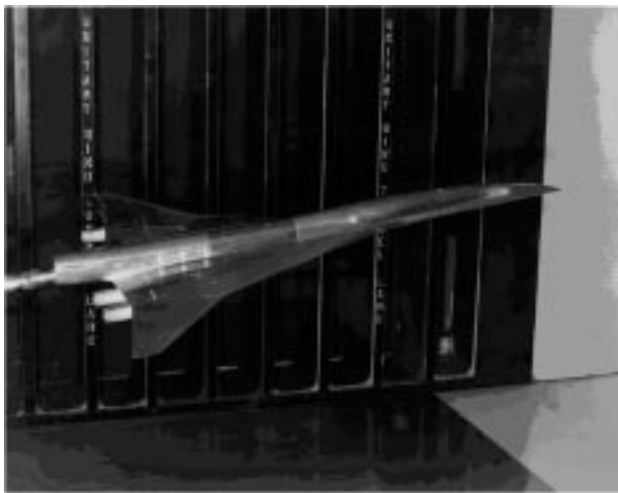


Fig. 1. Ames nonlinear optimized model in the NASA Langley 4- by 4-Foot Unitary Plan Wind Tunnel.

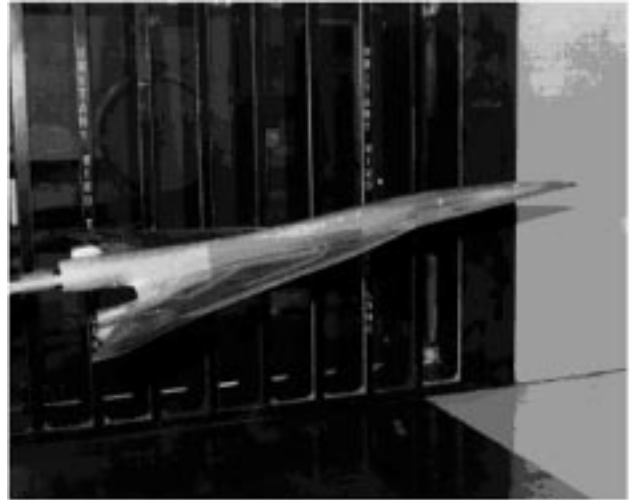


Fig. 2. McDonnell Douglas nonlinear, optimized model in the NASA Langley 4- by 4-Foot Unitary Plan Wind Tunnel.

optimization methods to evaluate them in terms of aerodynamic performance changes versus linear designed baseline configurations. The goal was to evaluate how much of the design space was exercised by these methods using a limited number of design variables, resulting in as large an effect on the aerodynamic performance as possible. Additional focus was placed on the efficiency of these aerodynamic design methods, in terms of computational efficiency and overall turnaround time.

Boeing and Ames applied their nonlinear, design optimization tools to the linearly designed Boeing Reference H configuration. McDonnell Douglas and Langley optimized the McDonnell Douglas M2.4-7A. The only design variables were wing camber, wing twist, and fuselage camber. Although all the design methods changed the cruise lift-to-drag ratio (L/D), the Ames design showed the most substantial effect.

In order to validate the Boeing, McDonnell Douglas, and Ames designs, three 1.7% scale models of the optimized configurations were built under Ames' guidance. Ames engineers tested the three models, plus two baseline configurations, in the Langley 4- by 4-Foot Unitary Plan Wind Tunnel. The figures show the Ames (first figure) and McDonnell Douglas (second figure) optimized designs, both in the wind tunnel. Force and moment data were acquired using an internal, sting-mounted, 6-component balance at the test conditions of -4° to 10° angle of attack and a Mach number of 2.40. Boundary-layer transition verification studies were carried out using sublimation techniques and colored oilflow visualization. During a later entry,

the Langley design was tested. Data repeatability for both tunnel entries was excellent (0.5 drag count).

Although the wind tunnel data compared to the computational predictions varied some between the different organizations, all were close. The Ames computations closely matched the wind tunnel data. For absolute drag, the computations were within 1.5 drag counts of the wind tunnel data. For the delta resulting from the difference between the optimized and linear baseline drag values, the computations were within 0.5 drag count of the wind tunnel data delta.

Point of Contact: D. Bencze
(415) 604-6618

Aeroacoustic Interactions Between the Noise Suppressor Nozzle and Airframe of the High-Speed Civil Transport

Chris Allen, Paul Soderman, Brian Smith, Fanny Zuniga

Reducing takeoff noise of the high-speed civil transport (HSCT) is a critical goal of the NASA High Speed Research (HSR) Program. Acceptable takeoff noise will be achieved by a combination of reducing noise from the jet exhaust nozzles and improving the lift-to-drag ratio (L/D) performance of the airframe. The current noise suppressor nozzle concept uses a mixer/ejector system that entrains large quantities of air into ejector inlets located near the trailing edge of the HSCT wing. The High-Lift/Engine Aeroacoustics Technology (HEAT) Program was initiated to assess the effects of the wing flow field on the suppressor acoustic performance (as well as the effects of the suppressor inlet flows on the aerodynamic performance of the wing). The overall objective of the program is to document interactions between the jet noise suppressor and the high-lift system at airspeeds and angles of attack consistent with takeoff, climb, approach, and landing.

To determine the installation effects on suppressor acoustic performance, a series of experiments were performed in the 40- by 80-Foot Wind Tunnel at Ames Research Center's National Full-Scale Aerodynamics Complex. These experiments included aeroacoustic measurements of the noise suppression of first-generation mixer-ejector nozzles, both isolated and installed on a 13.5% scale model of the Boeing Reference-H HSCT. The suppressor nozzles were provided by General Electric Aircraft Engines.

The figure shows the semispan HSCT model mounted in the acoustically treated 40- by 80-foot test section with a noise suppressor nozzle installed at the inboard station. A flow-through nacelle was mounted at the outboard station. The model was mounted on a symmetry plane to minimize the effect of the boundary layer on the test section floor.

The symmetry plane was acoustically treated to prevent contamination of the acoustic data by reflections. A turntable located below the floor of the test section permitted aeroacoustic measurements at angles of attack of up to 16 degrees.

Most of the acoustic measurements were made using a traversing microphone system to capture the noise radiated below the aircraft at flightpath angles required to predict the community noise level of the aircraft as specified in the Federal Aviation Administration Regulations. The acoustic data were scaled to full scale and extrapolated to the proper distance required to calculate the appropriate flyover noise metrics.

The acoustic data were compared with similar data acquired on the isolated suppressor nozzles to



Fig 1. HSCT model with installed noise suppressor nozzle. Traversing microphones are positioned underneath the model.

determine the acoustic installation effect on community noise. Microphones were also mounted sparsely on the ceiling of the test section to get an indication of the acoustic installation effect on the side of the aircraft.

In addition to the acoustic installation effects at the takeoff nozzle and the flight conditions, the sensitivity of the acoustic installation effect to parametric variations was also determined. The parameters that were varied included flight velocity, jet thrust, aircraft angle of attack, trailing-edge flap deflection, ejector acoustic treatment, nozzle geometry, and orientation.

A secondary objective of the test was to measure the effect of nozzle inlet flow on the L/D characteristics of the airframe. The test documented the overall forces and moments generated by the powered configuration as well as the pressures induced on the airframe by the nozzle inlet flows. The aspiration ratio and total and static pressures within the inboard, powered nozzle were measured for correlation with the acoustic data. These data were used to quantitatively determine the effects of the nozzle inlet and jet plume flows on the high-lift performance of the airframe.

The HEAT test series was a cooperative effort among the researchers at Ames and Lewis Research Centers, Boeing, General Electric, and McDonnell Douglas.

**Point of Contact: C. Allen
(415) 604-0074**

High-Speed Research Guidance and Flight Control

Jeffery A. Schroeder, Chima Njaka, Shawn A. Engelland, Charles S. Hynes, Karl Bilimoria, Robert W. Gardner

Two piloted flight simulation studies on the high-speed civil transport were performed on the Ames Vertical Motion Simulator as part of NASA's High-Speed Research Program. Engineers and pilots from Boeing, McDonnell Douglas, Calspan, and Langley Research Center participated in the studies.

The first simulation had three objectives; the first objective was to evaluate a new control system that allows a designer to quickly implement invariant vehicle dynamic responses over a large range of operating points, ranging from approach airspeeds at sea level to Mach 2.4 at 60,000 feet. The control system was evaluated at a range of flight conditions, and it performed as expected.

The second objective of the first simulation was to evaluate the adequacy of the horizontal tail size of the latest version of the vehicle. Since the aircraft is designed without inherent longitudinal static stability, the proper sizing of the tail is of paramount importance. Several key configurations were flown with different size tails in different geometrical locations on the aircraft. The control system described under the first objective was used to create identical aircraft pitch responses for these different configurations, until the tail reached a control limit, in order to make a fair comparison.

The third objective of the first simulation was to develop jointly with Honeywell a guidance system architecture for the high-speed civil transport that

(a) has system design integrity based upon proof of logical correctness at the design level; (b) allows a significant simplification and cost reduction in system development and certification; and (c) allows for improved operational efficiency. Pilots evaluated a prototype of the system and stated that the modeling of the system was transparent and that the operation was simple.

The second simulation had one objective: to jointly select the preferred vehicle pitch response characteristics that the airplane should have. That is, would a pilot prefer to have direct control over vehicle angle of attack, or should it be pitch angle or flightpath angle. A set of different response characteristics were analyzed by NASA, Boeing, Honeywell, and McDonnell Douglas throughout the year. Several promising response characteristics were jointly selected for a piloted study. A set of (jointly agreed upon) metrics was used to measure the value of each response characteristic.

The figure (see Color Plate 7 in the Appendix) shows a visual database representation of the general class of vehicle used for the tests in both the simulations described.

Point of Contact: J. Schroeder
(415) 604-4037

Obstacle Detection Systems to Augment a Windowless Cockpit

Phillip Smith

To achieve aerodynamic and weight savings for future supersonic commercial transport aircraft, it has been proposed to replace forward-looking windows with a synthetic vision system (e.g., to avoid drooping the nose). The detection of potential obstacles, both in the air and on the ground, is one function previously supported by windows. Since a synthetic or sensor-derived display of the outside world may not fully replicate the salient characteristics of the true scene, additional sensors and systems may be necessary to provide the pilot with sufficient obstacle information. The focus of this effort is to develop and demonstrate concepts that assist pilots in detecting obstacles in the air and on the ground in the absence of a forward window by using information from onboard sensors.

A real-time capability has been developed for the detection of obstacles on a runway based upon images from an onboard camera. The algorithm detects obstacles having vertical relief relative to the runway surface so that surface-level markings such as

tire marks are not classified as obstacles. The current real-time implementation processes seven frames per second, visually highlighting detected obstacles that are more than six feet tall.

An image-based runway detection algorithm has also been developed as an automated check for a Global Positioning System-based landing system to ensure that the aircraft is homing to the desired runway. A geometric model of the runway allows robust detection in the presence of image noise.

Several approaches for improving the ground-clutter suppression ratio for radar returns against a cluttered background were investigated in order to increase the likelihood of detecting airborne obstacles below the horizon. Both phase monopulse moving-target-indicator radar and amplitude monopulse radar have been studied.

Point of Contact: C. Null
(415) 604-1260

Computational Fluid Dynamics Analysis in Support of the X-33 Program

William Henline, Grant Palmer

The X-33 program is a partnership between NASA and private industry to develop a fully reusable, single-stage-to-orbit launch vehicle. The goal of the program is to significantly reduce the cost of placing payloads in orbit with increased reliability and turnaround time. Ames Research Center is the agency lead for the development of thermal protection systems (TPS) that support the X-33 and similar programs.

Three companies were chosen to participate in phase I. Each developed different vehicle concepts. Lockheed Martin proposed a vertical-takeoff, horizontal-landing, lifting body. Rockwell proposed a vertical-takeoff, horizontal-landing, wing body similar to the Space Shuttle. McDonnell Douglas proposed a vertical-takeoff, vertical-landing vehicle similar to the Clipper Graham experimental vehicle.

As requested by the companies, Computational Fluid Dynamics (CFD) analysis was performed on each of the vehicle concepts to obtain such things as surface heat flux and temperature, pressure loading on control surfaces, and the effects of turbulence and transition. The General Aerodynamic Simulation

Program's (GASP) three-dimensional flow solver was used to compute the flow field around the vehicle at several points along the descent trajectory. A finite-rate, catalytic, radiative equilibrium wall boundary condition was built into the GASP solver to correctly model the surface of the TPS material. To capture the jump in surface temperature that occurs at the junction of two TPS materials with different catalycities was important.

Using the CFD analysis to provide surface heat flux and temperature, a one-dimensional thermal analysis code was used to estimate the overall TPS mass needed to maintain structural and cryogenic tank temperature limits. Various TPS material combinations were investigated. The figure (see Color Plate 8 in the Appendix) shows the resulting TPS material map over the Rockwell wing-body vehicle. The TPS material is shown first followed by the underlying structure or tank.

**Point of Contact: W. Henline
(415) 604-6623**

Thermal Protection Information System

Ann Patterson-Hine

The scientists and engineers who are developing advanced thermal protection system materials for next generation launch vehicles produce a vast amount of data, reports, and images during the testing and evaluation of candidate materials. The process flows of the current Shuttle program delineate the maintainability issues associated with various thermal protection materials and systems. The Thermal Protection (THERMPRO) information system was designed to provide ready access to this information by materials developers in the early stages of materials testing throughout system integration and operation. The electronic information system

enables automation of experimental data analysis supporting the rapid transfer of experimental results to the design of thermal protection systems.

THERMPRO is accessible from the World Wide Web and allows secured data storage and retrieval by industrial partners in the Reusable Launch Vehicle (RLV) Program. Information categories that are supported by THERMPRO include Ames arc-jet facility descriptions, experiment data storage, and the ARC JET WIZARD, a tool for automatically plotting data from the arc-jet facilities using Excel 5.0; Ames high velocity impact facility descriptions

and experiment data storage including images of test panels after impacts; a Shuttle processing baseline report provided by Rockwell; results from Ames advanced materials flight testing on the DC-X; and the Robustness Test Matrix describing the tests to

which advanced materials are subjected in order to qualify them for use in the RLV program.

**Point of Contact: A. Patterson-Hine
(415) 604-4178**

Fiber Optic Strain and Pressure Sensors

Charles Gary, Meriç Özcan

Fiber optic sensors were constructed and tested to measure strain in spacecraft fuel tanks and pressure on aircraft wings. Prototype sensor systems were constructed and tested as proof of concept demonstrations that should lead to use of such systems in operational environments.

A critical enabling technology for the Reusable Launch Vehicle (RLV) is a health management system that facilitates the maintenance of the vehicle. One aspect of this system is the maintenance of the cryogenic tanks that hold the liquid hydrogen and oxygen fuel. To meet the current goal of a 6-hour recertification time for the tanks between each flight, new sensors must be designed that can be embedded in the tanks and survive the harsh space environment, while providing an accurate measure of the stress and other factors affecting the tanks. Specialized fiber Bragg sensors are designed to monitor the condition of the cryogenic tanks aboard an RLV. This work was performed as part of the X-33 Technology Program with Lockheed Martin.

The system concept is shown in the figure (see Color Plate 9 in the Appendix). Fiber Bragg sensors measured the strain experienced by the tanks up to 2500 microstrain, with a resolution of 10 microstrain or better. Fiber sensors are ideal since they provide accurate data with a small, lightweight sensor that can be embedded into the composite walls. Furthermore, the sensors operate in a wide temperature range (-423°F to 700°F), present no spark hazard, and are immune to electromagnetic interference.

The fiber Bragg sensor works by converting the strain experienced by the fiber to an optical signal. A periodic pattern, called a Bragg grating, is burned into the fiber at a given location. Typically, the Bragg grating is approximately 1 centimeter in length (the

fiber itself has a 125 micrometer diameter). The index of refraction of the fiber varies periodically throughout the grating, with a period of approximately 1.3 micrometers. When light with a wavelength identical to that of the Bragg grating strikes the grating, it is reflected. All other light passes through the grating unperturbed. Since the spacing between the individual elements of the grating will increase as the fiber is stretched, the amount of strain experienced by the fiber can be measured by measuring the wavelength of the reflected light.

Pressure sensors were constructed using extrinsic Fabry-Perot cavities in place of the Bragg gratings. The principle sensitive element of the sensor is a diaphragm attached near the end of the fiber. A space between the mirrored diaphragm and the fiber end forms a Fabry-Perot cavity. The distance between the fiber end and the diaphragm can be shown to change the spectrum of the light returning from the cavity. By monitoring the amplitude and frequency of the returning light in the fiber, the distance between the fiber end and diaphragm can be judged. Pressure on the diaphragm pushes it toward the fiber end, so that by measuring the distance between the diaphragm and fiber, it is possible to determine the pressure.

These fiber pressure sensors are desirable because they are less than 1 millimeter thick, allowing minimal disturbance of the airflow, and the fibers carrying the signal are extremely small (125 micrometer diameter) and are not subject to electromagnetic interference.

**Point of Contact: C. Gary/Y. Cho
(415) 604-3590/4139**

Human Motion Perception: Performance Measures and Computational Models

Leland S. Stone, Preeti Verghese, Brent R. Beutter

Pilots and astronauts need to make accurate judgments of their self-motion (or the motion of the craft that they are controlling) to navigate safely and effectively. When they are flying a helicopter at the nap-of-the-Earth with low-contrast, small-field-of-view night goggles or with a head-up display over nearly featureless terrain or landing the shuttle after several weeks of adaptation to microgravity, their ability to determine their heading (direction of self-motion) is pushed to its limits, yet any perceptual errors could have disastrous consequences. This research effort explores different facets of how humans use visual motion information to perform self-motion judgments.

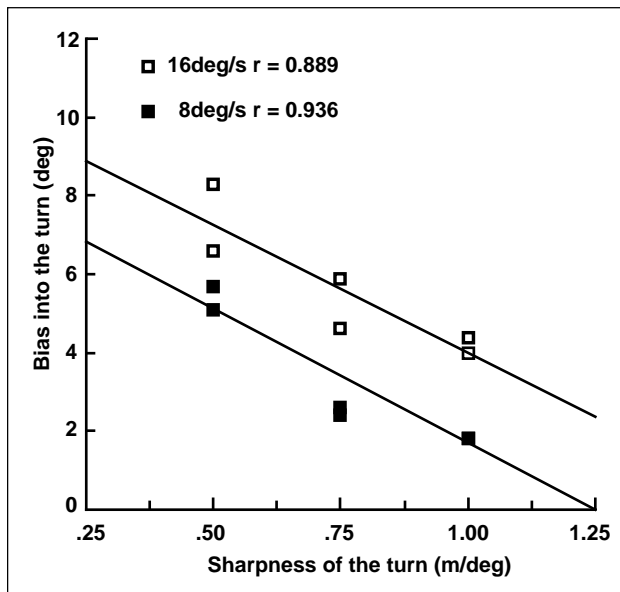


Fig. 1. Heading error as a function of the sharpness of a turn. This graph plots the average error for 4 observers in 12 conditions simulating 12 different combinations of translation and rotation rates. Note that the sharper turns generate larger errors, but even at fixed sharpness the faster rotation rate generates larger errors.

In collaboration with the University of York in the United Kingdom, Ames researchers have identified human errors associated with low-contrast motion stimuli (such as motion seen through fog). In 1995, many current models were tested and rejected for these effects. Research has examined how effectively the information in multiple motion stimuli can be processed simultaneously, and quantitative models that predict the same trends found in the human performance data have been developed. Other research has led to the development of a neural model of human heading and depth estimation from the visual motion experienced during self-motion. A rapid prototyping software package for generating the range of self-motion stimuli needed to test this model (and others) was developed in FY95. This package has been used to show that heading judgments during simulated motion around a curve show systematic errors related to the sharpness of the turn and the turning rate (shown in the figure).

The two overall goals of the research are (1) to develop computational models of human performance in heading estimation and related motion perception tasks; and (2) to empirically identify those conditions that lead to human error as part of an effort to test, refine, and ultimately validate the model(s). The availability of validated, quantitative models of human self-motion perception will aid in the design of training regimes for pilots and in the development of displays and automation systems that interact more effectively with human pilots while they fly aircraft and/or spacecraft.

Point of Contact: C. Null
(415) 604-1260

Fatigue Countermeasures Program

Mark Rosekind, Kevin Gregory, Donna Miller, Lissa Webbon, Ray Oyung, Julie Johnson

The Fatigue Countermeasures Program (FCP) has been investigating the extent of fatigue, sleep loss, and circadian disruption in flight operations and its impact on flight crew performance and alertness since the early 1980s. Data from the Aviation Safety Reporting System has consistently shown that about 20% of aviation incidents are fatigue related. Flight crew fatigue was first cited as the probable cause in a major aviation accident (Guantanamo Bay, Cuba) in 1994.

The FCP conducts ongoing field and laboratory studies to document the extent of fatigue and to evaluate potential fatigue countermeasures. These studies support activities in: (1) research in new operational environments; (2) education and training provided to the operational community; and (3) input to and support of industry/regulatory activities. A program goal is to deliver information and products to the operational community. Research and technology accomplishments are given herein.

(1) In 1995, FCP research activities concentrated on the following operational environments: augmented long-haul, corporate/executive, and regional. The final two phases of the field study investigating augmented long-haul operations were implemented and completed. The focus of this research was to study the role of onboard crew rest facilities as an operational countermeasure. Data were collected from three airlines flying 747-400s, 767s, and a corporate Gulfstream IV. Collected data included physiological (electroencephalogram), behavioral (actigraph), performance (psychomotor vigilance task), and subjective measures.

An extensive survey of corporate/executive operations was also implemented. With support from the Flight Safety Foundation (FSF) and National Business Aircraft Association (NBAA), approximately 11,000 surveys were made of more than 2000 NBAA member organizations. Of the 11,000 surveys

mailed, 1482 were completed, returned, and entered into a database.

The survey of regional operators was started. The carriers studied were identified as small, medium, and large (by number of enplanements) in each of the nine Federal Aviation Administration (FAA) regions. The survey has been completely implemented by 25 of 27 carriers, with more than 1200 surveys received and entered into a database.

(2) The FCP developed and produced the Fatigue Resource Directory, a first-of-its-kind, 120-page document providing information on current industry, research, educational, and government fatigue-related activities.

(3) In response to the FAA requirement to update the duty/rest requirement regulations, a scientific working group was formed to consolidate scientific findings. A document was developed that was used by the FAA as input to the proposed Notice for Proposed Rulemaking. The FSF also requested support in developing a set of procedures and guidelines regarding the fatigue issue for corporate operations. A document was produced through the efforts of a corporate working group. In addition, the FAA tasked an Aviation Rulemaking Advisory Committee Working Group to develop an FAA Advisory Circular (AC) based on the education and training module. This group developed a draft of the proposed AC.

The long awaited Overnight Cargo Study, the first field study of that environment, entitled "Crew Factors in Flight Operations: Psychophysiological Response to Overnight Cargo Operations," was published.

**Point of Contact: M. Rosekind
(415) 604-3921**

Boundary Layer Transition Induced by Convected Vorticity

Anthony Dietz

Instability waves are excited in the boundary layer of a flat plate by the interaction between surface roughness elements and a time harmonic wake convected above the layer, the first time such waves have been excited aft of the leading-edge region by controlled, convected vorticity. The study of this excitation mechanism is relevant to the greater problem of boundary layer transition due to free-stream turbulence.

Linear stability theory can describe how instability waves (known as Tollmien-Schlichting (TS) waves) grow in a boundary layer to levels where nonlinear and three-dimensional effects cause the flow to break down into turbulence. However, the process by which these instability waves are first excited is yet to be fully explained. This process, known as boundary

layer receptivity, transfers energy from the typically long-wavelength acoustic waves and convected disturbances in the free stream to the shorter-wavelength TS waves in the boundary layer. Theoretical analyses have shown that coupling between the free-stream disturbances and the TS waves occurs in regions with rapid streamwise variations in the boundary layer flow. Such regions occur at the leading edge of a surface or downstream at roughness elements or suction holes. These analyses have also suggested that receptivity to acoustic waves is an order of magnitude more efficient than receptivity to convected vorticity.

Acoustic receptivity has received much attention in recent years, and good agreement between theoretical predictions and experimental data has

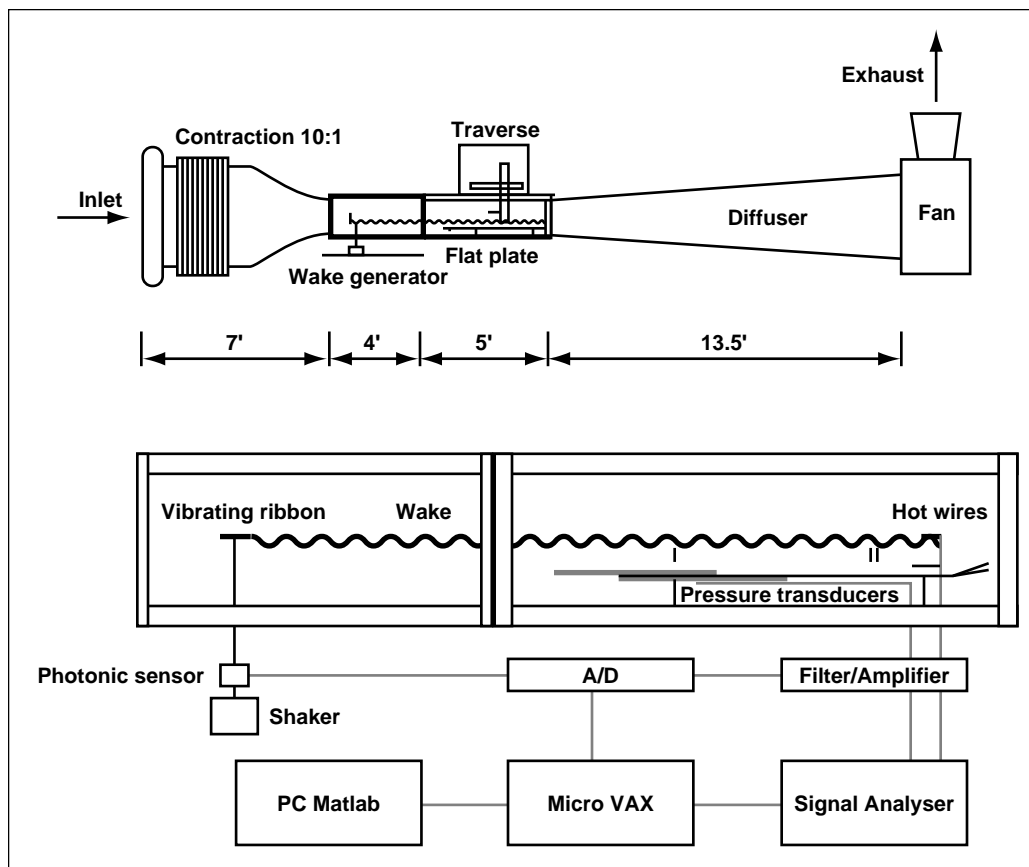


Fig. 1. Experiment layout.

been obtained. In contrast, experiments measuring the boundary layer response to free-stream turbulence have yielded confusing results that are not easily explained by existing theories. A simpler experiment is to measure the boundary layer response to a controlled, convected disturbance such as the wake from a vibrating ribbon placed upstream of a flat plate. In the experiment described herein, the receptivity of a flat-plate boundary layer to convected vorticity over distributed roughness was successfully measured.

The experiment was conducted in the Ames Fluid Mechanics Laboratory's low-speed indraft wind tunnel. Substantial modifications to the tunnel were necessary to reduce the angularity, nonuniformity, and turbulence intensity of the flow to the level required for a receptivity experiment. A 0.4-meter \times 1-meter flat plate with a 56:1 elliptic leading edge was installed in the test section and adjusted to give a zero pressure gradient along the plate's upper surface. A 25-millimeter (mm)-wide, 63-micrometer

(μm)-thick ribbon was mounted 0.6 meter ahead of the plate's leading edge. The ribbon was tensioned until its resonant frequency was greater than the desired forcing frequency. The motion of the ribbon was measured by a light sensor aimed at its center. The distributed roughness receptivity site was provided by strips of 25-mm-wide, 40- μm -thick polyester tape attached to the plate just downstream of the leading edge/plate junction in the region where TS waves in the boundary layer first became unstable. A schematic of the experimental arrangement is given in the first figure.

The mean velocity profile measured with a hot wire at the rear of the plate is shown in the second figure along with an exact solution for the flow over a flat plate with zero pressure gradient. The ordinate is the nondimensional length scale η defined as the plate normal coordinate y divided by a reference length $\sqrt{2\nu x/U}$ where ν is the kinematic viscosity of the flow, x is the distance from the leading edge, and U is the free-stream flow velocity. The boundary

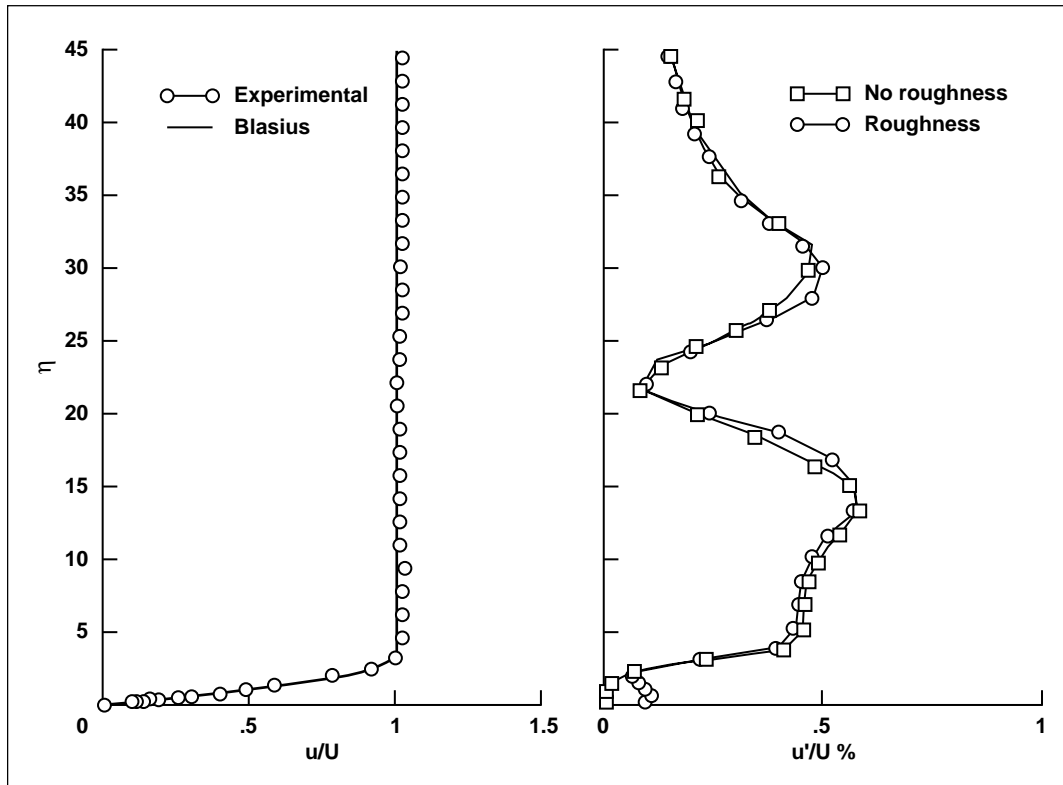


Fig. 2. Mean velocity (u) and root mean square (rms) velocity fluctuations at ribbon forcing frequency (u'). $\eta = y/\sqrt{\nu x/U}$; measurement point: $x = 0.72 \text{ m}$; $U = 19 \text{ m/s}$; $f = 172 \text{ Hz}$.

layer is the region close to the wall where the velocity decays to zero. Streamwise velocity fluctuations through the boundary layer and the wake are shown in the second plot of the second figure. The component of the velocity fluctuations occurring at the ribbon vibration frequency for flows with and without roughness elements on the plate is included in this plot. The double-peaked structure of the wake turbulence from the ribbon is typical of wakes of this type. With no roughness on the plate, the fluctuations decay monotonically through the boundary layer, and there is no evidence of any boundary layer

instabilities. However, when roughness elements are introduced, the form of the wake remains unchanged but the velocity fluctuations at the forcing frequency in the region close to the surface increase. The mode shape of the instability caused by the introduction of roughness on the plate (the difference between the two curves) matches the mode shape expected of the TS instability waves predicted by linear stability theory.

Point of Contact: A. Dietz
(415) 604-4137

The Structure of Stable and Unstable Waves in a Blasius Boundary Layer

Sanford S. Davis

The classical theory of boundary layer stability is based on exponentially growing Tollmien-Schlichting (TS) waves in a laminar, flat-plate boundary layer. These eigenmodes are but one of many possible waves belonging to the governing Orr-Sommerfeld equations. The complete modal set consists of numerous possible oscillations, but all except the TS wave are damped. However, some authors argue that other modes may be relevant in the following way: Since experimental evidence indicates that higher turbulence levels induce earlier transition, important flow effects must appear at the outer part of the boundary layer. Previous work showed that some of these heretofore neglected damped waves have large oscillatory peaks closer to the edge of the boundary layer, and these modes may be more "receptive" to free-stream disturbances.

This report describes a new method to compute the higher modes. If second-order differences on a uniform mesh are used, a complex pentadiagonal system $\mathbf{Ax} = 0$ is the discrete form of the Orr-Sommerfeld equation. The n -vector \mathbf{x} is an eigenvector that maps the singular matrix \mathbf{A} onto a null space. The first step is to find the spectrum of eigenvalues and the second is to compute the eigenmode \mathbf{x} for selected eigenvalues. The eigenvalues are chosen

as the complex phase speed c . The one eigenvalue with a positive imaginary part is the classical TS wave. A simpler way to ensure that \mathbf{A} is singular is to use a method based on decomposing \mathbf{A} into its upper and lower triangular component matrices. From the theory of determinants, the determinant of a product is the product of its determinants, and the determinant of a triangular matrix is the product of its diagonals:

$$\det[\mathbf{A}] = \det[\mathbf{LU}] = \det[\mathbf{L}]\det[\mathbf{U}] = \prod_{j=1}^n L_{jj} \prod_{j=1}^n U_{jj}$$

A standard decomposition of algorithms of this class forces the diagonals of \mathbf{U} to be unity. Thus

$$\det[\mathbf{A}] = \prod_{j=1}^n L_{jj} = P + iQ$$

The zero contours of P and Q divide the complex c -plane into positive and negative regions. Crossing points define the complex eigenvalue $c_r + ic_i$. Once the eigenvalues are defined, the eigenvectors are computed by setting one component of \mathbf{x} to unity and solving the resulting nonsingular system using standard methods. A complete spectral search took about 2.5 minutes on a DEC 3000/800S Alpha/AXP

Server. An advantage of the current method is that the dispersion relation can be searched in parameter space for a large number of eigenvalues. The algorithm is ideally suited to parallel computation.

The first figure shows the output of the stability code for spatially growing waves as a map of zero trajectories belonging to the real (P) and imaginary (Q) parts of the determinant of the system equations. The intersections of solid and dashed lines represent zeros of the determinant, hence allowable eigenvalues. Contours are shown in the complex plane of phase speeds. Discrete modes are shown at points A and B, and a continuous spectrum is shown as the shaded, concave arc. Point A is the slightly unstable TS mode that appears at this particular frequency and Reynolds number. There is speculation in the literature regarding the presence of discrete modes with negative phase velocities. The figure shows no

evidence of eigenvalues belonging to upstream traveling modes.

The second figure shows an instantaneous velocity vector map of the wave pattern for two selected modes. The upper trace shows the slightly unstable TS wave A over a distance of 1.5 wavelengths, or about 7 boundary layer thicknesses. The undulating wave has maximum energy in the lower portion of the boundary layer. This peak is at the "critical layer," where the mean velocity equals the real part of the phase speed (0.354 in this case). The lower trace shows wave C moving with a phase speed of 0.975 near the free-stream velocity. This wave is much longer than the TS mode, extending almost 20 boundary layer thicknesses. Note that this linear wave is damped as it propagates. Vigorous mixing and cross-stream momentum transfer are localized in the outer portion of the boundary layer.

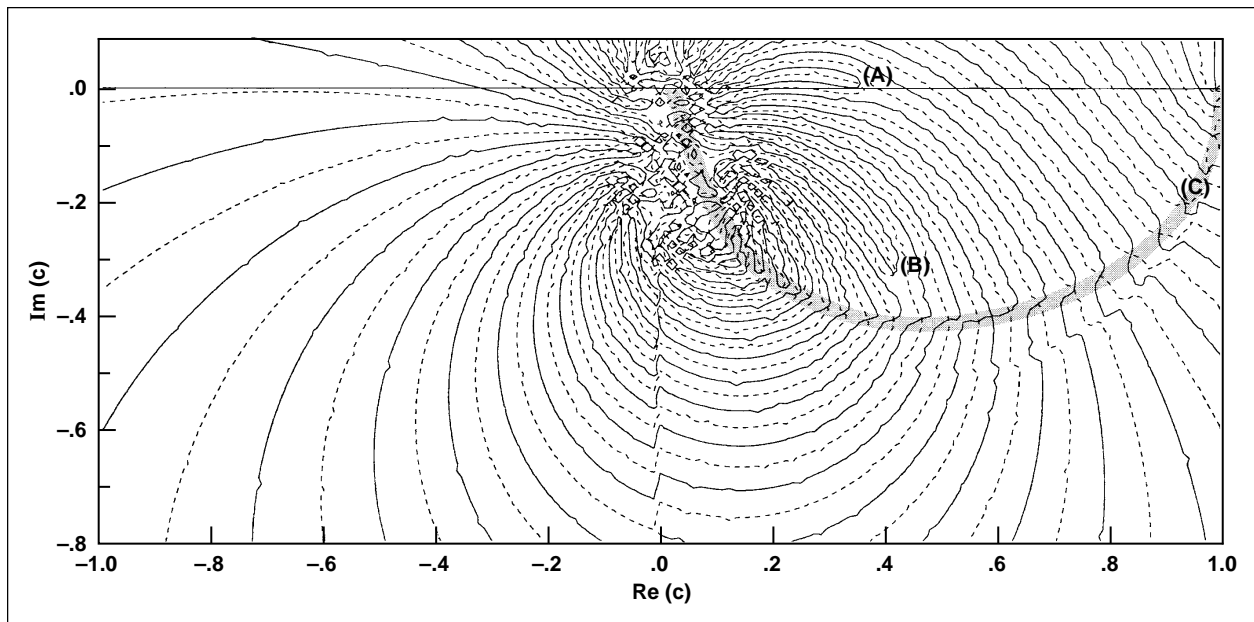


Fig. 1. Zero crossing contours for spatial stability in the plane of positive and negative phase speeds. Frequency = 112; Reynolds number = 580. Shading indicates approximate location of the continuous spectrum.

Strong cross-stream mixing seems to characterize these waves, which may be receptivity sites for free-stream disturbances.

In summary, an efficient method for computing normal modes of the Orr-Sommerfeld equation was developed by tracing zeros of the system determi-

nant. Normal modes other than the TS wave may be excited by free-stream disturbances.

Point of Contact: S. Davis
(415) 604-4197

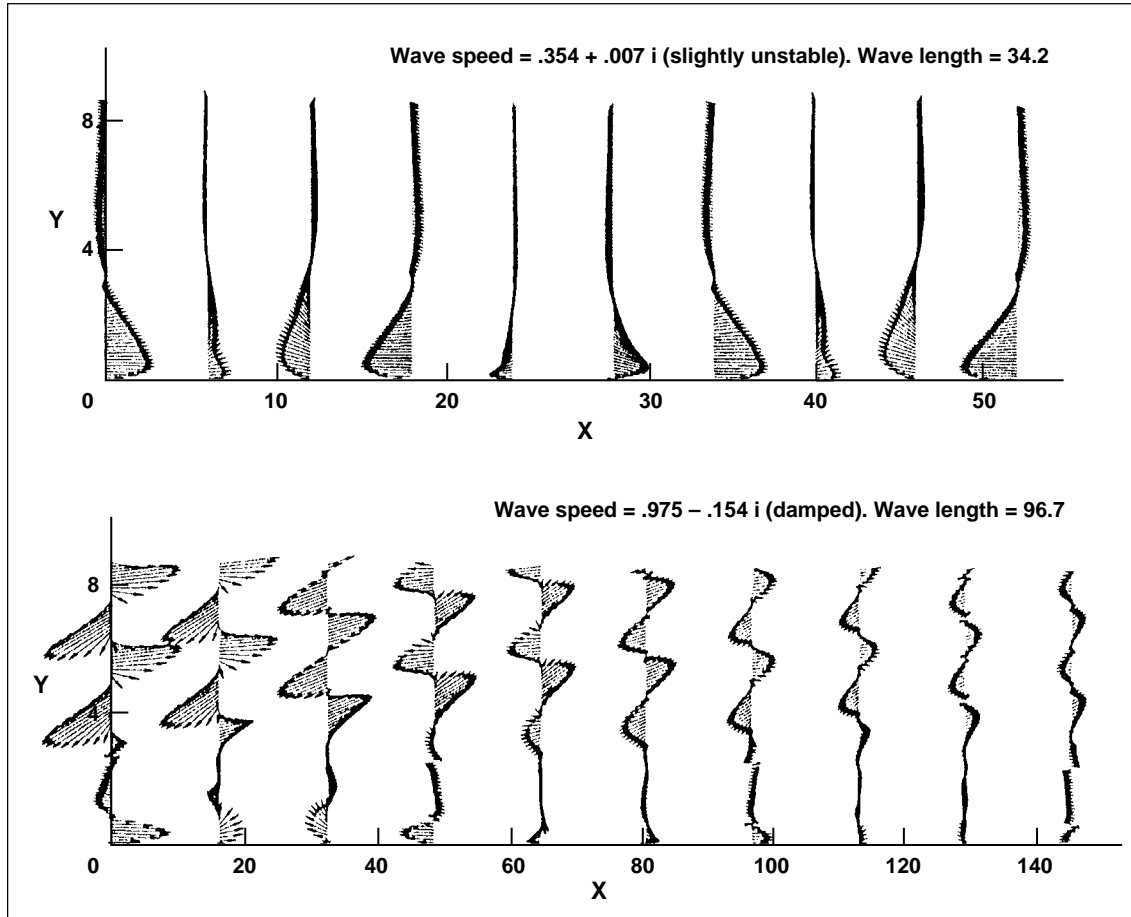


Fig. 2. Spatial pattern of instantaneous velocity vectors for a TS wave and an eigenmode along the continuous spectrum. Frequency = 112, Reynolds number = 580.

Measurement of Attachment Line Transition in a Supersonic Quiet Tunnel

Colin Coleman

The attachment line divides the air flow passing over and under the leading edge of a swept-back wing. Failure to ensure a laminar attachment line will lead to turbulent flow developing over the rest of the wing, resulting in increased drag and poor aerodynamic performance. Unfortunately, attachment line transition is one of the least understood boundary layer transition mechanisms, posing a problem for the high-speed civil transport (HSCT), where a swept-back wing with low drag is required for efficient cruise performance. Experiments conducted on swept cylinders at supersonic speeds can be used to study this flow since generation of flight-scale viscous layers is possible. In this way, important design information directly applicable to the HSCT can be generated, requiring no extrapolation or other form of scaling.

As shown in the first figure, the HSCT leading edge was modeled with a swept cylinder placed in the Mach 1.6 Laminar Flow Supersonic Wind Tunnel

at Ames Research Center. High Reynolds number transition data were produced for “natural” flow and for direct tripping of the boundary layer (the latter to simulate bug splats and steps/gaps in the wing’s leading edge). “Natural flow” means having a clean cylinder and checking for the amplification of small disturbances in the boundary layer. Computational codes exist for this case, but they have not yet been experimentally validated. Direct tripping is very important to the airplane manufacturer since machining tolerances must be set and insect impacts must be accounted for. This case cannot be computationally modeled.

The feasibility of taking hot-wire measurements in a supersonic attachment-line boundary layer (which, at 0.008 inch, was just over two human hairs in thickness) was demonstrated. This work was accomplished in collaboration with D.I.A. Poll of the University of Cranfield in the United Kingdom.

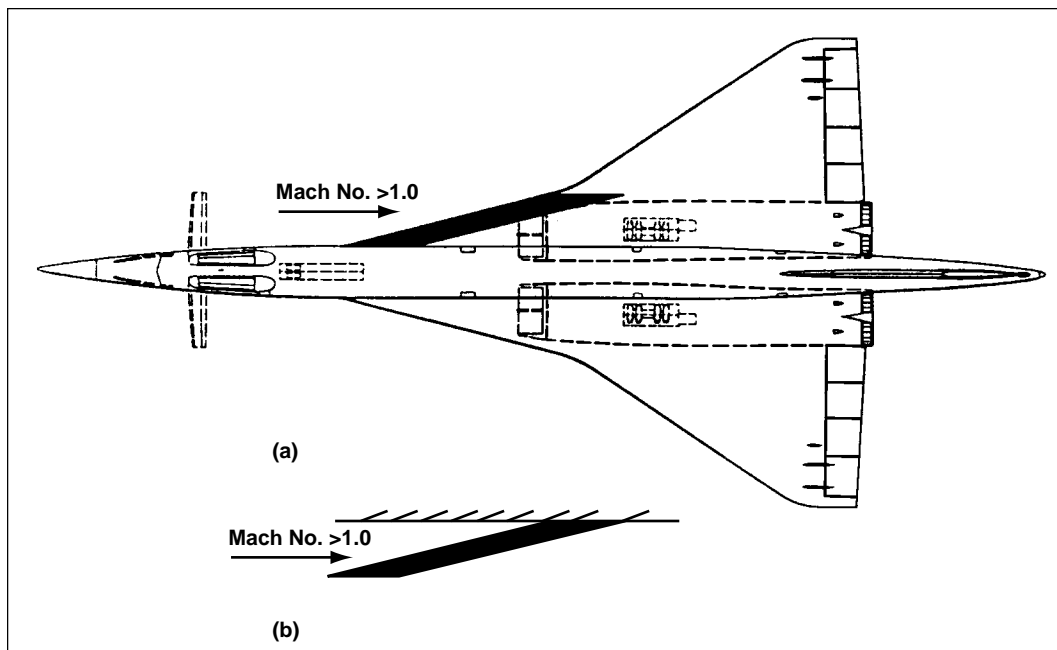


Fig. 1. HSCT leading edge is modeled (a) as a swept cylinder in the Fluid Mechanics Laboratory's quiet tunnel (b).

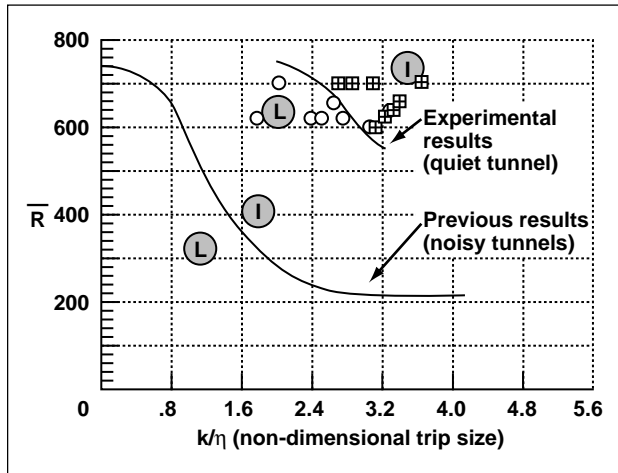


Fig. 2. Effect of boundary layer trip size on laminar flow—intermittent disturbance boundary, showing that a quiet tunnel can accommodate larger disturbances.

The first significant finding was that the “natural” laminar flow is quite robust up to an \bar{R} of approximately 700 (Reynolds number based on a viscous length scale, η —a common parameter for this type of flow) with an s/η of 3300 (spanwise distance in terms of η). As shown in the second figure, another significant finding was that disturbances twice as large as were previously thought allowable can be introduced to the attachment line before the boundary layer begins to transition to turbulence through intermittent bursts. These findings indicate that current design and manufacturing practices are conservative (bugs twice as large can hit the leading edge and machining tolerances can be relaxed, thus saving money).

Point of Contact: C. Coleman
(415) 604-0613

A Particle Representation Method for the Distortion of Homogeneous Turbulence

W. C. Reynolds, S. C. Kassinos

Prediction of many turbulent flows that involve complex, three-dimensional, time-dependent, mean flow, where the turbulence is subjected to very rapid deformation, is necessary to advance technology. Since the turbulence structure takes some time to respond to these imposed mean changes, eddy-viscosity models become inadequate. This report shows that tensors with information about the structure of the turbulence must be introduced in order to model the changes in the turbulence under these conditions.

The changes in the turbulence under rapid imposed deformation are determined by rapid distortion theory (RDT). The RDT equations are derived from the Navier–Stokes equations by introducing Osborne Reynolds’ decomposition for velocity and pressure, and then neglecting the nonlinear interactions between turbulent fluctuations (and usually the viscous terms as well). The resulting equations are linear in the velocity and pressure fluctuations. Closed equations are derived for

two-point statistics, but not for one-point statistics because of the nonlocality of the pressure fluctuations. Two-point closures seem impractical for engineering analysis and not competitive computationally with large-eddy simulation (LES), hence efforts were initially focused in developing a good one-point model for RDT. Because the present modeling efforts involved new structure tensors for which databases were not available, a convenient and computationally efficient method for executing RDT calculations that would give the evolution histories for the structure tensors was needed.

The particle representation method (PRM) was initially developed as a tool for evaluating the one-point structure model in the RDT limit. In a PRM, numerous key properties and their evolution equations are assigned to hypothetical particles. The idea is to follow an ensemble of “particles,” determine the statistics of the ensemble, and use those as the representation for the one-point statistics of the corresponding field.

A velocity vector, a gradient vector, a vorticity vector, and a pressure property are assigned to the hypothetical particles. The evolution equations for these properties are formulated using the exact RDT equations as the basis. The linearity of the RDT equations means that the PRM equations are closed and no modeling is required. As a result, with enough particles the PRM can reproduce exact RDT results!

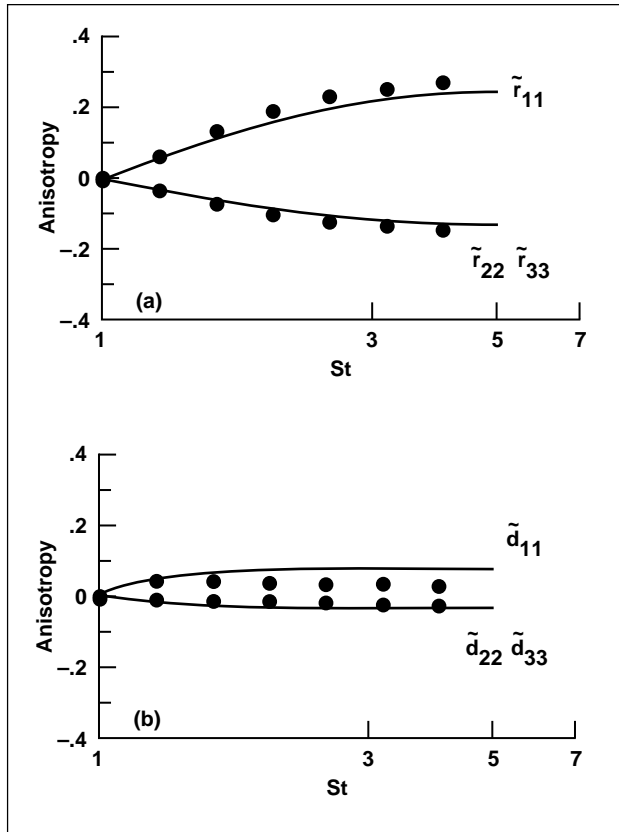


Fig. 1. IPRM predictions (shown as solid lines) for slow, axisymmetric expansion ($Sq_0^2/\epsilon_0 = 0.7$). Symbols are from the direct numerical simulation of Lee and Reynolds (1985). (a) Reynolds stress anisotropy; (b) structure anisotropy.

This characteristic is key in the present PRM, setting it apart from standard PRM methods traditionally used in the combustion community in the form of probability density function (PDF) methods. This advantage has, in fact, been recognized by the combustion community.

The PRM has recently been extended so that it handles flows in which the mean deformation is slow, the regime where eddy-viscosity representations are valid. Under these conditions, the nonlinear turbulence/turbulence interactions become important in the governing field equations. In the context of this interacting PRM (IPRM), these nonlinear processes are represented by a simple model for the particle/particle interactions.

The IPRM matches RDT exactly when RDT is applicable or appropriate, and produces excellent agreement with the results of eddy-viscosity theory when the latter is applicable. In that sense, it exhibits the proper viscoelastic character that would be desirable in any good engineering turbulence model. For that reason, the IPRM is currently used as the basis for constructing the present one-point, viscoelastic, structure-based model.

The figure shows the IPRM predictions for the slow, irrotational, axisymmetric expansion flow, an important and particularly challenging test case. The two plots show the anisotropies of the Reynolds stress \tilde{r}_{ij} and structure dimensionality tensor \tilde{d}_{ij} plotted against total deformation (St). The axisymmetric expansion flow is an important test case because of its close relation to axisymmetric diffuser and impinging-jet flows. Presently, the IPRM is the only model that can handle this test case.

Point of Contact: W. Reynolds
(415) 604-4731

A One-Point, Structure-Based Turbulence Model for Engineering Use

S. C. Kassinos, W. C. Reynolds

Modern engineering analysis of systems involving turbulent flow relies heavily on one-point, Reynolds-averaged models. The reliable prediction of turbulent flows with complex, three-dimensional, time-dependent, mean flow, where the turbulence is subjected to very rapid deformation, is becoming increasingly important for the advancement of technology. This new emphasis on nonequilibrium flows exemplifies some of the limitations of traditional modeling approaches and underlines the need for a new approach.

In simple flows, where the deformation rates are mild and the turbulence has time to reach an equilibrium with the mean flow, eddy-viscosity models have traditionally been used with success. In such flows the Reynolds stresses are determined by the applied strain rate, and relating them to the mean strain rate through the eddy-viscosity assumption is reasonable. In the modern family of k - ϵ models, the eddy viscosity is modeled in terms of the turbulent kinetic energy k and dissipation rate ϵ , for which partial differential equations (PDE) are used. Such models have proven to be very useful in predicting near-equilibrium turbulent flows, where the applied mean deformation is slow.

The present research has shown that the Reynolds stresses do not always provide a complete description of the turbulence state. This situation poses a fundamental problem for standard Reynolds stress tensor (RST) models, which use the RST (along,

perhaps, with the mean velocity gradient) as the unique tensorial base for modeling the unknown terms. As a result, standard RST models are in many cases inconsistent with rapid distortion theory (RDT), the theory that applies to turbulence undergoing rapid deformation. Proper characterization of the state of turbulence in nonequilibrium flows requires the inclusion of *structure* information to complement the *componentality* carried by the turbulent stresses.

These considerations motivated the structure-based model, which incorporates the key structure information in a simple, phenomenological approach. The goal is to construct a simplified engineering model with proper viscoelastic character that will reduce to the form of a k - ϵ model when the mean deformation is weak and to RDT when the mean deformation is strong. The derivation of the structure-based model is based on the particle representation method (PRM), which ensures full realizability.

The backbone of the structure-based model is a one-point, structure-based model of RDT for homogeneous turbulence. The development of this RDT model has been completed successfully, and the model can handle a remarkable variety of flows involving rapid mean deformation. Currently no other turbulence model can handle the RDT regime so successfully.

The figure shows predictions of the structure-based model for two particularly challenging cases of rapid mean deformation. The first case corresponds to incompressible, axisymmetric contraction with axial swirl, emulating swirling flow through an axisymmetric nozzle. The second case corresponds to axisymmetric, swirling flow that is subjected to axial extension, similar to the flow encountered in an

internal combustion engine. In both cases, the mean rotation and dilatation have a very strong effect on the anisotropy level, and the structure-based model is able to reproduce these effects successfully. No other one-point model can reproduce these effects.

Point of Contact: S. Kassinos
(415) 604-0546

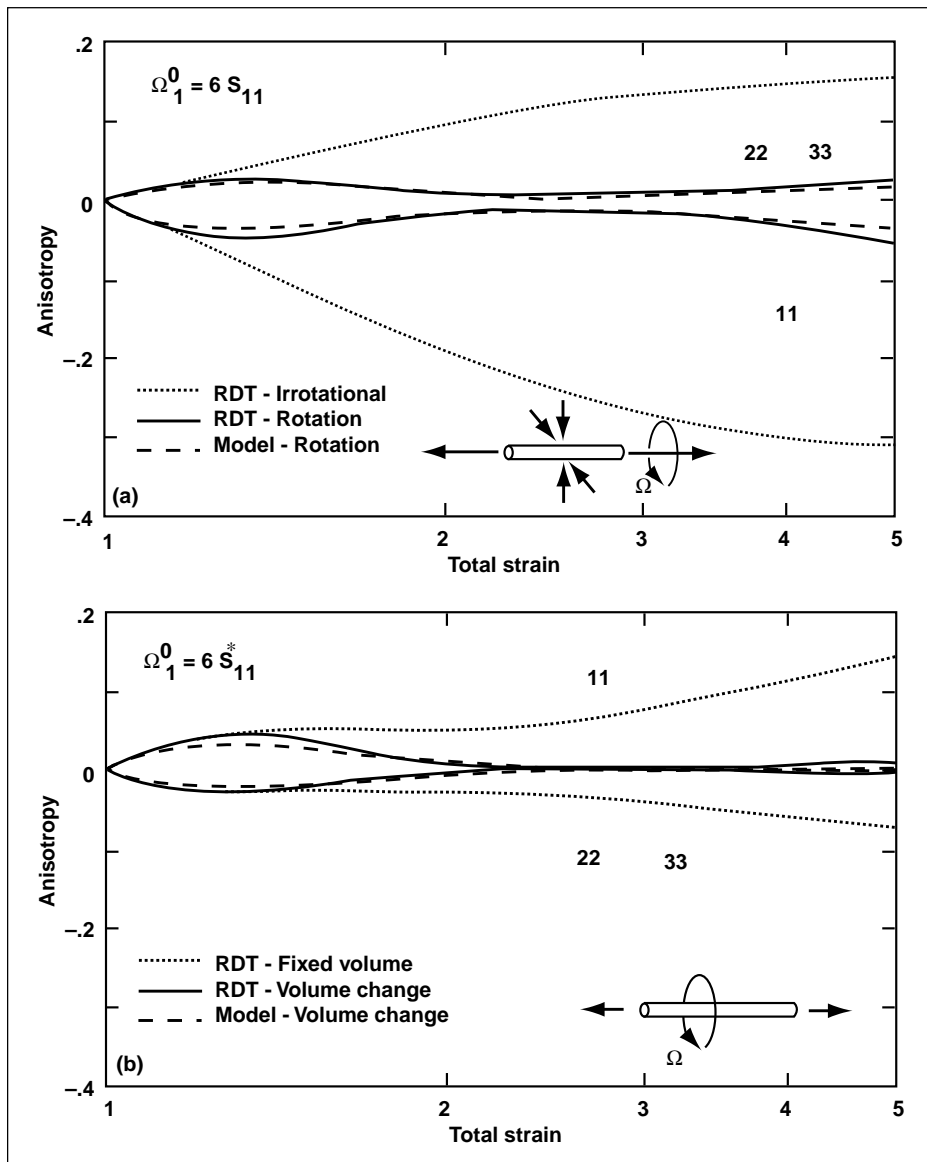


Fig. 1. The Reynolds stress anisotropy plotted against total strain for two relatively complex cases involving rapid mean deformation. (a) Incompressible axisymmetric contraction with swirl; (b) one-dimensional dilatation with swirl.

Three-Dimensional Separating Flow Study for Turbulence Modeling

David M. Driver

In general, separation limits the lift that an airfoil can generate, increases drag, and often leads to flow unsteadiness. Predicting whether or not a given flow will separate, and to what extent, remains one of the greatest challenges to computational fluid dynamics, primarily because of inadequate turbulence models. Consequently, a coordinated experimental and computational effort was undertaken, in the interest of evaluating and developing turbulence models for high-lift applications.

Three-dimensional (3-D) flow separation was produced on the flat wall of a wind tunnel by subjecting the boundary layer to a combination of streamwise and spanwise pressure gradients (accomplished with tunnel wall divergence and localized suction). A classic 3-D separating flow pattern was produced, much like that seen on wings at high angles of attack (see the first figure). This simplified flow field requires fewer computational resources than most other 3-D flow fields, because of its centerline symmetry and inviscid boundary on all surfaces of the domain except the test surface.

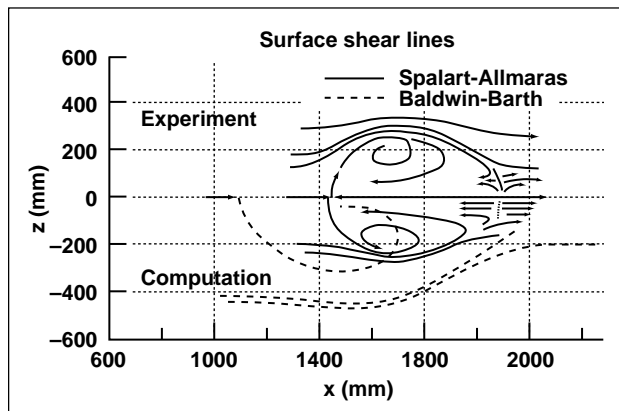


Fig. 1. Measured and computed surface shear lines.

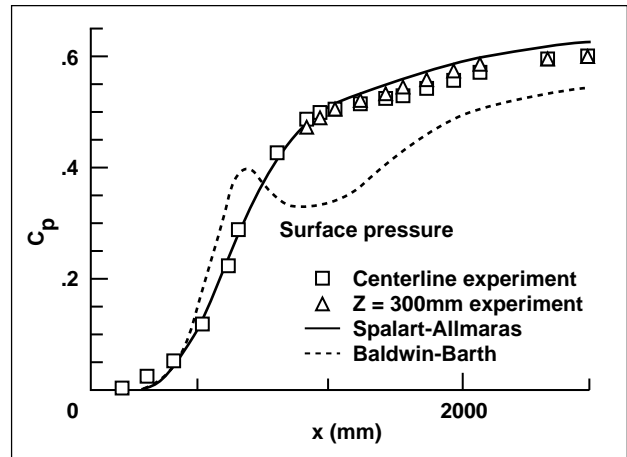


Fig. 2(a). Measured and computed pressure.

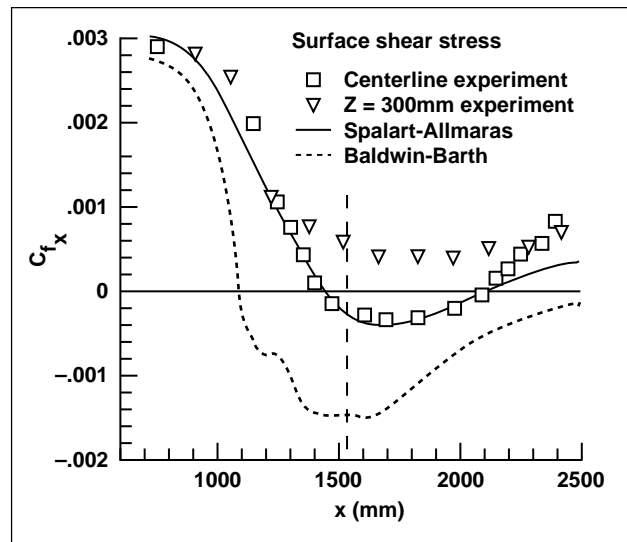


Fig. 2(b). Measured and computed skin friction.

Several cases of separation were studied experimentally, ranging from small to massive separation. A case of medium separation is shown in the first figure. In addition, the inlet boundary layer was systematically disturbed to test the sensitivity of the 3-D separations to perturbations. Computationally, the Spalart–Allmaras turbulence model produced the best results, whereas the Baldwin–Barth turbulence model produced separation patterns that were far too large. Surface pressure and skin friction (shown in

the second figure) are quite well predicted by the Spalart–Allmaras model. The large variation in the two computational results indicates the high degree of sensitivity of the flow to the turbulence model. Using a good turbulence model is essential to obtaining accurate flow predictions.

Point of Contact: D. Driver
(415) 604-5396

Analysis of Three-Dimensional, Separated Flows Using Topological Concepts

Murray Tobak

Topological concepts have proven to be useful in the interpretation and understanding of steady, three-dimensional, separated flows. Recently, these concepts have been used to interpret water-channel experiments and computations aimed at demonstrating the existence of certain structures in the skin-friction-line pattern underlying flow approaching a cylinder mounted on a flat plate. Confirmation of the presence of a saddle point of attachment, rather than one of separation, proved that the flow approaching the obstacle was able to find an alternative to separation in the classical sense. The first figure illustrates

the form of the flow in the symmetry plane for (a) a saddle point of separation and (b) a saddle point of attachment in the skin-friction-line pattern. As shown in the second figure, the two flows share the same surface pattern. It is, therefore, impossible to determine from the surface patterns alone whether the saddle point in the pattern is one of separation or attachment. The discovery of an alternative to separation raised some important questions: (1) What determines whether a flow separates, originating from a saddle point of separation, or takes the alternative path, originating from a saddle point of attachment?

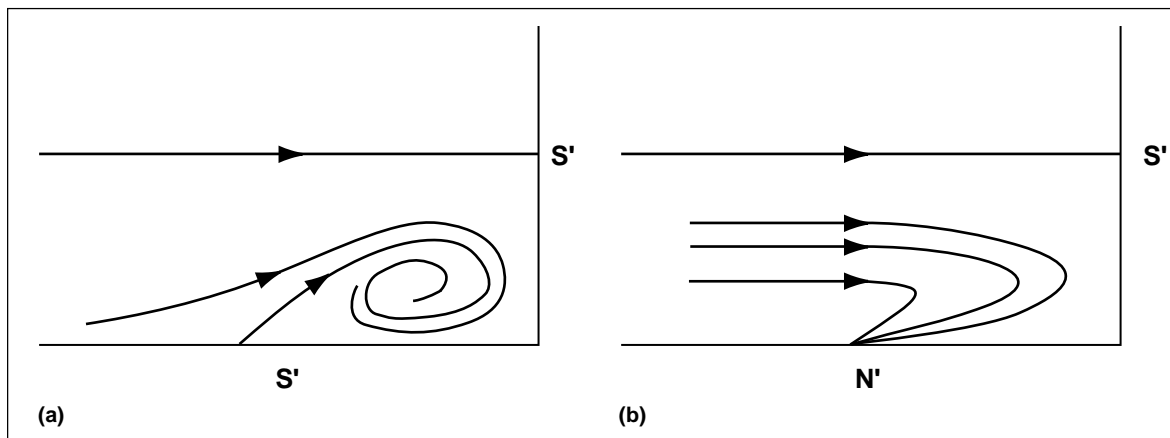


Fig. 1. Symmetry plane schematics. (a) Saddle point of separation in skin-friction-line pattern; and (b) saddle point of attachment in skin-friction-line pattern.

(2) What can be said about the relationship between the surface skin-friction-line pattern and the surface pressure distribution? (3) Can criteria be derived that will help remove the ambiguity in the interpretation of external flows on the basis of surface oilflow patterns alone? Topological concepts again prove useful in addressing these questions.

To address question (1), testing began with virtually two-dimensional flow conditions by imagining the cylinder diameter to be very large. The flow approaching the cylinder necessarily had to separate in the classical sense, originating from a saddle point of separation at the wall and occurring on the symmetry plane of the approaching flow. Successive reductions in the diameter of the cylinder enabled following the evolution of the singular points and loci of zeroes of the velocity-field components in the symmetry plane. The evolution led eventually to a critical condition at which the singular point in the external flow merged with the singular point at the wall, changing the saddle point of separation to one of attachment. It was the three-dimensionality of the flow approaching the obstacle, characterized by the presence and magnitude of the transverse velocity (that is, the velocity component normal to the symmetry plane), that allowed the flow to take an alternative route around the obstacle. Rather than undergoing separation, with the flow rising around a separation stream surface, a sufficient quantity of flow could be diverted outward to allow the remainder of the flow to turn downward into a saddle point of attachment.

In response to question (2), topological concepts have been used to analyze two flow examples: a laminar juncture flow and flow past a hemisphere/cylinder at a moderate angle of attack. The analysis has proven that the relationship between skin friction and surface pressure gradient is very close indeed: every singular point in a pattern of skin-friction lines must be accompanied by a corresponding surface pressure extremum. A theorem has been presented that formalizes the relationship. Available experimental results confirm the thesis for the hemisphere-cylinder case.

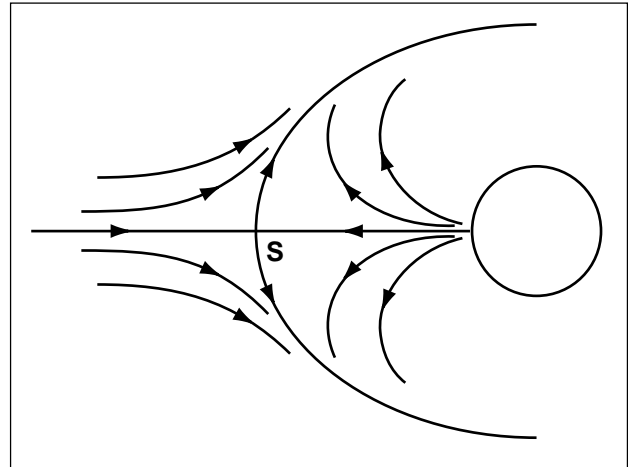


Fig. 2. Skin-friction-line pattern common to figures 1(a) and 1(b)

In response to question (3), topological ideas have been adapted to derive a criterion for the onset of separation, for both two-dimensional and three-dimensional flow. The two-dimensional result is a rederivation of the well-known Stratford criterion, giving it a firm topological basis. The three-dimensional result applies to flow in a symmetry plane. It is a simple modification of the Stratford form, showing how the pressure-rise term must be supplemented to account for the presence of a transverse velocity. As expected, if the transverse velocity is inward toward the symmetry plane, a smaller pressure rise than that needed to separate the equivalent two-dimensional flow is required to separate the flow in the symmetry plane. If the transverse velocity is outward, the opposite is true.

Point of Contact: M. Tobak
(415) 604-5855

Computational Fluid Dynamics Design of NASA/DeBakey Ventricular Assist Device

Cetin Kiris, Dochan Kwak

Mechanical blood pumping devices are in demand as a life support system to assist ailing hearts. Currently, commercially available circulatory support involves large, complex, and expensive pulsatile devices. These diaphragm type or cable-driven devices require large external support equipment resulting in little or no patient mobility. In 1989, NASA's Johnson Space Center began a joint project with DeBakey Heart Center of the Baylor College of Medicine in Houston to develop a new implantable total left ventricular assist device (LVAD) complete with a control electronics package. This LVAD is based on a fast, rotating axial pump using magnetic propulsion requiring a minimum number of moving parts. To make it implantable, the device must be made as small as possible, requiring a very high rotational speed.

The major problems related to fluid dynamics were the excessive blood damage due to high shear stress and the blood clotting in local regions of recirculation. To make this design usable, it was essential to lower the blood damage to an acceptable level and to prevent blood from clotting, as well as to increase pumping efficiency so that the power requirement can be minimized.

Depending on the usage, the requirements for LVAD varies. The current effort was to develop a two-week pump that is mainly for use in post-surgical heart failure and emergency cases. Due to its unconventional size and severe operating conditions, it was essential to employ the computational fluid dynamics (CFD) technology to guide the experiments and to evaluate different design possibilities. Thus the objective was to develop and apply flow simulation procedures for developing an implantable LVAD. The flow in the proposed heart pump is viscous, incompressible, and three-dimensional. The inflow to the pump is pulsatile at the frequency of a human heart. The flow in this device involves rotational and

stationary parts in addition to the three-dimensional (3-D) geometry. For this task, the Ames-developed computer code, INS3D, was used for parametric study of different design configurations. The code was validated using the inducer data made available through the Propulsion CFD Consortium activity at NASA's Marshall Space Flight Center.

Starting from the baseline design, many design ideas were numerically simulated leading to a new configuration, which includes an inducer generated from a rocket engine (shown in the figure). This improved the hemolysis problem and increased the pumping efficiency significantly. Because of extensive computational analysis conducted to improve the performance, the thrombus problem near the bearing region was also removed.

The final design has passed two-week requirements by the National Institutes for Health. A summary of performance comparison between

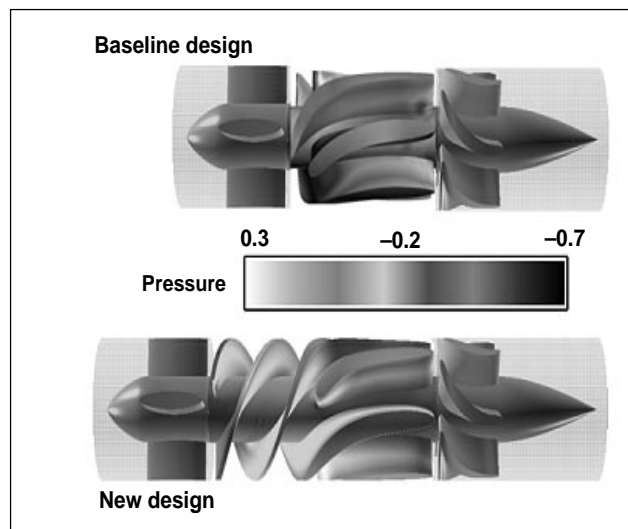


Fig. 1. Geometry of the baseline and the new design.

Table 1. Clinical results for the baseline and the new design

	Baseline design	New design
Pumping efficiency	0.25	0.33
Hemolysis index	0.02	0.002
Power required, watts	12.6	9.8
Rpm	12,600	10,800
Thrombus formation	Yes	No
Two-week test	Failed	Passed

the baseline design and the final design is given in the table.

The current design is compact and provides patient mobility. The major bottleneck was the excessive thrombus and blood damage; however, the present invention has eliminated those problems, enabling the device to operate efficiently as a life support system.

Point of Contact: C. Kiris/D. Kwak
(415) 604-4485/6743

Progress in Computational Fluid Dynamics for High-Lift Aerodynamics

Stuart E. Rogers

One of the major challenges confronting the application of computational fluid dynamics analysis tools to problems in high-lift aerodynamics is that of complex geometry. When a typical subsonic aircraft wing deploys its high-lift system slats and flaps, the wing is no longer a relatively smooth and continuous single body, but is a series of closely positioned bodies with many sharp edges and discontinuous surfaces. In addition, the physics of the air flow over a high-lift wing is dominated by the merging viscous boundary layers, wakes, and vortices, requiring fine resolution of the geometric features.

Significant promise has been shown in applications of overset grid technology to this problem. A computer program that automatically generates a "wingcap grid" on the spanwise ends of the wing, flaps, and slats was developed. This wingcap program utilizes a suite of overset-grid-generation utilities, and results in a high-quality, fine-resolution grid, capable of resolving the wing-tip vortices formed by each of these elements.

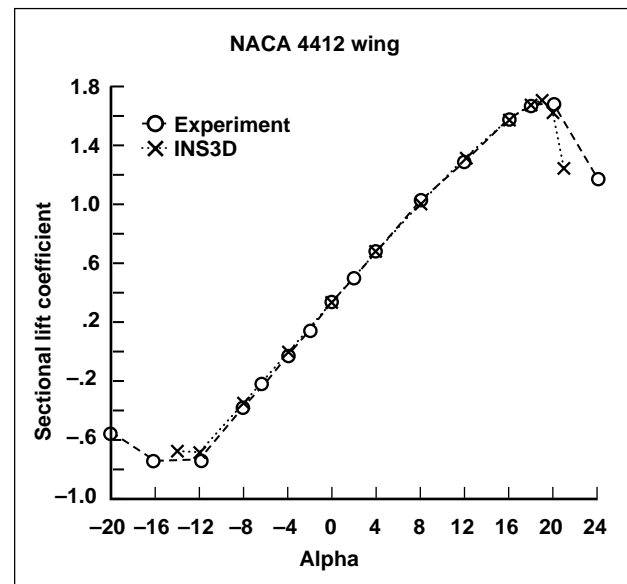


Fig. 1. Lift prediction for NACA 4412 wing.

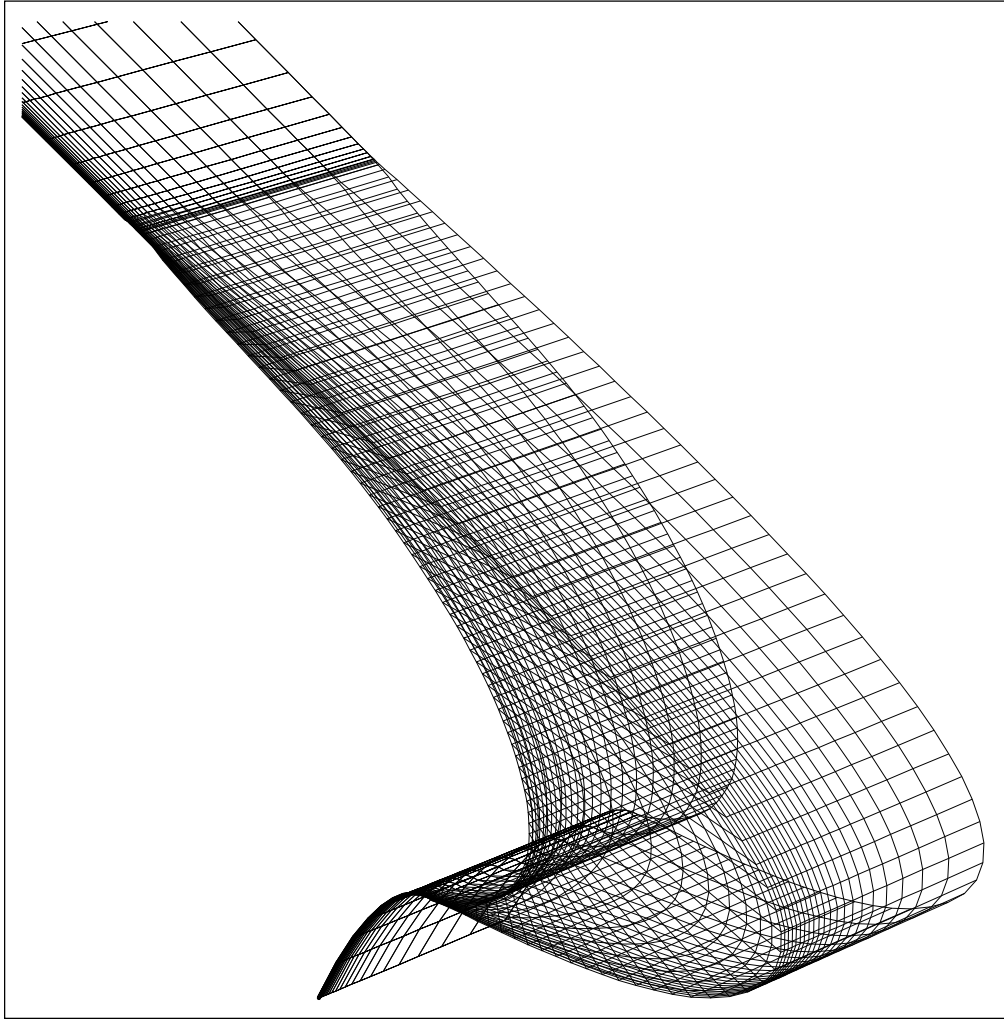


Fig. 2(a). Wingcap surface grid on a slat.

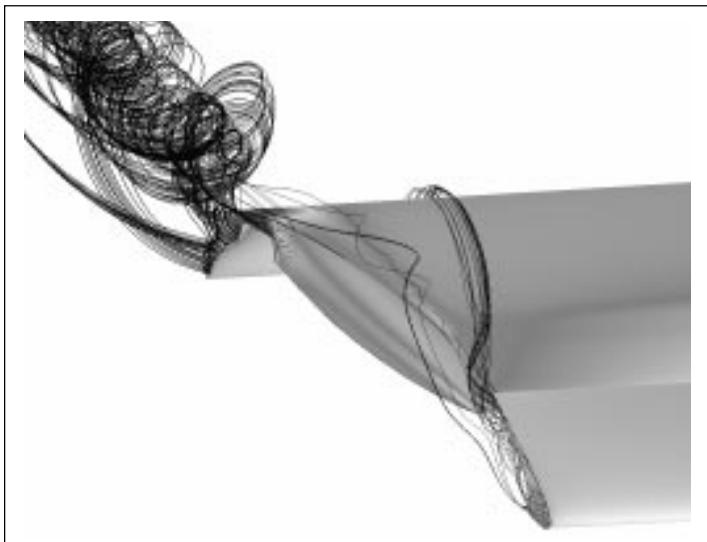


Fig. 2(b). Wing-tip vortices on a three-element wing.

The wingcap-grid concept has been applied to numerous cases. A validation case of the flow around a NACA 4412 wing was run using wingcap grids to resolve the wing tip. The results from the INS3D code are shown in the first figure, in which the lift coefficient is plotted versus angle of attack. Excellent agreement is seen between the computation and the experimental results, which were taken from a 1936 report of the National Advisory Committee for Aeronautics. The wingcap program has been applied to many different high-lift geometries, one of which

is shown in the second figure. Three wingcap grids were used to resolve the tips of the slat, main element, and flap of this high-lift validation wing. In this figure, the wingcap grid on the end of the slat is shown. Particle traces, which reveal the structure of the vortices formed at the end of this wing, are shown.

Point of Contact: S. Rogers
(415) 604-4481

Three-Dimensional Cartesian Computational Fluid Dynamics Technology: Improvements and Applications

John E. Melton, Michael J. Aftosmis

An automated Cartesian Euler computational fluid dynamics method has been applied to a wide variety of advanced aircraft configurations in support of numerous industrial and national programs. Since the method was designed to accept geometries of arbitrary complexity, it has proven to be extremely useful for configurations that require rapid yet detailed analyses. The first figure (see Color Plate 10 in the Appendix) shows the surface pressure distribution computed about the Apache helicopter. This solution demonstrates the ability of the method to compute solutions for extremely complex configurations. The analyses of five major configuration variations of the Apache were completed within a two-month time frame in support of upcoming flight

tests. All the computations were performed on the CRAY C-90 computer.

The accuracy of the Cartesian solver has been extensively evaluated on a variety of two- and three-dimensional test cases. For example, parts (a) and (b) of the second figure (see Color Plate 11 in the Appendix) show the Cartesian grid and the pressure contours about a circular cylinder in low Mach number flow, respectively, and part (c) shows the computed and analytic surface pressure distributions as functions of vertical position on the cylinder.

Point of Contact: J. Melton
(415) 604-1461

Wing-Body-Control Aeroelastic Computations on IBM SP2

Guru P. Guruswamy, Chansup Byun

The accurate prediction of aeroelastic loads is necessary for the design of large flexible aircraft. Furthermore, correct prediction of loads and the resultant structural deformations is essential to the determination of the aircraft stability and control characteristics. Since the experimental evaluation would involve considerable cost and the risk of structural damage in a wind tunnel, it is necessary to complement the investigation through theoretical analyses.

The objective is to conduct static aeroelastic computations of wing-body-control configurations using a parallel, multizonal version of the ENSAERO code on the IBM SP2 computer. For demonstration purposes, the steady and unsteady Navier–Stokes

flow simulations are performed for an arrow wing-body-control configuration with and without flap deflection. Static aeroelastic computations on this configuration are also made by modeling the wing structure as a flexible flat plate. The figure (see Color Plate 12 in the Appendix) shows the effect of control surface deflections on the wing displacements. The computer performance obtained indicates that about nine computational nodes of the IBM SP2 computer are equivalent to the speed of a single Cray C-90 processor.

Point of Contact: G. Guruswamy
(415) 604-6329

Automated Computational Fluid Dynamics for Subsonic Transports

Steven M. Nash, William M. Chan, Jin J. Chou, Pieter G. Buning

The overall purpose of this project is to create an automated way to run computational fluid dynamics (CFD) analyses of subsonic transport configurations. The system starts with an initial graphics exchange standard (IGES) description of the geometry, and returns force and moment data with selected pressure coefficient cuts on the wing. The automated process includes surface and volume gridding, overset (Chimera) grid hole cutting and connectivity, batch submission of a flow solver run, and postprocessing.

The current system handles wing/fuselage configurations, as shown in the figure (Color Plate 13 in the Appendix). Accurate lift and drag values in the cruise range have been verified, with typical runs requiring 10 hours of computing time on a Cray C-90 and 24 million words of main memory. The system also has the capability to simulate flow about a semispan model in the NASA Ames 11- by 11-Foot Transonic Wind Tunnel.

The automated system uses the Chimera overset grid strategy, with viscous simulation of all configura-

tion surfaces. The thin-layer Navier–Stokes equations are used to model the flow. The system comprises a set of UNIX scripts, which in turn call a collection of CFD software tools, including SUPERG and Collar Grid Tools for surface gridding, HYPGEN for volume grid generation, PEGSUS for overset grid joining, OVERFLOW for the flow solution procedure, and FOMOCO for force and moment postprocessing. Interactive control of many operating parameters is possible, whereas default values handle most configurations.

The script system enables users with a background in CFD to generate overset grids without a detailed knowledge of the specific CFD tools used here, while modification and tailoring of the system can be accomplished by experts.

Point of Contact: S. Nash
(415) 604-4517

Validation of ENSAERO for an Elastic Supercritical Wing

Guru P. Guruswamy, Mehrdad Farhangnia

In an ongoing effort to improve the performance of advanced subsonic civil transports (ASCT), modern elastic wings are being developed with supercritical airfoils to help delay the formation of strong shocks. However, these wings are susceptible to undesirable aeroelastic behavior, such as transonic buffeting outside the design envelope. Due to the expensive nature of experimental studies of this type, numerical computations are used to study the mechanism of this unsteady phenomena.

The goal of this phase of the study is to validate static aeroelastic computations of an ASCT-type wing with a state-of-the-art experiment which uses a realistic spar-rib-skin type wing model. For this, the Advanced Research Wing that was tested at Langley Research Center was selected. The three-dimensional, thin-layer, Navier-Stokes equations for

fluid flow coupled with modal analysis for the structural dynamics are solved using a pseudo-dynamic approach with body-adaptive grids by using the computer code ENSAERO. The converged solution shows a good correlation with the experimental results in both the structural deformation, as well as the pressure coefficients about the wing. The figure (see Color Plate 14 in the Appendix) shows the pressures on rigid and flexible configurations. The pressures computed by ENSAERO for the flexible case compares well with the experimental pressure data. In addition, the spanwise deflections compare well between the wind-tunnel and computed data.

Point of Contact: G. Guruswamy
(415) 604-6329

The Unsteady Flow Analysis Toolkit

David L. Kao

Numerical simulations of complex, three-dimensional (3-D), unsteady flows are becoming increasingly feasible because of the progress in computing systems. Unfortunately, because many existing flow visualization systems were developed for steady (time-independent) flow solutions, they do not adequately depict those from unsteady flow simulations. Furthermore, most systems handle only one time step of the solution at a time and do not consider time in the calculation.

The unsteady flow analysis toolkit (UFAT) was developed to assist computational fluid dynamics (CFD) scientists with the analysis and visualization of unsteady (time-dependent) fluid flows. Many CFD scientists have used UFAT to compute particle traces, which are very effective for visualizing physical flow phenomena such as vortex breakdown and vortex shedding.

The size problem of 3-D unsteady flow simulation is increasing as the hardware technology continues to improve. It is common to have a grid containing several million points, and the file size for one time step can easily exceed several megabytes. If there are tens of thousands of time steps, then the total disk requirement for storing the entire solution would be thousands of gigabytes. Interactive visualization of data with this magnitude is clearly impossible with current hardware technology. UFAT supports postvisualization, an approach commonly used in numerical flow visualization. The advantage of postvisualization is that the flow visualization parameters can be changed without recalculation of the solution. Graphics objects can be displayed interactively as they are computed or saved for later playback. By saving the graphics objects to disk, the

scientist can repeatedly play back the graphics objects without recalculation.

UFAT computes particle traces in unsteady flows with moving grids. The following types of particle traces can be computed using UFAT: streaklines, timelines, streamlines, and pathlines. UFAT allows the user to compute particle traces using many time steps. It can assign color values to the particles based on their seed points, time at release, ages, positions, and scalar quantities. UFAT saves the particle traces to a graphics file for playback. With the latest version, UFAT 3.0, the following features are now available: physical seed specification, particle trace

subsetting, stream surfaces/ribbons, and color contoured grid surfaces.

The first figure (Color Plates 2(a) and 2(b) shown in the Appendix) illustrates the use of this tool and depicts streaklines about a V-22 rotor in hover. Another example of the use of this tool, illustrated in the second figure (Color Plate 6 in the Appendix), shows the visualization of nonsteady surface pressures and surface-flow patterns at one instant in time.

Point of Contact: D. Kao
(415) 604-4375

Recent Enhancement to the Navier–Stokes Code OVERFLOW

Dennis Jespersen, Thomas Pulliam

The computer code OVERFLOW finds a numerical solution of the compressible Navier–Stokes equations using finite differences in space and

implicit time stepping. To handle complex geometries, OVERFLOW uses the “Chimera” approach: grids are generated independently for different zones,

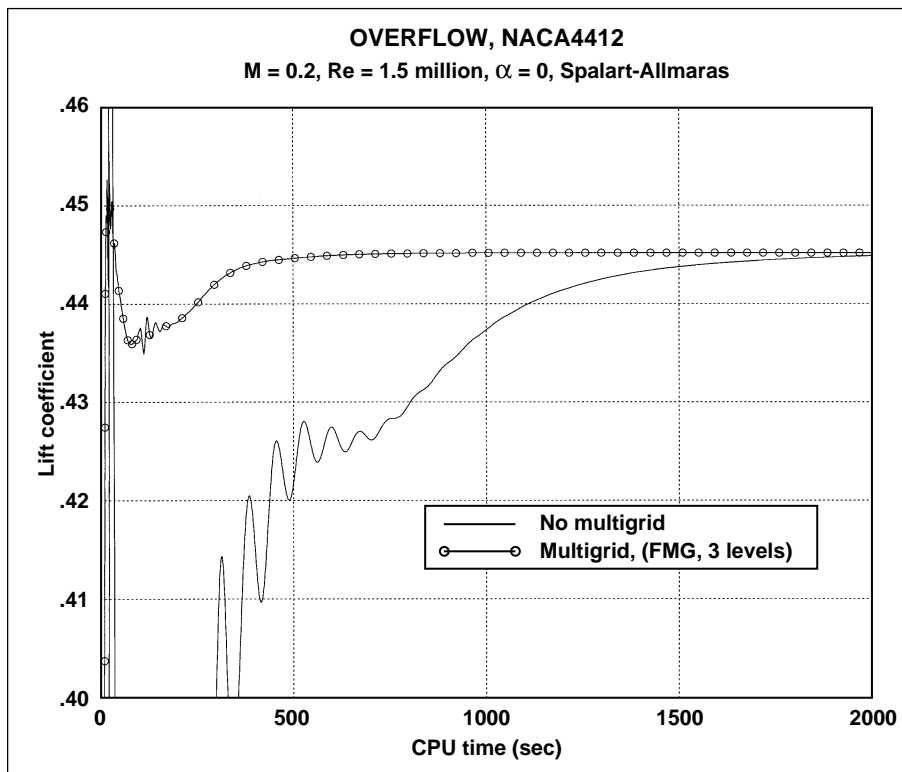


Fig. 1. OVERFLOW + multigrid: convergence of lift as a function of CPU time.

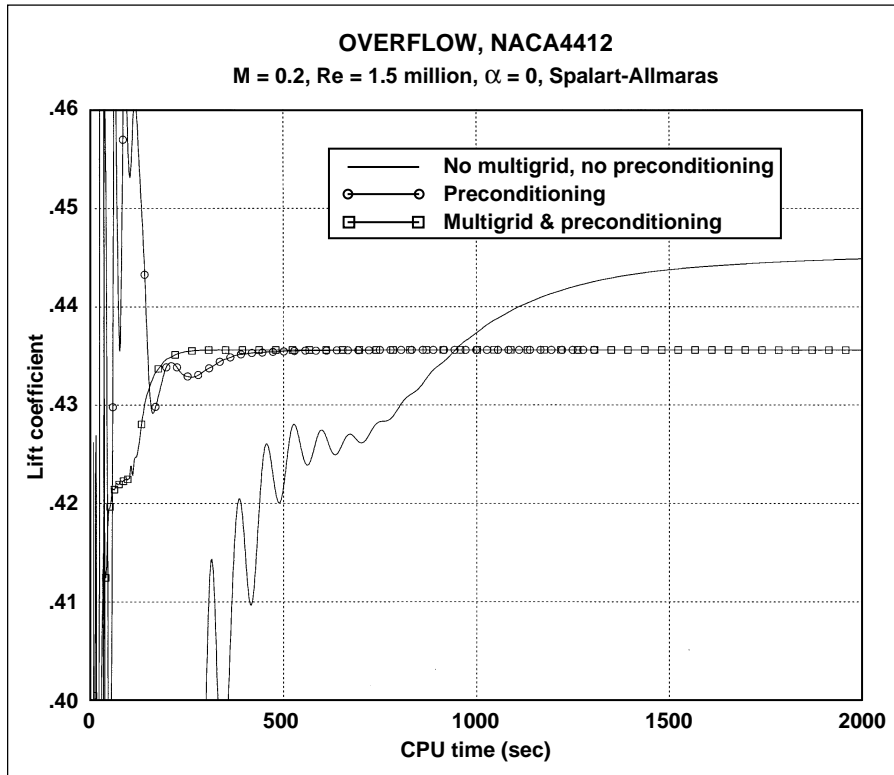


Fig. 2. OVERFLOW + multigrid + preconditioning: convergence of lift as a function of CPU time.

with arbitrary overlap permitted. Some zones will get their boundary data by interpolation from another zone or zones. OVERFLOW has a demonstrated capability to solve flow problems with a large number of unknowns in complex geometries.

One of the difficulties encountered with the use of OVERFLOW has been possible slow convergence for steady-state flow problems. If tools such as OVERFLOW are to make an impact on aerodynamic design cycle processes, the convergence rate of the code for steady-state problems needs to be improved. A multigrid algorithm was added to provide a solution to this problem. The basic implicit algorithm in OVERFLOW is quite efficient. The multigrid algorithm imposes a substantial overhead (at least 50%), but does produce an even more substantial decrease in iterations, and, therefore, in central processing unit (CPU) time to convergence. A sample case: NACA4412 airfoil, 257×81 mesh, Mach number 0.2, 0 degree angle of attack, Reynolds number 1.5 million, Spalart-Allmaras turbulence

model is run on a two-processor Silicon Graphics Inc. Power Challenge, 75-megahertz machine. The first figure compares a nonmultigrid run with a three-level full multigrid (FMG—coarse grids are used for initialization). Converged lift is obtained in 2000 CPU seconds for the nonmultigrid run. Improvement by a factor of 4 is gained with the multigrid algorithm.

Another difficulty with compressible Navier-Stokes codes in general is slow convergence for low Mach number flows. This difficulty can be traced to a disparity between the acoustic and convective speeds, and can be addressed by a preconditioning algorithm. Furthermore, for very low Mach number flows, the solution produced by a compressible code is usually of poor quality, with pressure oscillations visible in contour plots. The low Mach number preconditioning algorithm also provides a solution to this problem. The preconditioning algorithm has been implemented into the OVERFLOW code.

The same test case is shown in the second figure. Here the preconditioning reduces the required 2000 seconds of CPU time by a factor of 4. The preconditioning changes the form of the artificial dissipation term in the numerical algorithm and thus changes the asymptotic values of lift and drag.

Finally, a combination of multigrid and preconditioning produces a total improvement of approximately a factor of 8, as shown in the second figure.

Point of Contact: D. Jespersen
(415) 604-6742

Improved Numerical Methods for Large-Eddy Simulation of Complex Turbulent Flows

Parviz Moin, Thomas Lund, Sandip Ghosal, Kenneth Jansen, Youhei Morinishi

Large-eddy simulation for complex turbulent flow requires a flexible yet accurate numerical method. Historically, spectral methods have been used to simulate three-dimensional, unsteady turbulent flows since they are able to accurately differentiate the important small-scale turbulent fluctuations. Applying spectral methods in complex geometries is very difficult, however, and as a result, finite difference or finite element methods are usually used in these cases. Unfortunately, discrete methods such as these introduce errors that increase in severity with the inverse of the turbulent length scale. Simulations performed during the past few years have shown evidence of these errors, but a quantification of these effects, as well as possible remedies, has been lacking. Several efforts have been undertaken recently to understand the role of truncation errors and to investigate various means of minimizing their impact.

A novel statistical analysis of finite difference errors revealed that the magnitude of the truncation error overwhelms the magnitude of the modeled subgrid stress over much of the wave-number range for central difference schemes lower than sixth order. Alternatively, it was shown that truncation error can be brought to an acceptable level if the filter width used to define the large-eddy field is taken to be at least four times the grid width. Numerical experiments substantiated this observation. Additional analysis of aliasing errors revealed that these errors impact the solution the most when high-order finite difference methods are used. Furthermore, it was found that alternative, analytically equivalent forms of the convective terms lead to different levels of aliasing error; in particular, the skew-

symmetric form has very good alias error reduction properties.

In parallel with the analysis of numerical errors, several studies aimed at improving the accuracy of discrete methods for turbulent simulation are in progress. Fully conservative fourth- and sixth-order finite difference schemes were constructed and tested in simulations of turbulent channel flow. Whereas the higher-order schemes showed more rapid convergence to the expected result as the mesh was refined, the results were not entirely satisfactory when a relatively coarse mesh was used. This particular problem can be circumvented to a degree by locally refining the mesh in regions where the turbulence is characterized by small length scale, yet important eddies (that is, near a solid surface). Mesh stretching alone is not sufficient to accomplish this task efficiently since it is often desirable to refine the mesh in a given coordinate direction as a function of the other two directions. Unstructured mesh techniques, on the other hand, provide a large degree of flexibility in refining the mesh only where needed. Fundamental tests of a finite element-based unstructured mesh technique for turbulent simulation indicate that it behaves much like a fourth-order finite difference scheme. Unlike a conventional finite difference method, however, the residual truncation error can be controlled through localized mesh refinement. The figures (see Color Plates 15 and 16 in the Appendix) show results of the unstructured mesh method applied to the three-dimensional flow over an airfoil at maximum lift.

Point of Contact: P. Moin
(415) 604-5127

An Improved Grid Generator

Reese L. Sorenson

In 1989 a general-purpose computer program for three-dimensional (3-D), elliptic, multiple-block, volume grid generation for computational fluid dynamics (CFD) research and design was developed. Subsequently, significant improvements have been added by researchers at Ames and Lockheed Martin, and are included in the newest release of the code. Improvements include more powerful mathematical terms for controlling grid cell size and skewness, enhanced control versatility and ease of use, improved error checking, improved initialization, convergence acceleration, and the addition of a simple graphical user interface.

The objective of this work was to make available to U.S. scientists and engineers the world's best 3-D elliptic multiple-block volume grid generator. The program was intended to be applicable to all types of CFD simulations, including viscous and inviscid aerodynamics, multidisciplinary aerodynamics/structures applications, and all other types of computational physics. It was intended to be easy enough to use and sufficiently fast to run so that it would be valuable in the product design cycle.

The new grid-generator program, called 3DGRAPE/AL, consists of approximately 49,000 lines of FORTRAN-77, and is documented.

Beta testing of the program was performed by scientists and engineers from U.S. industry, academia, and government, including Boeing, Bell Helicopter, Sverdrup, Raytheon, Lockheed Martin, Rockwell, Dow Chemical, Cray Research, the Universities of Tennessee and Florida, Old Dominion University, NASA, and the U.S. Air Force, Army, and Navy. The program has been used to generate grids for fundamental research on vortex interaction and for development of the F-14 and F-18 fighter aircraft, the V-22 tiltrotor aircraft, the U.S. Navy's standard

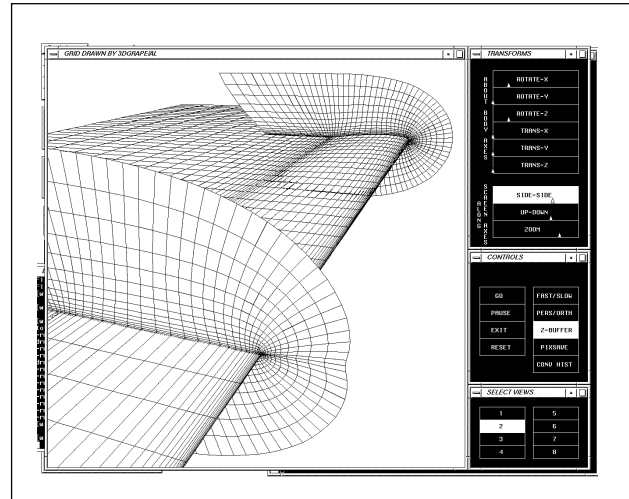


Fig. 1. Computer screen showing the program generating a C-H type grid about an isolated wing.

missile, a ballistic gun chamber, a ducted rocket motor, a high-speed civil transport, a turbine, and a chemical mixing tank. These tests were performed on a collection of more than 15 different computer types. Numerical convergence by an additional order of magnitude has been observed, in less than 25% of the computer time compared to the earlier program.

The graphical user interface is seen in the figure, which is a view of the computer screen when generating a C-H type grid about an isolated wing. The program is distributed by the Computer Software Management and Information Center (COSMIC).

Point of Contact: R. Sorenson
(415) 604-4471

Surface Movement Advisor

Brian Glass

The Surface Movement Advisor (SMA) project is a joint National Aeronautics and Space Administration (NASA)-Federal Aviation Administration (FAA) effort that will electronically connect the air traffic control, airline, and airport operations user communities to facilitate unprecedented information sharing. Users will be able to make many more informed decisions, leading to savings estimated at an average one minute of taxi delay saved per operation (based on a TRW (Thompson, Ramo, Woolridge) study for the FAA). Eventual national implementation of SMA at the 34 largest U.S. airports is projected to save users at least 5 to 15% of the \$1.6 billion annual ground delay costs caused by inefficient taxi and runway queuing—based on FAA simulations and Air Transport Association cost figures.

To address the problems associated with this ground operations bottleneck, SMA will provide air traffic and ramp controllers with automated aircraft identification and tracking. SMA will combine tracking and identification data with arrival and departure flight sequencing data (such as surface operations and aircraft taxi routing information provided to air traffic controllers, airline operators, and airport operators). In FY95, work was begun on the first SMA proof-of-concept/prototype (Build-1) to

demonstrate many SMA functional capabilities at the FAA-selected test site (Atlanta, Georgia's Hartsfield International Airport).

In December 1994, a User Requirements Review was conducted at Atlanta involving air traffic controllers, airline operations, and airport representatives. Work on early exploratory SMA software coding and user display mock-ups then began in parallel with top-level SMA design formulation and trade-off studies. This stage progressed through a successful Initial Design Review in April 1995, leading to detailed design work. In the next stage, the integrated system design was refined and completed in detail, leading to a Final Design Review (FDR) in July 1995, which established the baseline prototype SMA design. Following the FDR, the first set of SMA hardware was procured and assembled at Ames Research Center, a local area network was put in place by NASA at the Atlanta tower to enable data access, and the first SMA software was coded, resulting in an initial (alpha) version of Build-1 running in the laboratory by mid-September 1995.

Point of Contact: B. Glass
(415) 604-3512

An Automated Instrumentation and Monitoring System

Jerry Yan, Melisa Schmidt

Whether a researcher is designing the next parallel programming paradigm, another scalable multiprocessor, or investigating resource allocation and data partition algorithms, a facility that enables program execution to be captured and displayed is invaluable. The Automated Instrumentation and Monitoring System (AIMS) is a software toolkit that demonstrates innovative methodologies in performance instrumentation, monitoring, modeling, post-mortem analysis, and visualization for parallel programs. AIMS does not require the user to modify the application, and it provides an easy-to-use interface involving minimal user interaction. As shown in the first figure (see Color Plate 17 in the Appendix), AIMS first gathers performance data during the execution of applications. AIMS analyzes these data to generate statistical and animated views

to quickly reveal performance bottlenecks and allow the user to examine program execution in greater detail, as shown in the second figure (see Color Plate 18 in the Appendix).

AIMS is the only performance tuning environment that supports message passing paradigms—parallel virtual machine and message passing interface—as well as data-parallel programs (written in High Performance FORTRAN) on the IBM SP-2 multiprocessor and a network of heterogeneous workstations (from vendors such as Sun Microsystems, Silicon Graphics, Inc., and Hewlett Packard).

Point of Contact: J. Yan
(415) 604-4381

The Numerical Aerodynamics Simulation Trace Visualizer

Louis Lopez

The development of correct and efficient computer programs is always difficult, but it is particularly difficult for parallel programs. This is due to the fact that experience in debugging and tuning this type of program is limited. Techniques and tools for developing sequential and vector codes have been developed over the years, but parallel programs present special challenges and there is no well-developed paradigm for debugging and tuning of these codes. One technique that is available traces all significant parallel events. This technique writes a record of every significant parallel event to a file (for example, when a message is sent or received or a processor goes into a wait state, etc.). This data can then be studied to determine how the program performed and what can be done to improve the performance. Because trace files can be very large and contain complex data, they are difficult to analyze without the aid of trace visualization tools.

The Numerical Aerodynamics Simulation (NAS) Trace Visualizer (NTV) is a parallel trace visualization tool that accepts traces generated by The Automatic Instrumentation and Monitoring System or the native IBM SP2 trace facility using the Message Passing Library. NTV has two major components. The first presents profiling information in the form of bar charts for various quantities useful in getting an overview of the program's performance. The second component is a static (non-time varying) time-line display showing processor status as a function of time. Superimposed on this display are lines showing the messages being passed between nodes. Zooming is provided, as is the ability to select particular messages to be displayed, for example, all messages between specific nodes.

The figure shows two views of the data for a simple example run on the IBM SP2. There is a horizontal bar for each node. The bars are color coded to show the status of the nodes at every point in time (time is the horizontal axis). The angled lines are the messages being sent between nodes. The display at the top shows all of the data from the trace. An examination of this display shows that this is a poor program, since most of the time is spent waiting for communications and very little time computing (the green sections in the color figures, dark sections in the black and white figures). There should be some computation at the points where the messages arrive.

The bottom figure was produced by zooming-in to a small section of the top figure (the area selected by the two vertical lines in the top figure). The display of messages is turned off. Small computational blocks can be seen that were not visible in the top display because they are so small.

The current version of NTV, the version supporting the IBM SP2, was completed and a Beta version was made available for testing through the NAS Software Archive on the World Wide Web.

Point of Contact: L. Lopez
(415) 604-0521

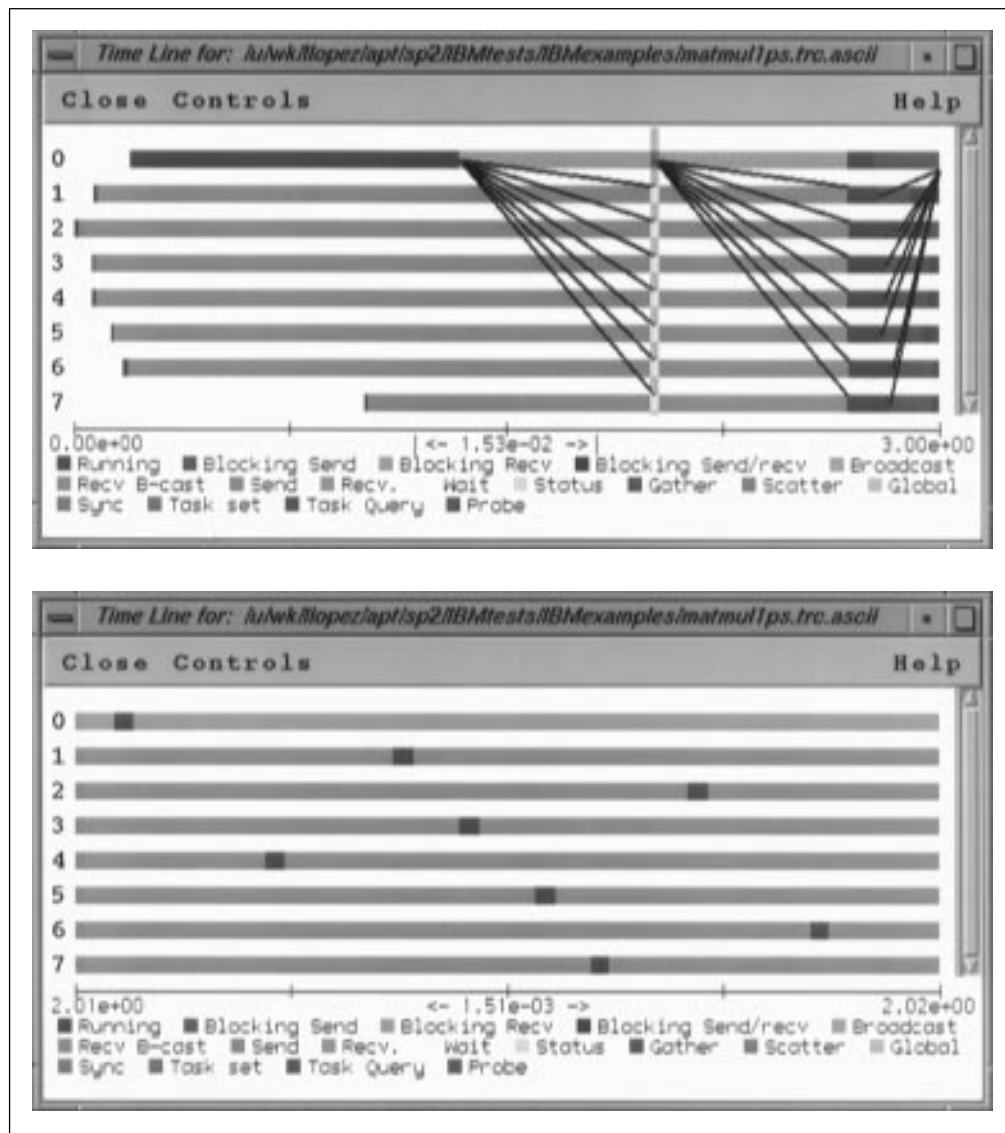


Fig. 1. Two views of an NTV time-line display.

An Emerging Standard for File Access on Parallel Systems

Sam Fineberg, Bill Nitzberg, Parkson Wong

Message Passing Interface-Input/Output (MPI-IO) is a breakthrough in the area of high performance parallel I/O. Ames researchers, along with researchers from International Business Machines (IBM) Watson Research Center began defining MPI-IO, a new standard interface for parallel file operations. MPI-IO is an extension to the popular MPI standard. Together, they will enable truly portable programs to be written for parallel machines. However, in the scientific world, portability and performance are inseparable; a program is not considered truly portable unless it not only compiles, but also runs efficiently. MPI-IO has the potential to solve both performance and portability problems.

Creating a new standard requires industry-wide participation. The MPI-IO effort was opened up to the global high-performance computing community at the IEEE Supercomputing '94 conference in November, where a Birds-of-a-Feather (BOF) session was held to describe the initial proposal and solicit greater participation. In addition to the BOF, NAS

created a mailing list and a Web site to facilitate communication. The MPI-IO effort was joined by approximately 100 organizations in 18 countries. Based on the feedback received, a revised draft standard was published.

Finally, the "collective buffering" algorithm for speeding parallel I/O was developed. Collective buffering is an extension of the file buffering provided by sequential operating systems, where the data is permuted before writing (or after reading) in order to collect and combine small file accesses into large blocks. Experiments on the IBM SP2 Parallel I/O File System and on the Intel Paragon Parallel File System demonstrated a performance improvement of two orders-of-magnitude using collective buffering for complex three-dimensional data distributions.

**Point of Contact: B. Nitzberg
(415) 604-4513**

Monitoring Human Motion Perception by Measuring Eye Movements

Leland S. Stone, Brent R. Beutter, Philippe Stassart

Classical psychophysical methodologies (for example, two-alternative forced choice) for measuring human perception are difficult, if not impossible, to use in an applied aerospace setting because the method itself interferes with the task being performed by the pilot. However, the passive measurement of eye movements in cockpits or simulators not only is feasible but also has the potential to provide much of the desired information without causing such interference. There are two major obstacles to using eye-movement information as a real-time monitor of human perception: (1) the lack of a noninvasive, nonintrusive, yet high-quality eye tracker, and (2) the difficulty in quantitatively relating the eye-movement data to perception. In 1995, considerable progress was made in these areas.

One of the problems with using noninvasive, video-based eye trackers is that commercially available systems have low temporal resolution (60 hertz) at full spatial resolution. In collaboration with ISCAN, Inc., of Cambridge, Massachusetts, Ames researchers have developed a low-cost, noninvasive eye tracker by combining a high-speed (240 hertz) commercially available camera with a PC-based tracker system to generate 240-hertz eye position data with 256- by 256-pixel spatial resolution. It has been determined that the shape of the viewing window can cause humans to misperceive the visual motion behind the window. In addition, a new analysis technique has been developed by simultaneously performing classical psychophysical measurements and measuring eye movements; this technique shows that the errors in perceived direction are mirrored in the direction of the eye movements, as shown in the figure. As can be seen, what observers see can be predicted quantitatively by monitoring their eye movement, without any active participation by the observers.

The technical and analytical progress over the last year has provided strong validation of the idea that eye-movement measurements could be used to monitor human perception during the performance or simulation of aerospace tasks without interfering with the task. This approach, therefore, shows

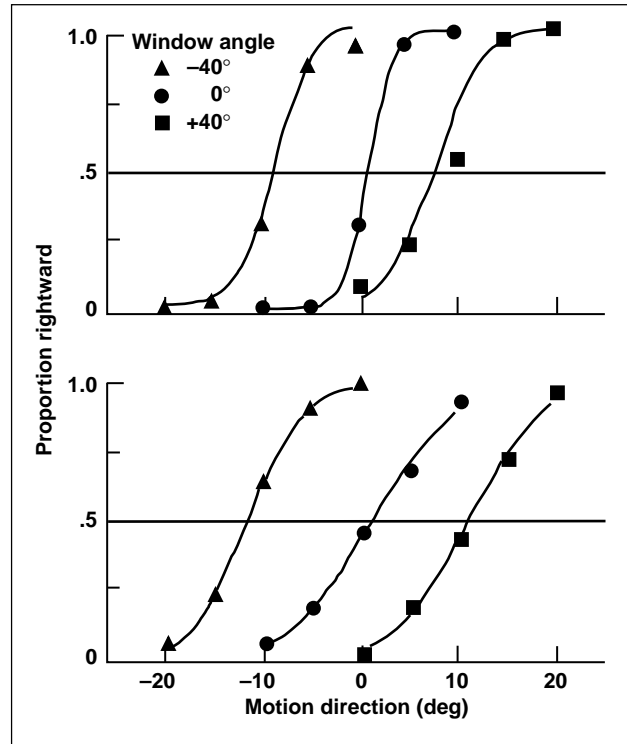


Fig. 1. Quantitative comparison of perception and eye movements. Top panel: Standard psychometric curves showing the proportion of rightward judgments as a function of the actual direction of motion. Note that the window angle of an elongated window biases the perceived direction by ~10 degrees. Bottom panel: Oculometric curves derived from the simultaneously recorded eye-movement data using a new analysis technique. Note that the oculometric curves show the same behavior as the actual psychometric curves.

considerable promise as a tool for evaluating pilot training regimes, for designing safe and effective displays, and even as a potential early warning system that alerts the pilot to the fact that he/she is misperceiving the display.

Point of Contact: L. Stone
(415) 604-3240

Three-Dimensional Sound Synthesis: Measuring Personalized Head-Related Transfer Functions

Durand R. Begault, Elizabeth M. Wenzel

Previous work has resulted in the development of a very-high-speed digital signal processor, the Convolvotron, for presentation of spatial audio cues in real time over headphones. This device uses filtering by time-domain finite impulse response filters based on head-related transfer functions (HRTFs). Although it is both successful and useful for presenting spatial information in a variety of aerospace applications, the Convolvotron is still limited in the complexity of environmental (room) modeling that can be achieved and that requires enormous computational resources. This limitation is important because research indicates that synthesis of purely anechoic sounds can result in a variety of perceptual errors, and these errors tend to be exacerbated when virtual sources are generated from nonpersonalized HRTFs, a common circumstance for most spatial auditory displays. Other research suggests that such errors may be mitigated by providing more complex acoustic cues from reflective environments. Thus, there is a need to resolve the issue of using nonpersonalized HRTFs and to develop a much more computationally efficient method of synthesizing complex acoustic environments in real time than is currently realizable.

The primary objective of the present advanced technology development effort is to develop display systems that maximize perceptual accuracy by presenting to the listener a carefully designed set of veridical acoustic cues that have been validated in psychoacoustical studies. The approach taken to achieve this goal is twofold: (1) improve the ability to make reliable measurements of HRTFs in any environment for any listener; and (2) develop techniques for rendering complex environmental cues in real time.

Development of a relatively low-cost portable system for measuring HRTFs, called Snapshot (shown in the figure), was completed at Crystal River Engineering (now Aureal Semiconductor, Inc., Fremont, California) and installed at Ames Research Center. The system employs a single speaker mounted on an adjustable arm. The subject, seated on a swivel chair, is outfitted with blocked-ear-canal microphones, and



Fig. 1. The Snapshot measurement system used for measuring head-related transfer functions.

HRTFs are measured using Golay code sequences. By constraining the geometry to ensure that no early reflections arrive within the first few milliseconds after the direct path arrival, the need for an anechoic chamber is eliminated—simple windowing techniques are used to extract the desired HRTF from the measured impulse response. Initial acoustical studies have verified that, for most subjects, measurements using a blocked-ear-canal microphone are comparable to those made with probe (inside the ear canal) microphones.

Point of Contact: E. Wenzel/D. Begault
(415) 604-6290/3920

Head-Mounted Displays of Virtual Objects for Assembly and Maintenance

Stephen R. Ellis, B. D. Adelstein

An optoelectronic testbed, an electronic haploscope illustrated in the first figure, has been used in experimental studies to guide development and evaluation of head-mounted, see-through displays of nearby virtual objects. This kind of display, illustrated in the second figure, has been developed by the U.S. commercial aircraft industry to assist in aircraft assembly. It provides a medium through which computer-based models of the objects to be handled may be directly displayed before the assembly or maintenance workers who must assemble or service them, thereby reducing the need for workers to interact with paper instructions and blueprints. Pilot

studies by Boeing Computer Services and the U.S. Air Force have shown that such displays can dramatically increase industrial worker productivity.

Experiments have determined the accuracy with which alternative viewing conditions may be used to present the depth of virtual objects such as those needed by the industrial displays. Users' visual ability to locate static and to track dynamic virtual image targets has been tested, for example, with monocular, biocular, and stereoscopic display formats. Measures of performance and visual fatigue have shown that, whereas the biocular displays may present depth with accuracy similar to stereo displays, these displays are



Fig. 1. An optically and mechanically adjustable see-through head-mounted display called an electronic haploscope is used to view a computer-generated irregular path. The operator is attempting to trace a virtual ring over the path without making contact with it. Experiments with various configurations of this display are used to provide advice for the ultimate configuration of similar industrial displays.

associated with much higher visual fatigue. Objects presented on monocularly viewed displays are subject to the largest errors in judged static depth, especially when the virtual images of the objects are overlaid on real surfaces. Attempts to counteract these errors by introduction of high-fidelity dynamic cues to depth, such as motion parallax, are being advanced by current work aimed at improving the

dynamic fidelity of the computer graphics rendering the object. Hardware and software techniques have been developed to allow the computer graphics to generate stereoscopic virtual objects at 60 hertz with latencies near 30 milliseconds.

Point of Contact: S. Ellis
(415) 604-6147



Fig. 2. A prototype of an industrial head-mounted display at Boeing Computer Services is used to present a path that a real wire will follow as part of an aircraft wire harness. The green path has been overlaid on the photograph to indicate the kind of wiring information the display can provide. Not only can such displays indicate where wires should be drawn, but they also can clearly present complex assembly sequences that are difficult to represent on paper.

Ames Spatial Auditory Display

Durand R. Begault, Elizabeth M. Wenzel

The first three-dimensional audio processor designed especially for multiple communication channels has been developed (as shown in the figure). The enabling technology behind the Ames Spatial Auditory Display (ASAD) was awarded U.S. Patent 5,438,623 in 1995.

Over headphones, the ASAD places up to five different communication channels at fixed virtual auditory positions about the listener, giving the listener a spatial sense of each channel originating from a unique position outside the head, that is, as if five people were standing about you, speaking from five different directions. This audio-communication breakthrough provides a substantial increase of intelligibility and safety in virtually all simultaneous, multichannel applications. The system can be effectively combined with other technologies, integrated into existing systems, and has the potential for further miniaturization.

The ASAD is ideal for teleconferencing, dramatically enhancing current technology for listening to several people from a remote location. It can be an important tool for emergency communication, command, and control centers that require constant simultaneous communication monitoring. The ASAD was originally developed to enhance aeronautical communications by air traffic controllers and by airplane, helicopter, and rotorcraft pilots.



Fig. 1. The Ames Spatial Auditory Display.

This technology enables significant intelligibility improvement for multiple communications channels and reduces auditory fatigue.

**Point of Contact: J. Salute
(415) 604-5596**

Coordinated Haptic-Visual Virtual Environments

Bernard D. Adelstein, Stephen R. Ellis

Haptic perception involves the inherent cognitive processes and physiological apparatus (for example, touch, force, and motion sense organs) through which the mechanical dynamics of our surroundings are perceived. However, by comparison with other sensory modalities, haptic perception has received considerably less attention in the scientific literature. Thus, many of the issues key to the design of effective haptic virtual environments (VEs) such as hardware performance requirements, VE simulation and modeling techniques, and intersensory trade-offs for

multimodal VE presentation have only begun to be examined by the research community.

By making available force and/or tactile sensory feedback, computer-modulated haptic interfaces offer the potential to enhance manipulative interaction in activities such as training, rapid design prototyping, and scientific data visualization. The figure shows an example of this type of activity.

The goal of this work is development of guidelines and specifications for effective computer-controlled haptic information presentation—both for

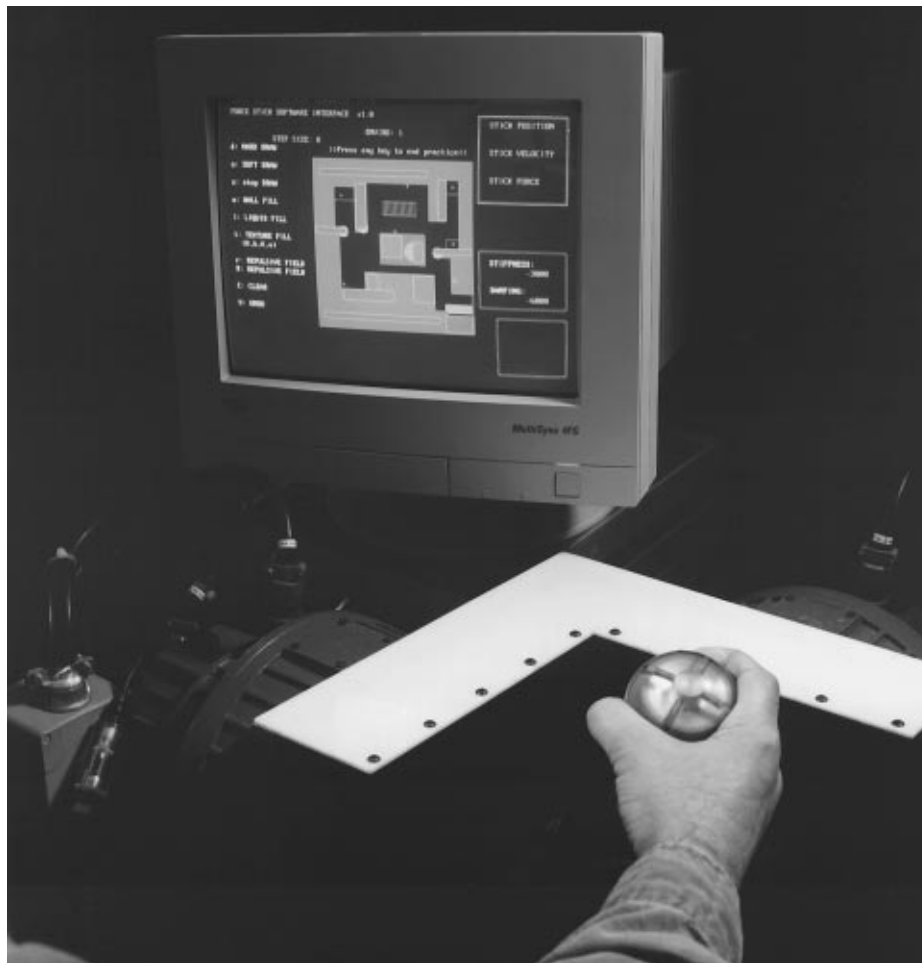


Fig. 1. Prototype two-degree-of-freedom force-reflecting manual interface being used to design and explore combined haptic-visual virtual environments.

haptic display in isolation and for combination in a coordinated haptic-visual interface.

This task has three major components. The first is the design and construction of an innovative force reflecting a manual interface capable of very-high-fidelity haptic interaction and information display. The second component is integration of the haptic display into a thoroughly calibrated, temporally and spatially conformal haptic-visual VE. The third is the study of haptic spatial and temporal dynamic factors coordination in a coordinated haptic-visual VE.

The kinematic analysis of a novel three-degree-of-freedom mechanical linkage for the force-

reflecting interface was completed in FY95. The linkage components are sized to provide at least 5-pound interaction forces in any direction to the human hand within, at minimum, a 6-inch spherical workspace. (A family of haptic interfaces of different sizes ranging from an individual finger up to whole arm devices can be designed and built based on these linkage kinematics.)

Point of Contact: S. Ellis
(415) 604-6147

Skin-Friction Measurements on a Commercial Transport Configuration

David M. Driver, George Mateer

Improved diagnostic techniques are needed to diagnose aerodynamic flows on production wind tunnel models for the purpose of assessing such phenomena as transition and flow separation. A newly developed skin-friction measurement technique, called oil-flow interferometer, was successfully demonstrated in the Ames 12-Foot Pressure Wind Tunnel on a commercial transport model.

The wing, flaps, and winglet were selected as the locations to demonstrate the technique. A chordwise strip of glossy black mylar was attached to each of the test surfaces using the mylar's adhesive backing, as shown in the first figure. Prior to the run, oil with a nominal viscosity of 2000 centistokes was applied in discrete locations on the mylar surface. Testing was performed at an intermediate Reynolds number of 4,500,000 per foot in the Ames 12-Foot Pressure Wind Tunnel.

After the tunnel was shut down, the oil-flow patches (seen in the first figure) displayed streaks of light and dark interference patterns that are aligned with the leading edge of the oil. These interference



Fig. 1. Oil-flow patterns on MD-11 winglet.

lines (referred to as fringes) are contours of constant oil depth. The spacing between "fringes" is proportional to the skin friction and can be determined from simple lubrication theory. Skin friction was

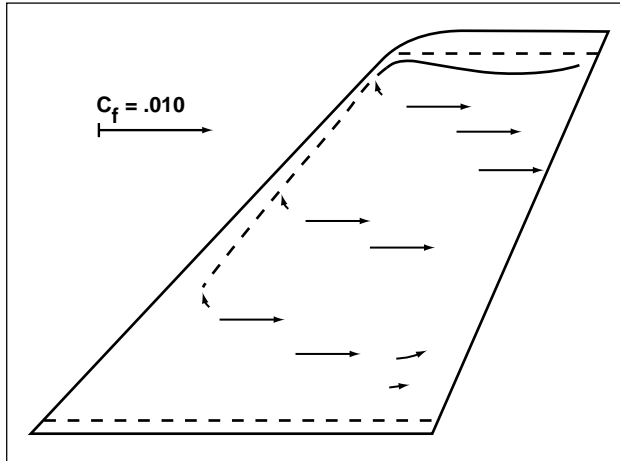


Fig. 2(a). Skin-friction vector direction.

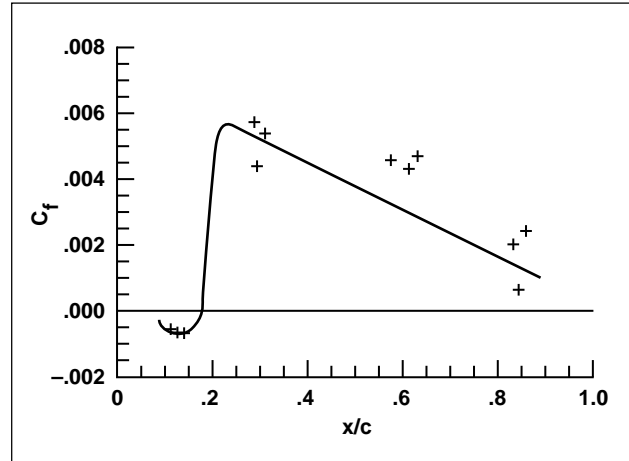


Fig. 2(b). Measured skin friction.

accurately ($\pm 10\%$) deduced from the oil-flow interferometric pattern, and those results are shown in the second figure.

There were no surprises on the flaps and wing, with the oil flow showing well-behaved attached flow with fairly healthy skin-friction (C_f) levels at the trailing edge (that is, $C_f > 0.001$ everywhere). The interesting region of the flow was the winglet, which showed a laminar leading-edge separation bubble (5% chord) that rolls up into a vortex and travels along the leading edge of the winglet where it merges with the winglet tip vortex.

These measurements demonstrate an ability to obtain high-quality, skin-friction data in the Ames 12-Foot Pressure Wind Tunnel. The measurements

are the first measurements of skin friction using the oil-flow interferometry technique in this tunnel. This technique has also been successfully demonstrated in the Ames 11- by 11-Foot Transonic Wind Tunnel, the Ames 40- by 80-Foot Wind Tunnel, and the Ames 9- by 7-Foot Supersonic Wind Tunnel.

These and similar measurements are useful to the Advanced Subsonic Transport program by providing a method of validating current computational fluid dynamics codes and assessing the aerodynamic performance of various wind tunnel models.

Point of Contact: D. Driver
(415) 604-5396

Surface Imaging Skin Friction Instrument Package

James L. Brown, Jon Naughton

The objective of this project is to develop a simple, easy-to-use instrument package to measure the variation of skin friction, C_{fx} and C_{fz} , over extensive regions of three-dimensional (3-D) flow surfaces such as aircraft wing models located in wind tunnels. Skin-friction “drag” accounts for approximately one-half of the drag for transonic commercial aircraft at cruise conditions, while the other half results from pressure “drag.” Yet, in a typical wind-tunnel experiment, the skin friction is rarely measured because of the difficulty in applying older skin-friction instrumentation. The new instrument directly addresses this lack of skin-friction data by dramatically improving the accuracy and ease with which extensive regions of skin-friction measurements can be accomplished on 3-D wind-tunnel models. A significant enhancement in wind-tunnel productivity and information yield is expected to result from the new instrument.

Essentially, the new instrument is a “Quantitative Oil-Flow” method, made possible by combining recent mathematical advances with modern computer data acquisition and charged-coupled device (CCD) imaging technologies. A thin film of oil is placed on the 3-D aerodynamic test surface. This oil film will thin as a result of the flow over the test surface. The optical arrangement of the figure is used to measure the oil film thickness that varies with surface location (x,z) and with time, t . The light source is an inexpensive monochromatic fluorescent tube array. A selected Hg-line optical filter at the camera renders the instrument monochromatic. Light from this source is directed toward the test surface, where a portion of the light is reflected from the oil-air surface, while a portion of the remaining light is reflected from the oil-solid test surface. The path

length difference between these two light reflections is related to the oil-film thickness at that surface position, and as a result, optical fringes form which may be captured by the CCD array. Analysis of these fringes over the test surface is accomplished by a newly innovated, automated, Hilbert transform image processing method which results in the measured oil thickness variation, $h(x,z,t)$, at the particular test time that the image was acquired. Several images are obtained during the wind tunnel run, avoiding wind tunnel startup and shutdown transients. The surface flow direction is also determined for the same tunnel run by means of fluorescent tracers placed in the oil, using the same camera but a different filter rotated into place. Using the information from these several images taken at different times, a newly innovated inverse solver for the 3-D thin oil-film equations can then be solved for the wall shear stress variation with position.

An important point is that skin friction can be measured in one run for relatively large regions of 3-D wind-tunnel models. The project has been accomplished with a high level of technology innovation that has been absorbed into the software and instrument package development so as to lead to an easier to use and inexpensive instrument package that enhances wind-tunnel productivity. The new information gained from use of the new instrument should prove of value not only to basic research but also in the design and production testing of the next generation of commercial aircraft.

Point of Contact: J. Brown
(415) 604-6229

Interferometric Fringe Analysis Software Development

Gregory G. Zilliac

Currently, interferometry is being used by experimentalists in many fields to measure a myriad of different phenomena. Common to many interferometric systems is the necessity to accurately determine the spacing between interference lines. In the past, techniques ranging from fast Fourier transforms to neural networks have been used for this purpose. Most of these approaches to fringe measurement have little or no physical basis and are inaccurate.

Recently, a new fringe model, based on the theoretical behavior of light interference, has been developed. At the heart of this model is a nonlinear

expression with nine independent parameters.

Nonlinear regression analysis is used to determine the parameters. The model is very general and can be used to describe an interference pattern arising from nonuniform lighting on curved surfaces, noisy fringes, or a combination of these factors.

A PC-based application has been written that incorporates the nonlinear fringe model along with frame grabbing and limited surface registration capability. This application is currently being used to measure the skin friction on the surface of a wing as part of a fringe-imaging skin-friction interferometry

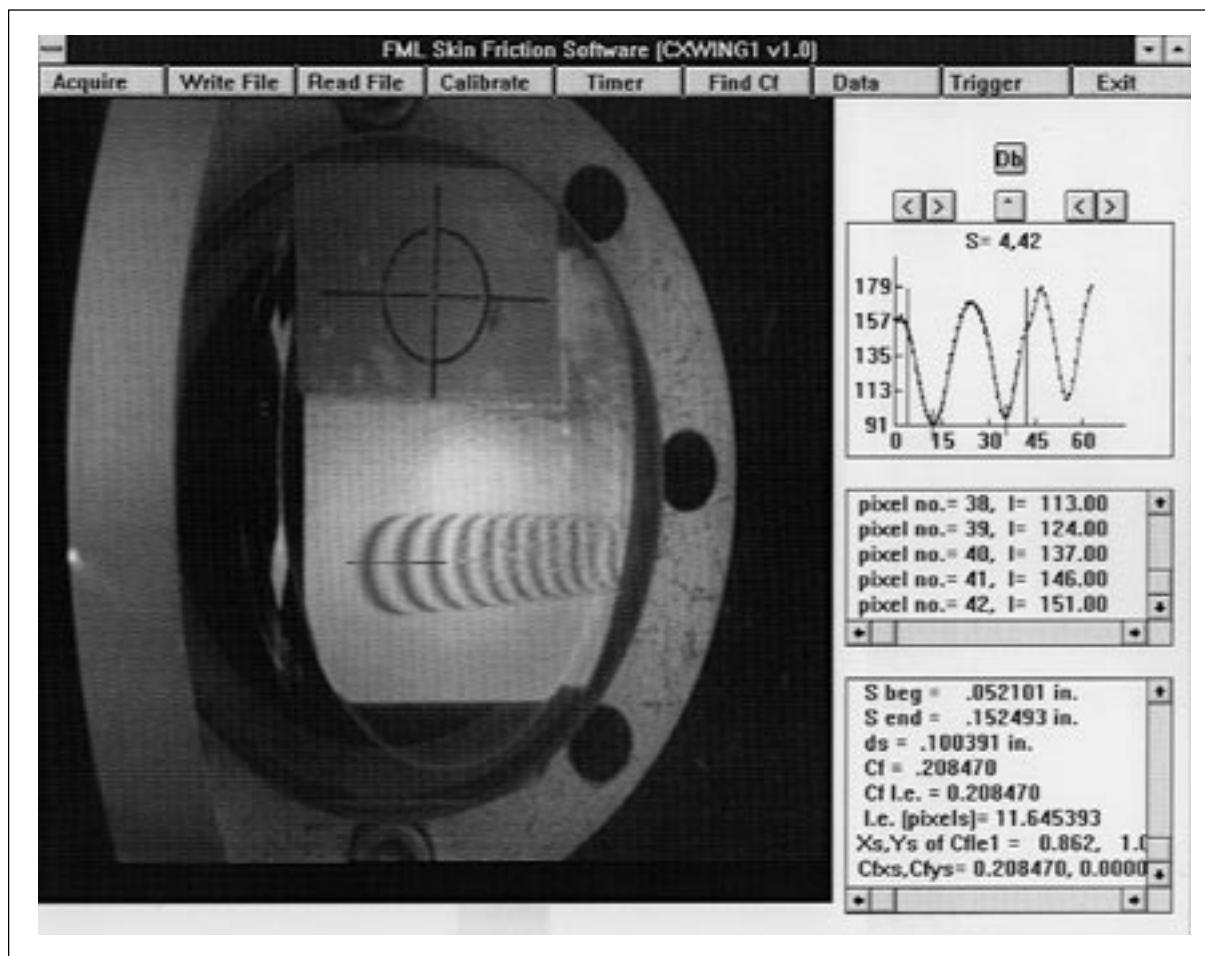


Fig. 1. Screen shot of FISH PC-based software.

(FISH) measurement system. Presented in the figure is a screen shot that shows the PC application in operation. The window in the upper right-hand corner shows the intensity distribution along a line perpendicular to the fringe pattern and the regression

result. The corresponding skin-friction measurement results are in the lower right-hand window.

Point of Contact: G. Zilliac
(415) 604-3904

A New Method for Obtaining Full-Surface Measurements of Shear-Stress Vector Distributions Using Liquid Crystal Coatings

Daniel C. Reda, Michael C. Wilder, John R. Lehman

The objective of the present research is to develop an image-based instrumentation system for the areal visualization and measurement of the instantaneous shear-stress vector distribution acting on any aerodynamic configuration.

The approach has been to systematically explore the color-change responses of shear-stress-sensitive liquid crystal coatings (LCC) to applied shear stresses of known magnitudes and known directions relative to the observer.

The liquid crystal phase of matter is a weakly ordered/fluid-like state that exists between the nonuniform/liquid phase and the ordered/solid phase of certain organic compounds. Liquid crystals can exhibit optical properties that are characteristic of solid, crystalline materials. If a thin film of liquid crystals is applied to a solid surface and the molecules within the coating are aligned by frictional forces into the required planar state, then this molecular structure selectively scatters incident white light as a three-dimensional spectrum or "color space."

For normal white-light illumination and oblique above-plane observation, LCC color-change response to shear depends on both the shear-stress vector magnitude and the direction of the applied shear vector relative to the observer's inplane line of sight. At any point, the maximum color change is always measured when the shear vector is aligned with, and directed away from, the observer; the magnitude of the color change at this vector/observer aligned orientation scales directly with shear-stress magnitude. Such color changes are rapid (as little as 1 millisecond), continuous (over entire surfaces), and reversible (results are valid for dynamically changing flow conditions).

Based on this knowledge, a full-surface shear-stress vector measurement methodology was formulated in FY94. An image-based system, incorporating a rotatable, three-chip, color video camera linked to a frame grabber and computer was devised to test the method. Full-surface color images of LCC response to a three-dimensional turbulent wall jet flowing over a planar surface were acquired in FY95 over a range of inplane view angles that encompassed the vector directions to be measured. These hue images were then converted to surface shear-stress vector fields. One such data set is shown in the figure (see Color Plate 19 in the Appendix), where vector magnitudes are given by the color contours and vector directions are given by the white streaklines. Flow is left to right.

In this data set, the highest shear magnitudes are seen to occur along the central core of the wall-jet flow, with decreasing shear magnitudes occurring symmetrically to either side. A slight, symmetric confluence of streaklines is seen to occur along the jet centerline, while outflow occurs on the jet periphery. Comparisons of these first-ever such results to conventional point measurements, obtained via the oil-drop interferometry technique, yielded very good agreement, corroborating the liquid crystal method. It has been shown that the liquid crystal coating technique can be utilized to obtain areal measurements of surface shear-stress vector distributions on planar surfaces, with accuracies equivalent to conventional point-measurement techniques.

Point of Contact: D. Reda
(415) 604-6034

Atmospheric Gas-Sampling Probe

Kevin D. James, James C. Ross, Gerald M. Vogel

As part of the National Aeronautics and Space Administration (NASA) Tropospheric Chemistry Program and the NASA Atmospheric Effects of Aircraft/Subsonic Assessment Program, extensive research has and will be conducted on the Earth's atmosphere. NASA's DC-8 has proven to be an important platform for measurements of trace species in the upper troposphere and lower stratosphere, and it will continue to serve in this role in the foreseeable future.

The use of exterior sampling devices on the DC-8 that collect samples of trace gases and aerosols has been a cause of concern for atmospheric scientists. The samplers (probes) have been empirically designed and, in most cases, have not been subjected to rigorous aerodynamic design studies. Inconsistencies in recent measurements of reactive nitrogen gases and in amounts of other trace gases and aerosols have raised the possibility that sampling processes are flawed, or at the very least, could be improved. The conditions imposed by these samplers (shapes, pressures, and pressure differences) have not traditionally been the subject of published aerodynamic studies. Thus, little literature exists for guidance to the atmospheric scientist.

This new instrument, an atmospheric gas-sampling probe, is one of several that have been proposed and funded to measure the hydroxyl (OH) and hydrogen peroxy (HO₂) radicals from the DC-8. Since OH and HO₂ are reactive gases that are easily lost on instrument surfaces, this probe was designed

to be effectively "wall-less," with no air contacting an instrument surface before entering the optical detection chamber. This probe was a combination of aerodynamic and chemical studies.

The following are some of the accomplishments of this particular project.

(1) Sampled flow is not mixed or contaminated. The mixing of sampled air with that from around the inlet would potentially ruin the OH measurements.

(2) Velocity of sampled air is slowed from aircraft velocities (400 meters per second), without turbulence, to a user controlled range of 5–40 meters per second.

(3) The sampler works for a majority of the speed ranges, attitudes, and altitudes flown by the DC-8.

The process of determining the proper aerodynamic shape for the sampling probe involved a constrained-optimization approach using PMARC (Panel Method Ames Research Center), TranAir (full potential code) (results are shown in the first figure (see Color Plate 20 in the Appendix)), and CONMIN (constrained optimization code). The computational results were verified through a low-speed wind tunnel test, flight testing, and the successful deployment of the sampling probe on the NASA Ames DC-8 SUCCESS Mission (flight model shown in the second figure (see Color Plate 21 in the Appendix)).

Point of Contact: K. James
(415) 604-0178

Wind Tunnel Flow Quality and Boundary Layer Transition

Jonathan H. Watmuff

Experimental investigations of boundary layer transition require an extremely low background unsteadiness level. Controlled disturbances can then be introduced and their characteristics measured to validate numerical studies or to justify the use of simplifying analytical assumptions, for example, linear stability theory. One especially troublesome source of background unsteadiness is associated with weak streamwise vortices (Klebanoff modes). The vortices originate at the leading edge and appear to be caused by amplification of almost immeasurably small nonuniformities in the free stream. The vortices alter the mean flow, and are therefore (by definition) detrimental, nonlinear phenomena.

Immense care and effort has been necessary to improve the flow quality of a small standalone wind tunnel to the point where nonlinear interactions between remaining vortices and the controlled disturbances of interest are insignificant. Major (but insufficient) improvements were observed after installation of (1) a variable-speed axial fan with

adjustable blade angles; (2) three turbulence grids in the diffuser to improve the flow uniformity at the exit; (3) two honeycombs; and (4) six high-quality screens with open areas greater than 60%. The screen cloth was selected after inspection of several batches. Each screen is attached to a solid aluminum frame under a high, uniform tension.

Despite a reduction in free-stream unsteadiness (root mean square (rms) velocity (u)/free-stream velocity (U)) from 0.12 to 0.05%, the final acceptable flow quality was achieved only after considerable additional effort. Contours of the background unsteadiness in a spanwise plane through the layer on the test surface are shown in the first figure. The uniformity of the free stream in the vicinity of the leading edge was within $\pm 0.1\%$ for this intermediate configuration. After these measurements were made, the variation in screen porosity was explored by traversing each screen between a laser and photodetector, as shown schematically in the first figure.

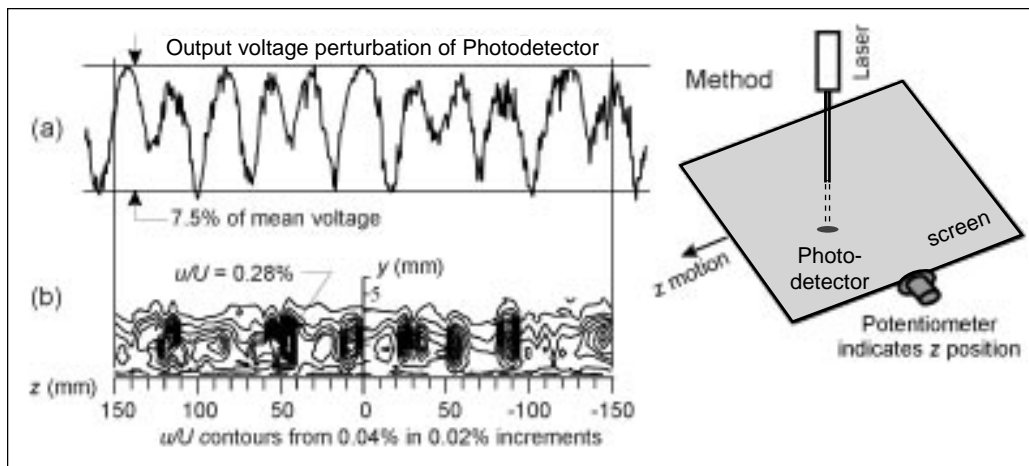


Fig. 1. Intermediate configuration (after major modifications). (a) Laser scan to determine spanwise variations in porosity of last 46-mesh wind tunnel screen with a 61% nominal open area. (b) Contours of rms unsteadiness u/U in spanwise plane within layer. The variation of U in spanwise plane upstream of leading edge was within $\pm 0.1\%$ over this span.

The results for the downstream screen are also shown and the spanwise variations can be attributed to small nonuniformities in the weave of the screen cloth. The screen order was changed on the basis of the porosity measurements, that is, from least to most uniform porosity. However, even more refinements were required to achieve the final acceptable base flow, including (1) installation of 6 additional screens; (2) increasing the screen spacing to over 200 mesh widths; (3) doubling the length of the settling region; (4) sharpening the leading edge; and (5) reducing the unit Reynolds number such that all screens are subcritical ($Re_{wire} < 40$).

A comparison between the initial and final configurations for $Re_x = 1.0 \times 10^6$ is shown in the second figure. The maximum unsteadiness within the layer (measured over 50 layer thicknesses in the spanwise direction) has been reduced by a factor of 50. Present results suggest that the quantities

generally used to define acceptable flow quality are inadequate for laminar flows. For example, the free-stream unsteadiness remained essentially unchanged since the first set of major modifications, yet the unsteadiness within the boundary layer was halved and it was less concentrated, as shown in the figures. Fundamental studies are needed to account for these and other unresolved issues concerning wind tunnel screens and to establish more stringent specifications for acceptable flow quality. These specifications are of particular relevance for model tests of aircraft, where laminar flow control techniques are used. Such studies could help explain why tests performed with the same model in different wind tunnels often produce such widely differing results.

Point of Contact: J. Watmuff
(415) 604-4150

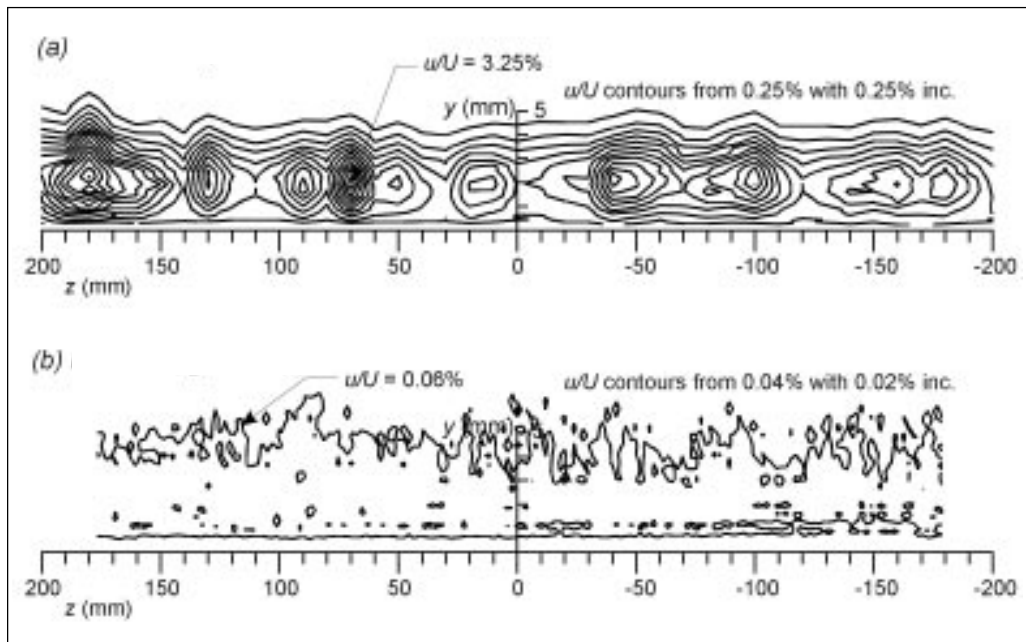


Fig. 2. Contours of rms unsteadiness u/U in spanwise plane within layer (a) initial and (b) final configuration. The background unsteadiness within the boundary layer has been reduced by a factor of 50.

Multielement Acoustic Array Calibration

Stephen Jaeger, Srba Jovic, Marianne Mosher

An ongoing Ames Research Center program has been the development of phased microphone arrays to locate and measure acoustic sources on wind tunnel models. One goal of this program is to obtain absolute measurements of propulsion and airframe noise for comparison with flight measurements.

The phased microphone array assembly, shown in the figure, contains a pattern of microphones mounted in a flat, rectangular metal plate installed in an aerodynamic fairing. The microphones are covered by an acoustically transparent screen that protects them from the flow. The installation of the microphones, the mounting of the array, the fairing edge diffraction, and the complexity of the array pattern influence the response of the individual microphones and the total response of the array. To account for these phenomena, an intensive calibration procedure was developed to ensure that correct noise levels are measured when the array is installed in the wind tunnel.

The first step of the calibration was to evaluate the acoustic response of the array to a controlled noise source within an anechoic chamber. A single directivity- and magnitude-calibrated horn driver was used to characterize the response of all the elements of the array over a range of horizontal and vertical source/receiver angles.

Also, the array acoustic response was measured with the source at one specific distance and direction in the anechoic chamber. This correspondence was used with the same calibration source and array installed in the Ames 40- by 80-Foot Wind Tunnel as part of a test to measure the airframe noise of a 5%-scale DC-10 model. In this manner, the free-field response of the array obtained in the anechoic chamber was compared to the response of the array as mounted in the wind tunnel test section.



Fig. 1. A motorized mount rotated the multielement array and fairing to various orientations within an anechoic chamber. An acoustically transparent screen covers the microphone pattern in this photo.

The use of a single source calibration scheme eliminated the requirement for time-consuming amplitude calibrations of the individual microphones during the course of specific tests.

**Point of Contact: S. Jaeger/P. Soderman
(415) 604-1472/6675**

Software Acoustics Project

Kevin McCabe

The Visualization Laboratory (Vis Lab) in the Ames Numerical Aerodynamic Simulation (NAS) Facility produced an acoustic analysis library (AAL) and a prototype application in support of research being done in computational acoustics. The research helps to identify noise sources in aircraft, and will ultimately lead to the design of quieter vehicles, reduction of noise pollution in urban areas, and increased pilot safety in military applications.

This work represents the first time researchers in computational rotorcraft acoustics were able to hear data they had calculated. The prototype application, built using AAL, xyplot, and NAS Viewer, enables researchers to interactively view a model of an AH-1 Cobra helicopter while at the same time listen to the sound that the helicopter makes.

Traditionally, these data have been analyzed using two-dimensional plotting techniques. A series of such plots is necessary to gain a comprehensive volumetric understanding of the data. AAL employs a binaural sampling technique that enables the user to gain this volumetric understanding by listening directly to the acoustic signal. The advantages are that large amounts of data can be analyzed quickly, and the researcher can actually hear what the vehicle sounds like.

Point of Contact: K. McCabe
(415) 604-4460

Adaptive-Grid Wake Survey System

Timothy T. Takahashi

In a wind tunnel test, it is often desirable to measure the flow of air both around and behind the test body. The flow properties of interest are the local static pressure, the local total pressure, and the angularity of flow. Although the actual flow may be turbulent, and hence unsteady with respect to time, the probes measure the mean, or quasisteady, properties. An automated system using seven-hole cone probes was developed to make detailed measurements in wakes with complex flow topology.

To improve the efficiency of the wake survey procedure, an array of three seven-hole cone probes mounted on a single sting were traversed through the wake. A recursive algorithm was developed to automatically generate orthogonal "multigrid" survey domains keyed to the local vorticity of the flow. In regions where the flow was relatively uniform, it was sampled at a coarse spatial resolution. In regions

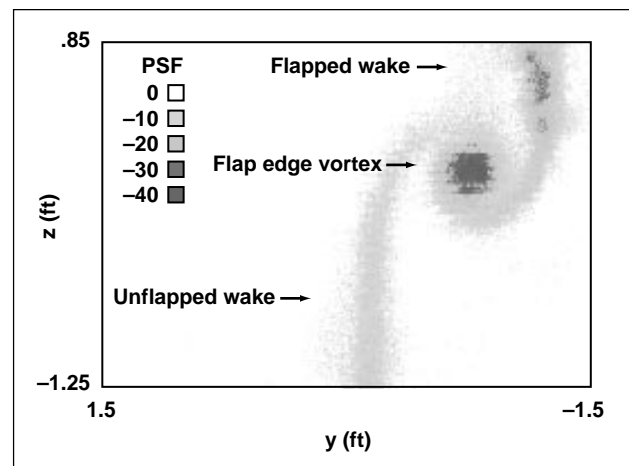


Fig. 1. Example wake survey: total pressure defect behind a wing with a half-span single-slotted flap.

where the flow was unsteady, vortical, or otherwise interesting, the computer adjusted the size of measurement grid to give a fine spatial resolution.

The system was used to acquire wake data on a recent multielement wing high-lift test at the Ames Research Center's 7- by 10-Foot Subsonic Wind Tunnel. The model consists of an NACA 63-0215 section wing fitted with a half-span single-slotted flap. It was tested at Mach 0.22. The figure demonstrates the losses in total pressure in the wake of this wing system.

This system shortens the time needed to survey the wake of a wing by reducing the number of

required survey stations. Most of the flow field contains little vorticity, and as such was sampled on a coarse grid. A much smaller fraction, approximately one-sixth of the survey domain, contained higher vorticity and, hence, was sampled at the fine spatial resolution. Even with such refinements, a complete wake survey required three hours of continuous tunnel operation.

Point of Contact: T. Takahashi
(415) 604-4976

Surface Development and Test Facility

Stanton Harke

The Federal Aviation Administration (FAA) has formed an alliance with Ames Research Center to build a simulation facility that will be used to validate future airport surface and air traffic control tower technologies prior to field deployment.

The operational benefits provided by the Surface Development and Test Facility (SDTF) will include in-depth studies using air traffic controllers, flight data/clearance delivery personnel, traffic management coordinators, tower cab coordinators, supervisors, ramp controllers, pseudopilots, and airport operators in a real-time, interactive, operational airport environment. These validation and predeployment site adaptation studies will result in a reduction of cost and associated risks of new technologies. The SDTF will also be used to evaluate related computer/human interfaces that will be presenting integrated information from existing data sources to multiple users. By giving air traffic controllers and other airport users the opportunity to interact in a simulated air traffic control tower environment, researchers and developers will be able to determine the proper mix of software advisory capabilities and human interaction.

The SDTF is designed to take advantage of commercial off the shelf components that will be integrated into a full-scale air traffic control tower. The SDTF will consist of five major components:

(1) a two-story physical structure replicating a full-scale, Level V air traffic control tower, including work areas to support pseudopilots, ramp controllers, airport operators, simulation specialists, and software developers; (2) air traffic control simulation software components; (3) computer, network, audio, video, and communications hardware to support the simulator, users, and researchers; (4) reprogrammable user displays; and (5) a computer-generated, seamless, 360-degree, out-the-window field of view.

During the concept, design, and development phase of the SDTF, a Preliminary Design Review and a Critical Design Review took place with future users of the SDTF. The users included representatives from FAA, airlines, National Air Traffic Control Association, and airport management. The users provided their requirements for a fully operational airport simulation environment. This phase also included trade-off studies and market analysis to identify and consider a range of alternatives in the areas of air traffic control simulation software, computer hardware, video projectors, screen materials, and construction options.

**Point of Contact: S. Harke
(415) 604-5012**

Ames Research Center 12-Foot Pressure Wind Tunnel

Thomas N. Aiken

The restored 12-Foot Pressure Wind Tunnel is the only large-scale, variable-density, low-turbulence, subsonic wind tunnel in the United States (see the first figure). It provides unique testing capabilities for the development of high-lift systems on commercial transport and military aircraft and for the testing of maneuvering aircraft at high angles of attack.

The 12-Foot Pressure Wind Tunnel is unique because it incorporates two very desirable characteristics—low turbulence and high Reynolds number. Reynolds number is a measure of how realistic the air flow over a model is relative to a full-size aircraft. By pressurizing the wind tunnel up to 6 atmospheres, a 1/6-scale model can be made to produce accurate full-scale results.

The original 12-Foot Pressure Wind Tunnel was completed in 1946 and, over the next four decades, tested virtually every U.S. commercial and military aircraft. In 1986, the pressure shell was found to have severe cracks, rendering it unusable for pressurization. In 1988, the wind tunnel was demolished down to the foundation, and construction started on a restored facility with significant improvements.

The new facility includes several key features that significantly improve the productivity of test operations. The entire test section can be isolated from the rest of the circuit and rotated laterally 90 degrees, allowing access to the model for small changes without costly and time-consuming depressurization of the entire circuit. This isolation also allows



Fig. 1. Ames 12-Foot Pressure Wind Tunnel.

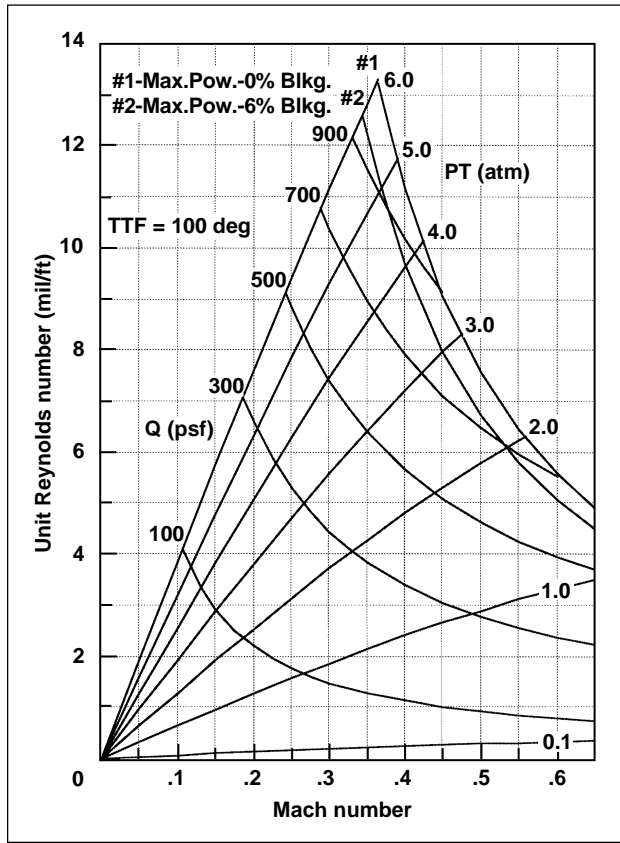


Fig. 2. Ames 12-Foot Pressure Wind Tunnel operating envelope.

installation and removal of fully assembled models through the upstream end of the rotated test section. Models are built up in either of two preparation rooms, where the instrumentation can be completely checked prior to installation in the test section. A modern distributed control system provides automated control of model attitude, test section flow conditions, and data acquisition.

Power for the single-stage fan is provided by a 15,000-horsepower, variable-speed, synchronous electric motor. Pressurization and evacuation of the circuit are accomplished using a 50,000-cubic-foot-per-minute compressor that allows the 12-Foot Pressure Wind Tunnel operating envelope shown in the second figure.

Other features include a modern data system to measure forces, pressures, and temperatures. That system can be accessed through a remote computer by customers at their home offices. Flow visualization techniques such as pressure sensitive paint and global Doppler velocimetry are feasible, and a 3000-pounds-per-square-inch compressed air system is available for propulsion simulation.

**Point of Contact: M. Betzina
(415) 604-5106**

DARWIN Remote Access Systems

David Korsmeyer

Development Aeronautics Revolutionizing Wind Tunnels with Intelligent Systems for NASA (DARWIN), uses information systems technology for development aeronautics to redefine the classic wind-tunnel test.

DARWIN provides remote access to the Ames Research Center wind tunnel facilities through a dedicated site-wide fiber-optic intranet. This internal network is currently supporting the fiber distributed data interface protocol and is configured to allow a bandwidth of 100 megabits per second to all of the

aeronautical test facilities at Ames. A dedicated, remote-access, wind tunnel network, DARWINnet, is developed. From DARWINnet the connection to industry is made by the AEROnet nationwide network provided by the Numerical Aerodynamics Simulator facility. AEROnet is composed of dedicated high-speed connections to the U.S. aeronautics industry. No connections to the open internet are permitted on either DARWINnet or AEROnet.

The DARWIN remote access software is based on a three-tier client/server/server architecture. The main server is a secure web and database server. The third-tier server is a system hosted in an aeronautics test area. The remote client software is composed of a secure web browser, an executive, and a set of additional visualization and collaboration tools.

Many of the small remote applications are written in Java and JavaScript as remote agents that are either executed or started by the browser. The figure illustrates the process model for the interaction between the different software layers.

Point of Contact: D. Korsmeyer
(415) 604-3114

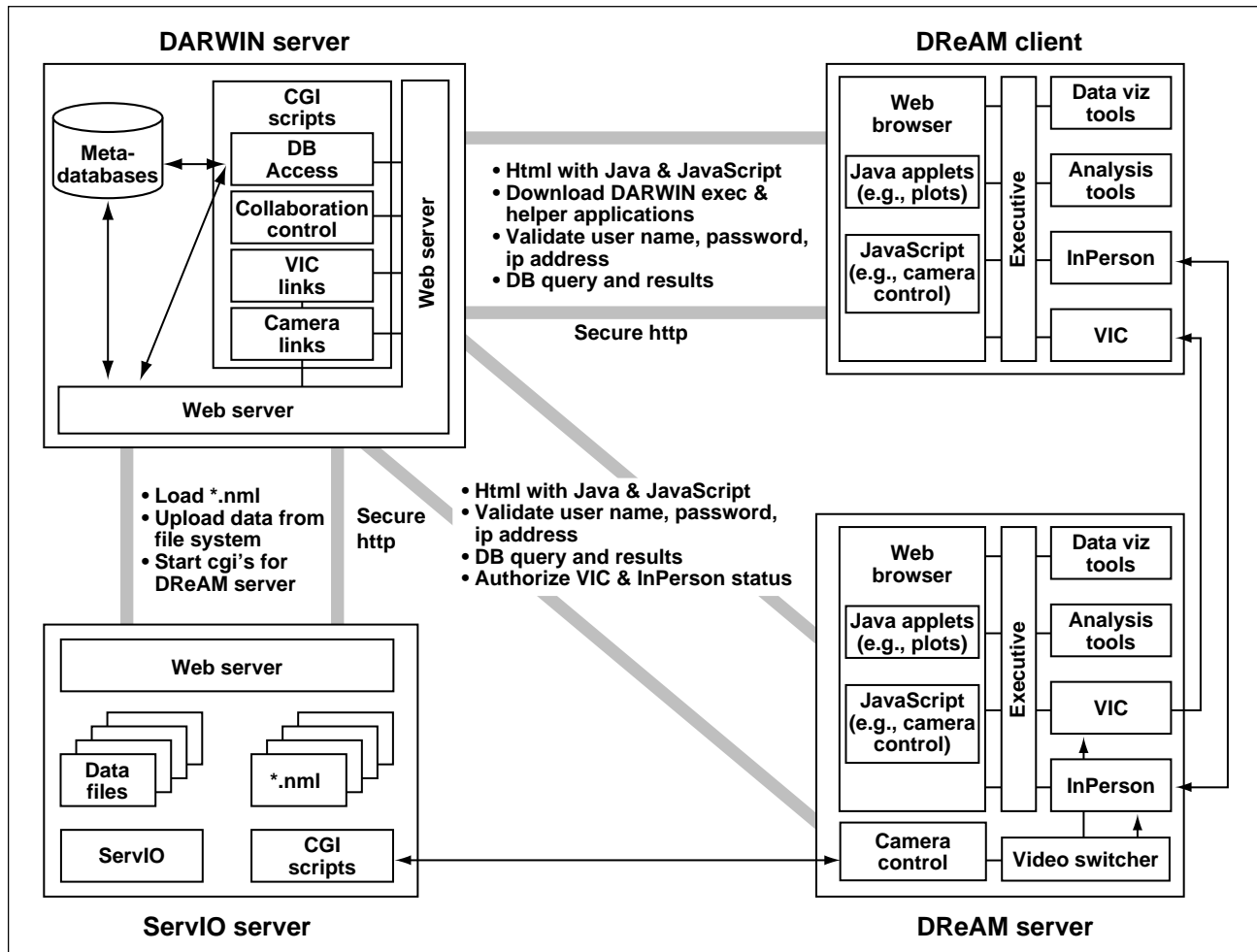


Fig. 1. DARWIN Software process model.

Qualification Testing of the Laminar Flow Supersonic Wind Tunnel

James A. Laub, Stephen W. D. Wolf

Most attachment line, cross-flow instability, and transition receptivity research in the supersonic regime is presently conducted in the high-risk, flight test environment, primarily because the noise and pressure disturbance levels in conventional supersonic wind tunnels are higher than that found in the atmosphere, and are therefore unsuitable for transition research. This situation has provided the impetus to develop a unique Laminar Flow Supersonic Wind Tunnel (LFSWT) that operates continuously at Mach 1.6 to match flight test experiments. The LFSWT is designed specifically for low-disturbance (quiet) operation to match the quiescent atmosphere in which a high-speed civil transport would fly at cruise altitudes. Furthermore, the LFSWT operates at low unit Reynolds numbers ($2.0 \leq Re \leq 4.0$ million per foot) that match flight. The aim of the present effort is to demonstrate quantitatively that the LFSWT is sufficiently "quiet" for meaningful transition research.

Current consensus in the quiet wind tunnel community is that flow is low disturbance if the free stream is spatially and temporally uniform, with pressure disturbances less than 0.1%. Quiet flow is achieved at low supersonic Mach numbers with primarily excellent flow quality upstream of the supersonic nozzle (in the settling chamber) and laminar boundary layers along both walls of the supersonic nozzle and the test section. To better understand the sources and influence of flow disturbances, a series of qualification testing using a combination of test instrumentation has been undertaken. Flow quality measurements have been made in the settling chamber and in the test section using dynamic pitot probes, 5-hole cone probes, and temperature probes. In addition, hot-wire probes were used to gather qualitative data in the wall boundary layers. Flow visualization, using non-intrusive Schlieren/shadowgraph techniques, was used to observe the effects of minute wall disturbances on the test section boundary layers.

The LFSWT settling chamber has many flow conditioning components that were designed to reduce total pressure fluctuations $\leq 0.2\%$. Present test measurements indicate that this loosely defined goal has been achieved. However, during traverses across the settling chamber, random pressure fluctuations and a tendency for one side of the settling chamber to have a higher disturbance level were noticed. These effects were observed in the test section, as discussed later. The observations were traced to the pressure reduction section at the inlet to the settling chamber. Changes to the configuration of the pressure reduction section minimized the pressure fluctuations being fed into the test section, and also controlled flow nonuniformity.

Flow quality measurements in the 8- by 16-inch test section have included dynamic pitot pressures, local Mach numbers, and flow angularities. In addition, the state of the wall boundary layers has been examined to confirm the flow quality in the test section. These measurements show that the total pressure fluctuations (during normal tunnel operation) are below the low-disturbance criteria (previously described) for most of the LFSWT Reynolds number envelope up to 3.5 million per foot. The fluctuations grow with Reynolds number as disturbances increase from the pressure reduction section of the settling chamber because of the higher mass flow (as shown in the first figure). Total pressure fluctuations are presented here as the ratio of root mean square (rms) total pressure fluctuations to mean total pressure (P_{rms}/P_t). The present Mach number uniformity (≤ 0.01) and the flow angularity (≤ 0.1 degree) match current standards of flow uniformity in wind tunnels. The floor boundary layer exhibits laminar properties back to the exit of the empty test section, with run lengths up to 108 inches. Additional profiles are required to confirm this observation on all walls.

Further qualification testing was performed using a well-documented NASA Langley Research Center 10-degree cone. Transition on this cone represents an international pseudostandard for flow quality in wind tunnels. Heat-transfer properties of laminar and turbulent flow are such that skin temperatures of the cone vary, depending on the state of the boundary layer (turbulent flow induces higher skin temperatures). The thin-skinned cone is 15 inches long (but only 8 inches are available for studies of transition due to shock reflections), highly polished, and

represents 4.2% blockage in the LFSWT. The cone was tested at Mach 1.6 over a Reynolds number range from 2.8 to 3.8 million per foot. Transition could not be detected on the cone at 0-degree angle of attack, but was detected on the leeward side at angles of attack ≥ 5 degrees. Transition was also detected when turbulent boundary layers were induced along the test section walls, resulting in noisy flow where the free-stream pressure fluctuations had grown by 500% (see the first figure). The cone mounted in the LFSWT test section is shown in the second figure, together with skin temperature distributions for both high and low free-stream disturbance levels. The data clearly indicate the onset of transition in a simulated noisy environment of a conventional wind tunnel, and no transition onset in the normally quiet LFSWT environment. The results of this 10-degree cone test prove that the flow field in the LFSWT is indeed low disturbance at these test conditions.

Qualification testing to date indicates that at Mach 1.6 the LFSWT provides a unique low-disturbance test core that is strongly influenced by upstream disturbances. During this effort, sources of disturbances were found, documented, and minimized for future wind tunnel operation and design. Further mapping of the test core is now required to determine the extent of quiet flow, and to examine the profiles of the wall boundary layers. This mapping will provide a firm foundation for future transition research in the LFSWT.

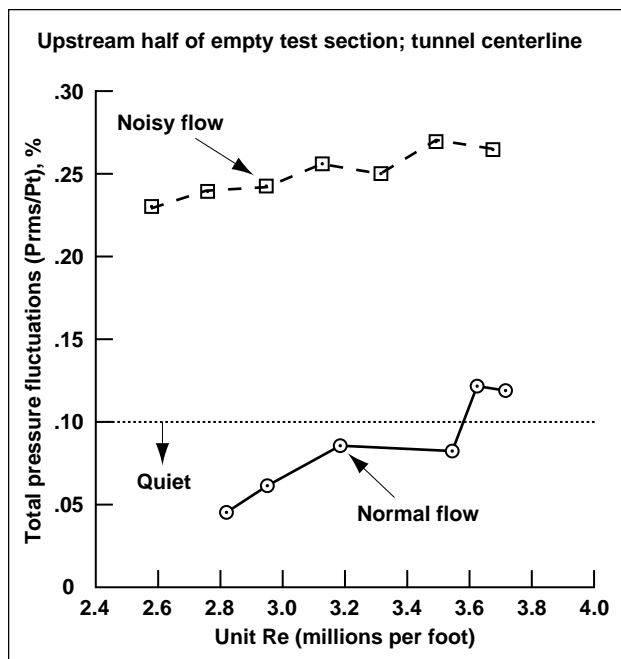


Fig. 1. Variation of test section total pressure fluctuations with Reynolds numbers for two different flow conditions (normal and noisy).

Point of Contact: J. Laub
(415)604-4136

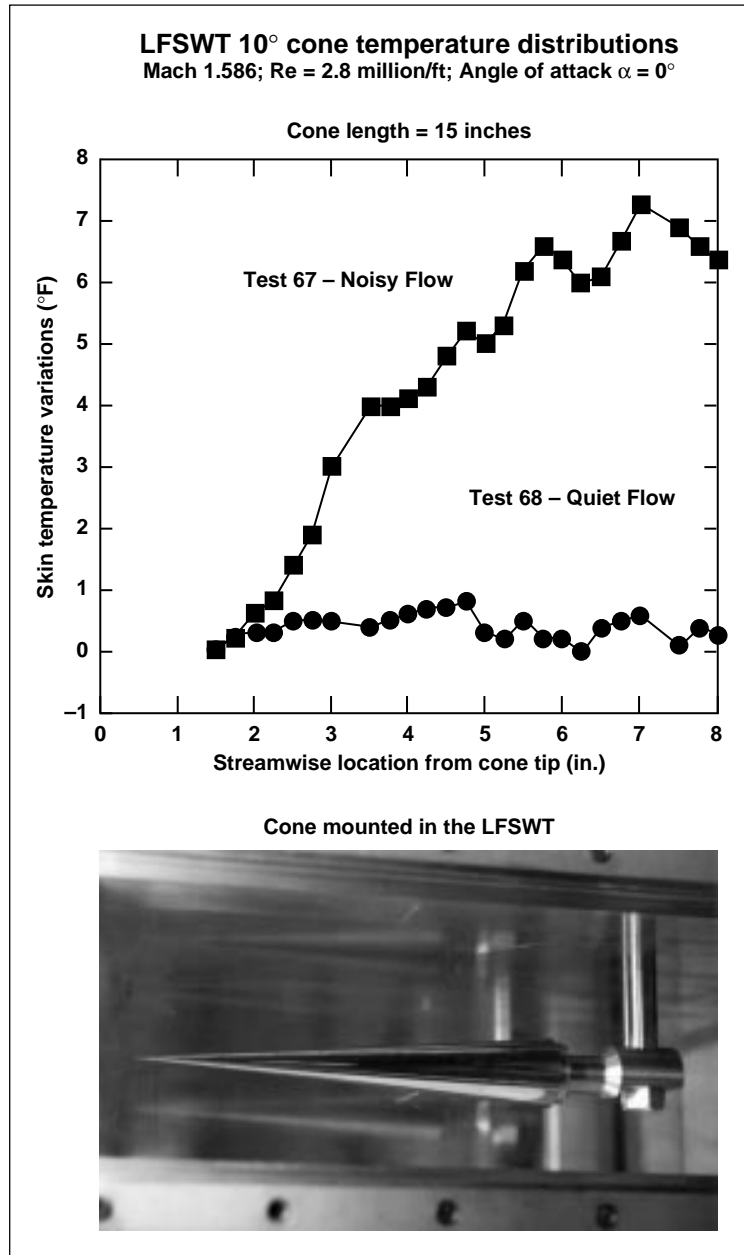


Fig. 2. Comparison of cone temperature distributions with quiet and noisy free streams.

Separation Control in a Wind Tunnel Diffuser System

David Yaste, Rabindra Mehta, Jonathan Watmuff

Mean flow unsteadiness in a wind tunnel can adversely affect the flow characteristics over a model under investigation. In addition, flow unsteadiness may also impact the overall accuracy of the obtained data. A primary cause of mean flow unsteadiness in wind tunnels is flow separation in the diffuser sections. The most critical diffuser section is the "wide-angle diffuser," which is generally installed between the compressor section and the heat exchanger or settling chamber. The purpose of a wide-angle diffuser is to expand the flow in a relatively short streamwise distance, thus reducing the overall wind tunnel length, and hence capital costs. However, the relatively rapid expansion also makes the boundary layers prone to separation, and some form of boundary layer control is normally required in a wide-angle diffuser.

A wind tunnel leg has been built at the Ames Fluid Mechanics Laboratory to simulate flow through the compressor and heat exchanger of a typical closed-circuit wind tunnel. The main objective of this work was to evaluate, in a controlled environment, the characteristics of the flow through these critical components and to investigate ways of improving the overall flow quality. Another objective was to obtain detailed measurements for comparison with computations being run simultaneously by a team at Northrop Grumman. A successful computational tool would be invaluable in testing and developing new diffuser configurations and also in assessing Reynolds number effects so that the model test results may be applied to the full-scale design.

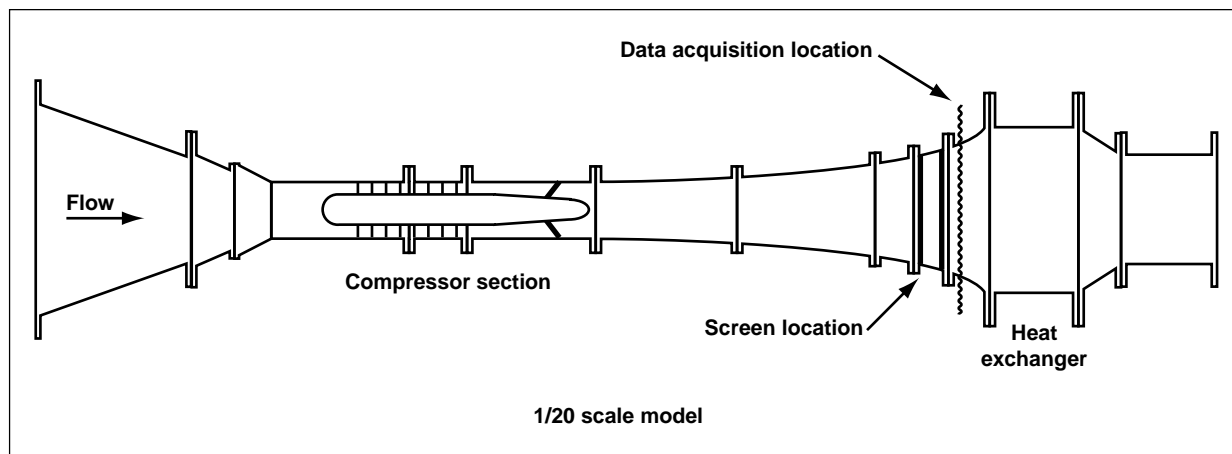


Fig. 1. The 1/20 scale model.

The design of this portion of a common wind tunnel was scaled from some preliminary designs of a proposed large-scale wind tunnel (see the first figure). A 1/20-scale model was built with several separable flange locations to allow the insertion of flow manipulation devices, such as fine-mesh screens (to reduce turbulence) and coarse-mesh grids (to enhance mixing). Three small windows were installed in the wide-angle diffuser so that a qualitative assessment of the flow may be made by observing wool-tuft behavior on the diffuser walls.

Most of the testing has been performed at a Mach number of 0.17 at the entry to the compressor section, which corresponds to a test section Mach number of 0.7. With no screens/grids installed in the wide-angle diffuser, the wool tufts indicated a very unsteady boundary layer behavior with intermittent flow reversal. The mean velocity profile measured near the exit of the wide-angle diffuser supported the qualitative wool-tuft observations since extremely low (near-zero) velocities were measured close to the diffuser walls (see the second figure). Installing a 76% open area ratio resulted in a marginal improvement—the flow velocities near the diffuser walls increased slightly. This result is not too surprising since this particular screen produces only a relatively small pressure drop coefficient of about 0.3 at the operating Reynolds number. However, installing a screen with 51% open-area ratio (pressure drop coefficient of about 1.3) resulted in a significant increase in the velocities in the near-wall region and an improvement in the overall flow uniformity (see the second figure). The higher velocities close to the wall translate into a higher mean velocity gradient, and hence a higher skin-friction coefficient.

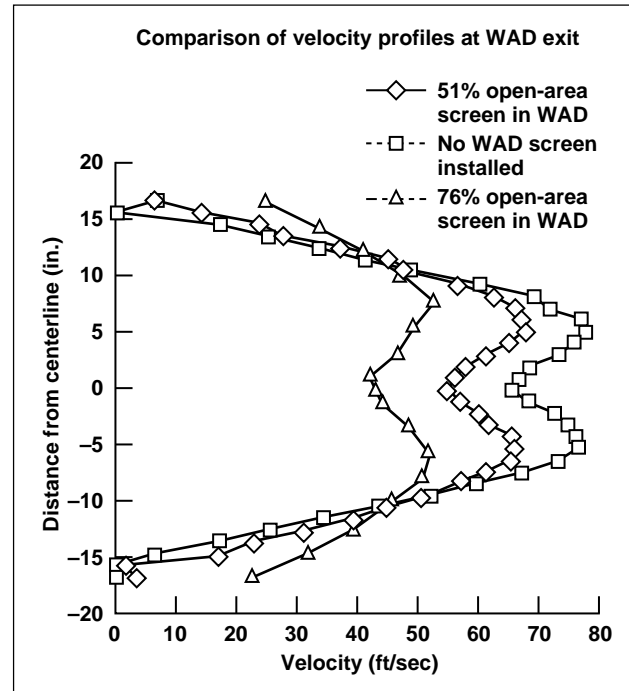


Fig. 2. Comparison of velocity profiles at exit of the wide-angle diffuser.

In simple terms, these results indicate that the boundary layer is “healthier” and is less likely to separate in the wide-angle diffuser. The uniformity of the flow entering the heat exchanger is also improved, and thus the spatial variation in flow temperature obtained in the test section is reduced.

Point of Contact: D. Yaste
(415) 604-4148

Arc Jet Characterization

D. G. Fletcher, T. Gökçen, M. E. Newfield, C.-S. Park

The primary role of arc-jet facilities in aerospace research and development has been to serve as a source of long-duration, high-enthalpy flow for testing and development of thermal protection materials for aerospace applications. Despite their extensive use for this purpose, arc-jet flows are not well understood. This is partly due to a lack of detailed flow measurements over the full range of facility operation. The hot, supersonic, low-density flow environment also places severe limits on the type of instrumentation that can be used to remedy this situation. Nonintrusive optical methods, including emission- and laser-spectroscopy, are well-suited to this type of flow environment, and can provide

useful information about the thermochemical state of the flow. With these considerations in mind, a combined experimental and computational investigation of the flow character of Ames Research Center's Aerodynamic Heating Facility (AHF) arc jet has been undertaken.

The experimental approach involves the use of emission measurements from the shock layer formed over the surface of a flat-faced, 15-centimeter diameter cylinder located 35 centimeters downstream of the nozzle exit plane, in conjunction with simultaneous two-photon, Laser-Induced Fluorescence (LIF) measurements of atomic species in the free stream ahead of the shock layer.

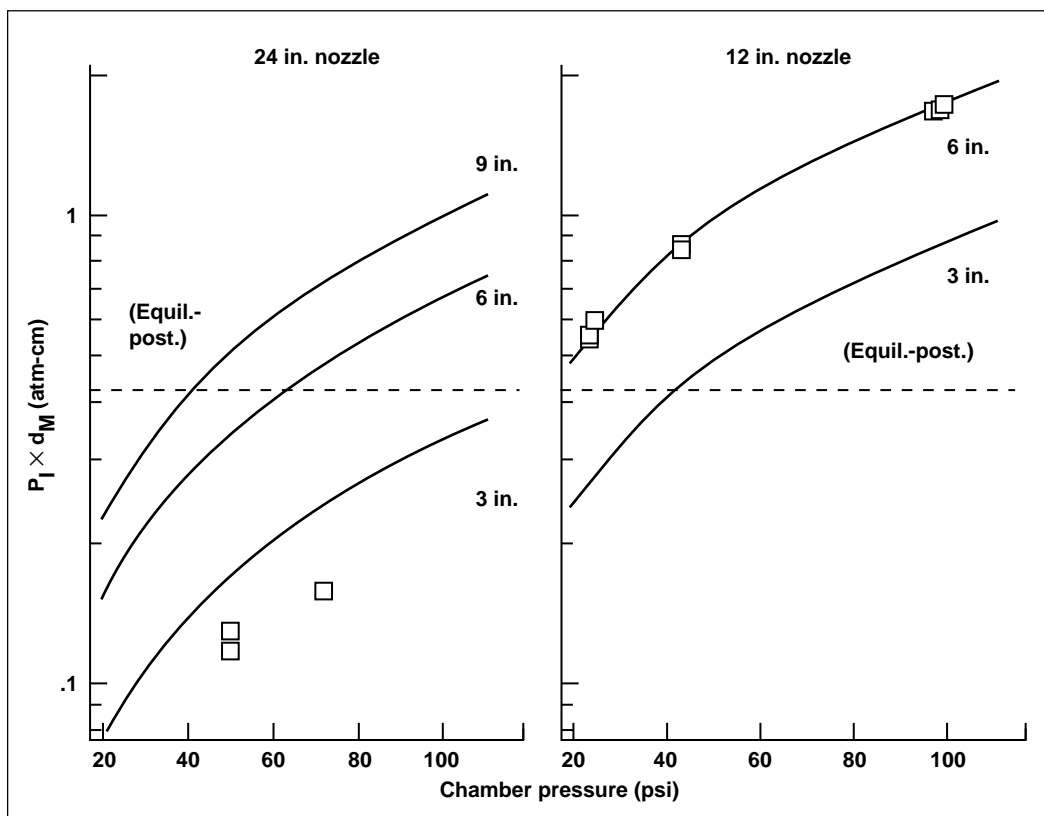


Fig. 1. Impact pressure-model diameter product range as a function of chamber pressure in two nozzles of the AHF arc jet. Equilibrium flow conditions in the shock layer are expected for product values greater than 0.42 atmosphere-centimeter.

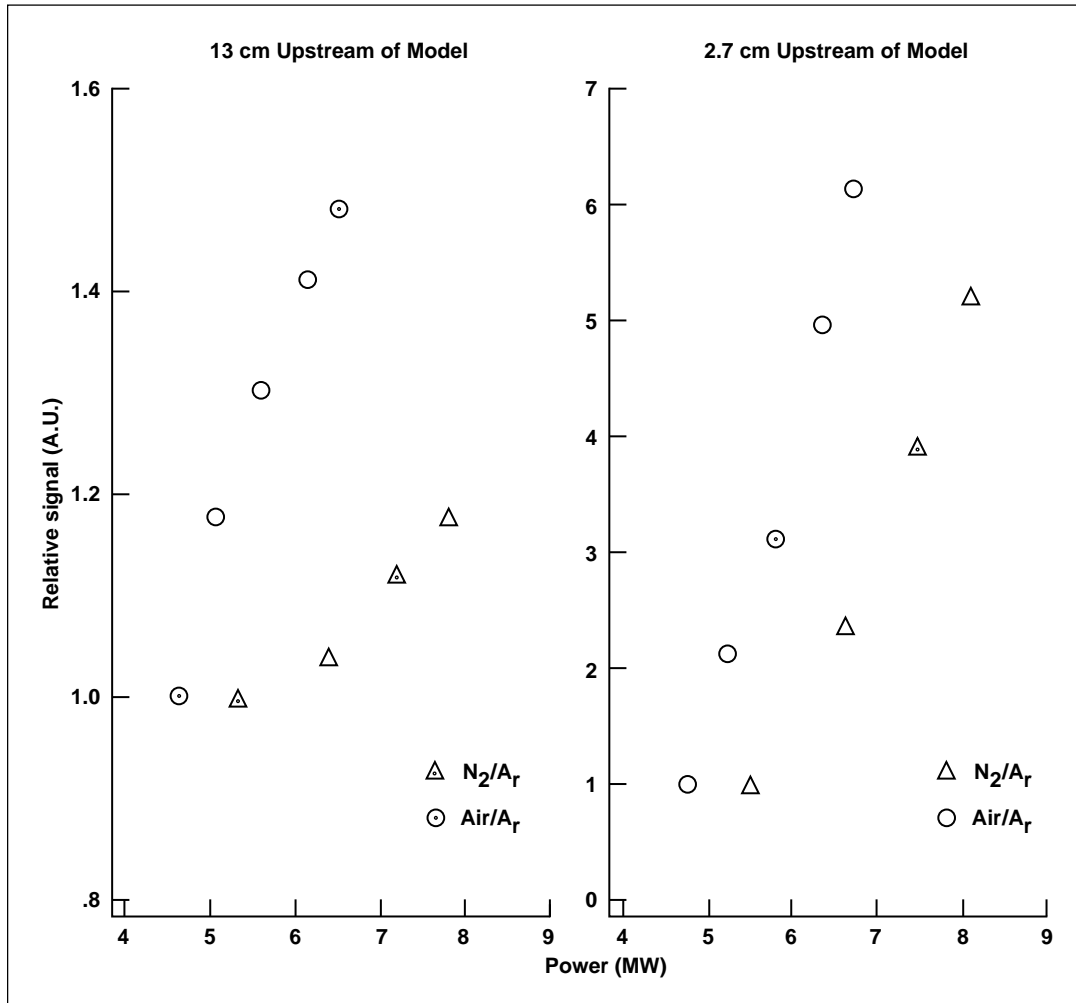


Fig. 2. Nitrogen atom LIF signals from the free stream and nitrogen atom emission signals from the shock layer as a function of arc power. Two different stream mixtures were tested: air/argon and nitrogen/argon.

Presently, the investigation is directed toward determining whether or not thermochemical equilibrium is reached within the shock layer and evaluating the test conditions at which it occurs. If equilibrium is achieved, then the emission radiated from within the shock layer provides a unique determination of the flow enthalpy, which is the most important parameter required for interpreting materials test results. The establishment of thermochemical equilibrium in the shock layer depends on the product of

impact pressure and model diameter. The first figure shows the range of this product for various model sizes as a function of arc chamber pressure for two of the AHF nozzles. The dashed line in the figure indicates the pressure-diameter product above which equilibrium has been postulated to occur, and the symbols represent test conditions investigated as part of this present effort.

Although earlier spectroscopic experiments have been conducted in the AHF, they were implemented as a part of concurrent materials tests. Consequently, the test conditions were not selected with flow diagnostics in mind. As part of the present investigation, a dedicated entry was available, and provision was made for an extended run where the arc current was varied while chamber pressure was held constant. Preliminary results from simultaneous LIF and emission measurements made in this experiment are shown in the second figure. The LIF measurement was made using two-photon excitation of atomic nitrogen that exists in the stream as a result of partial molecular-nitrogen dissociation. Each symbol represents the spectrally integrated absorption profile, which is proportional to nitrogen concentration. The emission measurement was obtained near the shock front and the symbols represent the integrated intensity of nitrogen atom emission at 869 nanometers, which depends on nitrogen atom concentration and local temperature.

Results are shown as a function of increasing arc power level, and both plots show similar trends. The increase in both signals reflects increases in nitrogen atom concentration with increasing arc power, and the increase is more rapid for the air/argon flow than for the nitrogen/argon flow. Increases in signal levels are more substantial in the shock layer because of an exponential dependence of emission signal on temperature, which also increases as the arc power (flow enthalpy) is raised.

It is anticipated that the analysis of these results and other experimental and computational studies will establish a better understanding of the relaxation processes within the arc-jet, shock-layer flow, and will improve the understanding of how test conditions relate to flight environments.

**Point of Contact: D. Fletcher
(415) 604-1647**

Spectroscopic Study of the Arc Column in an Arc-Jet Wind Tunnel

Imelda Terrazas-Salinas, Chul Park, Anthony W. Strawa, Jaswinder S. Taunk, Nigel K. J. M. Gopaul

Spectroscopic measurements in the region of 350 to 900 nanometers (nm) were made in the arc heater of the 20 megawatt Aerodynamic Heating Facility at Ames Research Center. The emission measurements were used to augment the transition probability values of the neutral nitrogen (NI) lines in the wavelength range of 410 to 430 nm.

In the present work, up to 2000 amperes of electrical current were passed through the arc heater to produce mass-averaged enthalpies corresponding to flight speeds in the range of 3.3 to 6 kilometers per second. The airflow inside the arc heater forms an arc column, which emits radiation because of the high temperature produced by arc-heating.

In order to record the radiation from the arc column, a window assembly was provided in the wall of the arc heater in the direction normal to the central axis of the arc column at both the upstream

and the downstream ends of the arc heater. The window was made of a single-crystal sapphire disk 1 centimeter in diameter, fitted with a protective O-ring and a plastic spacer, all enclosed in a threaded insert. The sapphire disk had an optical transmittance range of 150 to 5000 nm. The window assembly views a narrow conical region across the arc column. The viewing solid angle of this system is approximately 4 degrees.

The radiative flux reaching the wall of the arc heater is transmitted through the sapphire window to an optical fiber. A lens mounted outside of the exit plane of the optical fiber imaged the exit plane onto the entrance slit of a 0.3-meter McPherson scanning monochromator, partially covering the slit. The monochromator had a nominal spectral resolution of 0.27 nm. The radiation power emerging from the exit slit of the monochromator was measured by a

photomultiplier tube, and the output of the photomultiplier tube was connected to a data acquisition system for recording in a digital form.

A relative calibration of the optical system was performed using a tungsten lamp, the calibration of which is traceable to the National Bureau of Standards (NBS). The signal from the lamp was imaged through the fiber optic cable onto the entrance slit of the monochromator. The output obtained from the photomultiplier was then referenced to the spectral radiance values of the lamp to obtain the system response values.

The first figure shows typical spectra of the radiation emission in the wavelength region of 410 to 430 nm under differing thermodynamic conditions. Despite great differences in the thermodynamic conditions, the ratios among the intensities of the NI lines are very similar among the three cases, thus indicating that the populations of the upper states of the transitions involved are in equilibrium among themselves over a wide range of conditions.

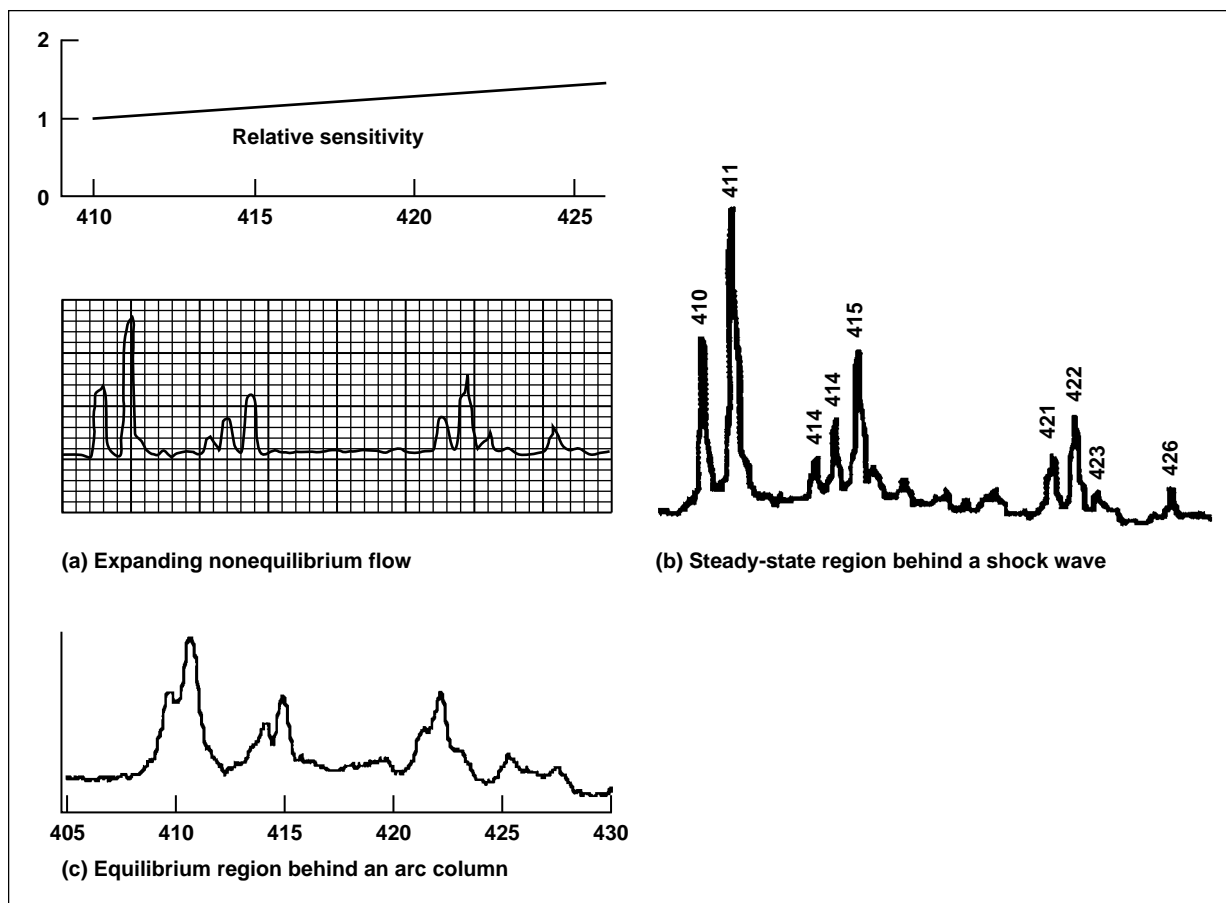


Fig. 1. Comparison of relative intensities of NI lines in the 410–430 nm range. (a) Low-pressure, cooling, nonequilibrium flow; (b) near-equilibrium, steady-state region behind a shock wave at a relatively low pressure; (c) equilibrium, high-pressure region in an arc column.

Part (a) of the second figure shows the spectrum calculated by using the values of the transition probabilities from the NBS Tables. As seen here, the calculated relative intensities of the lines are very different from those in the first figure. Since this difference is common for the three different thermodynamic states, the difference is attributed to the errors in the transition-probability values. The observed discrepancy is important because the spectral flux reaching the wall of a spacecraft is maximum at a wavelength around 400 nm: the Planck function reaches its maximum value at approximately this wavelength at temperatures typical of the aerospace entry environments.

The transition-probability values for the above-mentioned NI lines were determined experimentally to an accuracy of $\pm 30\%$ by comparison of their

measured intensities with that of the atomic oxygen multiplet at around 615 nm. The procedures are only approximate; nevertheless, the determined transition-probability values are more accurate than those listed in the NBS Tables, and therefore are expected to serve at least the purpose of determining the radiation characteristics in aerospace environments to an engineering accuracy. Part (b) of the second figure shows the spectrum calculated using the transition-probability values derived from the present work. These revised transition-probability values result in better agreement between the calculation and the measurements.

Point of Contact: I. Terrazas-Salinas
(415) 604-3730

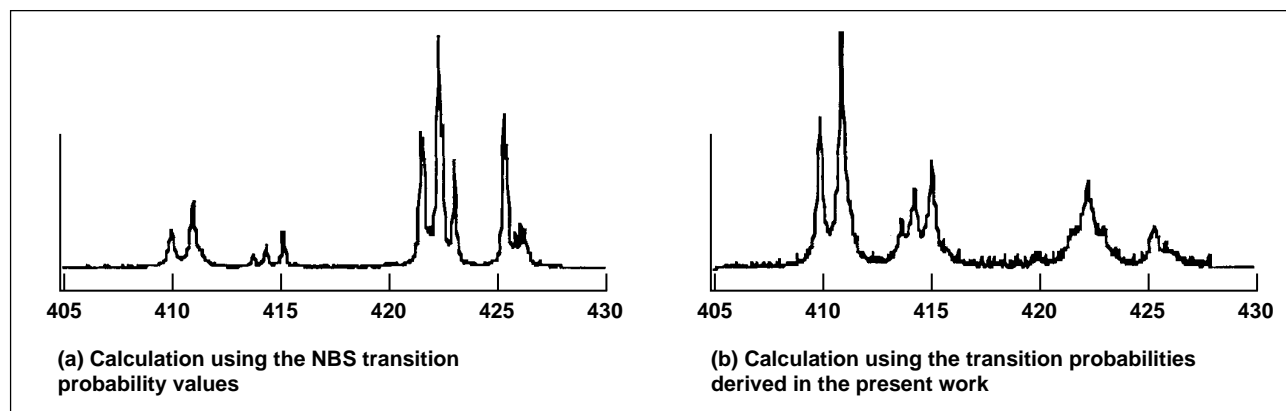


Fig. 2. Comparison of calculated intensities of NI lines in the 410–430 nm range. (a) Calculation using the NBS transition-probability values; (b) calculation using the transition probabilities derived in the present work.

Portable Batch System Project

David Tweten

The Portable Batch System (PBS) project is intended to enable batch program processing across Unix computers of all scales and architectures. Its independent scheduler provides complete freedom of choice in scheduling policies. It began production use in FY95 on two of the more unusual machine architectures in the Numerical Aerodynamic Simulation (NAS) Facility, as the first step toward production use across all scientific computation resources.

Unlike its predecessor, the Network Queuing System (NQS), which was developed a decade ago, PBS supports complete freedom of choice in the method of selecting what batch jobs to run and which to suspend to make way for others. All currently available commercial batch systems provide a fixed, general scheduling method (such as NQS's first-in, first-out queues). By contrast, PBS allows specification of any scheduling method that makes use of information about machine load, the characteristics of queued jobs, and the characteristics of running jobs. Once specified, the PBS scheduler can use any PBS command available to a human administrator to perform its scheduling task. Choice also extends to the language used to specify the desired scheduling method; one can use C language and a support library, tool control language and a support library, or PBS's own batch scheduling language.

In FY95, PBS was put into production use on the NAS 160-node IBM SP-2. Its scheduler emphasized scheduling subclusters of the machine's 160 nodes for dedicated use by multinode message passing parallel jobs. It filled in the remaining time and space with smaller and shorter waiting jobs. Immediately after it was installed, machine utilization jumped from 20 to 70%. A similar effect was seen after installing it on another IBM SP-2 at Langley Research Center. PBS was also installed on a Silicon Graphics Inc. Power Challenge cluster, and the user commands PBS were installed across all NAS workstations.

The conversion to PBS means that users will need to know only one set of commands to access all resources. Conversion also means that the benefits of PBS's scheduling flexibility will facilitate greater cooperation among scientific computing resources. PBS will help toward achievement of the goal of combining heterogeneous computing resources into a virtual computing facility targeted at solving a wide range of scientific and engineering problems.

**Point of Contact: D. Tweten
(415) 604-4416**

Super Home File System Offers Increased User Productivity

Alan Powers

NAS has created a “super home” file system on the NAS Cray C90 (von Neumann) by combining the functionality of the home and migrated file systems. This file system will help new users become immediately productive by reducing the number of file systems they must learn, and increase the total user disk capacity.

Some benefits of the super home file system include: (1) simplifies use of the system; (2) increases total home disk capacity and disk performance; (3) splits file metadata lookups for migrated file system across four super home file systems, increasing file access speed and reducing overhead; (4) improves file transfer rates to and from big and fast file systems; and (5) shortens backup and restore times.

Previously, two-user file systems existed—homes and migrated, as well as two temporary directory file systems, big and fast. This old configuration worked well for users who were aware of the purpose of each file system. However, when new users were added to the system, they tended to overuse their home file systems to run batch jobs, causing longer job turn-around times—and sometimes causing their jobs to fail because of full file systems and degradation of interactive response times.

Prior to the super home configuration, each home file system consisted of 6.3 gigabytes (GB) of slow-access (10 megabytes per second) storage space residing on Cray DD42 disks. Using Cray Research Inc.’s (CRI’s) Data Migration Facility, the migrated file system data was stored on both tape and disk. The disks used for the migrated file system were CRAY DD60s and Maximum Strategy’s redundant array of independent disks (RAIDs) with a total capacity of about 150 GB online; total off-line storage was 1.1 terabytes. All data files larger than 1 megabyte (MB) were archived to tape, leaving 65 percent of the files always online. When space was needed for newly created files or to retrieve migrated files, data

blocks of the oldest archived online files were released. Only files over one day old were eligible to be released. Active files usually stayed online for 2 to 3 days. On average, only 10 percent of files accessed were retrieved from tape; the rest were already online.

In mid-December, 1994, the home and migrated file systems were combined to form the super home file system. A prototype implementation of this system had been working on the staff file system since late August 1994.

For the new super home file system, the idea was to enlarge each of the four home directories using 8 DD60s and a RAID device, for a total size of 60 GB of disk space for each super home. The file system was configured so that small files (less than 1 MB) use the DD60s (20 MB per second) and large files (larger than 1 MB) use the RAID (greater than 50 MB per second). Also, the CRI’s Data Migration Facility used a configuration similar to the one on the migrated file system. Only files greater than 1 MB are being archived, leaving 89 percent of the files always online. This setup is similar to combining the functionality and disk from migrated and home file systems for each super home file system.

Users are allowed to use their home directories to run small input/output (I/O) batch jobs. Big and fast file systems are primarily used for highly I/O-intensive jobs. The home user disk quota is 10 GB, and the user file quota is 10,000. The super home file systems are for short-term storage (files less than 120 days old) and long-term data are archived to the mass storage system. Overall, the super home file systems increase user productivity, increase total user disk capacity, and reduce the complexity of the file system structure.

Point of Contact: A. Powers
(415) 604-3991

Asynchronous Remote Copy Program

Jude A. George

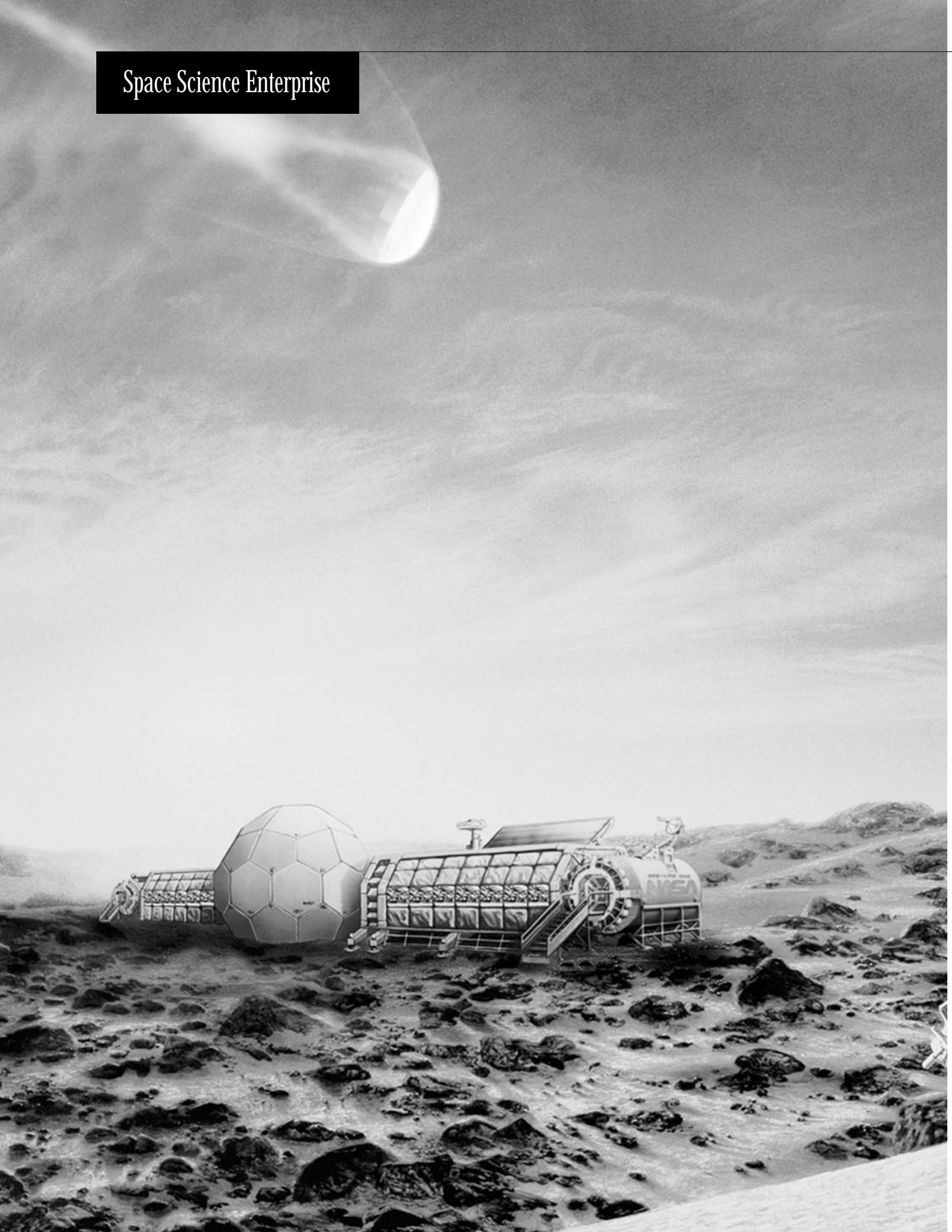
The primary use of NASA's wide-area networks by aerodynamics researchers is to transfer large solution files created on supercomputers to graphics workstations for visualization. Having a high-speed national network dedicated to aerodynamics research (AEROnet) allows the researchers to conduct their work at locations apart from the supercomputer facility at Ames Research Center. Numerous scientists at NASA's Lewis and Langley Research Centers and at industrial and university sites remotely use the supercomputing resources located at Ames.

The scientific datasets thus created typically range from 50 to 2500 megabytes. Because supercomputing resources are at a premium, these files often have to be efficiently moved off the supercomputers soon after they are generated. The files are transferred over local or wide-area data networks to graphics workstations for visualization, or to mass storage systems for archival. These file transfers can take anywhere from several seconds to several hours. In some cases, the file transfer is interrupted because of a less-than-perfect network connection, or a problem with the scientist's local computer system, and the transfer must be restarted. In the worst case, the original solution file has already been cleared from the supercomputer's disk and must be recreated, thus placing an additional strain on supercomputing resources.

The Asynchronous Remote Copy Program (ARCP) was totally designed to quickly and reliably transfer large scientific datasets from host to host with minimal input from the user. The existing tools, ftp (file transfer protocol) and rcp (remote copy protocol), require that the scientist restart failed transfers manually, and generally do not allow a broken transfer to pick up where it left off. ARCP solves this problem by continuously monitoring file transfers, and restarting those that terminate for any reason. Restarted transfers pick up where they left off, saving time and network utilization. Thus, the scientist does not need to be present, and can run a transfer overnight with the assurance that the software will try to complete the transfer. ARCP also transfers files more quickly than existing tools over high-speed, wide-area networks by increasing the amount of data that can be in transit over the network at any given time. At the end of a job, which may consist of the transfer of one or more files, a detailed report of the transfer is optionally provided to the scientist.

**Point of Contact: J. George
(415) 604-4516**

Space Science Enterprise



Overview

The scientific mission of NASA's Space Science Enterprise is to seek answers to fundamental questions about the origin and distribution of life in the universe; the galaxy and the universe; the origin and evolution of planetary systems; and the connections among the Sun, Earth, and heliosphere. Ames' program is focused on the broad, multidisciplinary objective to understand the origin and distribution of life in the universe. This theme is embraced within the term "astrobiology," and NASA has specifically designated Ames as the primary Center for research in astrobiology. During FY95, Ames supported the following goals of this Enterprise by making progress in exobiology, in astrophysics, and in planetology, and by continuing the development of space technologies:

- Determine the abundance and distribution of biogenic compounds conducive to the origin of life.
- Identify locations in the solar system where conditions conducive to life have existed.
- Survey and conduct surface exploration of the most fascinating and accessible planetary bodies.
- Discover the origin, evolution, and fate of the universe, galaxies, stars, and planets.
- Survey cosmic rays and interstellar gas as samples of extrasolar matter.
- Explore the frontiers of the heliosphere.
- Search for planets and planetary formation around other stars.
- Develop innovative technologies to enable ambitious, future space missions.

Exobiology

The study of life's origins and early evolution, including the search for evidence of life and its chemical precursors elsewhere in the solar system and beyond, are elements in the exobiology science discipline, and these elements form one of the goals of NASA's astrobiology efforts. Instrumental in pioneering and establishing exobiology as a new branch of science, Ames has been recognized as the world leader in this field from the beginning. Specifically, Ames conducts studies of organic materials in geological materials and in extrasolar matter; plays a key role as NASA's expert in planetary protection issues; and helps to focus the science for future Mars missions on issues related to the possibility of the independent origin of life on Mars.



Background art: Courtesy of Boeing

In this annual report, efforts related to geological materials, organic compounds, evolution of life, and flight hardware are highlighted.

Reports on geological materials include a development of a proof-of-concept instrument for possible Martian mineralogy studies; a study of the morphology and biogeochemistry of microbial mats to decipher stromalites in ancient rocks; and the formation of complex organic molecules by segregation in the solid state. The efforts relating to organic compounds follow: a new insight into the physical state of ices within cometary nuclei; a feasibility of forming biologically important molecules in interstellar clouds with only a few reaction mechanisms; and analysis of data of dissolved gases in perennially ice-covered lakes of Antarctica. A few issues regarding the evolution of life include insights into the evolution of cyanobacteria and the nature of ancient ecosystems; studies of enzymes synthesizing and hydrolyzing adenosine triphosphate, the energy-storing molecules used by cells to understand the evolution of life; and a model of prebiotic amino acids synthesis from sugar, leading to the generation of peptides. Developments in flight hardware for gas chromatography are porous-layer, open, tubular columns and new or improved miniature detectors.

Astrophysics

As NASA's lead center in airborne astronomy, Ames pioneered and developed this field and operates the world's only capabilities for astronomical observations from the stratosphere. Ames astronomers also contribute to space-based infrared science.

Ames played a key role in the successful launch and operation of the Mid-Infrared Spectrometer aboard the Japanese Infrared Telescope in Space mission, obtaining infrared spectra of more than 10,000 objects. The other accomplishments presented in this report include far-infrared emission from the arched filaments near the center of our galaxy using the Kuiper Airborne Observatory (KAO); the coordinated use of the Faint Object Spectrograph and of the Wide Field and Planetary Camera on the Hubble Space Telescope to study interstellar matter and gaseous nebula; quantitative opacity databases for titanium oxide and water using quantum mechanical methods; the contribution of water opacity in stellar spectra; standards for calibrating

mid-infrared spectra; and the characterization of the radiation environment of focal-plane sensor arrays.

The next-generation airborne observatory, the Stratospheric Observatory for Infrared Astronomy (SOFIA), is now entering development under Ames' management. SOFIA is designed around the lifting capacity of the Boeing 747 and will gather almost an order of magnitude more light than the KAO, achieving an improvement of as much as five orders of magnitude in capability. The aerodynamical and acoustical impact of having a large cavity in the fuselage, through which telescopic observations are made, is reported here.

A basic Space Science question related to understanding questions of life beyond our solar system is "Are there habitable planets around other stars?" The Kepler Mission, built around a 1-meter-class orbiting telescope capable of detecting Earth-sized planets in the habitable zone around 5000 solar-type stars in the galaxy, was proposed to provide the first survey of possible life sites beyond the solar system.

The airborne flight programs are coupled with a more general Ames capability in astrochemistry, including laboratory studies of interstellar and cometary analogs. In this report, the following efforts are presented: organic signatures in the interstellar medium; the composition of interstellar and cometary ices; techniques for providing the energetics and kinetics of reactions based on molecular orbital theory in the interstellar medium; infrared spectra of Polycyclic Aromatic Hydrocarbons bearing extra hydrogens for studying emissions from The Orion Bar; and the laboratory probing of the absorption and emission properties of cosmic material analogs.

A key question posed by the Space Science Enterprise concerns planetary origin and evolution. Ames' infrared astronomy and astrophysics expertise contributes constraints on the temperature, density, and composition of gas and dust clouds in the galaxy, as they interact with the winds and radiation fields of the protostars embedded in them. The gravitational collapse of these clouds forms protostars with orbiting dense, flattened, protoplanetary disks—the birthplace of planets. Critical issues in the dynamical collapse of these clouds and the evolution of these disks under the influence of turbulence, gravity, and energetic radiation are addressed. The primary accumulation of solids into small primitive

(unmodified) bodies, such as comets and asteroids, is strongly coupled to gas dynamics and is also studied. Research accomplishments include a computer-simulation study of the observed, double nucleus in the Andromeda Galaxy (M31); a study of the abundances of elements heavier than helium to probe the formation of a galaxy; and the impact of the rapidly varying ultraviolet field on the final stages of stellar evolution.

Planetology

Ames has a special role in Mars studies and missions and is contributing to new U.S. Mars programs and international collaborations such as the joint United States/Russia Mars Together initiative. The Russian Marsokhod can contribute the mobility needed to address questions about the possible past evolution of life on Mars. An Ames team, in collaboration with the Russians, carried out field testing of this rover on the flanks of the Kilauea Volcano in Hawaii. Such field tests represent the first realistic simulation of operating a mobile science robot on the surface of another planet.

The other Mars-related research accomplishments include the science rationale and measurement requirements for a micrometeorological network on Mars; simulations of mountain waves to study their role in the dynamical interaction between the Martian surface and the atmosphere; additional measurements of water adsorption onto Martian-like minerals; and validation of a chemical model for the origin of the oxidants on Mars.

The progress in planetology is also illustrated by the following studies: energetic effects of large asteroid or cometary impacts; some characteristics of ejecta plumes resulting from the collisions of Comet Shoemaker Levy with Jupiter; the development of simulation techniques for studying the primary accretion process related to planetary origin; computer simulations of thermal transport in a collapsing, protostellar cloud; and advances in conducting theoretical and empirical studies of planetary surface analogs.

Space Technologies

To support the Enterprise mission, Ames scientists and engineers also develop, validate and verify enabling, cutting-edge, high-payoff technologies for future space science and exploration missions at

substantially reduced costs. Cost reduction is addressed principally by using information technology to develop advanced flight and ground system autonomy technologies.

A new autonomous mission control architecture was developed jointly with NASA's Jet Propulsion Laboratory for New Millennium spacecraft. This architecture includes a model-based autonomous system, a planner, and an executive. The system uses sensors to model and reconfigure itself in response to failures. The planner is capable of automatically replanning the mission of a spacecraft in the event of the failure of one or more spacecraft subsystems. NASA selected Remote Agent—the core autonomous architecture—to control the first New Millennium Program flight, Deep Space One. The planner was also used to develop interactive schedulers for the scientific observations of the Extreme Ultra-Violet Explorer spacecraft and of Saturn's rings by the Cassini orbiter.

An integrated suite of Internet-based software tools was developed to improve the collaborative abilities of participants in the New Millennium Program, and consequently, reduce the life-cycle cost. Users of the tools suite can quickly and easily share many types of documents and communicate various kinds of information. Another information-system development, a diagnostic system using fuzzy logic, is for situations when either modeling of complex systems is mathematically unmanageable or neural networks cannot be constructed with a high level of credibility because of sparseness of data. These developments also support other Enterprises.

Other examples of efforts to develop innovative technologies include: the collection of invaluable heat shield performance data during the entry of the Galileo probe into the Jovian atmosphere; an aerothermal analysis for the feasibility study of the Mars 2001 Orbiter mission designed to use the aerocapture principle; a study of the dynamics of the holographic recording, readout, and erasure processes in bacteriorhodopsin films for optical data storage and processing; the development of a computer model to simulate a pulse tube cooler to increase the sensitivity and reduce the noise of detectors for space telescopes; and computer simulations for assisting in the development of new custom-made polymeric materials with specific properties.

Development of CHEMIN, an Instrument for In Situ Determination of the Mineralogy of Soil and Rocks on Mars

David Blake, Philippe Sarrazin, Friedemann Freund

It is generally accepted that Mars, now a cold, relatively dry (and apparently lifeless) planet, was once warm, with abundant liquid water on its surface and a dense atmosphere. Indeed, it has been suggested that Mars and the Earth had similar surface environments in the early Precambrian era (4.0–3.5 billion years before the present), when

evidence of terrestrial life can first be detected in sedimentary rocks. A major theme of the robotic exploration of Mars, therefore, is the characterization of the ancient Martian environment and the search for rock types that may harbor evidence of early life or of prebiotic chemical evolution.

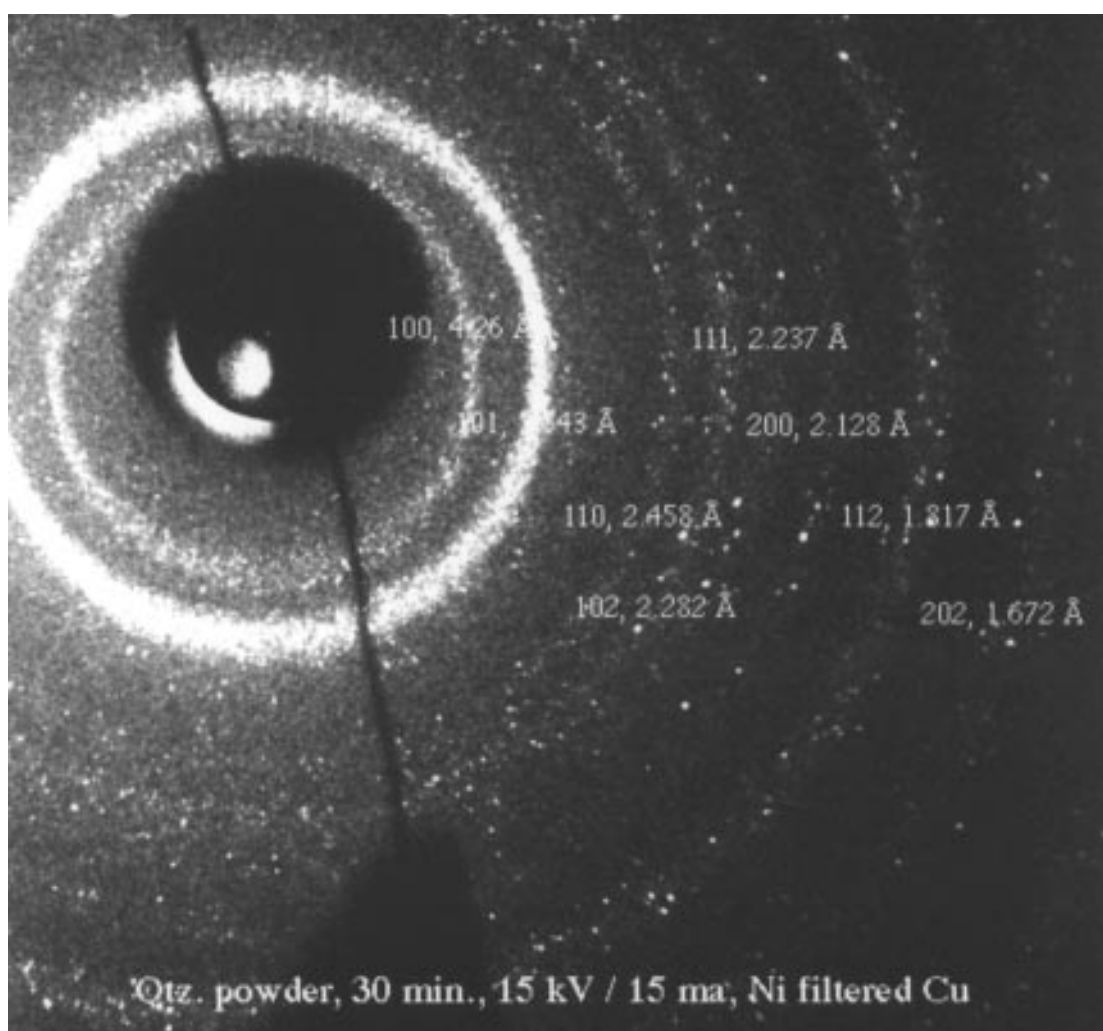


Fig. 1. Digital X-ray diffraction pattern of the mineral Quartz recorded directly onto an X-ray sensitive charge-coupled device (CCD). The placement and intensity of the rings uniquely identify the mineral.

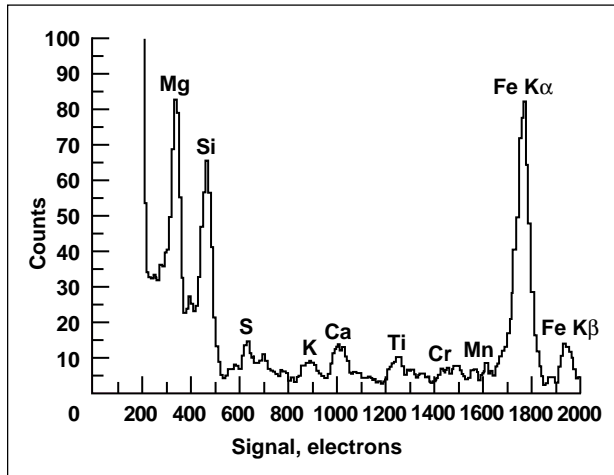


Fig. 2. Energy-dispersive X-ray spectrum recorded from a sample of Allende meteorite powder. Elements contained in the sample are identified by the energy of the fluorescent X-rays detected by the CCD. This information, in combination with diffraction information similar to that shown in the first figure, makes a unique mineral identification possible.

More than any other characteristic, the mineralogy of surface rocks and soil can be used to elucidate present and past conditions of the atmosphere, the surface, and the crust. Minerals are discrete phases that have known conditions of stability (pressure, temperature, and composition). However, surface mineralogy, which is critical to the geological, exobiological, and ultimately, human exploration of Mars, will remain unknown or will be poorly constrained unless X-ray diffraction (XRD) is performed.

Proposals for robotic XRD systems have been studied in the past and instruments for collecting simultaneous XRD and XRF (X-ray fluorescence, or elemental composition) data have been suggested, but the systems envisioned would have had limited capabilities. More recently, an XRD/XRF instrument called CHEMIN (for CHEMistry and MINeralogy) was proposed for inclusion on the Mars Surveyor landers, which will be launched in 2001, '03, and '05. The

instrument uses an X-ray sensitive, charge-coupled device (CCD) array that has the capacity to record both the positions and the energies of X-ray photons. The device will collect diffraction patterns characteristic of the structures of the minerals present, and energy-dispersive X-ray spectra characteristic of the elements present in the minerals.

The instrument will analyze fine-grained soil or powdered-rock samples that are collected onto a sticky substrate for analysis. Sample preparation is not necessary for soil analysis, and some information about soil grain size can be obtained from the quality and character of the diffraction patterns. Complex mineral mixtures can be characterized using diffraction information in combination with elemental analysis data.

A proof-of-concept instrument has been built that operates using a conventional laboratory X-ray source. The first figure shows an X-ray diffraction pattern recorded from a quartz mineral standard using the instrument. Minerals yield a characteristic series of lines (rings in the first figure) and are identified uniquely by the placement and intensity of these lines in the pattern. The same CCD detector that records the diffraction pattern also records fluorescence X-rays, whose energies are characteristic of elements present in the sample. The second figure shows an elemental analysis of powdered material from the Allende meteorite that is being used as a standard material for testing the XRF capabilities of the CCD.

The laboratory version of the CHEMIN instrument appears to have some commercial applications as a real time X-ray diffraction instrument and as a portable XRD/XRF for use in remote locations. A patent (#5,491,738, "X-ray Diffraction Apparatus") was recently issued to NASA that describes various embodiments of the design and uses for such an instrument.

Point of Contact: D. Blake
(415) 604-4816

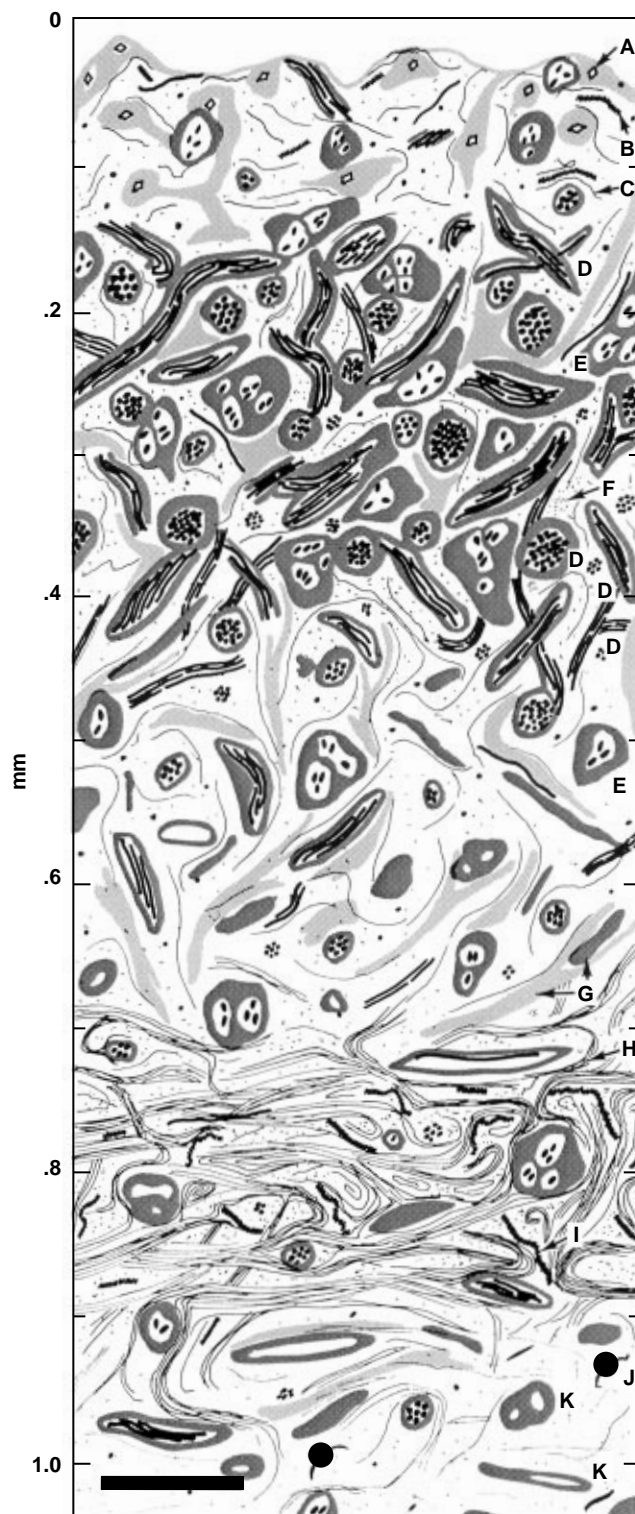
Dynamics of Microbial Mats, the Oldest Ecosystem

David J. Des Marais

Microbial mats are highly coordinated communities of microorganisms that create their own microenvironment within coherent films attached to sediment and rock surfaces. Successive, layered accumulations of microbial mats can form laminated, mineralized structures called stromatolites, which are the most abundant and oldest fossil deposits known in ancient rocks. Accordingly, if life ever existed on ancient Mars, it might have created deposits similar to stromatolites. In order to recognize and interpret the structure and chemical composition of stromatolites in ancient rocks, a study has been conducted of the morphology and biogeochemistry of those living microbial mats that are close analogs of ancient stromatolitic communities.

Some microbial mats are complete, self-contained ecosystems contained within laminae having a thickness of no more than a fraction of a millimeter (see the figure). Accordingly, studies of these mats required microscale techniques such as light and electron microscopy; fiberoptic sensors to measure the penetration of light into mats; microelectrodes to measure molecular oxygen (O_2), sulfide, and pH; and miniaturized incubation chambers to quantify the exchange of chemical species between mats and the overlying water. An examination was made of the mats whose primary producing biota are cyanobacteria, which are O_2 -producing, photosynthetic bacteria that have existed for billions of years.

Fig. 1. Schematic cross section of a cyanobacterial mat. Horizontal bar at lower left represents 100 microns. Letters along the right margin indicate the following: A: diatom algae; B: *Spirulina* spp. cyanobacteria; C: *Oscillatoria* spp. cyanobacteria; D: *Microcoleus chthonoplastes* cyanobacteria; E: nonphotosynthetic bacteria; F: unicellular cyanobacteria; G: fragments of bacterial polysaccharides; H: *Chloroflexus* spp. green bacteria; I: *Beggiatoa* spp. nonphotosynthetic sulfur bacteria; J: meiofauna; K: abandoned cyanobacterial sheaths.



In the modern marine environment, cyanobacterial mats grow most abundantly in coastal lagoons and salt flats characterized by salinities that are more than twice as high as that of seawater. Despite their millimeter-scale thickness, these mats are the most highly productive photosynthetic ecosystems on Earth (gross O_2 production rates >100 millimoles per square meter per day). We observed that a dynamic balance is maintained between mat growth and destruction. Mats situated above the coastal intertidal zone were disrupted physically on a seasonal timescale. Mats in the subtidal zone ultimately were degraded by bacterial decomposition that, at salinities two to three times that of seawater, required five to ten years to obliterate completely.

A study of the processing (recycling) of the elements carbon, sulfur, and free oxygen revealed

the dynamic nature of the mats. Production and consumption of O_2 and organic matter were closely balanced during each 24 hour day-night cycle. Oxic respiration was of variable importance in degrading organic matter within the mat; however, sulfate-respiring bacteria played a key role in organic degradation.

The microbial diversity observable by light microscope diminished greatly in mat laminae which were more than one year old. Ancient stromatolites harboring a diversity of fossilized microorganisms therefore experienced very early mineralization that possibly entombed even live bacteria. This early mineralization prevented these bacterial cells from being destroyed.

Point of Contact: D. Des Marais
(415) 604-3220

Rock-Made Organics

Friedemann Freund, Alka Gupta, Devendra Kumar

In the search for understanding the origins of life, many reaction pathways for the formation of organic molecules have been pursued—in the atmosphere, in the hydrosphere, and at gas/solid and liquid/solid interfaces. An unlikely place where delicate organic molecules would be expected to occur is inside minerals that have cooled from a hot magma.

For a number of years, researchers have known that carbon is present at a low level in otherwise very pure crystals of magnesium oxide (MgO) that have grown from the melt at temperatures above 3000 kelvin, half the temperature of the surface of the Sun. Because carbon dioxide (CO_2) was dissolved in the MgO melt and consequently entered into the growing crystals, the carbon became incorporated into the dense MgO structure. Once inside the structure, the CO_2 molecules changed into carboxy anions. In some of these carboxy anions, the carbon is not oxidized as it is in CO_2 but in a chemically reduced state. This is reminiscent of another impurity in the same MgO crystals, namely traces of dissolved

water (H_2O) in the form of hydroxyl anions (OH^-). It is also known that pairs of OH^- readily undergo a redox reaction that changes them into chemically reduced hydrogen (H_2) and peroxy anions, the oxygen of which is oxidized.

These two pieces of information are combined with the fact that impurities in crystalline solids have a tendency to segregate. In MgO crystals, reduced carbon and hydrogen play the role of such impurities. Segregation occurs during cooling, and it drives the carbon and hydrogen toward the crystal surface, subgrain boundaries, and dislocations. This entire process is an efficient way to concentrate carbon and hydrogen at these sites. By becoming locally concentrated, however, carbon and hydrogen are expected to react with themselves and each other creating carbon-carbon and carbon-hydrogen bonds.

The effect of segregation can actually be seen with the naked eye. The first figure shows a large MgO crystal (measuring nearly 20 millimeters at its

base) that was produced in a crystal growth furnace and cooled from 3000 kelvin to room temperature within a few hours. The crystal exhibits a clear rim (a few millimeters wide) from where the dissolved gases CO₂ and H₂O have escaped to the outer crystal surface. Further inward, where the gases could not escape, they precipitated in millions of very fine cavities, giving rise to a turbidity that pervades the bulk of the crystal. These cavities do not contain gases, but contain a very thin layer of solid matter covering their inside walls.

After crushing MgO crystals (like the one shown in the first figure) to a coarse powder and causing them to fracture preferentially along the planes of weakness where cavities abound, complex organic compounds can be extracted. Different compounds are separated using organic solvents of different polarity. For instance chloroform, an unpolar solvent, extracts preferentially long chain hydrocarbons with single and double bonds and hydrocarbons with one oxygen at the end. When a polar solvent such as tetrahydrofuran is used, dicarboxylic acids are extracted, specifically oxalic, malonic, and succinic acid with two, three, and four carbon atoms respectively. Part (a) of the second figure shows a single crystal of succinic acid that was separated from the

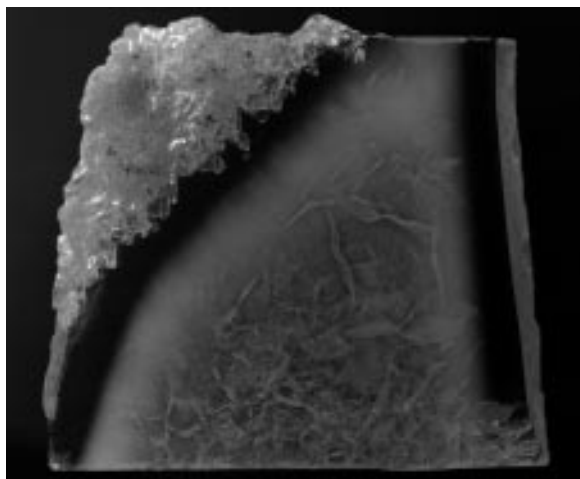
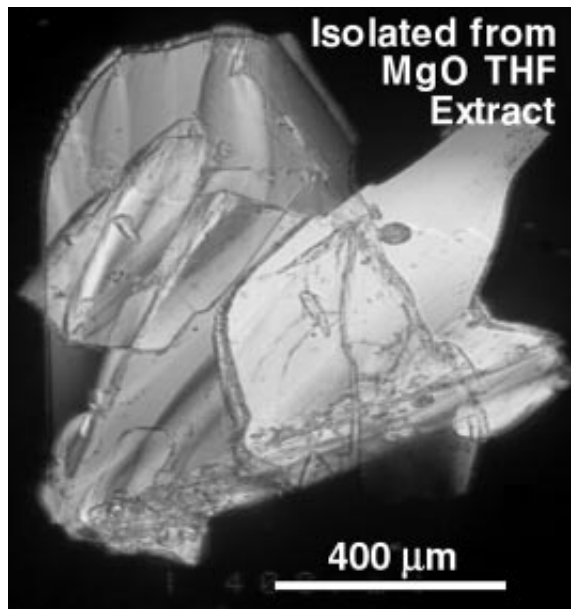
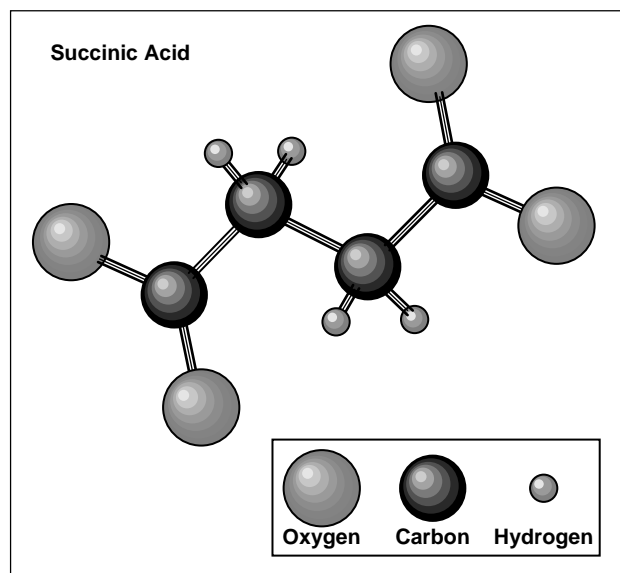


Fig. 1. Slice of a large magnesium oxide crystal, 20 millimeters at its base, grown from the melt. The crystal is bounded to the right and left by its natural irregular growth surfaces. The whitish polycrystalline material at the upper left is part of the wall of the former melt pool. Note the clear rim, a few millimeters wide, and the turbid interior.

tetrahydrofuran extract of crushed MgO crystals. The structure of this dicarboxylic acid (as determined by x-ray analysis) is depicted in part (b) of the second figure.



(a)



(b)

Fig. 2. (a) Crystals of succinic acid, extracted from coarsely crushed MgO crystals with tetrahydrofuran (THF). (b) A molecule of succinic acid, a four-carbon dicarboxylic acid, HOOC(CH₂)₂COOH, as determined by x-ray structure analysis.

This work shows that surprisingly complex organic molecules can be generated inside the dense matrix of crystals like MgO. The solid state processes by which these delicate molecules (or precursors thereof) form are well understood, though much work is still needed to determine how much of the total carbon contained in the MgO crystals turns into organic matter. It is also necessary to map out the complexity of the organic molecules and to relate them to the crystal structure from which they segregate. For instance, the long-chain aliphatic and olifinic molecules listed in the table suggest that they derive from carbon-carbon backbones that segregated into dislocation lines. The dicarboxylic acids suggest that some of the carbon atoms remain bonded to lattice oxygens while also making carbon-carbon and carbon-hydrogen bonds.

These findings are important for Exobiology and the search for the origins of life. The MgO crystals are a model and their study represents only the first step aimed at extending this study to natural minerals. The MgO crystals have already helped to decipher the

fundamental processes that lead to the formation of complex organic molecules by segregation in the solid state. Similar processes are expected to take place in rocks which solidify from magmas saturated with the common volcanic gases CO₂ and H₂O. When the rocks cool, carbon and hydrogen within their constituent minerals can be expected to segregate to internal defects. When the rocks are exposed at the surface of the Earth because of volcanic or tectonic forces, their minerals disintegrate through weathering. During disintegration they will release whatever carbon-carbon and carbon-hydrogen entities they contain, thus releasing rock-made organics into the surface environment.

That magmatic rocks from the depth of the Earth may be carriers of complex organic molecules is a fascinating prospect. If this is true, rock-made organic matter may have played a role during the early history of the Earth when life began.

**Point of Contact: F. Freund
(415) 604-5183**

Table 1. Sequence of longchain hydrocarbons extracted with chloroform from crushed upper mantle-derived olivine single crystals and analyzed by GC-MS (gas chromatography-mass spectroscopy; amu: atomic mass units)

Probable mass fragments	amu
CH ₂ =CH ⁺	27
CH ₃ -CH ₂ ⁺	29
CH ₂ =CH-CH ₂ ⁺	41
CH ₃ -CH ₂ -CH ₂ ⁺ or CH ₃ CO ⁺	43
CH ₂ =CH-CH ₂ -CH ₂ ⁺	55
CH ₃ -CH ₂ -CH ₂ -CH ₂ ⁺ or CH ₃ -CH ₂ CO ⁺	57
CH ₂ =CH-CH ₂ -CH ₂ -CH ₂ ⁺	69
CH ₃ -CH ₂ -CH ₂ -CH ₂ -O ⁺ or CH ₃ -CH ₂ COO ⁺	73
CH ₂ =CH-CH ₂ -CH ₂ -CH ₂ -CH ₂ ⁺	83
CH ₃ -CH ₂ -CH ₂ -CH ₂ -CH ₂ -O ⁺ or CH ₃ -CH ₂ -CH ₂ COO ⁺	87
CH ₂ =CH-CH ₂ -CH ₂ -CH ₂ -CH ₂ -CH ₂ ⁺	97
CH ₂ =CH-CH ₂ -CH ₂ -CH ₂ -CH ₂ -CH ₂ -CH ₂ ⁺	111
CH ₂ =CH-CH ₂ -CH ₂ -CH ₂ -CH ₂ -CH ₂ -CH ₂ -CH ₂ ⁺	125
CH ₂ =CH-CH ₂ -CH ₂ -CH ₂ -CH ₂ -CH ₂ -CH ₂ -CH ₂ -CH ₂ ⁺	139
CH ₂ =CH-CH ₂ -CH ₂ -CH ₂ -CH ₂ -CH ₂ -CH ₂ -CH ₂ -CH ₂ -CH ₂ ⁺	153

The Crystallization of Water Ice in the Solar System

David Blake, Peter Jenniskens

On the Earth, water ice is typically present as large hexagonal crystals, whether the ice is formed from vapor as snowflakes in the troposphere, or as sea ice frozen from ocean water. Hexagonal water ice, I_h , is the stable form of solid water at Earth surface pressures and temperatures below freezing. However, other structural forms of water ice occur naturally in the extraterrestrial environment, such as cubic ice, I_c , and several amorphous (non-crystalline) forms, I_a . In the cold vacuum of interstellar space, water ice exists primarily as amorphous rinds on dust grains. A variety of small carbon-containing molecules are co-deposited and trapped within the ice. It is within the matrix of amorphous ice that these molecules recombine to form the first organic compounds. During the formation of our solar system, interstellar ice grains coalesced to form icy planetesimals. These planetesimals are thought to have delivered primitive organic materials, water, and volatile gases to the Earth during the late bombardment of the inner solar system.

In the Space Science Microscopy Laboratory at Ames Research Center, interstellar and cometary ice analogs are vapor-deposited inside a Transmission Electron Microscope, and the ice structure is analyzed directly using electron diffraction. The diffraction patterns are recorded digitally in real time, which allows a detailed analysis of structure as the ice is warmed from 14 kelvin (–259 degree Celsius) up to room temperature, just as, for example, when a cometary body from the outer solar system approaches the Sun during its orbit.

Recent results of this research changed substantially the conventional view of how comets shed gases as they warm up in their approach to the Sun. The conventional view is that gases are expelled from the ice of the nucleus at the particular vaporization temperature of the pure gas impurity, or ultimately, when the water ice crystallizes. In fact, as cometary ice is warmed, we find that only a small fraction of the water ice ever crystallizes (<30%), and impurity gases remain trapped within the amorphous ice

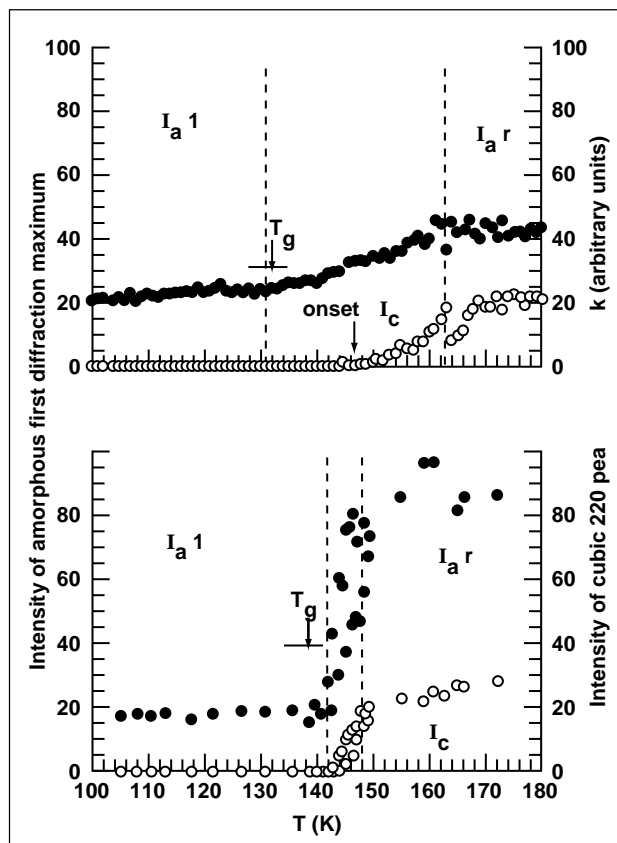


Fig. 1. Intensity of the amorphous and crystalline components of vapor-deposited amorphous water ice during a warming experiment. Upper: Change in the height of the first peak of the amorphous component (solid dots) and the height of the cubic crystalline 220 peak (open dots) from an experiment in which the ice was gradually warmed (1 kelvin per minute) after deposition at 14 kelvin. Lower: As above, except that the ice was warmed quickly (10 kelvin per minute) immediately after an 86 kelvin deposition. The onset of crystallization is preceded by the onset of a change in the height of the first amorphous diffraction maximum. The approximate position of the glass transition temperature (T_g) is indicated for both experiments.

structure. Most of the physical changes that result in gas release involve small modifications in the amorphous ice structure. For example, amorphous ice undergoes what is called a "glass transition" at a temperature slightly lower than the crystallization temperature (see the figure). At the glass transition, the local structure of the hydrogen bonded network relaxes, closing micropores in the ice and allowing gases adsorbed onto the surfaces of the pores to escape. Most of the remaining gases are retained in the amorphous ice that coexists metastably with cubic crystalline ice to higher temperatures. As the cometary ice warms further, the amorphous ice

component vaporizes directly without ever crystallizing, releasing the trapped impurities at the same time.

The retention and release of volatiles is almost entirely dependent on the structure of amorphous water ice and its response to irradiation and thermal cycling. These results provide new insight into the physical state of ices within cometary nuclei, and how and in what quantity volatiles and small organic molecules were delivered to the inner solar system and to the primitive Earth.

Point of Contact: D. Blake
(415) 604-4816

Formation of Simple Biomolecules in Interstellar Clouds

Steven B. Charnley

Dense molecular clouds are the sites where Sun-like stars form. Gravitational collapse of this dusty molecular material leads to the formation of a protostar surrounded by an accretion disk from which planets, comets, asteroids, and other debris eventually form. In our solar system, the bulk of the organic material initially available for the evolution of life may have been transported to the early Earth by cometary impacts. Many exotic classes of organic molecules have been discovered in carbonaceous meteorites, and the fact that this material is substantially enriched in deuterium constitutes one of the most convincing pieces of evidence for an interstellar origin. The initial organic mixture that led to the appearance of life in our solar system can therefore be traced back to chemical reactions that occurred in the parent interstellar cloud. Hence, understanding the organic chemistry of molecular clouds, particularly the formation of biologically important molecules, is fundamental to the study of the processes that lead to the origin, evolution, and distribution of life.

A large variety of gas-phase organic molecules have been observed in the dense interstellar medium, belonging to such classes as nitriles, acetylene derivatives, aldehydes, alcohols, ethers, ketones, and amides. These molecules can form in one of three ways: either (1) by ion-molecule and neutral reac-

tions in cold gas; or (2) by accretion of gas-phase species on interstellar dust grains where an active surface chemistry takes place to form molecular ices; or (3) by ion-molecule and neutral-neutral reactions among the evaporated molecules in so-called hot cores, where a nearby luminous protostar has heated the surrounding dust and removed the icy mantles.

Recent work has succeeded in explaining the entire inventory of observed organic molecules by invoking only the minimum number of reaction mechanisms on both grain surfaces and in hot core gas. On grain surfaces, the presence of the simplest mantle molecules can be attributed to formation in, and direct accretion from, cold gas or by exothermic hydrogen addition reactions (water, ammonia, and methane). Atom addition reactions to carbon monoxide (CO) forming carbon dioxide (CO₂) and the formyl radical (HCO) have been demonstrated to be important in laboratory experiments. Analysis of meteoritic organic material has shown that the original (interstellar) reactions were principally single-atom additions and that carbon chains were grown under conditions of radical stability.

The first figure is the simplest realization of grain surface chemistry incorporating the above facts. It shows the development of complexity arising from hydrogen (H) atom additions to CO followed by

addition of a hydrogen or one atom of each of carbon, oxygen, and nitrogen, to form, respectively, the primary molecules: formaldehyde, ketene, formic acid, and isocyanic acid. Carbon chain growth leads to a ketene backbone: large linear molecules with a carbonyl and an acetylenic functional group at either

end. Subsequent H-atom additions evolve the mantle composition from ketenes through aldehydes and on to alcohols. The remarkable fact is that many observed organic molecules can be accounted for in this single scheme—no other formation mechanism can explain their presence and relative abundances.

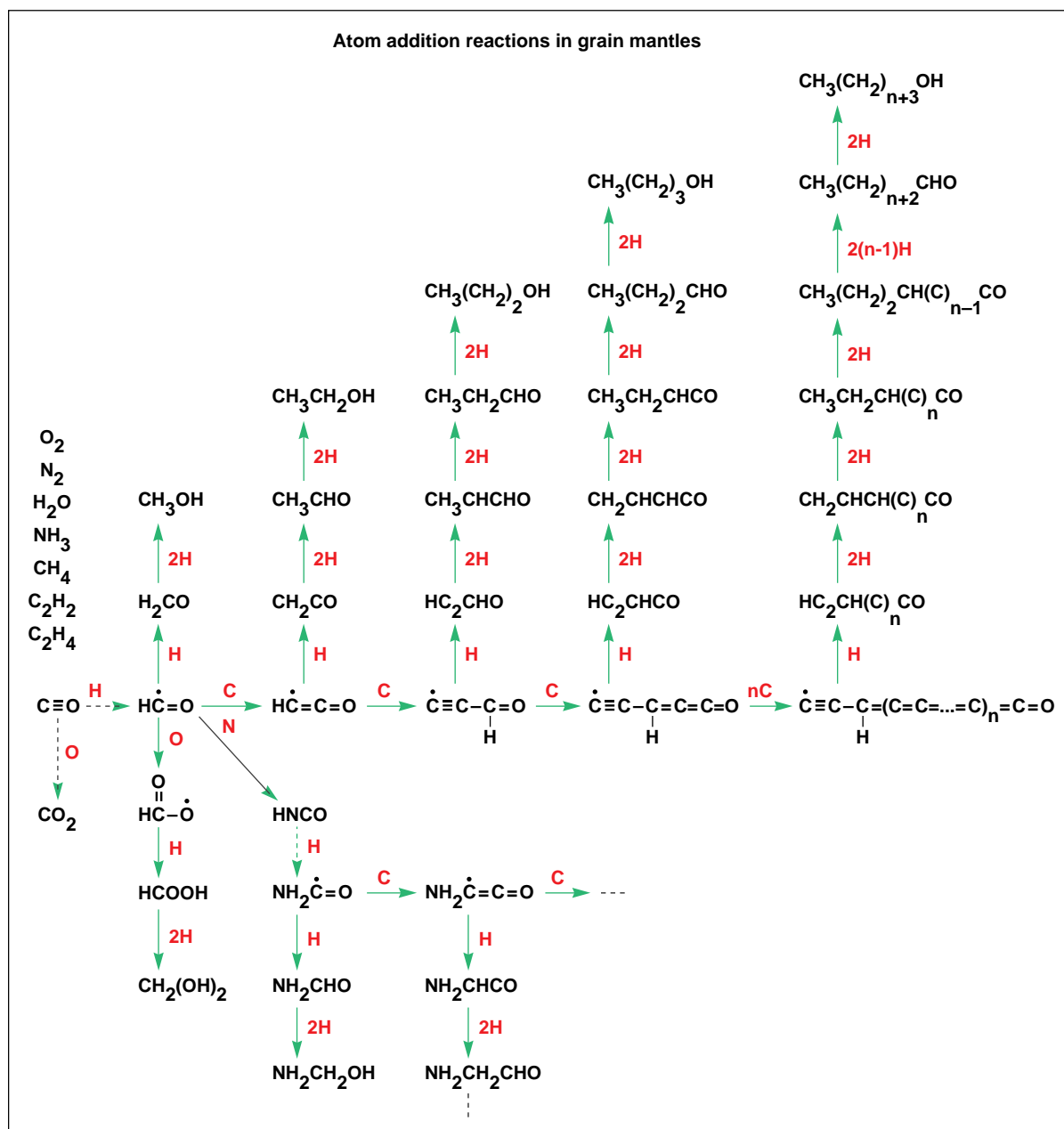


Fig. 1. The composition of interstellar grain mantles. The pristine mantle comprises simple molecules accreted from the gas or formed by exothermic H-atom additions. Energetic processing allows H-atom addition to unsaturated molecules, and a rich organic chemistry seeded by CO ensues. Broken arrows indicate reactions with activation energy barriers; where 2H is shown, a barrier penetration reaction followed by an exothermic addition is implicitly indicated.

The existence of a distribution of activation energy barriers involving penetration of double and triple bonds naturally explains the differences in organic composition between cold dark clouds and more energetic environments, because of varying degrees of mantle processing.

In the protostellar environment, increasing saturation leads to ice mantles, and eventually protostellar gas that is rich in simple alcohols. Ionization of a gas that is rich in evaporated methanol and ethanol produces their protonated forms that can react with the other evaporated molecules depicted in the first figure. Detailed calculations show that, among alcohols, these reactions produce large, pure, and mixed ethers. The second figure summarizes the organic molecules that can be

formed by this mechanism. Alkyl group transfer alone can, in fact, account for almost all the observed organics not produced on the grain surface (for example, acetone and methyl formate).

In this way, all positively-identified, organic, interstellar molecules can be produced by only a few reaction mechanisms. This theory explains why particular organics are seen and why others are not, makes definite predictions concerning the relative abundances of specific molecules in various environments, and also predicts the existence of many new, previously unconsidered, interstellar organic molecules.

Point of Contact: S. Charnley
(415) 604-5910

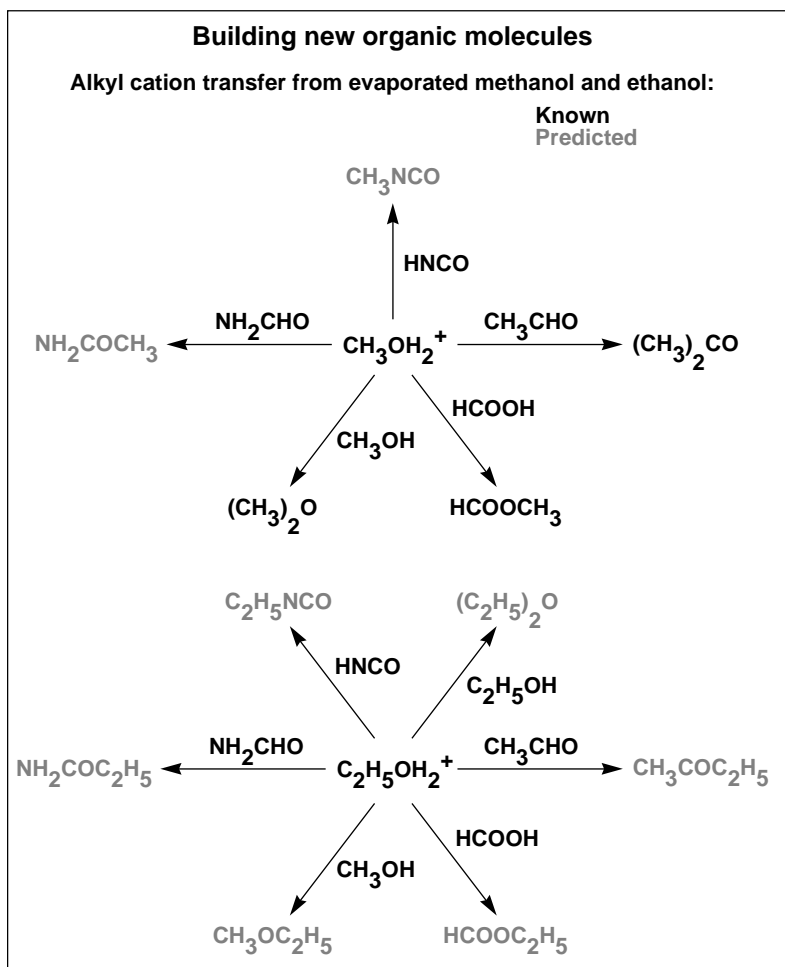


Fig. 2. Methanol and ethanol, when protonated, transfer an alkyl cation exothermically to other evaporated neutral mantle products. In this figure, the step involving the electron dissociative recombination of the intermediate, organic molecular ion has been suppressed for clarity.

Dissolved Gases in Perennially Ice-Covered Lakes of Antarctica

Dale T. Andersen, Christopher P. McKay

The McMurdo Dry Valleys of Antarctica contain perennially ice-covered lakes that are unique in that they neither freeze solid in the winter nor thaw completely during the summer. In this paper, a report is made on dissolved gases within four of these lakes; Hoare, Joyce, Vanda, and Miers. It has previously been recognized that the oxygen (O_2) gas and nitrogen (N_2) concentrations in the water column exceed atmospheric equilibrium. There are both biological and nonbiological sources of gas within the lakes; however, the contribution of each of these sources to the overall gas budgets is not well understood.

Most of our data are derived from the analysis of samples obtained at Lake Hoare ($77^\circ 38' S$, $162^\circ 53' E$), a perennially ice-covered lake located at the eastern end of Taylor Valley at an elevation of 58 meters. The lake is 4.1 kilometers long and 1.0 kilometer wide; it has a maximum depth of 34 meters and a mean depth of 14.2 meters. The lake is dammed at its eastern end by the Canada Glacier, an alpine glacier flowing into the valley from the Asgaard Mountains. Lake Hoare receives water and sediments from glacial melt and from Lake Chad during the austral summer.

Gases enter the lake as air dissolved in water and are concentrated in the water column as water freezes onto the bottom of the ice-cover. Water leaves the lake by sublimation from the top of the ice cover. Bubbles are present in the ice cover and are a major sink of gases from the lake. In addition to loss through bubbles in the ice, there may be some loss of gases through the peripheral moat that forms on the shore each summer. The noble gases have no known biological sources or sinks, and one could expect a buildup of these gases in the water column. Biological processes should have the most pronounced effect on O_2 , carbon dioxide (CO_2), and methane (CH_4) concentration due to photosynthesis, respiration, and the anaerobic conditions that are found in Lake Hoare below ~ 28 meters. Biological sources and sinks for N_2 are small compared to the dissolved input.

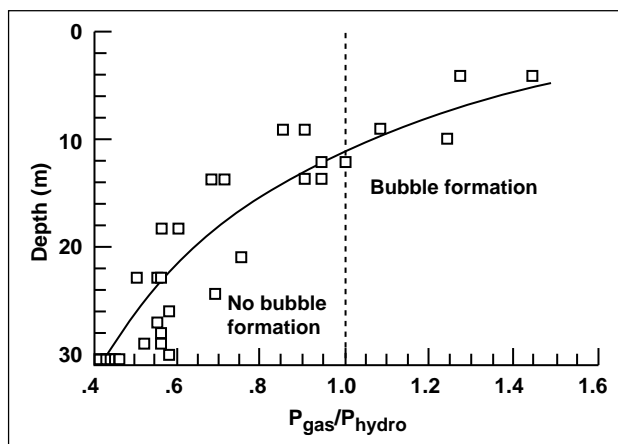


Fig. 1. Total pressure of dissolved gas (P_{gas}) for the average values of the measurements for Lake Hoare (see text) divided by the local hydrostatic pressure (P_{hydro}), shown by the solid line. Individual samples are shown by squares. When this ratio exceeds unity, bubbles in the water column grow, limited only by diffusion of gas to the bubble site. Bubbles form above 11 meters.

Results confirm previous reports that O_2 concentrations in the upper water column exceed atmospheric equilibrium and that N_2 and argon (Ar) are supersaturated throughout the water column. The mean supersaturation of N_2 was found to be $2.0 (\pm 0.37)$ and Ar was $3.8 (\pm 1.1)$. The ratio of N_2/Ar (20.3 ± 3.8), and O_2/Ar at the ice-water interface is consistent with that previously measured, suggesting that bubble formation is the main process for removing gas from the lake. However, the saturations of N_2 and Ar greatly exceed that previously predicted by degassing by bubble formation at the ice-water interface. Researchers proposed that bubble formation and the concomitant gas removal occur in the water column to a depth of 11 meters in Lake Hoare. Carbon dioxide concentration increases from near zero levels at the ice-water interface to 80–100 times saturation below ~ 28 meters. There is considerable

variability in the gas concentrations throughout the water column; samples separated in depth by one meter can vary by more than 50% in gas content. Researchers suggest that this phenomenon is real and results from the lack of turbulent mixing in the water column. CH₄ (~2 micrograms per liter) was detected below 28 meters and immediately above the sediment/water interface at a depth of 30 meters. Samples from Lakes Vanda, Joyce, and Miers also show supersaturations of O₂, N₂, and Ar at levels similar to those found in Lake Hoare.

The figure shows the ratio of total pressure of dissolved gas (P_{gas}) divided by the local hydrostatic

pressure (P_{hydro}). The curve represents the average conditions in the water column. When P_{gas} exceeds the local hydrostatic pressure, bubbles may form. Any bubble will grow with time, its growth being limited by the diffusion rate of gas through the water column to the bubble. When P_{gas} is less than the local hydrostatic pressure, bubbles will dissolve. As shown in the figure, bubble formation occurs for depths less than 11 meters.

Point of Contact: D. Andersen
(415) 604-5499

Cyanobacterial Biomarkers as Clues to the Nature of Ancient Ecosystems

Linda L. Jahnke

Many questions exist about the evolution of oxygenic photosynthesis within the cyanobacteria and the influence that molecular oxygen had on subsequent biological evolution. One of the most interesting questions deals with the development of aerobic metabolism and its subsequent influence on the cycling of carbon in paleoenvironments. Our knowledge about the timing of the events surrounding this transition from anaerobic to aerobic ecosystems must depend on interpretation of limited information from the geological record. In this respect, the study of the various types of hydrocarbons extracted from ancient sediments can provide firm connections to modern biology by linking unique chemical fossils, that is, carbon skeletons that survive more or less intact and serve as biomarkers for specific groups of organisms. Understanding the function and influence of environmental factors on the synthesis of such biomarker molecules within the source organism can then provide a basis for interpretation of this ancient organic record.

Important biomarkers for identification of cyanobacterial input to sedimentary organic matter are a group of straight chain hydrocarbons (alkanes) having seventeen to twenty carbons (C₁₇–C₂₀) with mid-chain, branched methyl groups such as

7-methylheptadecane (C₁₇). These methylalkanes are specific to cyanobacteria, are resistant to biodegradation, and form some of the oldest known biomarkers, having been isolated from Proterozoic rocks dated 1.7 billion years ago. While methylalkanes are quite commonly reported components in Proterozoic sediments, as well as in many modern, cyanobacterially dominated, microbial mat communities, these biomarkers are less obvious in younger Phanerozoic organic matter (less than approximately 0.6 billion years ago); even though cyanobacteria are still major contributors to modern organic sedimentary material. There are clues to explain this apparent paradox in studies with pure cultures of a cyanobacterium, *Phormidium luridum*, which may provide insights into the evolution of cyanobacteria and the nature of ancient ecosystems.

P. luridum is a filamentous cyanobacterium, similar to the thermophilic *Phormidium* species that occur widely in hot spring mat communities. This type of cyanobacterium is especially prominent in the formation of an important type of microfossil analogue, the modern conophyton-type microbial mats found there. Working with Roger Summons of the Australian Geological Survey Organisation,

researchers recently identified several types of dimethylheptadecanes with methyl branches at carbons 7,11 and 7,10 in this *P. luridum*. Lipid contents were found to vary markedly with growth conditions. An observation of particular interest and significance is that abundances of dimethylalkanes and of some esterified, polyunsaturated, fatty acids that are apparently biosynthetically related, are strongly regulated by the availability of dissolved inorganic carbon (DIC). Cells grown under high DIC conditions that resulted from sparging the culture with a mixture of 1% carbon dioxide (CO₂) in nitrogen or in air, produced mostly straight chain heptadecane with small amounts of monomethylalkanes. Cells grown as static cultures under air, where atmospheric CO₂ (0.03%) was limited by diffusion, produced a higher proportion of their alkanes as the monomethyl and considerable amounts of dimethylheptadecane. Moreover, the relative abundance of these methylated compounds

increased with the age of the cultures, with dimethylalkane sometimes representing 60% of the alkane fraction. Although such alkanes have been identified in a few microbial mats, these data constitute the first direct observation of dimethylalkane biosynthesis by a cultured cyanobacterium and reveal the specific conditions under which this biosynthesis is enhanced. They also suggest that dimethylalkanes constitute direct indicators of oxygenic photosynthesis and an indirect gauge for low levels of CO₂ in paleoenvironments. Further characterization of the biosynthetic pathways and environmental conditions involved in the synthesis of these biomarkers could provide valuable information about paleoenvironments, and allow for unambiguous identification of cyanobacterial input to sedimentary material.

Point of Contact: L. Jahnke
(415) 604-3221

On the Identification of a Chimeric ATPase in the Bacterium *Paracoccus Halodenitrificans*

Lawrence I. Hochstein

There are two types of proton-translocating ATPases: one is an enzyme that synthesizes adenosine triphosphate (ATP) (the F-ATPases); the other is an enzyme that only hydrolyzes ATP (the V-ATPases found in vacuoles of the Eucarya (organisms found in the plant and animal kingdoms)). Both ATPases are postulated to have arisen from a common ancestor at a time when the evolution of life underwent a bifurcation leading to the eucaryal/archaeal line as well as the bacterial lines. The F-ATPases were associated with the latter whereas the ancestral V-ATPase, which were also presumed to synthesize ATP, were associated with the eucaryal/bacterial lines. The V-ATPases found in Eucarya lost this synthetic function, and it was presumably retained in the Archaea. The appearance of F-ATPases in the Eucarya is ascribed to the phenomenon of endosymbiosis, a process in which a bacterium is engulfed by a eucaryote-like ancestor.

Recent results from this laboratory suggest another scenario which is that F- and V-type ATPases existed in the last common ancestor prior to the bifurcation. The occurrence of V-type ATPases in some bacteria and V- and F-type ATPases in the Archaea is consistent with this notion. Missing is a case where a member of the Domain Bacteria possess both ATPases.

A series of studies have been carried out with the bacterium, *P. halodenitrificans*. This organism is of particular interest from an evolutionary point of view since it is closely related to an organism (*P. denitrificans*) thought to have given rise to mitochondria by a process called endosymbiosis. Mitochondria are bodies in the cytoplasm of Eucarya that provide energy to the cell. The membrane-bound ATPase from *P. halodenitrificans* appears to be a chimeric enzyme (that is, possesses characteristics

of both V- and F-ATPases) as judged by the sensitivity of the enzyme to agents that are specific inhibitors of F- and V-ATPases. In addition, the structure of the enzyme from *P. halodenitrificans* resembles the structure of F-ATPases. Researchers proposed that this enzyme is indeed a Chimera and that it repre-

sents the last common ancestral ATPase prior to the bifurcation that leads to the three Domains.

Point of Contact: L. Hochstein
(415) 604-5938

The Isolation of a Gene that Codes for the F_0F_1 -ATP Synthase (F-ATPase) in the Extremely Halophilic Bacteria

Roberto Bogolmolini, Lawrence I. Hochstein

Adenosine triphosphate (ATP), the energy-storing molecule used by cells, is synthesized by an enzyme (the F-ATPase) located on mitochondrial, bacterial, and plant membranes. The nature of the ATP synthesizing system in the extreme halophiles has been an object of some controversy. ATP synthesis by *Halobacterium saccharovorum* was shown to be consistent with the operation of an F-ATPase and not the vacuolar-like ATPases which have been isolated from a variety of extreme halophiles (and other members of the Domain Archaea). These vacuolar-like ATPases are closely related to the vacuolar-ATPases (V-ATPases) found in the Eucarya (plants and animals). This leads to the question as to why an F-type ATPase has not as yet been isolated if one exists.

The reasons probably reflect a number of factors, one of which may be the peculiar characteristics of proteins from extreme halophiles. Therefore, a different approach was undertaken, which was to isolate one of the several genes that code for the F-ATPase. The ultimate strategy is to clone that gene in a suitable host organism, isolate the gene-product (the ATPase) from this host, and characterize the product. This approach reflects that all proteins are specified by their DNA in a code that is described by a unique combination of three nucleic acid bases. It is possible to search for this unique sequence using

the polymerase chain reaction (PCR). The polymerase is an enzyme that uses the information contained within a short segment of DNA (called the primer) to copy the nucleotide segments that stretch beyond the primer. By selecting a sequence that is unique to the gene in question, it is possible to isolate such genetic material from the DNA of interest if it in fact exists.

The researchers undertook to determine if the genomic DNA of extreme halophiles contained the DNA that specifies the F-ATPase. The primer was designed using the published sequences for the mitochondrial F-ATPase and did not contain sequences that are found in V-ATPases. If it did, it would have been a serious problem since these ATPases are sufficiently similar to possess regions of homology. Researchers examined the DNA from *H. salinarium* and *H. saccharovorum* with this primer and were able to produce a DNA product that reflects the segment amplified by the reaction. A similar experiment with the DNA from *H. saccharovorum* produced several products, but the yields were low and not of sufficient quantity to allow for identification.

Point of Contact: L. Hochstein
(415) 604-5938

Investigation into the Nature of the ATP Synthase in *Halorubrum Saccharovorum*

David Faguy, Lawrence I. Hochstein

Halorubrum saccharovorum is an organism that grows in the presence of high concentrations of salt. It is a member of the Archaea, now recognized as a third form of life—the other two being the Eucarya (plants and animals) and the Bacteria (the true bacteria). Although the Archaea resemble Bacteria in size and shape, the former differ in several fundamental ways and, in fact, are more closely related to the Eucarya than to the Bacteria. One of these differences may be how the Archaea synthesize adenosine triphosphate (ATP), the molecule that is the universal energy currency of cells.

Very early in the evolution of life, cells learned how to convert ion gradients (that is, differences in the concentration of hydrogen and sodium ions) into energy, and to store such energy as ATP. The catalyst responsible for this conversion is a ubiquitous enzyme complex, designated as an F-ATPase. It shares a common ancestor with a related enzyme, the vacuolar ATPases (V-ATPase) that is found in the intracellular vacuoles of plants and animals. The only ATPase described to date in the Archaea is an enzyme that is very closely related to the V-ATPases.

While it is well established that V-ATPases do not synthesize ATP, there is some controversy concerning how ATP is synthesized by the Archaea. There are those who believe it is brought about by the vacuolar-like ATPase. While attempting to verify this belief, ATP synthesis in *H. saccharovorum* was observed to be inconsistent with the operation of a vacuolar-like enzyme but could be explained by the action of an F-like enzyme. These studies were carried out using cells with a myriad of reactions occurring that could complicate the results. In addition, the critical bit of evidence for the presence of an F-type ATPase was the inhibition of ATP synthesis by sodium azide, a well-known inhibitor of F-ATPases. Therefore, an examination was made of ATP synthesis in *H. saccharovorum* in two ways at the physiological level.

To obviate the difficulties of working with cells, the researchers examined how ATP is made in membrane vesicles. These are cell membranes that are devoid of cytoplasmic material. Vesicles retain many of the functions associated with membranes including the ability to synthesize ATP. In addition, a definitive series of experiments were carried out to examine how sodium azide inhibited ATPase activity. ATP synthesis in vesicles was carried out using conditions that were physiological, unlike the earlier results reported.

The researchers observed that acidification of the bulk medium (so as to produce a gradient of hydrogen ions) resulted in the rapid synthesis of ATP, and that ATP synthesis was due to the imposition of that proton gradient since synthesis was inhibited by dicyclohexylcarbodiimide (a chemical that inhibits proton translocation) and carbonyl cyanide 3-chlorophenylhydrazone (CCCP) (which collapses the proton gradient). ATP synthesis was also inhibited by sodium azide but was unaffected by N-ethylmaleimide, an agent that reacts with thiol groups. This pattern of inhibition is characteristic of F-ATPases and unlike what is observed of V-ATPases. The inhibitory action of azide is complicated by its ability to act by collapsing the proton gradient as CCCP does, rather than by directly inhibiting the enzyme. If this were so, it would negate the conclusion that ATP synthesis occurs through an F-ATPase.

Therefore, an experiment was designed (elegant in its simplicity) using the distribution of the dye acridine orange to demonstrate that azide does not dissipate the proton-motive force. Observations were made of vesicles that took up acridine orange in response to a proton gradient, and that the presence of monensin (an agent that collapses proton gradients) prevented the uptake of acridine orange. When the same experiment was carried out in the presence of azide, the uptake of acridine orange was similar to

what was observed in the absence of the inhibitor. This result rules out the possibility that the action of sodium azide is indirect.

In conclusion, these physiological studies are consistent with the notion that ATP is not synthesized by the vacuolar-like ATPase found in the extreme halophiles and raises the question concerning the function of these enzymes. Furthermore, these results suggest that the enzyme associated with

ATP synthesis is similar to F-ATPases. This conclusion has important implications not only with respect to understanding energy metabolism in the extreme halophiles (and by extension the other Archaea) but also on the evolution of the ATPases.

Point of Contact: L. Hochstein
(415) 604-5938

New Prebiotic Synthesis of Amino Acids

Arthur L. Weber

Life maintains its existence by giving rise to offspring through reproduction. This reproductive process in contemporary life depends on the ability of DNA molecules to make copies of themselves (replicate), and the ability of protein molecules to speed up (catalyze) chemical reactions. Therefore, a central question about the origin of life is how the first replicating-catalytic molecules formed on the prebiotic Earth four billion years ago. Since the modern replicating molecule, DNA, is considered too complex to have been chemically made on the early Earth, the possibility is being investigated that the earliest life used very small protein molecules, called peptides, for both replication and catalysis. Peptides are good candidates for the earliest replicating-catalytic molecules, because they are constructed of very simple building blocks—amino acid molecules—that could have been made by chemical processes on the prebiotic Earth.

The approach used involves first analyzing how modern organisms make (biosynthesize) their constituent molecules. This knowledge of modern biosynthesis is then used to design experiments that simulate the chemistry of the prebiotic Earth that could have yielded biomolecules, such as amino acids and peptides. Our analysis of modern biosynthesis revealed that (a) amino acids are made primarily from sugar substrates, because only sugars contain enough energy to be converted directly to amino acids, and (b) the energy to make amino acids from sugars comes mainly from oxidation-reduction reactions.

In light of the above energy considerations that force modern life to make amino acids from sugars, researchers have started to investigate the pathway below that generates amino acids, and possibly peptides, from sugars under conditions that simulate the environment of the prebiotic Earth. So far, this model prebiotic pathway

Small sugars + Ammonia → Activated
amino acids → Peptide catalysts

has been shown to generate three amino acids (alanine, homoserine, and glycine) from small sugars under mild aqueous conditions at 40 degrees Celsius. This model of prebiotic amino acid synthesis has several attractive characteristics. It functions under mild aqueous conditions and employs oxidation-reduction reactions that resemble modern amino acid biosynthesis. Most importantly, it generates activated amino acids called thioesters that can spontaneously attach to one another to give peptide molecules, which could have been the first replicating-catalytic molecules. Other simulated prebiotic syntheses of amino acids do not produce activated amino acids, and usually require hydrogen cyanide—a molecule that is unstable in water.

Point of Contact: A. Weber
(415) 604-3226

Bonded Porous Layer Open Tubular Columns

Thomas C. Shen, Cindy X. Zhou

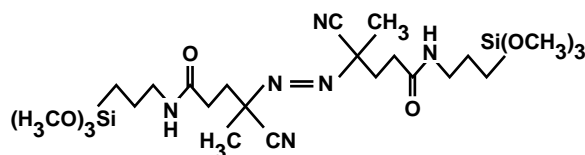
Gas chromatographic porous layer open tubular (PLOT) capillary columns exhibit high resolution and good reproducibility at flow rates and sample volumes that are compatible with flight mission requirements. However, the mechanical strength of these PLOT columns still poses a problem, as bleeding of the coating materials is found when a sensitive detector (that is, Ion Mobility Spectroscopy (IMS) or Metastable Ion Detector (MID)) or a high temperature is used.

A novel column preparation method, in situ polymerization, has recently been developed, but this method has not been able to make bonded PLOT columns reproducibly. Therefore, the purpose of the present efforts is to make strongly bonded in situ polymeric PLOT columns.

Bonded PLOT columns were previously prepared using hydrogen-sulfide (H-S)-bonded organosilicon as a free radical chain transfer site to polymerize divinylbenzene and form bonded porous polymeric particles. This process is not ideally reproducible, so our new preparation scheme involves the synthesis of an organosilicon compound containing an azo functional group, and then the bonding of this compound onto the inner surface of the stainless steel tubing.

The bonding process is done in three stages. First, the stainless steel columns are coated with a silica polymer to provide a link between the silicon and inner tubing surface. In the second stage, a specially

synthesized azo initiator with trialkoxysilyl groups is bonded to the silicon through the strong Si-O-Si bonds. Finally, the in situ polymerization technique is utilized to form the divinylbenzene porous polymeric particles that are bonded on the wall during the azo decomposition. The trialkoxysilyl-azo initiators are synthesized from azobis (cyanovaleric acid), oxalyl chloride, and 3-aminopropyltrialkoxysilane, and were identified by infrared spectroscopy, ^1H nuclear magnetic resonance, and elemental analysis (structure shown below).



The bonded in situ polymeric column was prepared with trimethoxysilyl-azo as the initiator and divinylbenzene as the monomer. Preliminary results suggest great improvement in mechanical strength, and no bleeding at temperatures below 150 degrees Celsius. These columns have shown good separation ability for the analysis of light hydrocarbons.

Point of Contact: T. Shen
(415) 604-5769

Ion Mobility Spectra of Unresolved Gas Chromatographic Peaks

Daniel R. Kojiro, Norishige Takeuchi, Maxine R. Shao

Gas Chromatographic (GC) detector research focuses on the development of new or the improvement of existing sensitive, miniaturized detectors, having both selective and universal response for gas chromatography. The focus of the research of GC detectors has been the Metastable Ionization Detector (MID). The flight prototype MID developed from this research and currently used in our laboratory

has an internal volume of 180 microliters and can operate over a concentration range of more than 10^6 .

Detector research of smaller detectors has produced Microvolume MID (μMID) having internal volumes of 12 microliters, with still smaller detectors being investigated. The small internal volume allows the μMID to operate at much lower carrier gas-flow rates than previous MID. These

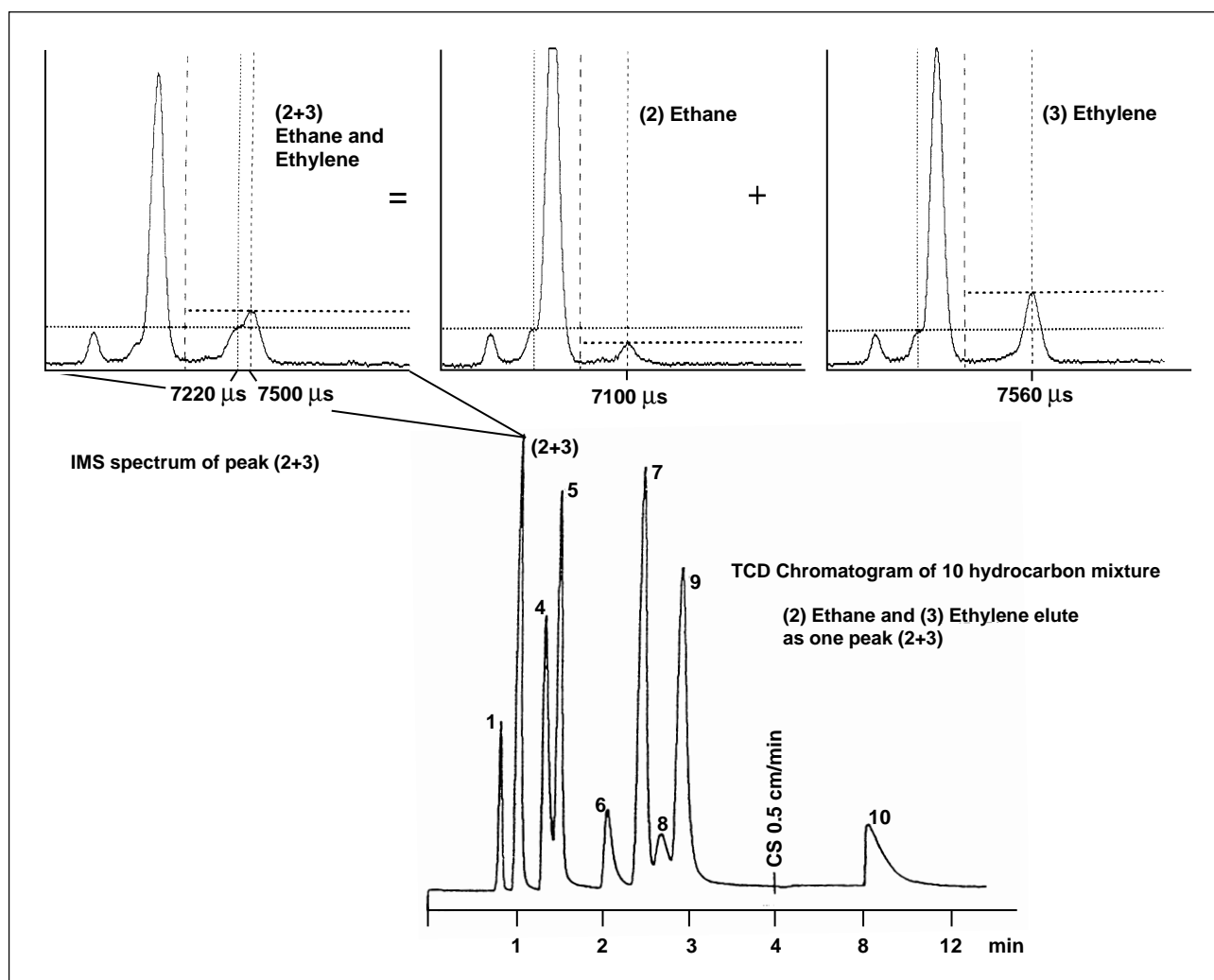


Fig. 1. Ethane and ethylene are unresolved in peak 2 (lower figure). IMS spectrum taken of peak 2 (upper left) shows the presence of both ethane and ethylene product ions from single component spectra (upper middle and right).

detectors, although tiny and highly sensitive, with wide response range and universal response, do not provide any sample identification information other than the GC retention time. The complex mixtures that may be encountered by exobiology flight experiments can place a heavy burden on the chromatographic column(s) to provide resolution of all species present. A GC detector providing sample identification independent of GC retention time can reduce the number of columns required for a given analysis as well as increase the analytical capability of the instrument.

To fulfill this sample identification role, the Ion Mobility Spectrometer (IMS) is being developed for use as a flight instrument. The IMS provides identifying spectra of sample components resulting from ionization of sample molecules and ion drift separation of the resultant sample ions. The flight prototype IMS uses very high purity dry helium and employs a reaction region/drift tube that is 2 centimeters \times 10 centimeters. Because conventional IMS systems use air or nitrogen drift gas, a helium-based IMS was a necessary development to use the helium required for the GC columns and MID. The dry helium also allows detection of many molecules that were not previously detected by conventional IMS.

The development of such flight instrument components also carries the burden of demonstrating

compatibility among the various components. New and advanced columns must not only perform the sample separations required, but must also be compatible with the advanced detectors. This often complicates matters since the detectors, such as the IMS and the MID, have very low tolerance to column bleed or any other source of carrier gas contamination. Sometimes, however, the detector eases the job of the column. In collaboration with Nori Takeuchi of TMA Norcal and Maxine Shao of the SETI Institute, one example of how the IMS fulfills this role has been demonstrated. A recently developed column prepared by incorporation of n-octyl and n-octadecyl groups on a siloxane skeleton provided quick separation of nearly all components of a ten hydrocarbon mix (see the figure). However, ethane and ethylene were not resolved at all (peak 2). Separate IMS analyses of ethane and ethylene alone produced the single component spectra shown in the upper right of the figure. Each component gives a unique product ion peak that can be seen in the IMS spectrum taken of the unresolved ethane/ethylene peak (shown upper left), demonstrating that both ethane and ethylene were contained in peak 2.

Point of Contact: D. Kojiro
(415) 604-5364

The Infrared Telescope in Space Experiment

Thomas L. Roellig

The Infrared Telescope in Space (IRTS) experiment is a joint National Aeronautics and Space Administration (NASA)/Institute for Space and Aeronautical Science (Japan's scientific space agency) project to perform a new astronomical survey of a significant fraction of the sky at infrared wavelengths. The IRTS was one of seven experiments

that flew on the maiden flight of Japan's reusable spacecraft bus, the Space Flyer Unit. The figure shows the location of the IRTS in the Space Flyer Unit spacecraft. This spacecraft was launched on March 18, 1995 from Tanegashima Space Center in Japan aboard a Japanese H-II expendable launch vehicle.

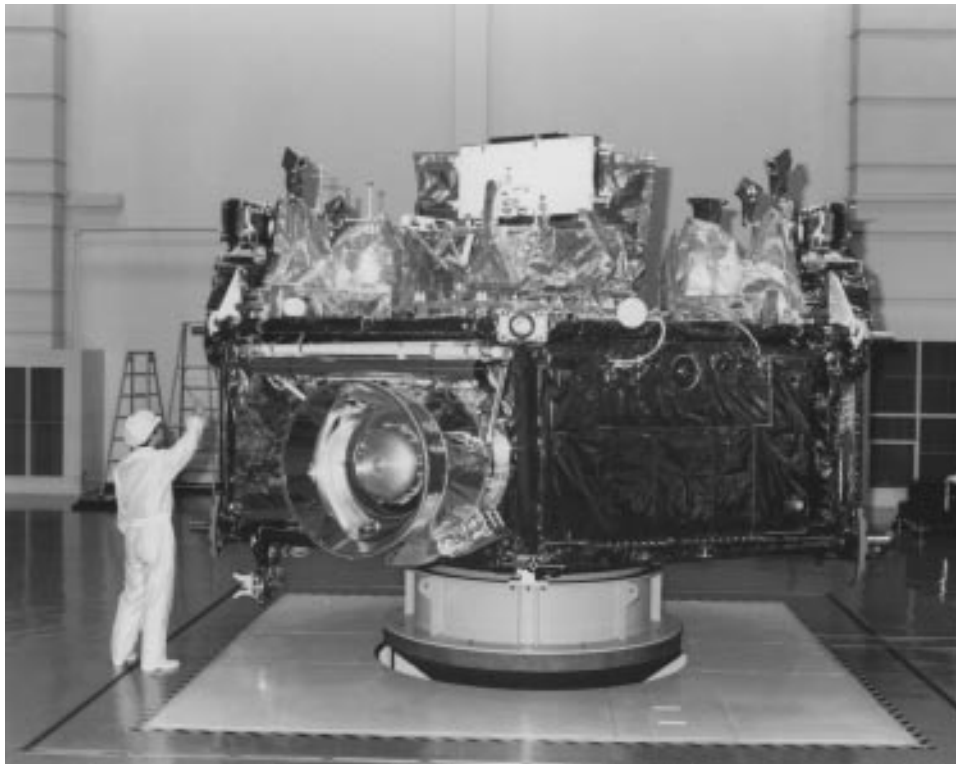


Fig. 1. The Infrared Telescope in Space mounted in the Space Flyer Unit spacecraft before integration into the launch vehicle. The telescope can be seen next to the worker. The telescope aperture is covered until the spacecraft has reached operational altitude. (Photo courtesy of the Institute for Space and Astronautical Science, Japan).

The Infrared Telescope in Space experiment was specifically optimized for very high infrared sensitivity. This included cooling the telescope optics with 100 liters of super-fluid liquid helium to less than 1.8 degrees centigrade above absolute zero. The liquid helium carried on board lasted for 38 days after launch before it was finally exhausted, which was slightly longer than expected. During this time period, the IRTS was able to perform an infrared survey of approximately 8% of the sky, which was sufficient to sample representative objects from all of the different regions in our galaxy. In order to carry out this survey, the IRTS employed four scientific focal-plane instruments to analyze the light collected by the telescope: a near-infrared spectrometer, a mid-infrared spectrometer, a far-infrared line mapper, and a submillimeter photometer. Throughout the duration of the IRTS mission, data from all the instruments was sent to the ground and was received using both NASA's Deep Space Network and Japan's own telemetry link system.

The Mid-Infrared Spectrometer (MIRS) instrument on the IRTS was developed in a collaboration between Ames Research Center and the University of Tokyo. During the course of the IRTS portion of the Space Flyer Unit mission, the MIRS continuously observed the infrared sky within a wavelength range of 4.5 to 11.7 microns and at a spectral resolution of approximately 0.3 micron. This instrument also detected approximately 20,000 discrete objects, in addition to making the measurements of the diffuse extended regions that were its primary design goal. The cold telescope optics, advanced infrared detectors, and the wide field of view allowed the MIRS to make these observations of the diffuse regions with sensitivities 1,000 times better than any previously obtainable.

**Point of Contact: T. Roellig
(415) 604-6426**

Excitation of the Arched Filaments near the Galactic Center

Sean W. J. Colgan, Edwin F. Erickson, Janet P. Simpson, Michael R. Haas, Mark Morris

The region immediately north of the center of our Galaxy contains long, remarkably thin, straight filaments of ionized gas that cross the plane of the galaxy at right angles. Their radio continuum emission is polarized, indicating the presence of large magnetic fields. At the northwestern tip of these linear filaments, they appear to be joined by a system of filaments curving back toward the galactic plane and the galactic center. These "arched" filaments emit radio continua indicative of ionized hydrogen, but without the usual accompanying signposts of massive star formation. The morphology of the straight and arched filaments seems to indicate that they are connected. The excitation mechanisms responsible for the emission from both sets of fila-

ments is controversial and include a variety of models invoking shocks and/or magnetohydrodynamic (MHD) interactions resulting from collisions between molecular clouds and strong magnetic fields, as well as simple photoionization by hot stars.

Using the Kuiper Airborne Observatory, observations were made of the far-infrared emission from eleven positions along a strip crossing two of the arched filaments. The measurements included six lines (one line each from neutral oxygen, singly ionized silicon and carbon, doubly ionized sulfur, and two lines from doubly ionized oxygen) and the 30- to 160-micron infrared continuum.

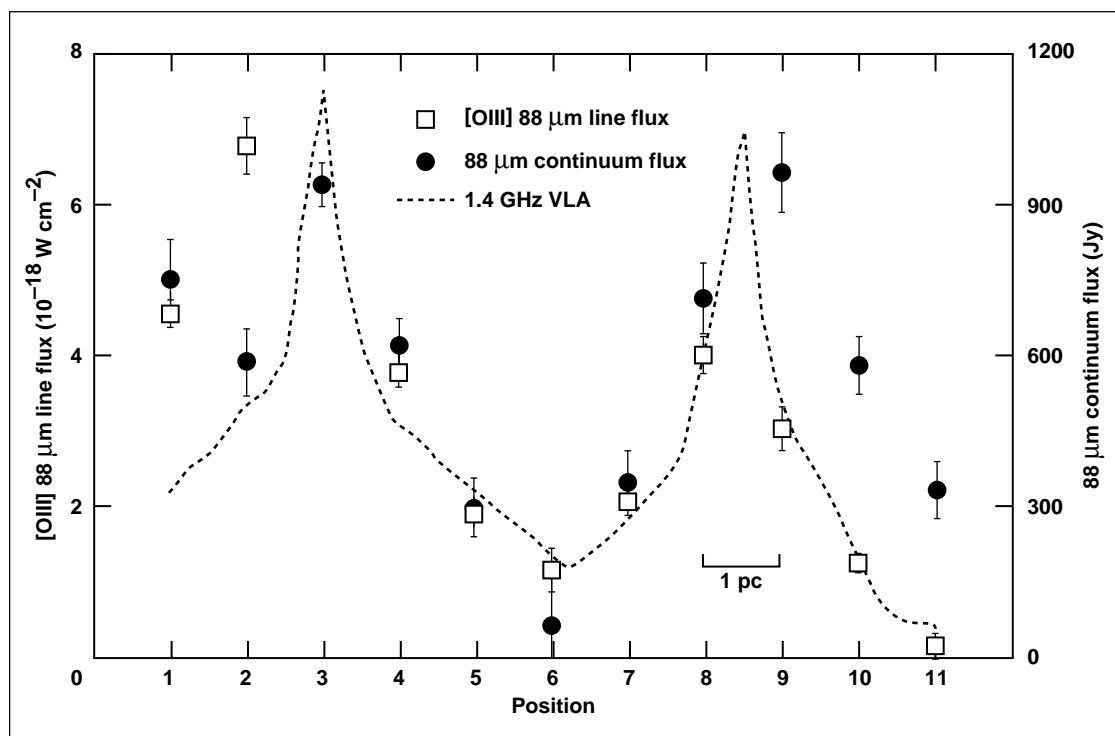


Fig. 1. The line flux from doubly ionized oxygen ([OIII]) at 88 microns (hollow squares) and the continuum at 88 microns (solid squares) are plotted as a function of position across the filaments. The location of the radio filaments is delineated by the sharply peaked radio continuum (dotted line).

The fact that the line and continuum emission strongly peak near the radio-continuum peak demonstrates that the same excitation source must be responsible for the line, the radio, and the infrared continuum emission (see the figure). The peak far-infrared luminosity and line intensity associated with the filaments poses difficulties for shock and MHD models. Photoionization by a quasi-uniform distribution of massive stars provides the most plausible excitation source for the arched filaments. A detailed examination of the data suggests that there is a

substantial contribution from a photoionizing source to the east (lower position number in the figure). Unlike the canonical situation found in many star-forming regions, the far-infrared luminosity and the singly ionized silicon emission appear to originate predominantly in the ionized gas.

Point of Contact: S. Colgan
(415) 604-0420

Studies of Interstellar Matter and Gaseous Nebulae

Robert H. Rubin

Observations were made by a Hubble Space Telescope (HST) team of investigators from several institutions. They were able to use two instruments simultaneously to observe the Orion Nebula. Using the Faint Object Spectrograph (FOS), parallel, coordinated Wide Field and Planetary Camera (WFPC2) images were obtained. Parallel FOS spectra were observed at the same time using WFPC2 primary imaging.

Observations were made on the Orion Nebula program with HST using the Goddard High Resolution Spectrograph (GHRS). These observations were made for eight orbits and comprised four separate bandpasses of approximately 40 angstroms. Observations also were made using the FOS and the WFPC2 in parallel for six orbits.

The results were very gratifying. For instance, in the earlier Cycle 3 HST observations of the Orion Nebula, the N II] 2142 angstrom line was identified. This was the first measurement of the line in an H II region. Actually, this is a doublet transition (that is, there are two lines). With GHRS, these components are clearly resolved with relative intensities close to what is expected theoretically. This is by far the best astronomical spectrum of these lines. The [O II] 2471 angstrom line also was observed with GHRS at the same position/aperture. The N/O abundance ratio can be addressed from the relative intensities of these lines. They will provide a new assessment of the important N/O abundance in Orion. The N II] 2142/[O II] 2471 ratio provides a direct measure of N^+/O^+ that is less sensitive to uncertainties in electron temperature, electron-temperature fluctuations, or extinction, compared with previous methods.

An important ingredient in the photoionization modeling code (NEBULA) is the ionizing flux from

hot stars that excite nebulae called H II regions—regions where stars are forming. Further collaboration with the Max Planck Institut für Extraterrestrische Physik led to including the influence of line blocking, with a detailed iron line treatment on the hot stellar atmospheres/winds and the emergent ionizing flux.

Together with the German scientists, a paper was written entitled “An Explanation for the [Ne III] Problem in H II Regions.” This refers to a persistent problem that was found when matching certain observed nebular emission line fluxes with photo-ionization models of H II regions. It is called the [Ne III] problem because the H II region models predict significantly less flux in the [Ne III] lines than is measured. Most of the data were taken with the Kuiper Airborne Observatory. The problem was resolved successfully by showing that more realistic stellar atmosphere models produce many more photons capable of creating Ne^{++} , and that when these are used in nebular models, the predicted line fluxes match the observed data very well.

Two Kuiper Airborne Observatory flights were made in August 1995. On the first flight, observations were made of the Seyfert/starburst galaxy NGC 1068, and on the second flight, three bright PNs, NGC 6210, NGC 6543 (Cat’s Eye nebula), and NGC 7027. From the observations of the [O IV] 25.9-micron line in NGC 7027, a measurement of the best wavelength can be made. This is a valuable contribution to atomic physics knowledge in that it is the best direct determination of the energy level separation of the states involved in the transition.

Point of Contact: R. Rubin
(415) 604-6450

Molecular Opacity Databases for Titanium Oxide and Water

Stephen Langhoff, David Schwenke, Harry Partridge

The titanium oxide (TiO) and water (H_2O) molecules play a dominant role in the opacity of M-type stars throughout the visible and near infrared. Thus, there has been considerable effort to determine accurate opacity databases for these two molecules. Quantum mechanical calculations are essential to this effort, because it is not possible to account for the tens of millions of lines that are present at stellar temperatures by experimental means. Theory offers the possibility of obtaining complete opacity databases, if the potential energy and transition moment (or dipole moment) surfaces can be determined with sufficient accuracy. Ab initio quantum mechanical methods have been used to obtain quantitative opacity databases for TiO and water. For the TiO molecule, all dipole-allowed transitions out of the ground triplet delta and low-lying singlet delta states have been studied. The calculated radiative lifetimes for the excited states agree very well with the recent laser-induced fluorescence studies carried out under

collisionless conditions in a molecular beam. The calculated oscillator strengths, however, are generally smaller than those being used in astrophysical studies. The exception is the delta-band system, where our calculated oscillator strength is twice that estimated from previous laboratory studies.

Considerable effort has been devoted to constructing a globally correct potential energy surface for the ground electronic state of the water molecule. Quantum mechanical calculations themselves are not capable of generating a potential energy surface (PES) of spectroscopic accuracy. The procedure that is followed is to determine the energy at a discrete set of geometries and then fit these to analytical form. The form of the potential is then adjusted empirically to match known line position, for example, those in the HITRAN database. For this procedure to give a quantitative PES capable of describing the H_2O molecule to near its dissociation limit, it is necessary to have ab initio data at all representative points on

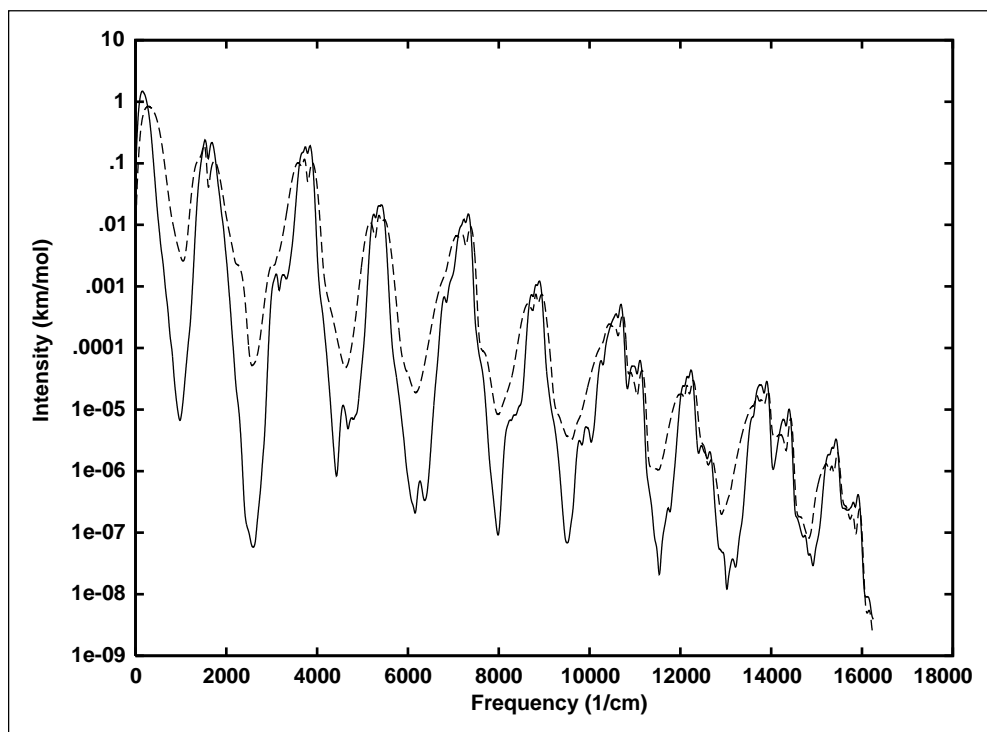


Fig. 1. The spectra of water vapor at 296 kelvin (solid line) and 1000 kelvin (dashed line).

the surface, to have an accurate analytical fit to the discrete energy points, and to have accounted for all differential energy effects, such as core-valence electron correlation that effects the shape of the potential. An empirical surface was constructed in this manner that describes all the energy levels in the HITRAN database with total angular momentum less than or equal to five with a root-mean-square deviation of about 0.044 centimeter^{-1} . The empirically corrected PES is believed to be of quantitative accuracy at all energies up to 35,000 centimeters^{-1} . Using the above PES and an analytical representation of our dipole moment surface, the transition intensities and energies were obtained using a variational procedure with the vibrational wave functions represented by linear combinations of analytical basis

functions. The exact kinetic energy operator is used in all calculations.

The water spectra at 296 kelvin and at 1000 kelvin based on this new potential are shown in the figure. The most intense peak corresponds to pure rotational transitions in the (000) band, the second peak to transitions in the (010) band, and so forth. At 296 kelvin, the spectra show a characteristic band structure that can be associated with the different normal modes. As the temperature increases to 1000 kelvin, the valleys become less pronounced, but still the bands can be clearly differentiated. At still higher temperatures the structure is less apparent.

Point of Contact: S. Langhoff
(415) 604-6213

Water as an Opacity in Stellar Spectra

Duane F. Carbon, David Goorvitch

Two new preliminary theoretical water (H_2O) line lists, one computed by D. W. Schwenke (Ames Research Center) and the other by R. T. Wattson (Steward Radiance Laboratory, Utah State University) have been carefully evaluated. The two independent lists differ considerably since they were generated with very different line intensity cut-off criteria. Nevertheless, by comparing the subset of transitions held in common by the two lists, we have found generally good agreement in the theoretical line positions (within 0.5 centimeters^{-1}) and oscillator strengths (gf values), most within 20%, with some differences ranging up to 100%. The differences appear to be largely traceable to differences in the molecular potential adopted by the two investigators.

The good agreement between these two independently generated lists has provided confidence in these theoretical computations and encouragement to begin a systematic comparison with stellar spectra. A series of high resolution spectra for typical cool giants and dwarfs over the spectral region from 1.0 to 4.2 microns has been synthesized. This interval was chosen because it spans the flux peak of cool stars; has strong H_2O bands; and, in the portion outside the

terrestrial H_2O bands, is accessible at high resolution from ground-based observatories.

An important result of this work stems from synthesis using model parameters characteristic of Alpha Tau, a cool giant that was studied extensively in another investigation. Although Alpha Tau (effective temperature = 3920 kelvin) is generally regarded as too hot for water vapor opacity to be important in its spectrum, the synthetic spectra based on the new line lists show quite extensive H_2O blanketing in this star, primarily, but not exclusively, in the regions blocked from view by the terrestrial H_2O . This result is significant because it indicates that the H_2O opacity contribution must be taken into account at higher effective temperatures than has been traditionally the case when computing model atmospheres. It is suspected that this has not been recognized earlier because of large, systematic errors in the comparatively primitive H_2O opacities hitherto available to modelers.

Point of Contact: D. Carbon
(415) 604-4413

Spectral Flux Standards for Infrared Astronomy

Fred C. Witteborn, Martin Cohen, Diane H. Wooden

Infrared spectra of bright stars and the asteroid Ceres that were obtained from the Kuiper Airborne Observatory (KAO) in 1995 completed three years of effort to provide celestial calibration flux standards at resolving powers of 100 to 200 and at wavelengths from 3 to 30 microns. These standards are required for calibration of mid-infrared spectra obtained from space observatories such as the Infrared Space Observatory, the Midcourse Space Experiment, and the Infrared Telescope in Space. They are also useful for calibrating astronomical spectra taken from airborne and ground-based observatories. The utility of a celestial standard is that it can be observed through the same optical path as the celestial object of interest, thus eliminating the need to correct for telescope transmission, instrument sensitivity variations across the spectrum, and atmospheric transmission (in the case of ground-based and airborne observations).

Of the three approaches to absolute calibration that were tried, the easiest and most reproducible observationally is to choose a good, theoretical, stellar radiation model for the simplest, most well-understood stellar atmosphere and make that star the primary standard. All other celestial standards are established by ratioing the measured spectrum of the secondary standard to that of the primary standard.

Robert Kurucz of the Smithsonian Astrophysical Observatory has produced theoretical spectra of Sirius and Vega, both bright stars near 10,000 kelvin. Their surface emissions are dominated by atomic hydrogen continua spectra (and well-understood line emission) that are not distorted by molecular absorption. Vega is surrounded by a thin dust cloud, which becomes noticeable at wavelengths above 15 microns, so Sirius was chosen as the primary standard.

It is important to have bright standards in many parts of the sky so that they are readily accessible for use by observatories. (Space telescopes have tight viewing constraints set by their sensitivity to off-axis sources such as the Sun and Earth and by their

restricted slewing capabilities.) The brightest infrared stars are usually giant (evolved) stars with cool atmospheres whose spectra are complicated by the presence of carbon monoxide (CO) and silicon monoxide (SiO). Measurements from the KAO have been used to establish the depths of CO and SiO spectral absorption features over a wide range of stellar temperatures (10,000 to 3,800 kelvin), so that there are 11 useful spectral-flux standards. When combined with data from other observatories, these standards are good from 3 to 30 microns with accuracies of about 3 percent.

The dependence of the primary standard on a theoretical model makes an alternative approach to calibration desirable. Two other types of absolute spectral-flux standards have been used: asteroid models and laboratory blackbody standards. During the past year, improvements have been made in the ability to use such standards.

High signal-to-noise spectra of Ceres (from 4.9 to 30 microns) were obtained. Unfortunately, spectral models of asteroids lack detailed information on surface composition, so they do not yield the high precision of hot stellar models. Asteroid models must be determined for the varying solar distance and earth distance and sometimes for variations in shape or other features that rotate into view. The only big advantage of the larger asteroids is their brightness at long wavelengths.

Laboratory blackbodies would seem to be the ideal calibration standards. Temperatures can be controlled to a millikelvin and emissivities kept between 0.999 and 1.000. Unlike the use of stars and asteroids, however, the atmospheric transmission, the telescope transmission, foreground brightness effects, and optical coupling effects are not automatically duplicated in the calibration of a celestial object against a laboratory standard. Good empirical and theoretical data exist for the atmospheric corrections. A temperature-controlled, optical coupler was built

between an excellent blackbody standard and a spectrometer for calibrating the latter across its entire spectral range. A new collimated infrared source has been used on individual optical elements of the KAO to give preliminary measurements of telescope transmission which are encouraging. Laboratory-

calibrated spectral shapes have been achieved that are within 20% of those based on stellar models with the expectation of further improvements.

Point of Contact: F. Witteborn
(415) 604-5520

Radiation-Environment Testing of Focal-Plane Sensor Arrays

Mark E. McKelvey, Robert E. McMurray, Jr., Craig R. McCreight

The development of focal-plane detector array technology that will allow reliable background-limited operation in the radiation environment found in earth orbit is a key requirement for successful infrared (IR) astronomy from space-based platforms such as the Space Infrared Telescope Facility (SIRTF). A team at Ames Research Center is evaluating the performance of a number of detector and readout-device technologies to determine their suitability in space-IR astronomy applications.

Impurity Band Conduction (IBC) focal-plane detector arrays produced by several manufacturers are potential candidates for applications in the 5–30 micrometer wavelength range. IBC detectors rely on a thin, highly doped, IR-active layer to provide high quantum efficiency from a small detector volume, minimizing the ionization cross-section for cosmic ray events. A high-purity blocking layer keeps the high doping levels in the IR-active layer from resulting in excessive dark current. IBC arrays also exhibit wider spectral response than alternative photoconductor (PC) architectures, without many of the anomalies associated with PC devices. IBC architectures are well suited to modern epitaxial fabrication methods, and the technology has progressed to the point where large-format, hybrid focal-plane arrays (FPAs) sensitive to IR wavelengths as long as 28 micrometers can be reliably produced.

Work in FY95 was concentrated on evaluating the performance of state-of-the-art, large-format (to 256×256 detector elements) IBC detector arrays in simulated on-orbit radiation environments. Inputs from the astronomy and manufacturing communities have been assembled to produce a test program that

can provide meaningful data on how these devices can be expected to perform in their intended application.

Our program uses the 76-inch Crocker Cyclotron on the campus of the University of California at Davis to provide a high-energy proton beam for device testing. Three field-test runs over the last twelve months have yielded data on devices from Hughes Aircraft Company and Rockwell International, including prototype arrays for the Wide-Field Infrared Explorer (WIRE) satellite, and the first proton tests of a large-format, antimony-doped IBC detector array. These tests featured strong cooperation with astronomers from Cornell University and the University of Arizona.

Preliminary evaluation of the test data show dose-dependent activation of dark current that could be of crucial importance to WIRE and SIRTF science missions. The results of the Ames tests on devices from multiple vendors are being fed directly back into the manufacturing process in order to help advance the state of the art.

Other recent efforts involve measurements of optical crosstalk and persistent image problems in large-format IR detector arrays. A spot-scanning optical system has been constructed and is being used to measure device resolution limitations in observation of point-source objects. Continuous software development has provided improved test flexibility, automation, and repeatability.

Point of Contact: M. McKelvey
(415) 604-3196

Stratospheric Observatory for Infrared Astronomy Simulated in Cruise Flight

Karlin Roth, G. R. Srinivasan

Stratospheric Observatory for Infrared Astronomy (SOFIA) is a planned, 2.5-meter aperture, Cassegrain telescope with a Nasmyth focus which will be housed in a Boeing 747 aircraft operating at altitudes from 41,000 to 46,000 feet. It will be a follow-on mission to NASA's Kuiper Airborne Observatory. SOFIA development and operations are funded jointly by NASA and Deutsche Agentur fuer Raumfahrtangelegenheiten (German Agency for Space Flight Affairs).

Although this observation telescope, which is housed in an airborne platform, offers many advantages over land-based systems, it also poses problems of a different nature. Experimental observations have shown that the telescope-housing cavity causes complex unsteady flow that is difficult to control. Specifically, observations show shear-layer oscillations accompanied by high noise levels. Without flow control in the cavity to decrease unsteadiness, the high levels of turbulence in the shear layer would limit the clear see-through vision of the telescope, decreasing its capability. Additionally, the flow unsteadiness of a resonant cavity affects aircraft fatigue life and the control surface effectiveness.

Unsteady, three-dimensional, computational simulations for SOFIA are made not only to complement the experimental test program but also to provide a database that is difficult to measure in a wind-tunnel test. The computational objectives are to aid in the design of an acoustically quiet telescope cavity and to understand the flow physics of the three-dimensional cavity.

The numerical method solves the thin-layer, Reynolds-averaged, Navier-Stokes equations on an

overset grid system using the OVERFLOW code. The flow domain is discretized using 45 grid zones containing a total of 4.1 million points.

Simulations were done with and without a cavity and at the free-flight cruise and wind-tunnel conditions for Boeing 747-200 and 747-SP platforms. Several unsteady flow quantities were extracted from the computed simulations, including time-averaged surface pressures on the empennage, sound pressure levels and power spectra within the cavity and on the telescope, unsteady loads and moments of the telescope, and incremental drag change because of the cavity. The numerical results showed good agreement with most of the experimental data except for the cavity noise levels that were underpredicted by 4–8 decibels. The chief findings from the computations are that (1) either the 747-SP or the 747-200 platform could be used; (2) the impact of the cavity on the control surface effectiveness is minimal; and (3) the drag increment due to the open cavity reduces the time of flight by about 2 hours.

The figure (see Color Plate 22 in the Appendix) shows a picture of the unsteady surface pressures for the full aircraft at the free-flight cruise condition. The color map ranges from 1.0 (top) to –1.3 (bottom). The cavity aft bulkhead region is seen as a region of high pressure followed by a small flow expansion region on the ramp of the cavity aperture.

**Point of Contact: K. Roth/G. Srinivasan
(415) 604-6678/4478**

Organic Signatures in the Interstellar Medium

Yvonne Pendleton

New telescopic observations of the interstellar medium (ISM), the space between the stars, have revealed additional differences in the dust absorption features between regions of differing interstellar dust densities. Those features which are exclusively associated with “processed” interstellar ice material, the 3.4 micrometer hydrocarbon absorption band and the 4.62 micrometer nitrile absorption band, reside in very different regions of space. The incorporation of organic material from the ISM into primitive solar system objects provides a link between the very early stages of planet formation and the present solar system. Therefore, a more complete understanding of the formation, destruction, and distribution of organic material on dust grains in the interstellar medium will aid in understanding how such material became incorporated into planetary systems like our own. The possibility that these basic building blocks played a role in the origin of life on Earth is not an insignificant one, and if the delivery of organic molecules was important to the early Earth, it stands to reason that it would also be important in the development of life elsewhere.

The 3.4 micrometer band, attributed to chains of hydrocarbons (saturated aliphatics), is found exclusively in regions of the diffuse interstellar medium. The diffuse ISM has a lower density ($n \sim 100$ particles per centimeter³) and higher temperature ($T \sim 100$ kelvin) than the dense molecular cloud regions where star formation occurs. Dust grains in dense clouds ($n \sim 10^6$ – 10^8 particles per centimeter³; $T \sim 10$ – 30 kelvin) accrete icy mantles which may be processed thermally or by ultraviolet or cosmic rays. The resulting organic material seen in the dense clouds does not reveal the same type of hydrocarbon substructure seen in the diffuse dust sight lines. This is puzzling, given the strong possibility that the hydrocarbons are produced in the dense cloud regime in the icy grain mantles. However, even if the hydrocarbons are produced in the diffuse ISM

itself, it is difficult to understand how the feature can be absent from the dense cloud sight lines because the cycling times for interstellar grains between the diffuse medium and the dense molecular clouds is short enough to allow adequate mixing of the two environments. It is worth noting that the hydrocarbon feature has now been detected along more than a dozen different sight lines through our galaxy and in four other galaxies. Therefore, it is a ubiquitous and hardy component of the interstellar medium and is available for incorporation into star and plant forming clouds.

In the dense clouds, another organic signature is seen at 4.62 micrometers. Laboratory experiments of ultraviolet-processed ices reveal that nitriles of various types produce a similar band near 4.62 micrometers. The exact peak of the nitrile feature varies slightly depending on the sight line observed, therefore an exact identification of the band has not been made. It is commonly called the X-C \equiv N band. The same laboratory ice mixtures that result in an organic residue that closely matches the diffuse medium 3.4-micrometer feature can also produce the X-C \equiv N band, so it seems likely that ultraviolet processes are important in the production of both of these organic signatures.

In the past year, the discovery was made that the X-C \equiv N band does not seem to be present in the molecular cloud dust when viewed through a cloud to a bright background source. In this case, the background star is unassociated with the molecular cloud, but it serves as a luminous source against which the large column density of dust can be viewed. In contrast, we have now detected the X-C \equiv N band toward several embedded protostars (stars which are associated with the dense molecular cloud). The absence of the feature along sight lines toward the background stars suggests that the carrier of the band dust does not reside in the intracloud

material. The presence of the feature toward luminous, embedded protostars suggests that production of the band may require close proximity to the protostar. The absence of the 4.62 micrometer band along sight lines through the diffuse ISM (where the hydrocarbon 3.4-micrometer feature is seen) seems to be consistent with the requirement of close proximity to an exciting source. The absence of the hydrocarbon feature in the dense clouds remains difficult to understand.

As researchers attempt to piece together the puzzle of interstellar dust evolution from the dense molecular clouds to the diffuse interstellar medium, they must analyze the physical processes that govern the formation and the destruction of icy grain mantle material.

Point of Contact: Y. Pendleton
(415) 604-4391

Identifying Stardust—Interstellar Nitrogen and Oxygen

Lou Allamandola, Scott Sandford, Max Bernstein, Robert Walker, Jamie Elsila

Experimental studies of materials produced under conditions similar to those in planets, comets, and interstellar space are carried out to provide the fundamental data needed to design future space missions, to interpret the measurements made with existing NASA telescopes and satellites, and to determine the characteristics of materials under extreme conditions. The principle goals are to: (1) identify the materials present in space, (2) determine the materials' role in the chemical evolution of the interstellar medium and the solar system, and (3) understand how these materials influence the physical and radiative properties of their environment.

Some of the latest results in the understanding of the composition of interstellar and cometary ices are reported here. These concern the long-sought-after disposition of interstellar nitrogen and oxygen in the denser regions of interstellar space, the birthplace of stars and planetary systems. After hydrogen, the most abundant elements in the universe are oxygen, carbon, and nitrogen. The distribution of both hydrogen and carbon are reasonably well understood. This is not so, however, for nitrogen (N) and oxygen (O). Indeed, these elements have been speculated about rather vigorously during the past decade. While their high abundance imply that they

must be important players in many interstellar and solar system phenomena, their disposition remains unknown. Thus, identifying the chemical forms they are in is very important.

Two potentially very important carriers of these elements are N_2 and O_2 . Unfortunately, these species cannot be detected by the spectroscopic techniques normally used to probe the composition of matter in space. However, if present in the cold, dense regions of interstellar space, some of these molecules will be frozen in ice. Their presence in ices will influence the spectral fingerprints of other species frozen in the same ice. A series of very sensitive experiments were performed in order to determine the spectral influence of these species on carbon monoxide (CO), a well-known interstellar ice constituent. The experiments focused on frozen CO since it has a very distinct infrared spectral fingerprint, one which has not been satisfactorily reproduced in spite of more than ten years of very active research by observers, experimentalists, and theoreticians.

The first in-depth study of the influence of O_2 and N_2 on the frozen CO fingerprint has been carried out. A comparison of the interstellar CO band with the band produced in laboratory ices of N_2 , O_2 , H_2O ,

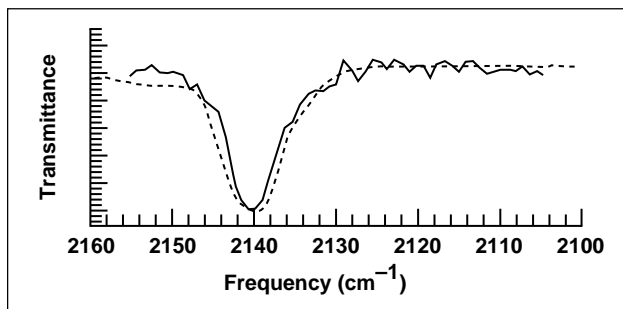


Fig. 1. The remarkable match between the infrared absorption produced by interstellar frozen CO (thick line), and the absorption produced by a laboratory ice comprised of N₂, O₂, CO₂, H₂O, and CO (dotted line). Previous attempts involving pure solid CO or CO frozen in simple ices containing species such as H₂O or CO₂ produce bands which are too narrow and which do not peak at 2140 centimeters⁻¹. The quality of the fit provides strong evidence that interstellar ices contain O₂ and N₂.

CO₂, and CO is shown in the figure. These laboratory ices provide the best match to the interstellar feature that has ever been achieved. In fact, it is so good that the uncertainties in the match are less than the uncertainties associated with the astronomical observations introduced by the relative motion of the solar system with respect to interstellar space. The excellent agreement shows that N₂ and O₂ are essential ingredients of interstellar ices. Researchers estimated that 30% to 40% of the cosmic N and O available are in the form of frozen N₂ and O₂.

This result gives great insight into the chemical and physical nature of the interstellar medium and sheds light on the materials from which the early solar system and comets formed.

Point of Contact: L. Allamandola/S. Sandford
(415) 604-6890/6849

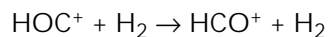
Gas-Phase Reactions in the Interstellar Medium

David E. Woon, Gilda H. Loew

Interstellar clouds are vast collections of dust and molecules that exist between stars. To date, over 100 molecules have been conclusively identified in various astronomical objects. These molecules and any others that may also be present are subject to a complex chemistry that alters the abundances of individual species over time. Theoretical models that incorporate hundreds of species and thousands of reactions are used to predict the abundances, but the predictions are only as reliable as the accuracy of the rates and the completeness of the models. The techniques of *ab initio* molecular orbital theory are uniquely suited to provide this vital information.

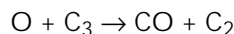
Two examples of the usefulness of these techniques are described: the first explains the recent detection of an unexpected interstellar species, and the other explores a proposed mechanism that may impede the growth of long carbon-chain species.

In 1995, the existence of HOC⁺ in Sgr B2 and other sources was confirmed. This was unexpected given that the HOC⁺ isomer is somewhat less stable than HCO⁺, and the hydrogen-catalyzed process



was thought to be fast enough to quickly destroy any HOC^+ that might form even at very cold temperatures. However, reexamination of the energetics and reaction rate of this process with very accurate methods found a barrier of 1.4 kilocalories per mole (see the figure). The resultant rate indicates slow destruction of HOC^+ at temperatures below 100 kelvin, explaining the presence of this isomer in concentrations large enough to be detectable in the interstellar medium.

The second study tested the hypothesis that some carbon-chain species may be vulnerable to attack by atomic oxygen. When small species are easily destroyed, growth of increasingly longer chains is seriously impeded. The concern about oxygen attack is based on measured rates for other neutral-neutral reactions that are sufficiently rapid at temperatures below 100 kelvin to be included in the interstellar cloud models. In this study, the reaction



was examined. A detailed investigation of the energetics and kinetics of this reaction led to the conclusion that it would be very slow over a wide temperature range because of a barrier of 2.1 kilocalories per mole. The implication is that C_3 and other C_n species with an odd number of carbons are stable when exposed to oxygen and may participate in other reactions that lengthen the chain. Whether other carbon-chain species are also able to resist attack by oxygen and by other atoms and radicals needs to be investigated.

Point of Contact: S. Chang
(415) 604-5733

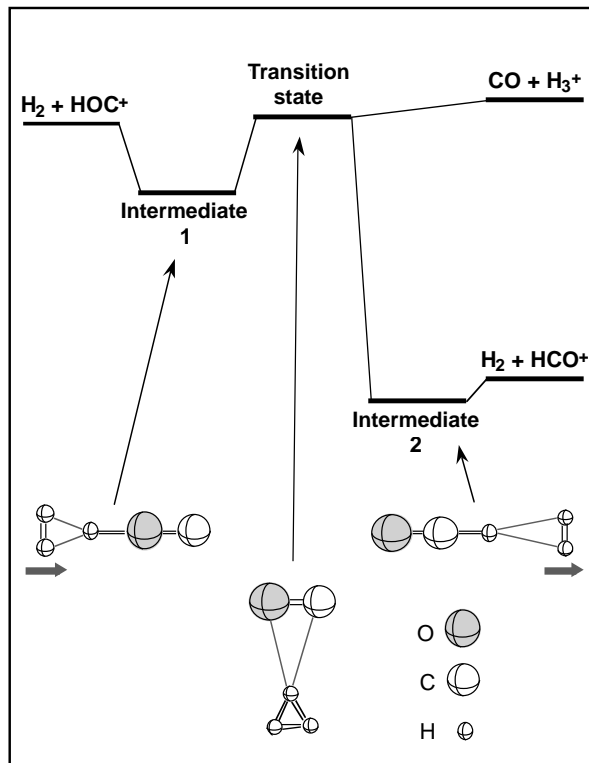


Fig. 1. Energy diagram for the $\text{H}_2 + \text{HOC}^+$ reaction. Two final product channels are shown, $\text{H}_2 + \text{HCO}^+$ and $\text{CO} + \text{H}_3^+$. The H_2 molecule approaches the H end of HOC^+ to form intermediate 1. The three H atoms then move in concert around CO. The transition state is essentially a weakly bound $\text{CO} \cdots \text{H}_3^+$ complex.

Complex Organics and the 3.4 μm Emission of The Orion Bar

Max Bernstein, Scott Sandford, Louis Allamandola, Robert Walker, Greg Sloan

The “unidentified” infrared emission from H II regions, reflection nebulae, and other objects, where ultraviolet radiation impinges on cold, dusty material, has been the subject of numerous observations and theories. Perhaps the best known source of such emission is The Orion Bar region, which was the subject of a recent study at 3 micrometers. While the main feature in the 3-micrometer region has been attributed to a type of robust organic molecule called polycyclic aromatic hydrocarbons (PAHs), the other features in this spectral neighborhood exhibit a different spatial distribution and seem to derive from a different (but perhaps similar) carrier. The figure shows laboratory spectra of an H_n -PAH (polycyclic aromatic hydrocarbon bearing extra hydrogen atoms) and compares it with the 3.4–3.6-micrometer emission from The Orion Bar, demonstrating that H_n -PAHs are very attractive candidates for the carriers of the 3.4–3.6-micrometer emission.

Point of Contact: M. Bernstein/G. Sloan
(415) 604-0194/5495

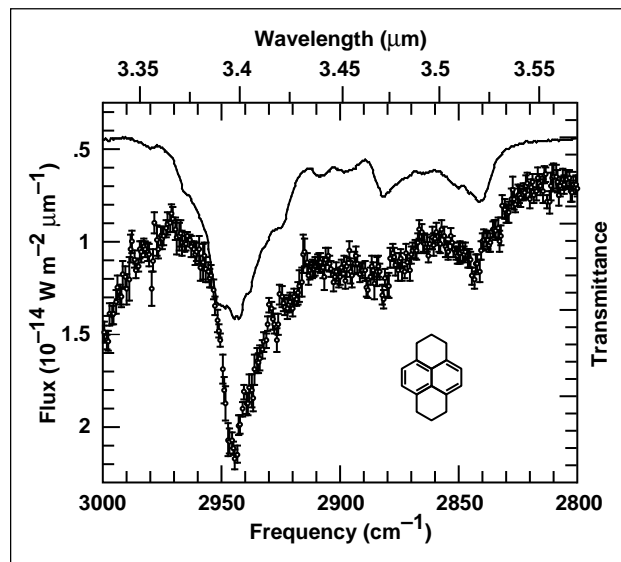


Fig. 1. A comparison between the lab spectrum of hexahydropyrene (a typical H_n -PAH) isolated in an argon matrix at 12 kelvin (solid line) and the corresponding infrared emission from The Orion Bar (error bars). This is the best astronomical spectrum of The Orion Bar, and its striking similarity to the laboratory data suggests that H_n -PAHs are the carriers of the 3.4–3.6-micrometer emission from The Orion Bar.

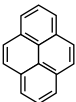
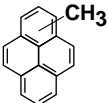
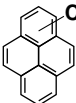
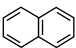
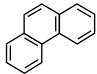
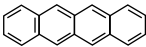
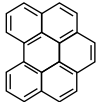
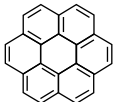
Ultraviolet-Near Infrared Spectroscopy of Organic Dust Analogs

Farid Salama, Louis Allamandola, Christine Joblin, Robert Walker

Understanding the origin, properties, and distribution of the biogenic elements in the universe is essential in Astrobiology. One of the major research areas under way in the Astrochemistry Laboratory at Ames Research Center is the study of the effects induced by ultraviolet (UV) photons on the building blocks of interstellar and planetary organic materials. The objective of this research is to provide quantitative information which is relevant for astrochemistry.

Recent contributions of the UV-Visible program include an in-depth assessment of the role polycyclic aromatic hydrocarbons (PAHs) may play in the interstellar medium (ISM) through their contribution to the UV interstellar extinction curve and the diffuse interstellar absorption (DIBs) and emission (Red Rectangle) bands seen in the visible. PAHs, present as neutral, positively, and negatively charged species,

**Table 1. Comparison of DIBs with PAH Cation Bands.
PAHs Isolated in Neon Matrices**

PAH ⁺		λ_{peak} (nm)	DIBs (nm)
Pyrene (C ₁₆ H ₁₀)		439.5 (443.0 in Ar)	442.9
1-Methylpyrene (CH ₃ – C ₁₆ H ₉ ⁺)		444.2	442.9
4-Methylpyrene (CH ₃ – C ₁₆ H ₉ ⁺)		(457.7) 482.8 757.6	482.4 758.1
Naphthalene (C ₁₀ H ₈)		674.2 652.0	674.1 652.0
Phenanthrene (C ₁₄ H ₁₀)		898.3 856.8	857.2
Tetracene (C ₁₈ H ₁₂)		864.7	864.8
Benzo(ghi)perylene (C ₂₂ H ₁₂)		502.2 758.4 755.2 794.3	503.9 (?) 758.1; 758.6 755.8 (?); 756.2 793.5 (prob.)
Coronene (C ₂₄ H ₁₂)		459.0 946.5	459.5 946.6

have been postulated to represent a substantial fraction of the organic component of stardust (up to 10% of the cosmic carbon).

Cosmic material analogs are produced in the laboratory under conditions close to those expected in the ISM (cryogenic temperatures, high vacuum). The absorption and emission properties of these materials are probed using the techniques of low-temperature, molecular spectroscopy. Laboratory measurements show that PAHs absorb strongly in the UV. When ionized, PAHs absorb also in the visible remarkably close to the positions of known DIBs as shown in the table for the smaller PAHs. Identifying the molecular carriers responsible for these, yet unidentified, bands is a key element for

understanding the energetic mechanisms governing the origin and evolution of the ISM.

The fluorescence and fluorescence excitation spectra of PAH cations isolated in neon matrices have also been measured for the first time to test their relevance as class emission DIB-carrier candidates. The figure shows the spectra associated with the PAH perylene. Based on these laboratory results, it is concluded that a distribution of neutral and ionized PAHs represents a promising class of candidates to account for the diffuse interstellar bands seen in absorption and in emission.

Point of Contact: F. Salama/L. Allamandola
(415) 604-3384/6890

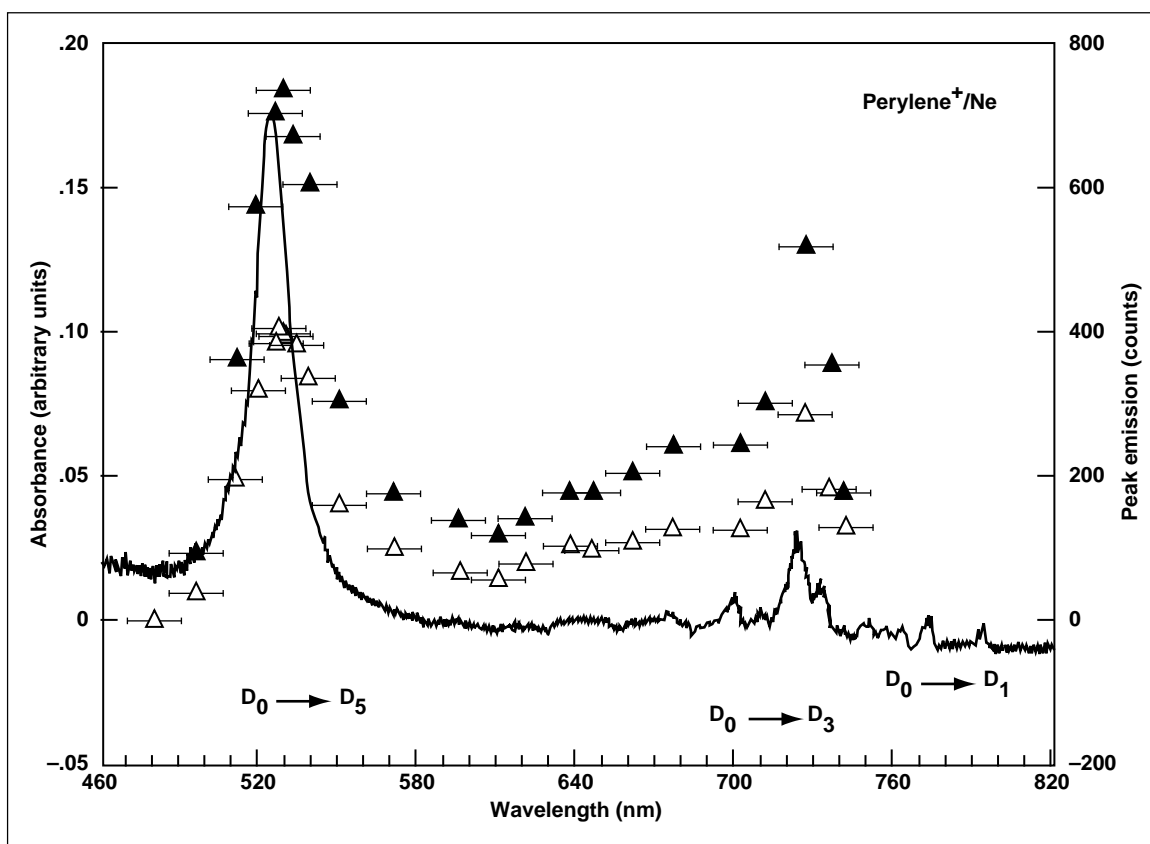


Fig. 1. The visible absorption spectrum of the perylene cation isolated in a neon matrix (solid line). The triangles represent fluorescence excitation spectra. The peak intensities of the strongest emission bands at 794.1 (plain triangles) and 817.3 nanometers (empty triangles) are plotted versus the central wavelength of the excitation band.

On the Central Regions of Galaxies

Bruce F. Smith

Numerical experiments on models of galaxies are providing fascinating new insights into the structure and dynamics of galaxies. Recent work is yielding important clues to the nature of activity often observed near the centers of galaxies, including our own Milky Way.

This work was done in collaboration with Dr. Richard H. Miller, University of Chicago. The numerical experiments were performed on the supercomputers at the Numerical Aerodynamic Simulation (NAS) Facility at Ames. The complex motions seen in the time evolution of the models indicate that the central regions of galaxies are very likely not in a static, steady state. Observations of galaxies indicate that the nucleus of a galaxy is often offset from the center as defined from the outer brightness profiles and that the central regions have complex velocity structures.

The recent Hubble Space Telescope (HST) discovery of a double nucleus in the Andromeda Galaxy (M31) brings into prominence the question of how long a second core can survive within the nuclear regions of a galaxy. The brighter core in M31 does not show up in the far ultraviolet in the HST observations, indicating that it is an ordinary collection of stars (perhaps the remnant of a star cluster), while the true nucleus is as bright in the far ultraviolet as it is in many galaxy centers. Over the past few years, several observations have been interpreted as indicating that there is a massive black hole in M31's nucleus. It was thought that tidal stresses produced by the black hole would disrupt any ordinary star cluster close to the nucleus. The observational papers, including the HST results, point out that the presence of a second core is difficult to reconcile in the black hole model.

However, physical conditions in the nuclear regions of a typical galaxy make it possible for a second core to survive and orbit for a long time, possibly for thousands of orbits. Given the nearly uniform mass density in a core, tidal forces within a core radius are compressive in all directions and help the core survive the disruptive forces of a second core as it orbits near the center of the galaxy. We have used the numerical experiments to illustrate these physical principles. Our method allows the full power of the experiments to be concentrated on the nuclear regions. Spatial resolution in the experiments is quite adequate to resolve details within the nuclear region of M31.

These physical principles are used to begin to understand M31's double nucleus. The numerical experiments are used to predict the changes a cluster would undergo as it settles into the M31 core region, as an aid to the interpretation of the HST observations. In conjunction with the numerical models, the HST observations can be used to place limits on the maximum mass of a black hole in cases where the black hole does not dominate the dynamics of the core region. Future HST observations of the core region, especially spectroscopic measurements of both the velocity of the brighter core and the velocity dispersion within the core, will help to deduce the nature of the core's progenitor—whether it was a globular cluster or some other kind of object such as a galaxy merger remnant.

Point of Contact: B. Smith
(415) 604-5515

Abundance Variations in the Galaxy

Janet P. Simpson, Sean W. J. Colgan, Robert H. Rubin, Edwin F. Erickson, Michael R. Haas

The Facility Cryogenic Grating Spectrometer onboard the Kuiper Airborne Observatory was used to measure far-infrared doubly ionized lines of nitrogen, oxygen, and sulfur in Galactic H II regions. H II regions are the interstellar gas ionized by hot young stars. H II regions (even in the very center of our galaxy) could be studied because the extinction from interstellar dust is practically negligible at far-infrared wavelengths. The abundances of singly ionized elements were corrected for in the H II regions by comparing the line ratios to those of a grid of H II region models.

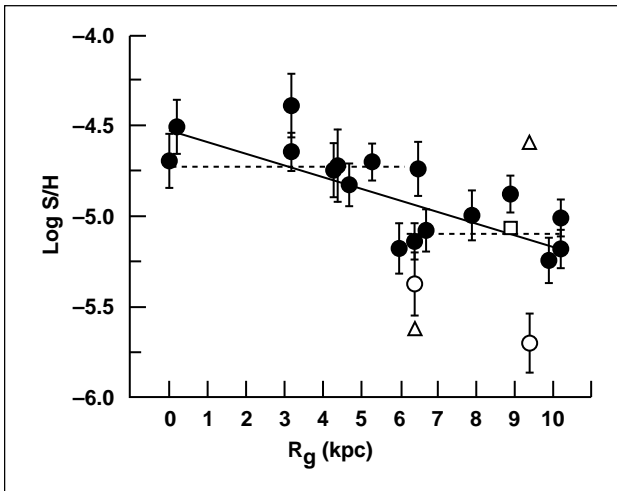


Fig. 1. S/H versus R . The solid line has a slope of -0.068 dex/kpc. The filled circles are the results of the current analysis, the open circles and triangles are the H II regions G45.13 + 0.14 and K3-50 analyzed here and by previously published detailed models; and the open square represents the Orion Nebula.

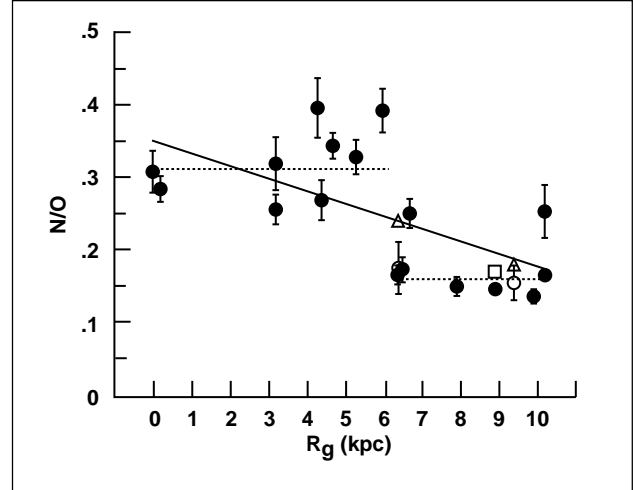


Fig. 2. N/O versus R . The solid line has a slope of -0.016 per kpc. The dotted lines are the step fit: $N/O = 0.32$ for $R < 6$ kpc and $N/O = 0.18$ for $6.4 < R < 10.2$ kpc.

The first and second figures show the sulfur/hydrogen (S/H) and nitrogen/oxygen (N/O) abundance ratios versus distance from the Galactic Center, R , measured in kiloparsecs (kpc) (1 kpc equals 3260 light years; the sun is approximately 8.5 kpc from the Galactic Center). Extensive observations of sulfur and oxygen in other galaxies show that S/O is essentially constant over a very large range of abundance. Thus, the overall abundance gradient of the galaxy can be seen clearly in the S/H ratio of the first figure. Likewise, there is an abundance gradient in N/O as shown in the second figure, although it is

also found that a step fit (the dotted line in the figures) is statistically better for N/O and approximately the same statistical significance for S/H.

The abundances of elements heavier than helium reveal much about a galaxy's star formation history and provide observational constraints on the nucleosynthesis of the elements. Heavy elements are formed in stars and returned to the interstellar medium through stellar winds and supernovae explosions. Thus, abundance studies probe the formation of a galaxy, as seen both in the relics of the very oldest stars and in the very enriched gas that has been recycled over and over.

Chemical evolution theories for galaxies predict gradients in the heavy element abundances with respect to hydrogen as a function of the distance from the centers of the galaxies. Such gradients occur, for example, if the inner parts of a galaxy form before the outer disk, thus providing more time for reprocessing of matter into heavier elements. "Primary" element formation is the direct result of hydrogen burning (as in the proton-proton chain to helium) or helium burning (even numbered elements such as carbon, oxygen, neon, and sulfur). "Secondary" production requires the presence of a basis element besides hydrogen or helium: for example, nitrogen is produced as the end result of hydrogen burning on carbon and oxygen. This gives a timescale for

nitrogen production in billions of years, which suggests that the oldest parts of a galaxy should show additional secondary nitrogen abundance compared to primary elements, such as oxygen.

Although the abundance gradients (as seen in the figures) are in general agreement with chemical evolution theory, the shape of the gradients is neither smooth nor monotonic, as is predicted. It may be that simple chemical evolution models with no mixing are not appropriate here—from radio and near-infrared observations, it has been suggested that the inner part of our galaxy is a barred spiral.

The radial velocities of the central gas clouds indicate that the clouds have noncircular orbits. Because there is radial as well as circular motion in a barred potential, it has been suggested that a bar would cause radial mixing of the matter in a galaxy. While uncertain, the parameters of the observed abundance gradients in the inner galaxy do not seem to agree with simple galactic chemical evolution theory, but are intriguingly in the direction of what might be expected from a galactic bar.

Point of Contact: J. Simpson
(415) 604-1613

Investigating the Evolution of Circumstellar Photodissociation Regions

William B. Latter, A. G. G. M. Tielens

The final evolution of a star with moderate mass is one of the least understood phases of stellar evolution. Through a combination of stellar pulsations and radiation pressure, an extended circumstellar envelope is deposited around the star during a heavy mass-loss phase. Often so much material is

cast off by the star that it can lose an amount equal to the mass of the Sun in less than 10,000 years. This “superwind” occurs near the end of a star’s nuclear burning lifetime and can have speeds in excess of 20 kilometers per second. Such large, mass-loss rates have a significant impact on the evolution of the

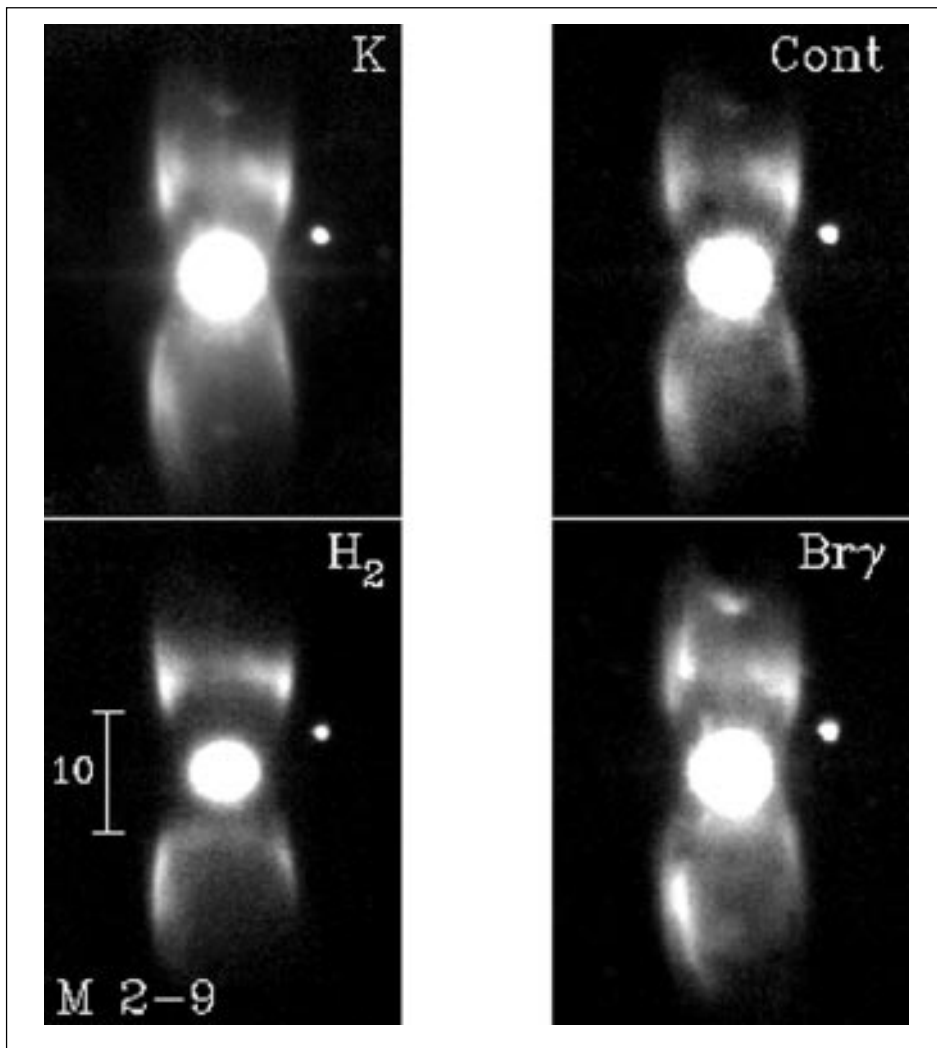


Fig. 1. These near-infrared images (broadband K = 2.2 microns wavelength; cont stands for continuum emission) of the planetary nebula M 2-9 reveal a great deal about the structure and evolutionary state of the circumstellar gas. In particular, we find that the molecular hydrogen falls in regions different from that of the atomic emission, clearly showing the location of the photodissociation region. Images like these are helping to guide further observations and numerical modeling.

star and on the general interstellar medium. Because of the high densities and low temperatures in the stellar atmosphere, the envelope is predominantly molecular. As the central star and circumstellar nebula evolve, ultraviolet (UV) emission from the star increases dramatically, and a molecular photodissociation front moves through the gas. The circumstellar envelope (known during this phase for historical reasons as a "planetary nebula," or PN) changes from molecular to atomic to ionized.

During FY95 a program was initiated to understand how the rapidly varying UV field impacts the final stages of stellar evolution through modeling and observations at near-infrared wavelengths (where the emission from molecular hydrogen is most prominent). Observations have shown that a considerable amount of neutral and molecular material can be present in PN, and, in some cases, most of the near-infrared emission comes from the UV-impacted photodissociation region (see the first and second figures). This work was performed in collaboration with Joseph L. Hora (University of Hawaii) and David Hollenbach (Ames Research Center).

Researchers have shown that the presence of molecules in the UV-flooded environment of a planetary nebula cannot be explained without highly nonspherical geometries and high densities, or clumping. Although there can be an ambiguity in the excitation mechanism (UV photons or shockwaves), the location of molecular hydrogen emission identifies regions of the nebula with sufficient dust shielding and density for the survival of molecular species.

Point of Contact: W. Latter
(415) 604-3385

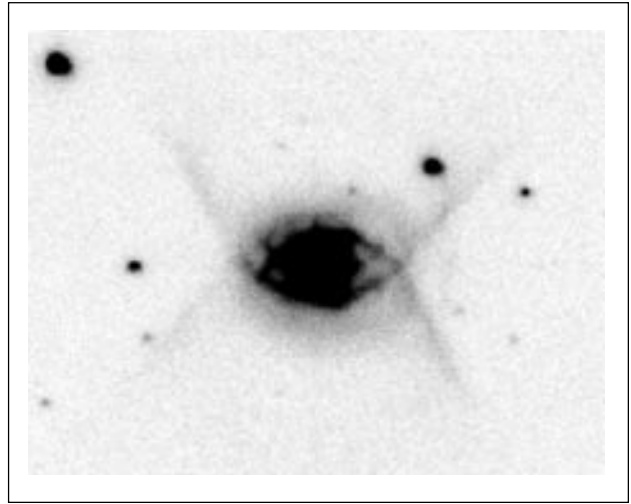


Fig. 2. This is the young planetary nebula Hubble 12, seen here in emission from molecular hydrogen only. Prior to these data, the full extent and structure of this object were unknown. This image and spectroscopic data are used to show that Hubble 12 is a remarkable "butterfly-type" nebula that apparently is in a very brief stage of rapid evolution.

Planetary Surface Rover Mission Simulation

Carol Stoker, Michael Sims

This project focuses on field testing of mobile robots that are operated using Telepresence and Virtual Reality as a user interface. In the last year, a simulation of rover missions on the Moon and on Mars was performed using Marsokhod, a Russian-built planetary surface rover. This simulation was performed on Kilauea Volcano, Hawaii, in March 1995.

The figure shows the Marsokhod rover, a six-wheeled, 300-pound rover equipped with stereo cameras, a fixed, body-mounted, high-resolution digital camera, a manipulator arm with a close-up camera, and onboard power and computing. The Marsokhod Rover was made available to Ames through a collaboration with the Russian Levochkin Institute. Russian engineers and scientists participated in the Kilauea mission. Marsokhod, which translates as "Mars Walker," was designed in Russia and is being considered for a joint U.S.-Russian mission called "Mars Together" to be launched in 2001.

The same Russian team built the successful Lunakhod rovers that operated on the Moon in

1970–71. The rover is roughly 5 feet long and 3 feet wide. Its wheels are 12 inches in diameter and are made of titanium. Each is driven by an individual motor, and the rover has a maximum speed of approximately 1500 feet per hour. Because of its unique design, the rover can overcome obstacles 50% larger than its wheels, and can climb slopes of up to 30 degrees. Onboard batteries allow untethered operation of up to 6 hours. The rover is equipped with a number of instruments for use by both vehicle operators and scientists. Up to six cameras may be used to provide views of the rover and its surroundings, and two of the cameras are used to provide stereo imaging. They are mounted to a mast roughly at human eye level. A high-resolution camera can provide views of details as small as 1 millimeter in size. This camera is placed by the remote scientists with the aid of a robotic arm. The rover transmits data and video via radio signals that are then sent by satellite to Ames Research Center, where they are used to create a three-dimensional computer model of the rover and surrounding terrain.



Fig. 1. Marsokhod Rover on Kilauea Volcano.

The Kilauea test site is a geologically unique area and is one of the few places in the world where such diverse geologic features are found both close together and in proximity to a paved road. The explosive eruptions at the summit of Kilauea in 1790 and 1924 produced terrains that are rare on Earth, but are thought to be analogous to those on the moon and Mars. In particular, Apollo astronauts found fragmental deposits on the moon that are similar in many ways to the 1790 Keanakakoi ash. The presence of thick volcanic ash deposits may also explain why a large portion of Mars reflects essentially no radar energy. Additionally, the rocks thrown from the 1924 explosions at Halema'uma'u are an excellent analog of the blocky ejecta from meteorite impacts.

The primary objective of the Kilauea mission was to evaluate how well a robot can be used to conduct scientific observations on other worlds. The tests evaluated the maneuverability and reliability of the rover over diverse terrains. Simulations of

teleoperated rover missions on Mars (with a communications time delay) and on the Moon (without communications time delay) were performed for three days each. During the simulations, science teams analyzed data from the Marsokhod and deduced the geologic setting and history of the field site. In the Mars simulation, the rover traversed 800 meters of terrain, made observations at eight science stations, and obtained several hundred images. We estimate that performing the same operation on Mars would require about 30 days. In the Lunar simulation, the rover was operated in real time with a continuous stereo video image transmission, and traversed 1.2 kilometers in 15 hours of operation. The experiment proved that mobile robots can be used to successfully perform field geology on other planets.

Point of Contact: C. Stoker
(415) 604-6490

A Micro-Meteorological Network Mission for Atmospheric Circulation Studies on Mars

Robert M. Haberle, Steven C. Merrihew, David C. Catling, Lawrence G. Lemke

The general circulation of the Martian atmosphere and how it relates to the planet's climate system are the main goals of post-Viking atmospheric science investigations. An unambiguous determination of the wind systems associated with the general circulation requires simultaneous measurements from at least 15-20 globally-distributed surface stations and a single, high-inclination, short-period orbiter. The required number of stations would be too costly using conventional multi-instrumented lander designs. However, truly global network science for meteorology can be accomplished using landers instrumented for a single measurement—namely pressure. Pressure is the most important meteorological parameter, and pressure sensors do not require deployment or orientation. This facilitates the design of relatively simple landers that are sufficiently small and light so that the required number can be launched on a single Med-Lite launch vehicle. Of

equal importance, the low-power demand of the stations would allow them to last for a Martian year and provide the necessary seasonal coverage.

During the past year, researchers have worked out the science rationale and measurement requirements for such a network on Mars, and have shown how it would contribute to the understanding of the Martian general circulation and climate system. A determination was made of the number and siting of stations and the basic science specifications for barometric pressure sensors and an atmospheric sounder. A mission was then designed that would meet these requirements and fit within the tight constraints of today's fiscal environment. The "Micro-Met" mission would launch sixteen probes to Mars aboard a Med-Lite launch vehicle. The probes would be deployed on approach from a spin-stabilized carrier using a single propulsive time-of-arrival

adjustment to achieve global coverage. The entry, descent, and landing of each probe would use an ablatable aeroshell, a parachute, and crushable material to reduce the impact shock. On the surface, the battery-powered stations would measure only pressure 25 times a day for one Martian year (1.9 Earth years). The data would be relayed to

an orbiter through an ultra-high frequency link and then transmitted to Earth. This mission would, for the first time, observationally define the seasonally varying global wind field on another planet.

Point of Contact: R. Haberle
(415) 604-5491

Martian Mountain Waves

Julio A. Magalhães

The objective of this work is to provide a theoretical basis for understanding the role played by mountain waves in the dynamical interaction between the Martian surface and atmosphere. It is well known that the thin carbon dioxide (CO₂) atmosphere of Mars responds rapidly to changes in heating, resulting in large variations in the thermal structure of the lowest 10 kilometers. During nighttime hours, strong and deep (up to 5 kilometers) thermal inversions are produced. In the inversions, the increasing temperature results in a highly stratified atmospheric layer in which vertical mixing of momentum and heat (turbulence) is strongly suppressed. In the absence of other effects, this near-surface, almost “friction-free” boundary layer between the bulk of the atmosphere and the surface effectively decouples the atmosphere and surface. Very strong, near-surface atmospheric jets are predicted under these conditions. On Earth, such layers are infrequent due to weaker thermal inversions produced in the thicker terrestrial atmosphere.

Mountain waves that are excited by wind flow over mountains when the atmosphere is stably stratified can transport momentum and energy through stratified atmospheric layers. If these waves are of large “finite” amplitude, they can, under

suitable conditions, “break” (much like ocean waves on a beach) and deposit their momentum in the form of both a local deceleration of the atmosphere and local turbulence. A semianalytical, hydrodynamic code was developed to compute the behavior of two-dimensional, finite-amplitude mountain waves in the atmosphere of Mars. The code incorporates the essential elements of the thermal stratification of the Martian atmosphere by incorporating two layers of constant atmospheric stratification—an upper layer representing the interior of the atmosphere and a lower layer representing the near-surface region of widely varying stratification with time.

The conditions leading to mountain “wave breaking” have been investigated. Two factors contribute to make “breaking” common during nighttime hours. First, the large stratification in the thermal inversion allows very small topographic obstacles (≥ 10 meters) to produce finite amplitude waves that overturn in the lowest few kilometers of the atmosphere, well within the highly stratified layer in which turbulence is suppressed. Second, the abrupt change in stratification, which occurs at the top of the thermal inversion at altitudes of a few kilometers, leads to partial reflections of the upward

traveling waves excited by the topography. The resulting downward propagating wave can interact with the original upward propagating wave to amplify (constructively interfere) or diminish (destructively interfere) the total wave amplitude within the lowest few kilometers of the atmosphere. The calculations suggest that the depth of the thermal inversion can lead to a particularly large enhancement of the wave amplitude (a resonance), thus significantly contributing to the occurrence of wave breaking.

Martian mountain waves appear to play a potentially fundamental role in affecting the boundary layer controlling the interaction between the

Martian surface and atmosphere. Such waves can provide a mechanism for dynamically coupling these two regions of the planet during nighttime hours. The amount of deceleration and turbulence produced when the waves break can quantify the impact of these waves. The results of this work will be fundamental to understanding the near-surface environment that will be encountered by robotic and manned spacecraft missions to Mars.

Point of Contact: J. Magalhães
(415) 604-3116

Water Adsorption on Mars

Aaron P. Zent

Adsorption is the process of accumulation of molecules at an interface. On Mars, where soil is a considerable amount of the surface area, adsorption is a dominant process in the water cycle. The understanding of the actual amount of water that was adsorbed on the surfaces of Martian soil particles has been based on a mathematical extrapolation of laboratory measurements made under conditions that were both wetter and warmer than the conditions that pertain to Mars. In 1994, the first measurements were made of how both water (H_2O) and carbon dioxide (CO_2) adsorb under Mars-like conditions, and a discrepancy was noticed between these results and the predictions that would derive from previous mathematical models.

In 1995, researchers made a series of additional measurements of H_2O adsorption of minerals such as

those that might be found on Mars, and they found that the previous predictions of H_2O adsorption overestimated the actual adsorption by nearly a factor of 30. This indicates that the role of the surface in supplying water to, and removing ether from, the atmosphere must be re-evaluated. In November 1996, the Mars Global Surveyor (MGS) will be launched. The Thermal Emission Spectrometer, carried by the MGS, should provide some measurement of water in the Martian atmosphere.

Point of Contact: A. Zent
(415) 604-5517

Oxidants in the Martian Regolith

Aaron P. Zent, Richard C. Quinn

In 1976, the Viking landers found that the Martian soil, or regolith, has unique chemical properties. When brought into contact with the soil, organic molecules were broken down and oxygen was released when exposed to water vapor. The traditional explanation of this chemical response has been that the regolith must contain oxidants. Oxidants are very reactive chemicals and can be harmful to organic molecules. The presence of oxidants on Mars may represent a threat to human health and safety. Moreover, oxidants will decompose ancient organic materials of Martian origin, if any, making their recovery all the more difficult.

In 1995, researchers tested a chemical model of the origin of the oxidants on Mars that relies upon the decomposition of water molecules by sunlight in the

Martian atmosphere, and the recombination of the reaction fragments to form gaseous oxidants. Those atmospheric oxidants can then form complexes on the surface of the soil particles. In particular, the focus was on the role of ozone (O_3) and hydrogen peroxide (H_2O_2). The researchers found that physically adsorbed H_2O_2 is capable of reproducing the responses seen in the Viking experiments, and that it requires only those species that are already understood to be present in the Martian regolith and atmosphere. This hypothesis can be tested with an atmospheric sensor.

Point of Contact: A. Zent
(415) 604-5517

Environmental Perturbations by Large Asteroid and Cometary Impacts

Owen B. Toon, Kevin Zahnle, David Morrison

The greatest natural disasters on Earth are caused by impacts of large asteroids and comets. Impacts are rare compared to floods, earthquakes, and other more mundane hazards; they are so infrequent that they are normally disregarded on the time scale of human evolution. However, impacts have occurred in the past with devastating effects (ask any dinosaur), and they will occur in the future.

We conclude that the energy range from 10^5 to 10^6 megatons (energies are in megaton TNT equivalent, 1 megaton = 4.18×10^{15} joules) marks the transition between regional and global effects. Such events occur at intervals of the order of 1–2 million years; they are caused by comets and asteroids some 2–3 kilometers in diameter. The greatest danger on a global scale appears to be

stratospheric hazes with climatologically significant optical depths of the order of 10, from impact-generated dust and sulfates and from soot produced by extensive wildfires sparked by the impact, as shown in the first figure. Impact-generated nitrogen oxides might also remove the ozone screen. Between 10^6 and 10^7 megatons (15 million years; 5 kilometer objects) stratospheric dust, sulfate, and smoke would be thick enough to reduce light levels below those necessary for photosynthesis, as shown in the second figure. At energies above 10^7 megatons, blast and earthquake damage reach the regional scale (10^6 kilometers²). Tsunami cresting to 100 meters and flooding inland 20 kilometers sweep the coastal zones of one of the world's ocean basins. Light levels

may drop so low from the smoke, dust, and sulfate that vision is not possible. Above 10^8 megatons (10^8 years), fires are set globally by impact ejecta re-entering the atmosphere, raising the temperature of the sky to >1000 kelvin for tens of minutes. Events

of this scale, although rare, punctuate the evolutionary record of life on Earth.

Point of Contact: K. Zahnle
(415) 604-0840

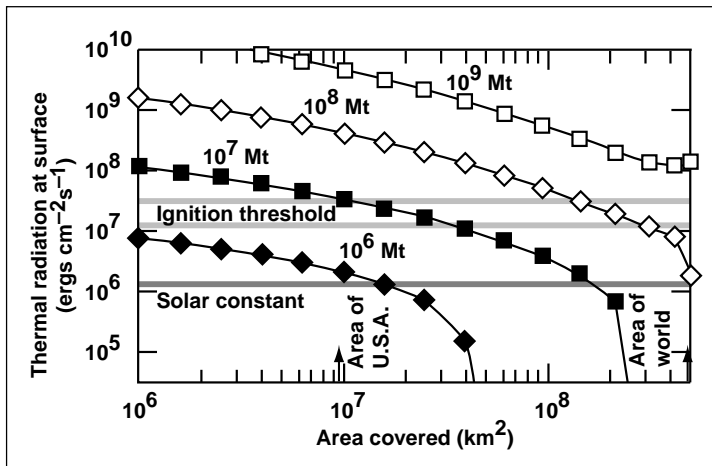


Fig. 1. Impact energies needed to set global wildfires. The cretaceous-tertiary (K/T) event was 10^8 – 10^9 megatons. Shown are asteroid impacts; comets are more efficient.

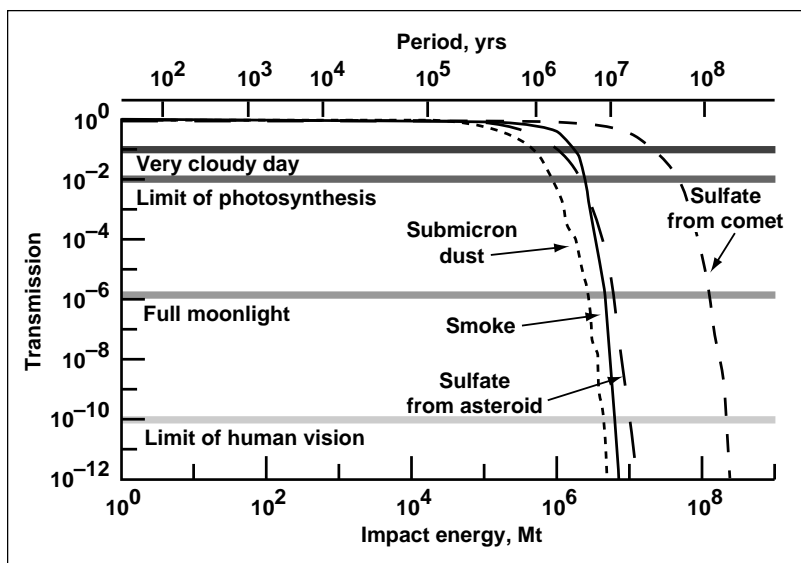


Fig. 2. Ambient lighting at the surface following large impacts. Smoke, dust, and sulfate optical depths are estimated independently and, although each is quite uncertain, their effects are probably additive. The approximate time-scale for untoward events is given at the top of the figure. Impacts larger than 10^6 megatons would probably devastate modern civilization, and impacts greater than 10^7 megatons might be large enough to cause mass extinctions.

Ejecta Plumes from the Collisions of Comet Shoemaker-Levy 9 with Jupiter

Kevin Zahnle

Comet Shoemaker Levy (SL9) collided with Jupiter in July 1994. The enormous energies of these impacts have produced huge explosions (the largest fragments were nearly 1 kilometer across and, hitting at 60 kilometers per second, released the equivalent of 100,000 megatons of TNT, or roughly ten times the potential energy stored in the world's nuclear arsenals). Unlike more familiar explosions, these were so large that they blew holes in the atmosphere, ejecting a mixture of Jovian air and former comet well into near-Jupiter space. Several of the plumes were imaged towering 3000 kilometers above Jupiter's limb, and thus were launched at velocities of the order of 10–13 kilometers per second, comparable to escape velocity from Earth. The plumes took some 10–15 minutes to fall back to Jupiter, landing over areas greater than the surface area of the Earth. When the plumes fell, the heat that was released was considerable and easily observed on Earth as thermal infrared events, prominent at wavelengths greater than 2 microns, starting about 5 minutes after impact and glowing for some 10–15 minutes thereafter.

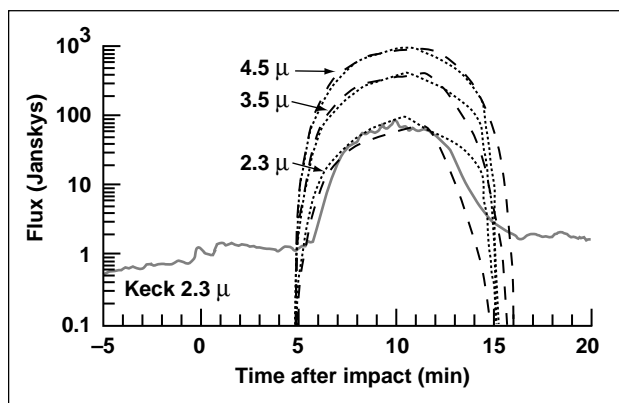


Fig. 1. A typical SL9 infrared light curve, compared to theoretical light curves using a ballistic plume model in which the energy of the plume is mostly radiated by warm dust.

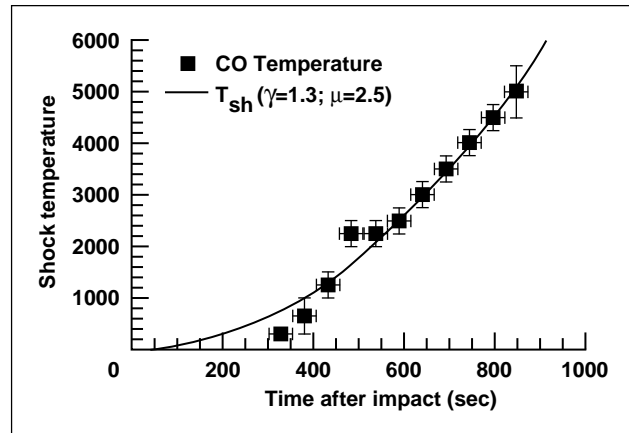


Fig. 2. Gas temperatures in the re-entry shock, as inferred from CO emissions at 2.34 microns, compared to the predictions of the ballistic plume model for a strong shock in an ideal gas.

A typical, infrared light curve at continuum wavelengths from a mid-size SL9 impact is shown in the first figure. Also shown are results from the first generation theoretical model. The model, which is based on an analytic generalization from a full-featured numerical code, treats the rise and fall of the plumes by elementary ballistics. The model light curves are generated by conservation of energy, in which the kinetic energy of the infalling ejecta is mostly converted to thermal radiation. The effective temperature is made to agree with the observed radiating temperatures (roughly 700–1000 kelvin) by adjusting the opacity of the radiating matter, which appears to have been warm dust (from the former comet) and/or soot (from the comet and also from shocked Jovian air).

By contrast, gas temperatures in the re-entry shock were much higher than dust temperatures, as shown in the second figure. Gas temperatures in the re-entry shock were inferred from carbon monoxide (CO) emissions at 2.34 microns. For a strong shock in an ideal gas, the ballistic approximation demands that temperatures rise as the square of time. There is but one free parameter. A good fit requires that the mean molecular weight of the gas in the shocked

plume be 2.5, which is similar to that of unshocked Jovian air and lower than what might be expected from a vaporized comet. In all likelihood, most of the higher molecular weight species from the comet were condensed and entered the atmosphere in the form of meteors rather than solely as a wall of gas.

Point of Contact: K. Zahnle
(415) 604-0840

Planetesimal Formation in the Protoplanetary Nebula

Jeffrey Cuzzi

Among the major unsolved problems of planetary origin is the “primary accretion” process—the process by which the first sizable objects (comets, asteroids, etc.) formed from solids that entered the protoplanetary nebula as micron-sized dust motes. Earlier work postulated a form of gravitational instability that was shown to be inoperative under nebula conditions. Instead, numerical models that provide realistic simulations of the conditions under which primary accretion occurred were developed; these models produced novel insights.

One accomplishment this year was the development of a new model of self-consistent turbulence generation with damping by thin, dense layers of large (10 centimeters radius and larger) particles that can settle to the nebula midplane. In earlier work, researchers discussed the self-consistent midplane situation in which a dense particle layer stirs the nebula gas, producing vertical velocity shear and associated turbulence. The turbulence diffuses the particles, as parametrized by their Schmidt number, and the end result is a self-consistent, steady-state particle layer of small but finite vertical extent (thousands to ten thousands of kilometers thick—small relative to the 10 million kilometers vertical thickness of the gas).

The first study neglected the role of the particles in damping turbulence in the gas; subsequently, a scheme was developed and implemented to account for this effect. The scheme begins with the Reynolds-averaged equation for the turbulent kinetic energy. The full, two-phase equations are averaged, and new

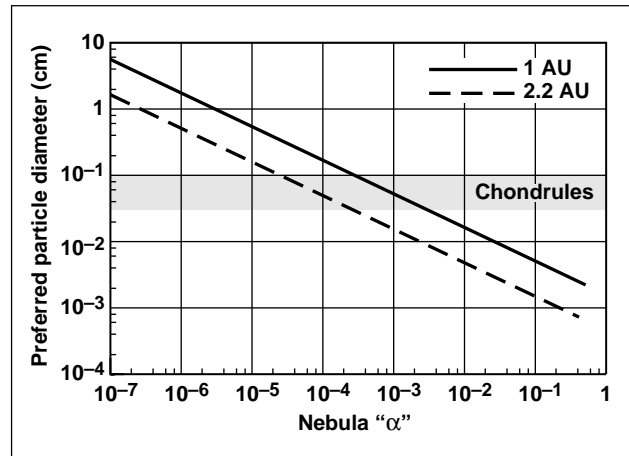


Fig. 1. Preferred particle size for concentration, as a function of nebula Reynolds number (as parametrized by scaling parameter α). In this parametrization, the turbulent viscosity is α times the product of the characteristic nebula length and velocity scales. Canonical values of α are in the 0.01–0.0001 range. Intriguingly, this range predicts a preferred particle size very close to that which is observed.

terms appear because of particle damping. These terms are modeled, as well as the vertically varying gas dissipation itself, and the effects of particle damping of turbulence can now be studied. This year the results indicate that the effect could be substantial if, but only if, the particle size distribution is strongly

concentrated at one particular size that optimizes the particle surface area and stopping time for a given mass.

In other research, considerable progress was made in the three-dimensional (3-D), direct numerical simulations of particles in turbulence. After significant coding improvements, we have extended the range of Taylor microscale Reynolds number from 80 to 140. Using one million particles at each of 16 Stokes numbers (the Stokes number is the ratio of particle stopping time to Kolmogorov eddy turnover time), and objective sampling, binning, and clump identification procedures, the dependence of the particle concentration on particle size can be modeled with good resolution for Reynolds numbers of 40, 80, and 140. This is the first time that this has been accomplished. Not only the preferred particle size, but the form of the particle size distribution seems to be in surprisingly good agreement with meteoritic data (shown in the first and second figures).

This research has shown that several key properties of the process are Reynolds number independent (including the size-dependent concentration factor shown in the second figure), strengthening the applicability of these results to plausible nebulae with Reynolds numbers orders-of-magnitude higher.

Point of Contact: J. Cuzzi
(415) 604-6343

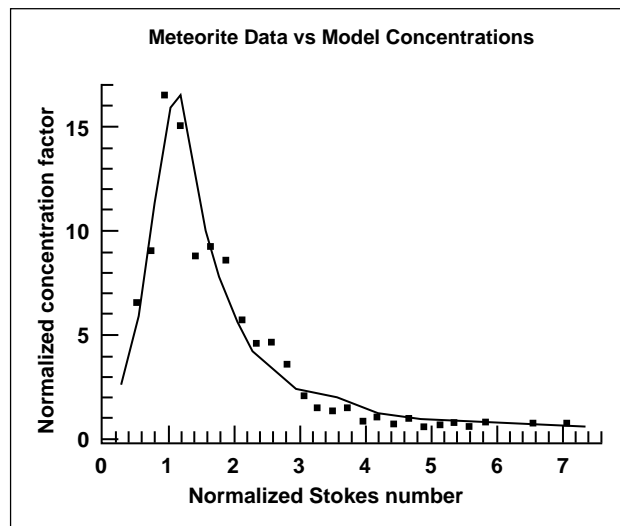


Fig. 2. Concentration factor as a function of Stokes number; $St = 1$ implies a stopping time equal to the turnover time of a Kolmogorov scale eddy. The curve is a set of model predictions, and the points are meteorite data (normalized in horizontal and vertical axes to the peak on the theoretical plot, and thus corroborating only the shape of the theoretical curve).

Interstellar Grains in the Solar System

Patrick Cassen

The objective of this work is to provide a theoretical basis for understanding the existence of presolar material in meteorites and comets. There is now abundant and unequivocal evidence that interstellar grains, essentially unscathed by cosmogenic events, reside in primitive meteorites. Comets can also contain such presolar material. Solid particles that have retained an interstellar signature since the formation of the solar system must have survived at least three potentially destructive environments: the collapsing protosolar cloud, an accretion shock through which collapsing material was decelerated, and the solar nebula itself. At each stage, sufficiently high temperatures would vaporize solid components and therefore erase, by homogenization in the gas phase, any recognizable chemical or isotopic interstellar identification. In collaboration with Kenneth M. Chick (University of California at Santa Cruz), researchers have examined theoretical models of the protosolar environment with the aim of determining what factors affect interstellar grain survival; what patterns one might expect to find in the abundances, type, and composition of interstellar material in primitive meteorites; and what can be deduced about the formation of the solar system if such patterns exist.

A radiative transfer code was developed to compute thermal transport in a collapsing, protostellar cloud. Temperatures were compared with the thermal processing that the dust grains underwent in the shock at the nebula surface and in the interior of the nebula, to estimate the distances from the Sun at which dust grains were vaporized. The code has special features to accommodate the shift in the dominant portion of the radiant spectrum from optical and ultraviolet wavelengths near the star, to the infrared radiation that determines the temperature far from the star. It also accurately calculates the intensity as it varies over many orders of magnitude between the inner and outer envelope, so that the

locations at which grains are destroyed (and opacity changes abruptly) can be determined.

The approach is to decompose the computational domain, so that for each subdomain the dominant source of radiation is on its interior surface. The transport problem is solved independently in each subdomain, subject to incident radiation computed in neighboring cells on a previous iteration. The iteration starts from the central subdomain and passes outward. Once the outermost subdomain is reached, the sweep reverses, and the iteration proceeds from the outermost subdomain inward. The incident radiation on the inner surface of each subdomain is rescaled to unity, which allows values spanning many orders of magnitude to be computed. Furthermore, the transport solution in each subdomain is tailored to local conditions. Photon balance algorithms are efficient near the origin where transport is diffusive; ray-tracing algorithms are superior far from the origin where the opacity gradually decreases.

The locations of the destruction fronts in the envelope were found for several representative interstellar constituents: silicates, iron, troilite (iron sulfide), refractory organics (kerogen), volatile organics, and water (H₂O) ice. The envelope temperatures along the surface of the nebula were used as boundary conditions to calculate temperatures within the nebula. The primary environmental determinant of survivability is the accretion rate through the nebula, which affects the thermal state of both the nebula and the collapsing cloud. During periods of rapid accretion, silicate grains might survive collapse and the accretion shock to within 2 astronomical units (AU), but would be destroyed in the nebula to distances beyond the terrestrial planet region. During periods of very slow accretion, those grains could remain intact to well within 1 AU. Typical destruction distances *above the nebula* of various interstellar constituents are as follows:

	Vaporization temperature, K	Rapid accretion, AU	Slow accretion, AU
Silicates	1050	1–2	<0.3
Iron	994	1–2	<0.3
Troilite	680	1.5–3	0.2–0.4
Kerogen	575	2–4	0.4–0.7
Volatile organics	375	3–8	1–2
H ₂ O ice	125	15–25	5–7

Rapid accretion corresponds to rates of about 2×10^{-5} solar masses per year; slow accretion corresponds to about 10^{-6} solar masses per year. The locations of destruction fronts *within* the nebula depend on nebula optical depths, but are never at radii less than that given above (until collapse ceases), and, for rapid disk accretion, can be considerably further from the Sun.

It is clear that there were vast regions of the outer nebula in which all nonvolatile interstellar species could have survived incorporation into solar system bodies with minimal modification. However, if major elemental fractionations in meteorites are the result of accumulation in a hot, inner nebula, the abundances of material with interstellar signatures should be correlated with elemental fractionation patterns, since both would then reflect the cooling history of the nebula. The calculations of thermal transport in protostellar envelopes have further applications with regard to such subjects as the interpretation of disk properties from observations and the calculation of chemical models of star forming regions. For example, the results are relevant for estimations of the sizes of the nebula-like disks seen around newly formed stars.

Point of Contact: P. Cassen
(415) 604-5597

Theoretical and Empirical Studies of Planetary Surface Analogs

Ted Roush

The common objective of this research is to characterize properties of diverse bodies in the solar system and to characterize the processes that are responsible for these properties. To this end, the research relies upon observational information obtained by earth- and space-based instruments, laboratory studies of analog materials, and radiative transfer computations used to describe the observations and laboratory measurements. High priority is placed on deriving qualitative (composition of surface materials) and quantitative (determination of the grain sizes and relative abundances of materials) information about solid surfaces throughout our solar system from analyses of their visible and infrared spectra.

One specific objective is to determine the optical properties of candidate materials observed on solar system surfaces. These include rock forming materials such as igneous minerals that are observed on terrestrial planets (pyroxenes and olivines), and their alteration products (phyllosilicates and oxide minerals), as well as condensed volatiles that are observed on surfaces in the outer solar system. A related objective is the use of these optical properties in radiative transfer calculations to determine the

relative abundances of materials present on solar system objects. Knowledge regarding the identity, relative abundances, and grain sizes of surface materials present on bodies throughout the solar system allows the assessment of internal and external processes that have been active on any particular body.

Accomplishments during the past year include: (1) determination of the mid-infrared optical constants of hydrous carbonate, sulfate, and sulfate/nitrate; (2) determination of the mid-infrared optical constants of amorphous carbon; (3) derivation of near-infrared geometric albedo of Pluto's moon, Charon; (4) determination of Mars dust optical depths from the 1993 Wyoming Infrared Observatory thermal-infrared imaging data; (5) compilation of the 1.0–2.55 micrometers high-resolution spectrum of Pluto; and (6) determination of the optical constants of water ice at 100 kelvin.

**Point of Contact: T. Roush
(415) 604-3526**

New Millennium Autonomous Spacecraft Architecture

B. Pell, D. E. Bernard, S. A. Chien, E. Gat, N. Muscettola, P. Nayak, M. D. Wagner, B. Williams

NASA has recently announced the New Millennium Program (NMP) to develop “faster, better, cheaper” spacecraft in order to establish a “virtual presence” in space. A crucial element in achieving this vision is onboard spacecraft autonomy, requiring the automation of functions that have traditionally been achieved by humans on the ground. These include planning activities, sequencing spacecraft actions, tracking spacecraft state, ensuring correct functioning, recovering in cases of failure, and reconfiguring hardware.

In response to this challenge, a joint team of Ames Research Center and Jet Propulsion Laboratory scientists and engineers analyzed the spacecraft domain to determine its unique properties and developed an architecture that provided the required functionality. This architecture integrates traditional real-time monitoring and control with constraint-based planning and scheduling, robust multithreaded execution, and model-based diagnosis and reconfiguration. In this architecture, autonomous operations are achieved through the cooperation of five distinct components, as shown in the figure.

Schedule execution is achieved through the cooperation of the *executive* and the other architec-

tural layers. The executive reasons about spacecraft state in terms of a set of component modes. The *mode identification* (MI) layer is responsible for providing this level of abstraction to the executive. MI takes as input the executive command sequence and observations from sensors to identify the current mode (nominal or failed) of each spacecraft component. The *monitoring* layer takes the raw sensor data stream and discretizes it to the abstract level required by MI. Finally, the *control and real-time system* layer takes commands from the executive and provides the actual control of the low-level state of the spacecraft. It is responsible for providing the low-level sensor data stream to the monitors.

The *planner/scheduler* is the only component that is activated as a “batch process” and dies after a new schedule has been generated. The other layers are always active and in concurrent execution. This ensures the high reliability required by the domain.

In a five-month, rapid prototyping effort during FY95, the team successfully implemented and demonstrated this architecture in the context of an autonomous insertion of a simulated spacecraft into orbit around Saturn, achieving the mission goals in

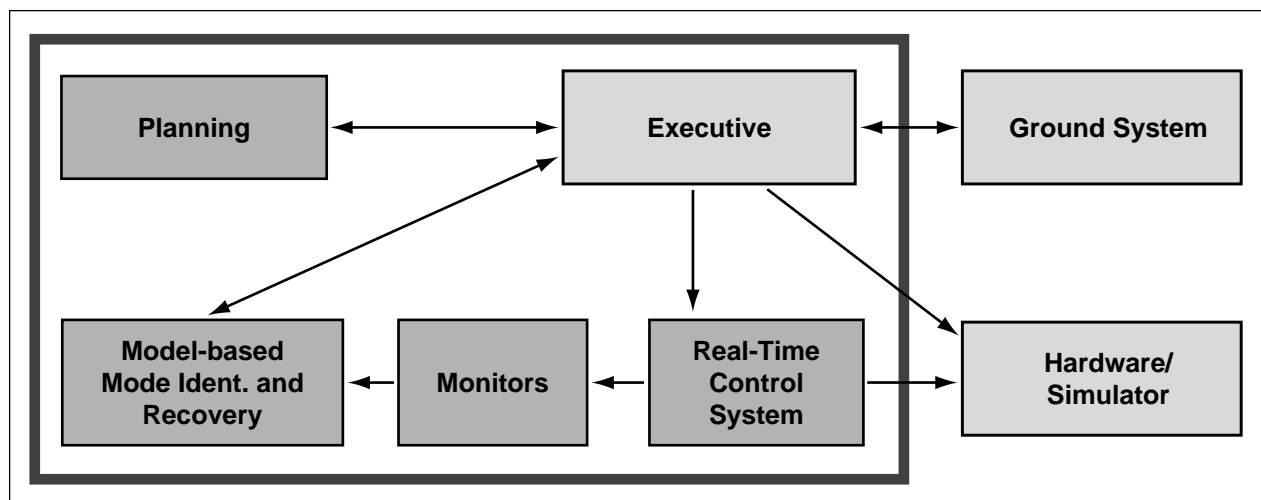


Fig. 1. New Millennium Program Autonomous Spacecraft Architecture.

the face of any single point of hardware failure. As a result of this success, the integrated architecture has been selected to control the first NMP flight, Deep Space One, in 1998. It will be the first artificial intelligence system to autonomously control an actual spacecraft.

D. E. Bernard, S. A. Chien, and E. Gat are from the Jet Propulsion Laboratory in Pasadena, California.

Point of Contact: B. Pell
(415) 604-3361

Model-Based Autonomous Systems

Brian C. Williams, P. Pandurang Nayak

The availability of cheap sensors, control processors, and networks is providing a new generation of sensor-rich, massively distributed, autonomous systems, such as spacecraft and smart buildings that have the potential for unprecedented performance. A control architecture that offers high performance for these systems by supporting self modeling, self configuration, and compositional, model-based programming is being developed. To achieve high performance, these autonomous systems use their sensors to model themselves and their environment on a large scale. They use these models to dramatically reconfigure themselves in response to failures. They are programmed solely through high-level compositional models, supporting fast, cost-effective design.

In the past year the centerpiece of this approach was developed, a system called Livingstone that is an implemented kernel for a model-based, reactive, self-configuring autonomous system. Livingstone is a reactive system that performs significant deduction in the sense/response loop by drawing on past experience at building fast, propositional, conflict-based algorithms for model-based diagnosis, and by framing a model-based configuration manager as a propositional feedback controller that generates focused, optimal responses. Livingstone's representation formalism achieves broad coverage of hybrid hardware/software systems by coupling the transition system models underlying concurrent reactive languages with the qualitative representations developed in model-based reasoning. Livingstone automates a wide variety of tasks using a single model and core algorithm, thus making significant

progress toward achieving a central goal of model-based reasoning systems.

Livingstone is integrated with a high-level planning/scheduling engine and an intelligent executive to form Remote Agent, the core spacecraft autonomy architecture for the new generation of NASA New Millennium spacecraft. Remote Agent was successfully demonstrated in the context of an autonomous insertion of a simulated Cassini-like spacecraft into Saturn's orbit, trading off science and engineering goals, and achieving the mission goals in the face of any single point of hardware failure. Based on this success, Remote Agent was selected to control the first New Millennium spacecraft, called Deep Space One, that will be launched in 1998. It will be the first artificial-intelligence system to autonomously control an actual spacecraft.

Moriarty, a model-based, autonomous systems component, was also developed to perform data-driven adaptive modeling. Moriarty is based on decompositional, model-based learning, a method developed by observing a modeler's expertise at decomposing large-scale, model-estimation tasks into smaller, more manageable parts. The method exploits a striking analogy between adaptive learning and consistency-based diagnosis. Moriarty was successfully applied to the thermal modeling of a smart building, demonstrating a significant improvement in learning rate.

Point of Contact: B. Williams
(415) 604-4776

Spacecraft Task Planning: New Millennium, Extreme Ultra-Violet Explorer, and Cassini

Nicola Muscettola, Sunil Mohan, Charles Fry, Kanna Rajan

The goal of this project is to develop technology for onboard task planning for highly autonomous spacecraft. Such spacecraft can execute mission profiles described by abstract goals and autonomously plan the detailed sequence of commands needed to achieve these goals. Onboard spacecraft task planning significantly expands the potential for unmanned exploration. It enables missions like long-term planet explorations with autonomous rovers where required reaction times make it impossible to have continuous control from Earth. It also greatly reduces operations costs.

During FY95, the Operations Scheduling project has further enhanced the Heuristic Scheduling Testbed System (HSTS) planning and scheduling technology, which has been under development since 1993. The capabilities of HSTS were demonstrated in three different domains. In collaboration with the Jet Propulsion Laboratory, researchers built a prototype of an onboard planner for the New Millennium Autonomy Architecture rapid-Prototype (NewMAAP). The reference mission was a maneuver inserting a spacecraft into a planet's orbit and performing scientific observations. The planner built the complete needed sequence of commands and sent it to the spacecraft's command execution system. When the execution system came across a simulated failure, the planner automatically built a modified plan starting from the new anomalous situation.

The success of NewMAAP led to the selection of HSTS as the onboard planner of Deep Space One, the first mission of the New Millennium technology demonstration program. HSTS was also applied to two ground-based decision support systems: an

interactive scheduler for the Extreme Ultra-Violet Explorer for the Center for Extreme-Ultraviolet Astrophysics at the University of California, Berkeley, and COSMO, an interactive scheduler to plan the observations of Saturn's rings by Cassini. A prototype of COSMO was built at Ames for the Cassini project. HSTS was enhanced in two areas: more powerful constraint-propagation mechanisms and communication with external software modules. Constraint-propagation mechanisms continuously adjust the range of possible values of decision variables by solving constraints (e.g., inequalities) on these variables. Selection of the exact value of a variable is delayed until constraints from the problem sufficiently restrict its range. This reduces the potential for making decisions with insufficient information and increases the efficiency of the task-planning algorithms. HSTS can now maintain temporal distance constraints on the start and end time of tasks, equality constraints on any variable, and functional dependency constraints such as those found in simple heat-exchange models.

Communication with preexisting and specialized software modules is essential for a task planner tackling realistic application domains. A planning interlingua format was developed to write and read partial task plans on files. This allows the task planner to exchange the results of partial computations with other software modules without the need to know the details of the module's internal organization.

**Point of Contact: N. Muscettola
(415) 604-4744**

A Fuzzy/Genetic Diagnostic System

Silvano Colombano

Modeling of complex systems for such areas as control or diagnosis is sometimes mathematically unmanageable because of nonlinearities or lack of sufficient knowledge about the system. Data-driven models, such as neural networks, are often very successful with these cases. There are problems, however, where the data are very sparse and cannot be relied on to build intrinsic models. These are the types of problems being addressed.

If some prior knowledge about the system exists, it is typically possible to cast it in the form of fuzzy rules. Most uncertainty about the system is then relegated to the definition of all relevant membership functions. The parameters which define these membership functions can then be coded into a "chromosome" string, and a genetic algorithm can be applied to improve the quality of the membership functions. The fitness measure is provided by the closeness in match between the results of the fuzzy modeling system and any data obtained from the real system. This technique differs from data-driven models such as neural networks by the fact that very few data points are required to achieve good generalization.

As an example, this technique was applied to a diagnostic problem. Given sensor readings from a panel that is subject to stresses and given a few fault instances on the same panel, a fuzzy system that could locate new surface faults with good accuracy was built and refined. Note that, while this work was done in the context of a real-world problem, researchers had to proceed in the absence of "real data" and thus take the view that this would simply be a "proof of concept."

A flat square panel of unit dimensions with a group of four sensors that would gather the necessary data was considered.

The panel was divided in 16 regions defined by horizontal and vertical axis labels as shown in the figure. Letters F, U, W, L and R stand for Far, Upper, loWer, Left and Right, respectively.

Sensor values were given linguistic labels HIGH, LOW, and NORMAL. Heuristic rules could be

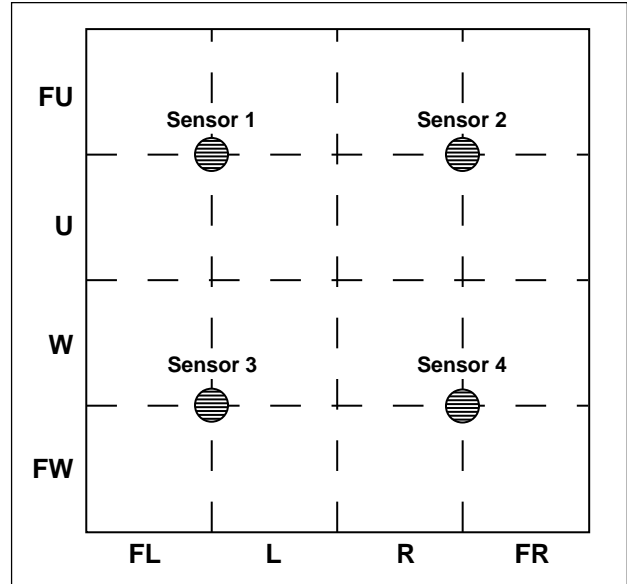


Fig. 1. Location of the strain gauge sensors on a test panel.

defined using these labels. They had a form such as: *If sensor-1 is LOW and sensor-2 is LOW and sensor-3 is HIGH and sensor-4 is NORMAL then fault location has x-coordinate L and y-coordinate FW*, where L and FW define one of the quadrants in the panel.

The designer was then left with the task of deciding what membership functions should be associated with each linguistic value, and of tuning their associated parameters until satisfactory results were obtained. The latter part of the process was assigned to a genetic algorithm for the optimization process.

Point of Contact: S. Colombano
(415) 604-4380

Galileo Probe Vaporization Data Reduction

Frank Milos

The Galileo probe contained an experiment that measured the thickness of the heat shield during the hypersonic entry into the atmosphere of Jupiter. Ten vaporization sensors were embedded in the heat shield at six streamwise locations (as shown in the first figure). Two sensors (1 and 2) were located on the spherical nose, six sensors (3 to 8) were distributed at intermediate points on the frustum, and two sensors (9 and 10) were located on the cylindrical base to measure the probe radius. The circumferential distribution (part (b) of first figure) provided an indication of vaporization asymmetry, which was minimal for the nominal axisymmetric entry. During the 50-second period when the probe decelerated from Mach 50 to Mach 1, each sensor was sampled 84 times at an average time interval of approximately

0.57 seconds. The experimental data were transmitted to Earth several times, and a complete data set of thickness versus time was assembled. The data is noisy during the first half of the experiment, but the probe's final shape is well defined.

The second figure shows the initial and final cross-sectional shapes of the heat shield and preflight predictions of the final shape obtained by two methods. The measured vaporization was 4.6 centimeters at the nose, decreasing to a minimum of 2.79 centimeters at mid-frustum, then increasing markedly to 4.05 centimeters on the frustum near the base. Over half of the heat-shield mass was vaporized. The most critical location was the end of the frustum at the cylindrical base, where the final heat-shield thickness was only 1.0 ± 0.1 centimeter.

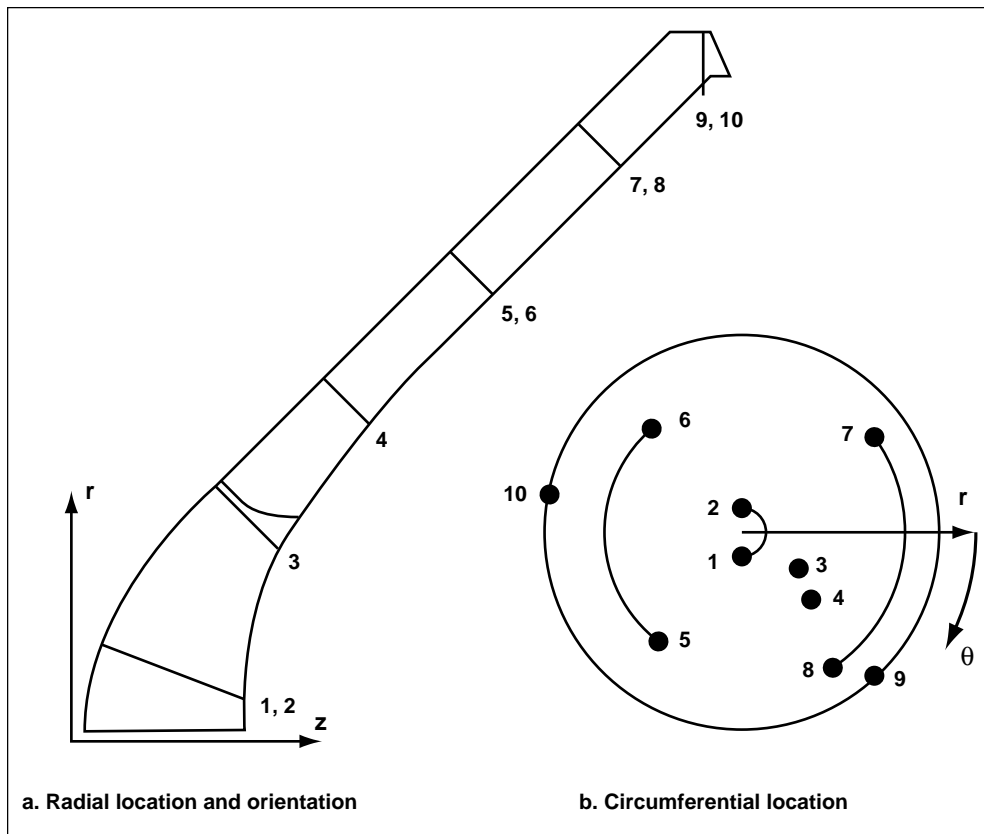


Fig. 1. Position of ten shape-change sensors in the Galileo heat shield. (a) Radial location and orientation; (b) circumferential location.

The predictions were intended to conservatively overestimate the total vaporization; however, both predictions underestimated vaporization over most of the frustum. The Thermodynamic Outer Planets Insulation Code (TOPIC) prediction shows vaporization of 8.75 centimeters at the nose, which is 90% high, and 3.27 centimeters at the end of the frustum, which is 19% low. The Coupled, Laminar, and Turbulent Solutions (COLTS) calculation shows 5.84 centimeters at the nose (27% high) and 2.29 centimeters at the end of the frustum (43% low). The ratio of nosetip to frustum-end vaporization was 0.37 and 0.39 in these two calculations, but the measured ratio was 0.88.

It should be noted that the preflight nominal trajectory was reasonably accurate, and the preflight nominal atmospheric model was surprisingly close to the actual reconstructed atmosphere in the altitude range of interest. Thus, the large discrepancy in heat-shield vaporization ratio warrants an explanation from heat-shield analysts. Nosetip vaporization predictions can be significantly reduced only by decreasing the absorbed radiative heat flux, which

can be accomplished by increasing the surface reflectance or by modifying the radiation model. However, such changes could also decrease the frustum heating and vaporization. Alternatively, the flow field may not be fully turbulent at the nose. To increase frustum vaporization, modification to turbulence modeling may be required, not necessarily to increase frustum convective heating, which is small in comparison with radiative heating at the vaporizing surface, but to alter flow-field species distributions to allow greater radiation penetration.

Some of the heavier, spalled particles from the nose region could impact the frustum and cause an erosion mass loss. However, the total spallation was calculated at only 6% of the forebody mass loss using spallation correlations for Galileo heat-shield materials. Since only a small fraction of spalled particles could have trajectories that impact the frustum, erosion by particle impacts was probably not significant.

Point of Contact: F. Milos
(415) 604-5636

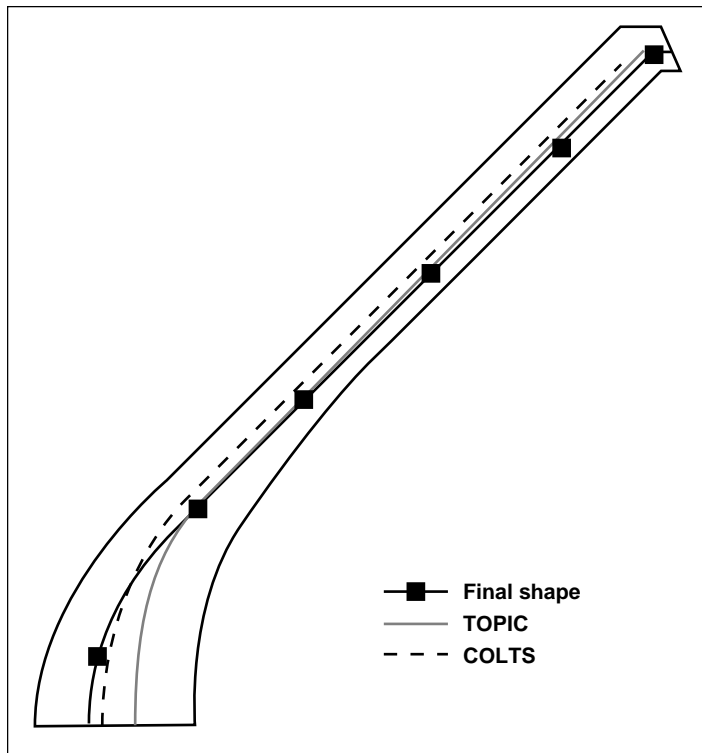


Fig. 2. Comparison of Galileo axisymmetric final shape with two preflight predictions.

Mars Aerocapture Entry

Paul F. Wercinski

Planetary exploration currently stands at a critical juncture in mission design development of orbiter missions in support of robotic planetary exploration. Current and previous studies of orbiter missions to Mars and the outer planets have clearly identified high-energy aerocapture as a critical and enabling technology. Aerocapture involves the use of aerodynamic lift to fly a trajectory through a planet's atmosphere to sufficiently decelerate an entry vehicle to capture planetary orbit. In the past, numerous studies of different configurations of lifting entry vehicles were studied to support the Mars Rover Sample Return, which identified aerocapture as a feasible yet complex and technically challenging concept.

The Mars 2001 Orbiter Mission is currently undergoing pre-Phase A mission studies led by the Jet Propulsion Laboratory. Ames is supporting an aggressive schedule for the feasibility study in the area of aerothermal analysis and thermal protection system (TPS) mass estimates. Planned launch for the spacecraft is February 2001 and arrival at Mars is November 2001. The aerocapture trajectory operation includes the time from atmospheric entry interface, maneuvers within the atmosphere to modulate the trajectory to obtain the desired atmosphere exit conditions, and finally ejection of the heat shield after the vehicle has exited the sensible Martian atmosphere. A typical aerocapture operations scenario is shown in the figure. The aerocapture trajectory was simulated for an inertial entry velocity of 6.52 kilometers per second (altitude = 125 kilometers) and the shallowest entry angle (overshoot trajectory). An overshoot trajectory (constant lift-down) was chosen to obtain the maximum integrated heat load over the range of possible aerocapture trajectories and thus yield a maximum heat-shield TPS mass estimate. In contrast, the undershoot trajectory (constant lift-up) yields the highest peak heating and deceleration forces.

The entry vehicle design was chosen by using proven concepts from the Viking missions and the Mars '98 Lander configuration. The heat load for

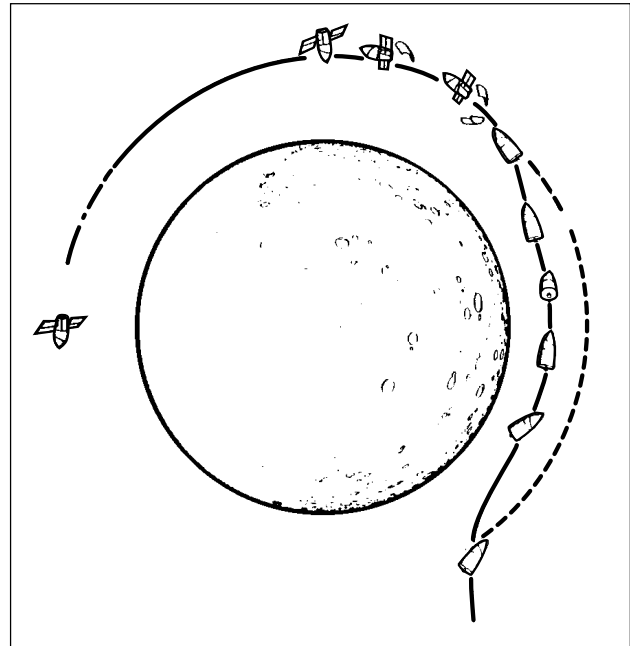


Fig. 1. Typical aerocapture operations scenario.

Mars 2001 is much higher than Mars-Pathfinder and, coupled with the long duration, the heat shield must remain attached to the entry vehicle. Aerothermal and TPS design are more critical for Mars 2001 than the Viking or Mars-Pathfinder.

Several important features of the entry environment of the overshoot trajectory relevant to the aerothermal analysis are: (1) Free-stream Reynolds numbers are lower than Mars-Pathfinder, so that boundary-layer transition to turbulent flow is much less likely for Mars 2001. (2) Shock layer dissociation is more energetic for Mars 2001 than Viking because of the higher entry velocities. (3) Peak heating for Mars 2001 occurs at relatively low pressures (~0.02 atmosphere) which is much lower than Viking or Mars-Pathfinder.

These features indicate the need to perform a full three-dimensional (3-D), reacting-flow, aerothermal flow-field analysis, using the best analytic tools for

modeling both surface and chemical reactions. The analysis represents the first time a series of aerothermal simulations of reacting flow for an axisymmetric blunt body at angle of attack were performed in the carbon dioxide atmosphere of Mars. To conduct a feasibility study, modeling of the complex, 3-D flow fields along the trajectory was performed using a relatively coarse computational grid that captured the unique characteristics of the solution problem, yet enabled rapid convergence and mini-

mized computational requirements. The confidence in the solutions was enabled as a result of experience from Ames' lead support for the Mars-Pathfinder heat-shield TPS design and experience obtained from other complex, 3-D, lifting-vehicle problems such as the reusable launch vehicle program.

Point of Contact: P. Wercinski
(415) 604-3157

Computer Model of a Pulse Tube Cooler

Pat R. Roach, Jeffrey M. Lee, Peter Kittel, Ali Kashani

Many NASA missions need cryo-coolers in space. The most common reason is to increase the sensitivity and reduce the noise of detectors for space telescopes. A new candidate is the Pulse Tube Cooler that can reach temperatures below 10 kelvin and has the advantage, at cold temperatures, of not requiring any moving parts. This advantage increases reliability and lifetime and reduces vibration.

To provide new and innovative pulse tube coolers, a computer model was developed that simulates all the components that make up the system. A pulse tube cooler requires a gas compressor, several heat exchangers where external heat is put into or removed from the system, a regenerator where temperature oscillations of the gas are damped, the open pulse tube itself where the cooling occurs, and an orifice and reservoir where a phase shift between pressure and mass flow is created. These components are shown in the figure that is a sample of the output from the model calculation.

To simplify the calculations, the model was limited to the consideration of only the fundamental-frequency component of the oscillating parameters and to the case of infinitesimal amplitude oscillations. This allows the study of all fundamental processes that affect the performance of the pulse tube cooler, but highly accurate estimates of performance of actual systems having large amplitudes of pressure oscillation or mass flow are not expected.

Nevertheless, the model provides a very useful guide to the optimum trade-off between many conflicting requirements.

The core of the computer model is the treatment of the gas-solid interactions that occur in the regenerator, because this is where the main design choices and compromises must be made to give the best cooler operation. The fact that the gas flow is oscillating back and forth while the gas pressure is also oscillating with a different phase makes an analysis of this part of the system much too complex. The model incorporates detailed equations for both the heat exchange and the pressure drop because of friction between the gas and solid. The regenerator must be designed to damp temperature oscillations in the gas while minimizing the pressure drop across it. While a large surface area and high heat capacity in the solid are needed to damp temperature oscillations in the gas, a large surface area also produces a large pressure drop in the gas. These are conflicting requirements, but the model is invaluable for finding the compromise that produces the best overall cooling.

This model has been designed to be accurate, fast, and easy to use. Its accuracy compares well with other models that either lack all the components of a real cooler or are very tedious and awkward to use.

The figure shows an example of the input data supplied to the model as well as the output information calculated and returned by the model. The calculation only takes a few minutes, and the user can then repeat the process with a different set of

input parameters to find the optimum design configuration.

Point of Contact: P. Roach
(415) 604-3191

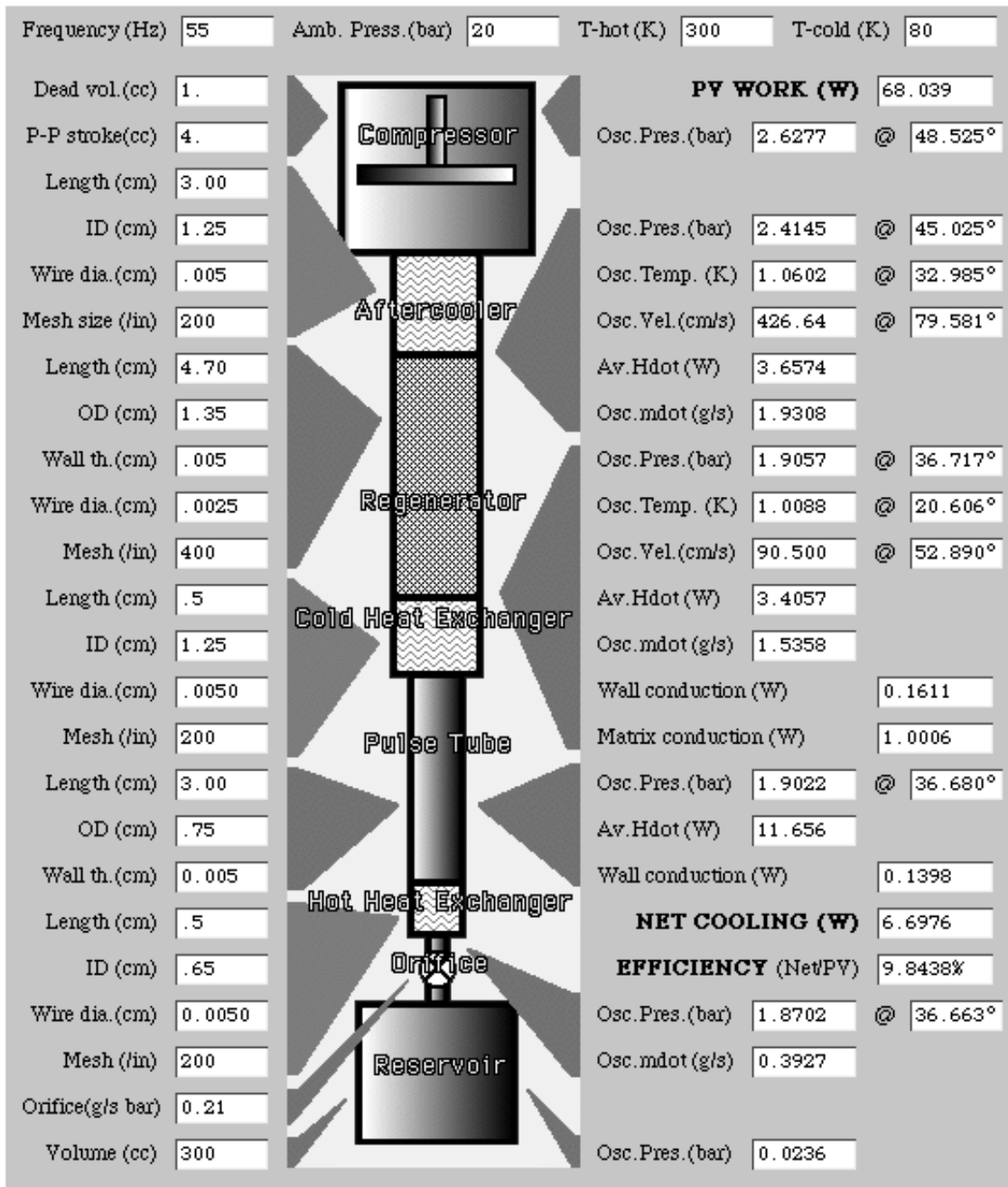


Fig. 1. The components of a pulse tube cooler shown with an example of the data provided by the computer model.

Bacteriorhodopsin Films for Optical Data Storage and Processing

John D. Downie, Dogan A. Timucin

Three-dimensional holographic digital memories promise much greater data density than present optical and magnetic memory media, and also promise increased access speeds since data can be read and an entire page can be written (up to 1 megabit) at a time. Bacteriorhodopsin (BR) is a photochromic protein molecule found in the cell membrane of a type of bacterium that has evolved to survive in harsh (oxygen-deprived) environments. The photocycle of this molecule comprises various stable and metastable states, each characterized by a different absorption spectrum in the visible region. Since the relative population densities of the various states can be controlled by the frequency and intensity of an incident optical field, information can be stored in, or processed by, a BR film by altering the refractive index and the absorption constant of the medium in a desired fashion. BR film is made from dry or hydrated polymer suspensions of BR molecules in an optically thick slab. This fact renders the BR films extremely suitable for a number of optical processing applications, some of which have been demonstrated in the past.

Some of the features that make BR films attractive are their high sensitivity, very high spatial resolution, real-time write/read/erase capability, and extremely low fatigue. The only obstacle for the use of BR films as optical memories has been the lack of a long-lived intermediate state, which made it impossible to store information indefinitely. Fortunately, this problem has been alleviated in the past year by the discovery of an indefinite-lifetime state through chemical alteration of the molecule, thus making BR films a prime choice for optical data-storage applications. Therefore, efforts have been directed toward investigating the potentials of this medium as an optical memory that can surpass other optical media such as photorefractive crystals, as well as magnetic and semiconductor memories, in terms of storage capacity and access time.

In FY95, several experiments were conducted to study the dynamics of the holographic recording, read-out, and erasure processes in BR films. Specifically, experiments with wild type BR films, as well as genetic variants of BR which exhibit longer upper-state lifetimes and a red- (instead of blue-) shifted upper state, were carried out to measure such properties as diffraction efficiencies and decay characteristics as functions of time and recording and read-out beam intensities. These measurements have demonstrated that BR films possess the capabilities to compete with and surpass other optical, magnetic, and electronic data-storage paradigms.

In order to assess the potentials and limitations of BR films more critically, as well as to determine their design parameters more intelligently, a theoretical formalism was also developed to describe the behavior of this medium. Semiclassically, a BR film can be modeled as a two-level medium whose upper- and lower-state population densities are governed by the intensity of the electromagnetic field interacting with the molecules. Since the refractive index and the absorption coefficient of the film are determined by these population densities, the material essentially reacts back on the field through the susceptibility function that appears in the wave equation governing the evolution of the field. The investigation of the dynamics of holographic data storage and retrieval in BR films thus involves the solution of an electromagnetic initial/boundary-value problem in a nonlinear, time-varying, inhomogeneous, absorptive, and dispersive thick dielectric slab. This formalism provides an analytical framework within which BR films can be studied and optimized as optical storage and processing devices.

Point of Contact: D. Timucin/C. Gary
(415) 604-1262/3590

Simulations to Determine Polymer Electrolyte Properties

Richard L. Jaffe, Grant Smith

Computational chemistry methods are being applied to a variety of polymeric materials for dual-use applications. In recent years, simulations of the structural, energetic, and dynamic properties of polymers have been made more reliable by using accurate molecular interaction energies. These interaction energies are obtained from quantum chemistry calculations carried out for model molecules representing monomeric, dimeric, and trimeric pieces of the polymer chain. This research has assisted in the development of new custom-made polymeric materials with specific properties.

An example of this work is the modeling of lithium-salt-poly(alkyl ether) electrolytes proposed for use in lithium-polymer batteries. In these systems, the lithium cation is complexed by several of the ether oxygens on one or more polyether chains. The battery performance is directly related to the mobility of the complexed cations in the polymer matrix. Quantum chemistry calculations were carried out for cation-model ether molecule complexes.

In the figure, a typical complex between Li^+ and 1,2 dimethoxypropane is shown. For this case and certain other conformations of this diether molecule, the cation can interact strongly with both oxygen atoms. (In the figure, the lithium is the cross-hatched sphere and the oxygen atoms are the dark gray spheres, while carbon atoms and hydrogen atoms are represented by medium gray and light gray spheres, respectively.) The interaction energy between a lithium cation and a diether, as determined by the quantum chemistry calculations, is -60 to -70 kilocalories per mole (the minus sign indicates an attractive interaction). These calculations have shown that the ions can complex simultaneously with at least four different ether oxygen atoms. On the other hand, typical anions from lithium salts are only weakly complexed by the ether molecules. For Cl^- and I^- , the interaction energy with an ether molecule is less than -10 kilocalories per mole.

Simulations of LiCl -polyether electrolytes have been carried out. The simulations use classical mechanics to describe the motions of the approxi-

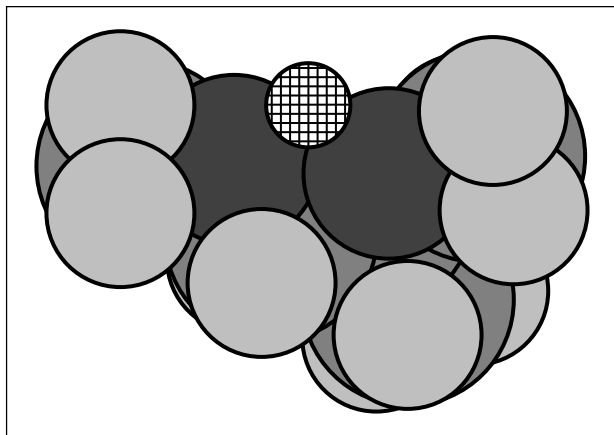


Fig. 1. Complex between Li^+ and 1,2 dimethoxypropane. The lithium is the cross-hatched sphere, oxygen atoms are dark gray, carbon atoms are medium gray, and hydrogen atoms are light gray.

mately 5000 individual electrolyte atoms whose interactions are given by the quantum chemistry calculations. The motions of the lithium cations, chloride ions, and polymer chains were monitored. The mobility of the cations and polymer chains was coupled and less than the mobility of the neat polymer melt. This indicates that the lithium cations act as cross-linking agents by complexing with oxygen atoms on more than one chain. The chloride ions have a greater mobility because they do not interact strongly with the polymer. The Li^+ and Cl^- ions also exhibit the tendency to form ion pairs. This occurs because the ion pairing energy is comparable to the sum of the interaction energies between Li^+ with the polymer and Cl^- with the polymer.

As a result of this work, guidelines for the formulation of improved lithium salt-polyether electrolytes have been identified. The cation transport rate can be increased by decreasing the Li^+ interaction energy with the polymer while also reducing the lithium-salt ion-pairing energy. The former can be achieved by modification of the polymer chain, and the latter can be achieved by switching the

lithium salt to one with a polyatomic anion (such as PF_6^-) where the negative charge is spread around several atomic centers.

This work has commercial applications in that Li-polymer batteries are widely used, for example, in lap-top computers. These batteries have considerable potential as backup energy sources on spacecraft.

Thus this work is of potential benefit to both the Space Science Enterprise and the Human Exploration and Development of Space Enterprise.

Point of Contact: R. Jaffe
(415) 604-6458

New Millennium Electronic Collaboration and Document Sharing

Michael Compton, Helen Stewart, Vinod Baya, Bob Kanefsky, Martha DeAlto

In order to develop "faster, better, cheaper" spacecraft, there is a need to dramatically improve the collaborative ability of the multidisciplinary scientists, designers, technicians, and managers who will be responsible for building and flying these spacecraft. The New Millennium Program Managers need to enable all the geographically diverse members from industry, academia, and other government laboratories to function, interact, and collaborate as effectively as a small, close-knit, co-located team.

The New Millennium Program's Electronic Collaboration and Document Sharing project is helping to meet these needs. The project is providing an integrated suite of Internet-based software tools to improve the collaborative abilities of participants in the New Millennium Program (NMP). Users of the system can quickly and easily share many types of documents (including many types of text files, spreadsheets, graphics, and other design documents) with other team members, regardless of any one user's geographic location or preferred type of computer. For example, a user may create a development plan, budget spreadsheet, and presentation on a Macintosh computer and submit those documents to the NMP web server. The documents will be translated automatically into a platform-independent format and made immediately available to another team member, who happens to use a UNIX workstation at a laboratory on the other side of the country. The system not only permits the sharing of documents, but also permits users to define

and transmit action items, notes, mailing lists, and numerous other collaborative tools. The system even permits the users themselves to dictate the organization of their documents and web pages. The system also includes a search engine for documents, and a database of program member information (e-mail addresses, fax numbers, affiliations, etc.) that can be edited by the users themselves.

One of the main accomplishments for 1995 was the support of the New Millennium Autonomy Architecture Rapid Prototype team, which planned and executed an extremely ambitious development effort that resulted in a very successful demonstration of spacecraft-based autonomy. That team of software developers became the core of the software team for the first New Millennium mission, Deep Space One, and continues to be among the most active users of the system.

The research objectives of the NMP electronic collaboration system include techniques and metrics with which to gauge the utility of various approaches to shared information management. In 1995, one of the main realizations in this area was that users tend to prefer structuring their information for themselves, rather than having to conform to a predetermined set of categories.

Point of Contact: M. Compton
(415) 604-6776

Human Exploration and Development of Space Enterprise



Overview

NASA's mission for the Human Exploration and Development of Space (HEDS) Enterprise brings the frontier of space fully within the sphere of human activity for building a better future for all humankind. Ames supports the HEDS Enterprise by conducting research and by developing technologies, hardware, and systems. An objective of these efforts is to seek knowledge of physical, chemical, and biological phenomena that can be fully explored only in very low gravity. This objective embraces the quest for knowledge of the role of gravity in living systems—one of the goals of NASA's astrobiology efforts, which are led by Ames as the NASA-designated Primary Center for Astrobiology. A complementary objective is to facilitate the application of this phenomenological knowledge, where feasible, to enrich life on Earth. A third objective is to develop information systems for achieving routine exploration of space—one of the goals of NASA's Center of Excellence for Information Technology at Ames. During FY95, numerous research and technology efforts were accomplished, addressing the following goals of the HEDS Enterprise:

- Increase knowledge of nature's processes using the space environment.
- Enrich life on Earth through people living and working in space.
- Achieve routine space travel.

New knowledge and an increase in the understanding of nature's processes related to the influence of gravity on living systems are acquired by a three-pronged approach: (1) Ground-based and flight hardware that range from small animal habitats for the space station to the human-powered centrifuge and powered linear sled (PLS) are developed to support life-sciences experiments in spaceflight. (2) A suite of unique ground-based facilities is used by investigators from around the world to study the role of gravity on living systems—from single cells in culture to humans. Among these unique capabilities are the Hypergravity Facility for Cell Culture (HyFaCC) and the Human Research Facility, where "head-down bedrest" microgravity simulations are conducted. (3) Ground-based and flight experiments

are conducted on the role of gravity in living systems, including biological systems as diverse as regulatory and metabolic, cardiovascular, neurological, and perceptual.

In this report, accomplishments related to the development of facilities, the performance of experiments and research, and the development of processes are highlighted. Facilities that were designed and built include a PLS for investigating how the body's balance organs function on Earth and after exposure to altered gravity, and the HyFaCC to study the effect of hypergravity on cell proliferation or differentiation under chronic, controlled conditions.

For the first time, a pilot study was conducted prior to a flight mission, dedicated to human life sciences space research to refine procedures, optimize timeliness, and resolve potential experiment conflicts. Experiments were conducted to further reduce or prevent the re-entry syndrome experienced by astronauts after spaceflight. Research was carried out to simulate voltage changes in neurons and their endings. Reports on the development of processes include one for efficiently monitoring and displaying physiological data using a Pentium-based system and the other for providing access to archived human biomedical data collected in space.

Research and technology development programs are continually evaluated for their potential commercial impact, economic benefits, and health applications. The potential and impact of ground-based facilities such as the PLS and the HyFaCC are assessed as they are used as research tools. One certainly might envision linear sleds being important in the testing of balance organs in human clinical populations; and understanding the basic function of cells in response to gravity levels greater than Earth's might lead to the use of hypergravity as a tool for investigating the use of drugs or other treatments for

bone-cell models of osteoporosis while controlling for gravitational loading.

Likewise, the space-based systems are evaluated for enriching life on Earth. Specifically, the application of remote sensing, geographic information systems, and related technologies is promoted for addressing issues of health on Earth. An example of this application is the reported prediction of the malaria transmission risk along the Pacific coastal plain of Chiapas, Mexico.

Knowledge and techniques in exercise physiology to maintain the health of astronauts in spaceflight also have the potential to enrich human health on Earth. For example, the Ames Autogenic Feedback Training System offers advantages to commercial health entities.

Exploration and development of space, the Moon, or Mars bring people and machines together to overcome the challenges of distance, time, and the environment. To achieve routine space travel, a major requirement is to make human/machine interactions efficient, effective, and reliable.

Progress reports, such as the following, are presented to illustrate the types of activities being performed to make space travel routine. (1) On board both the Space Shuttle and the Russian Mir space station during the STS-76 mission, a wireless server and two commercial-off-the-shelf mobile computers were successfully tested to demonstrate the feasibility of wireless mobile communications for noncritical applications in space. (2) In collaboration with NASA's Johnson Space Center, a Field Deployable Trainer was developed and implemented on a laptop computer to help astronauts learn an in-flight maintenance procedure. (3) A compact, relatively uncomplicated biological life-support system to grow a wheat crop was developed.

Powered Linear Sled for Research on Mammalian Gravity-Sensors

Dan Kalcic, David Tomko, Tom Wynn

Researchers at Ames Research Center established specifications for a Powered Linear Sled (PLS) to investigate the body's balance organs function on Earth and after exposure to altered gravity. The device was designed and built for installation in Ames' Vestibular Research Facility or for use in the field (for example, launch/landing sites). The PLS includes a payload carriage that rides on air bearings traveling on precision-ground ceramic ways, powered by a linear motor. As shown in the first figure, the device may be operated either horizontally or vertically, producing low-distortion sinusoidal linear motion to the payload.

The apparatus was designed to carry payloads up to 75 pounds, with a servo-controlled sinusoidal

acceleration from 1 to 5 hertz (0.75 gravity (g) peak). Engineering tests have shown that during horizontal operation at low gravity levels (<0.2 g) distortion (out of plane accelerations) and noise (acceleration profile deviation) levels do not exceed 0.001 g which is just below the threshold of perception of human and animal subjects. At gravity levels of 0.2 to 0.75, the distortion and noise levels are approximately 0.003 g during horizontal operation. During vertical operation, distortion and noise levels range from 0.01 to 0.03 g. The increase in noise levels when the sled is operated in the vertical mode is caused by friction in the equilibrator system. The equilibrator system is an air balancing system that equalizes the weight of moving components and greatly eases motor control.

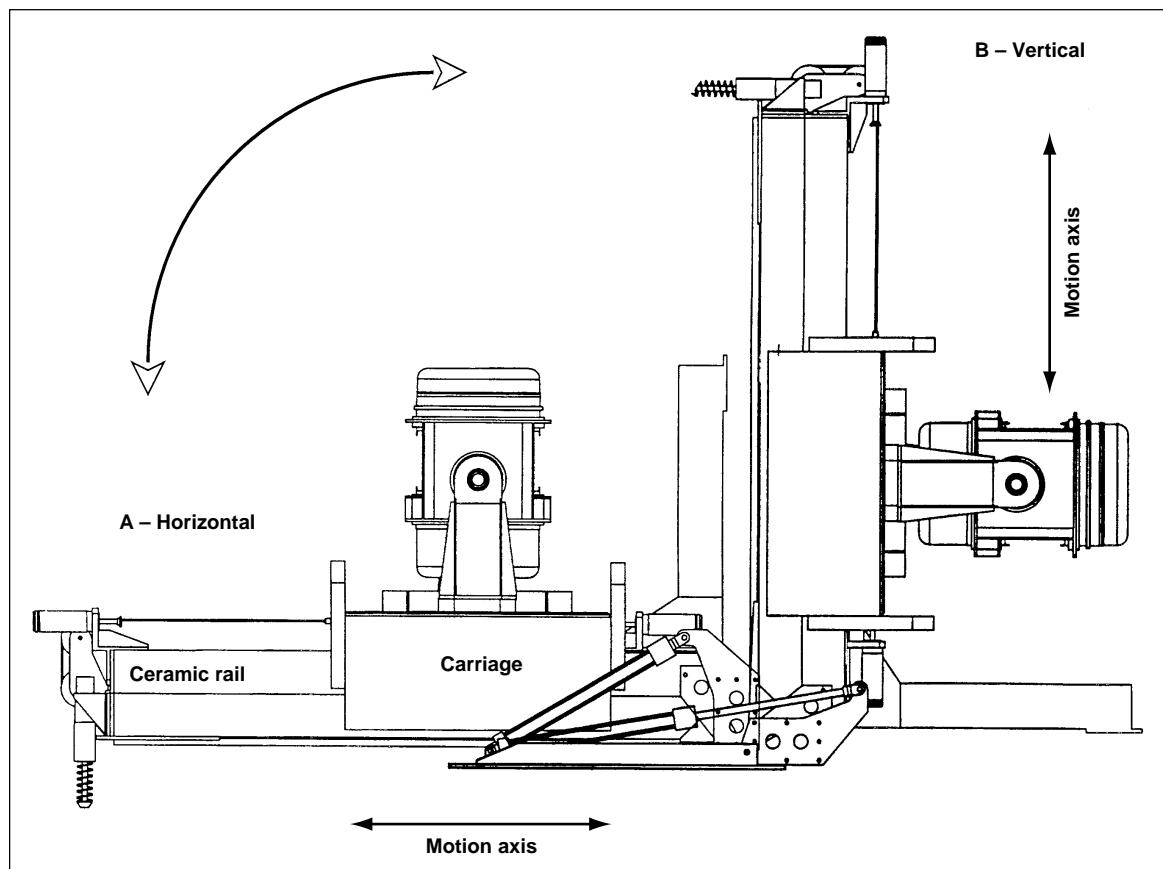


Fig. 1. Schematic drawing of PLS deployed in horizontal (A) and vertical (B) modes of operation.

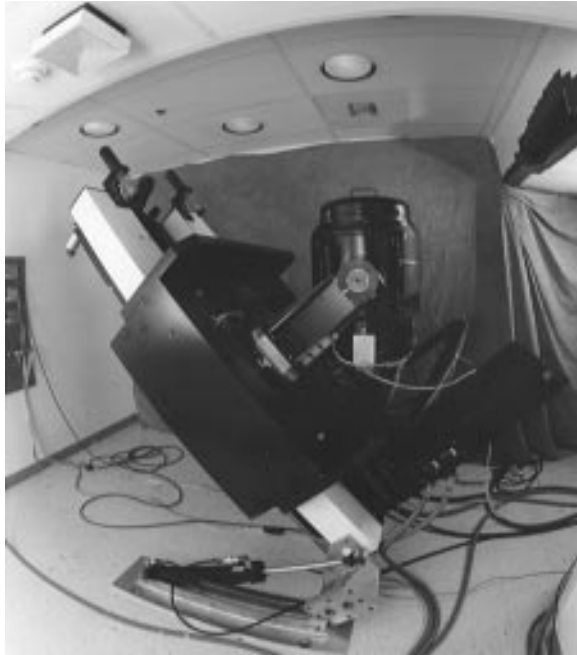


Fig. 2. Photograph of PLS deployed in 45 degree position, midway between vertical and horizontal.

The drive system consists of a brushless DC linear motor which features non-ferrous materials. The use of non-ferrous materials permits operation without “cogging” effects that occur when ferrous materials are used. This cogging effect can cause unwanted accelerations far in excess of the milli-gravity noise specification of the PLS. At the present time, the drive system is set up for sinusoidal motion, but the control system for the PLS can easily be modified to provide any desired motions.

The horizontal/vertical tilt mechanism for the PLS consists of a hand-operated hydraulic pump/overcenter valve system that permits change of operating mode within five minutes. The system is protected against a runaway load scenario as well as hose failure. Pitch, yaw, and roll positions of test subjects are also variable via roller-type bearings. When the desired position is achieved, over-center type clamps are locked and testing may begin. In the second figure, the device is shown during the transition between the horizontal and vertical positions.

Point of Contact: D. Kalcic
(415) 604-3761

Hypergravity Facility for Cell Culture

Alexandre C. L. Malouvier, Emily Morey-Holton

The effects of gravity at the cellular level are poorly understood. Many experiments have investigated the effects of spaceflight or clinostating on cultured cells, but very little is known about the effects of hypergravity on cell proliferation and/or differentiation under chronic controlled conditions. A facility that allows long-term hypergravity studies of cultured cells was designed and constructed: the Hypergravitational Facility for Cell Culture (HyFaCC).

An existing human centrifuge, the Human-Carrying Rotational Device (HCRD), has been modified by replacing the human cabin with a laboratory cell culture incubator. This new facility consists of the following elements as shown in the figure: (1) the HCRD; (2) the hypergravity incubator; (3) the unit gravity control carbon dioxide (CO₂)

incubator; and, (4) the control and data acquisition systems (not shown on the figure).

The HCRD is a single-arm, 2.74 meter (9 foot) radius centrifuge that is composed of a platform placed on an oil film bearing. Hydrostatic bearings provide for precise angular accelerations (0.1 degrees/second²) with a rise time of 0.1 second with minimal vibration. The 20 horsepower motor operates at a maximum of 45 revolutions per minute with a gravity force (g) onset of 0.007 to 0.52 radians/second². The maximum g level that can be safely obtained for long duration experiments is currently 6.5 g at the bottom of the incubator. Since this new facility was designed for long-term studies, an oil cooling system was added to enable precise control of the oil-bath and to avoid possible overheating of

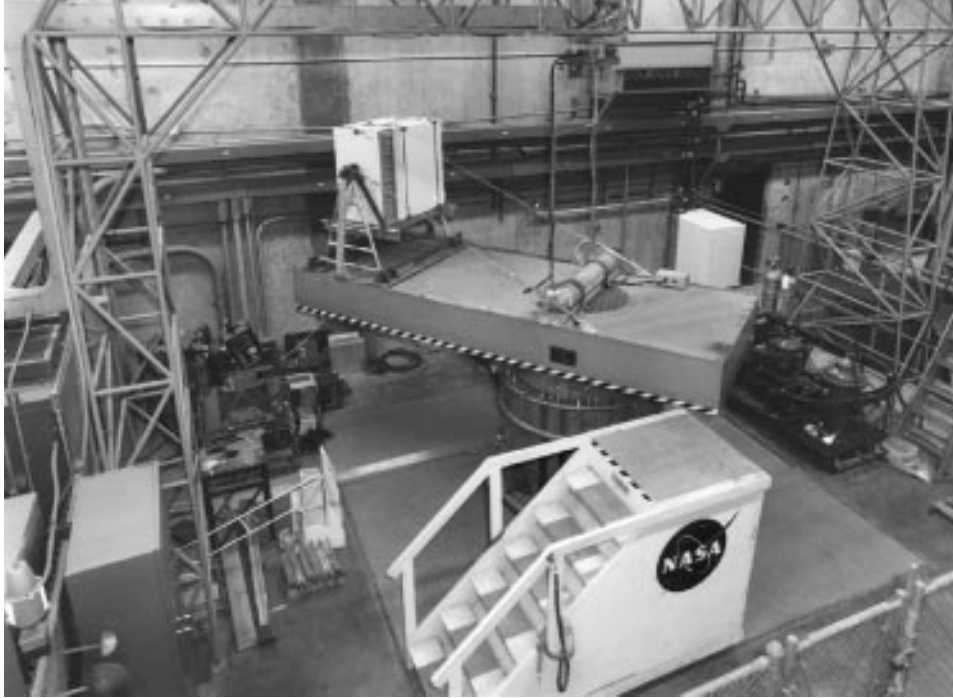


Fig. 1. Picture of the HyFaCC showing the centrifuge (HCRD) with an incubator mounted on a swinging platform, and the CO₂ cylinder placed on the center of rotation. The control incubator is located in a corner, behind the centrifuge.

the oil bearing. A modified CO₂ incubator is mounted on a swing platform with the attachment point located 2.33 meters (7.66 feet) from the axis of rotation. The Forma Steri-Cult 3033 is a high capacity CO₂ incubator and has an air jacket for temperature maintenance. Its internal dimensions in centimeters are 69.09 wide by 83.69 high by 51.44 front-back (19.20 × 32.95 × 20.25 inches). The incubator precisely controls temperature, CO₂ concentration, and relative humidity. The built-in HEPA-filtering system minimizes airborne contamination. The g forces are always applied in the z-axis, perpendicular to the floor of the swing platform. Accelerometers are placed under the incubator to monitor g-levels in the different axis. An onboard CO₂ cylinder is attached to the HCRD near the center of rotation, and is directly linked to the incubator CO₂ port through a two-stage pressure regulator. A built-in compartment is located under the incubator and provides additional space for control or recording hardware (for example, automated cell culture control unit). A CO₂ incubator, identical to the Hypergravity incubator, is

placed by the side of the centrifuge, in the same high-bay. The centrifuge and the incubators are controlled and monitored from a separate control room. A data acquisition system is added to monitor cell culture conditions.

Cells are cultivated at the Central Cell Culture Facility located in a building adjacent to the HCRD. They are transported in sealed, isothermal containers from the Cell Culture Facility to the centrifuge. Since the incubators are standard laboratory equipment, any type of culture dishes can be used in the HyFaCC. It is preferable to use sealed vessels (flasks instead of Petri dishes) for sterility reasons. Any type of equipment that can be placed in an incubator, for example, peristaltic pump or automated cell culture devices, can be used on the centrifuge provided it is previously tested and approved. Three conditions can be studied: 1 g in the laboratory, 1 g in the control incubator, and hypergravity onboard the centrifuge. Since the hypergravity incubator is placed on a swinging platform and the shelves are located at

different radii from the center of rotation, the cells experience an increasing gradient of g-levels when going from top to bottom in the incubator. As a result, different hypergravity conditions can be studied simultaneously. The centrifuge is stopped three times per week to allow media changes, but it can run unattended for at least a week. Experiments

last for three to four weeks of operation without major maintenance. The HyFaCC is a unique facility unequaled worldwide.

**Point of Contact: A. Malouvier
(415) 604-3057**

Pilot Study for Human Research Experiments Planned for the Life and Microgravity Sciences Spacelab Mission

Sara B. Arnaud, D. O'Hara

This pilot study was a type of dress rehearsal for the life sciences experiments selected for the Life and Microgravity Sciences Spacelab mission (LMS). Pilot studies were performed for Cosmos missions using surrogate flight animals and flight-like equipment, but this is the first study dedicated to human life sciences space research to precede a mission. The study was designed to provide data for eight subjects, a statistically more valid sample than the four mission specialists who will participate in the experiments during the mission. The overall goals of the study were to refine procedures, optimize timelines, and resolve potential experiment conflicts well before launch.

The scientific priorities of the flight experiments are to establish a comprehensive description of the effects of microgravity on the function of human skeletal muscles and to investigate the metabolic and cellular basis for the muscle weakness and wasting that occur in space. Experiments will also evaluate the organ systems essential to muscular activity, for example, the bone, lung, endocrine, and central nervous systems. The ground-based pilot study used the 6-degree head-down tilt bed-rest model to simulate spaceflight. Muscle structure and function were evaluated directly by a set of six muscle experiments. A second set of three experiments, grouped as metabolism studies, evaluated pulmonary function, energy metabolism, and bone; and a third set of three

experiments assessed the performance of the central nervous system before, during, and after bed rest. The pilot study mimicked the experimental procedures as closely as possible and used the equipment available for ground-based research as well as some of the equipment for the mission. The specialized torque velocity dynamometer, built for the LMS mission to measure forces during different types of muscle contractions, was unavailable for the pilot study. Instead, investigators used the more familiar equipment illustrated in the figure.

Scientists representing the 12 experiments arrived two weeks prior to the study to support the orientation, equipment installation, and safety checks that preceded the subject training exercises. Eight male volunteers were admitted in two groups (two days apart) to stagger the control (14 days), bed rest (17 days), and recovery (14 days) testing periods.

This pilot study demonstrated the feasibility of carrying out a number of planned experiments simultaneously. The integrated schedule for four muscle experiments developed for this study was critical to this achievement. Carefully planned daily schedules for two groups of four subjects, which allowed experiments to be repeated at the same time of day for each subject while maintaining regular controlled diet meals, were key to the success of the experiments.



Fig. 1. Two dynamometers (LIDO (left) and Cybex (right)) were used to study muscle function in the LMS pilot study.

At the beginning of the study, a major concern was partially resolved. Both the intensity and frequency of exercise from the muscle-testing protocols may have acted as a countermeasure for the problem under investigation (muscle testing and weakness). Some effect of bed rest was observed in most of the musculoskeletal experiments. Lean-body mass decreased in similar fashion to the change in nitrogen balance. In other experiments, there was indirect evidence of increased bone resorption and depression of body temperature, both indications that the bed-rest effect was not compromised by the muscle-testing protocols. Another concern was the potential effect of the rigorous muscle-testing schedule on cerebral function. Although insomnia occurred during the early bed-rest period, muscle testing did not appear to have a negative impact on cognitive performance.

Based on the pilot study experience, 6 of the 12 groups of scientists made minor revisions in the protocols for the flight experiments. The impact of one experiment on another was considered positive in four of the investigations because data sharing enabled scientists to study or predict related responses. One potential scheduling conflict was identified and resolved for the mission sequence. The scientists generally considered the pilot study to be of value to their flight experiments, the science program, and the science issues addressed. Proof of the head-down tilt bed-rest model for simulating microgravity effects will not be known until after the mission.

**Point of Contact: A. Hargens
(415) 604-5746**

Cycle-Powered Short Radius (1.9 m) Centrifuge: Exercise versus Passive Acceleration

J. E. Greenleaf, D. P. Gundo, D. E. Watenpugh, G. M. Mulenburg, N. Marchman, R. Looft-Wilson, A. R. Hargens, S. M. Bowley

In addition to extensive use of lower extremity physical exercise training as a countermeasure for the exercise component (work capacity) of spaceflight deconditioning, some form of additional head-to-foot (+Gz) gravitational (orthostatic) stress may be required to further reduce or prevent the signs and symptoms (nausea, vertigo, instability, fatigue) of the general reentry syndrome. This condition can potentially incapacitate astronauts during and after landing

in the space shuttle. Orthostatic stress, that is, blood moving into the legs, can be induced by lower body negative pressure and by +Gz acceleration. One important question is whether passive acceleration training alone, or with concurrent leg exercise training, can provide sufficient additive stimulation to reduce the general reentry syndrome. A new human-powered centrifuge, shown in the first figure, may be the answer.

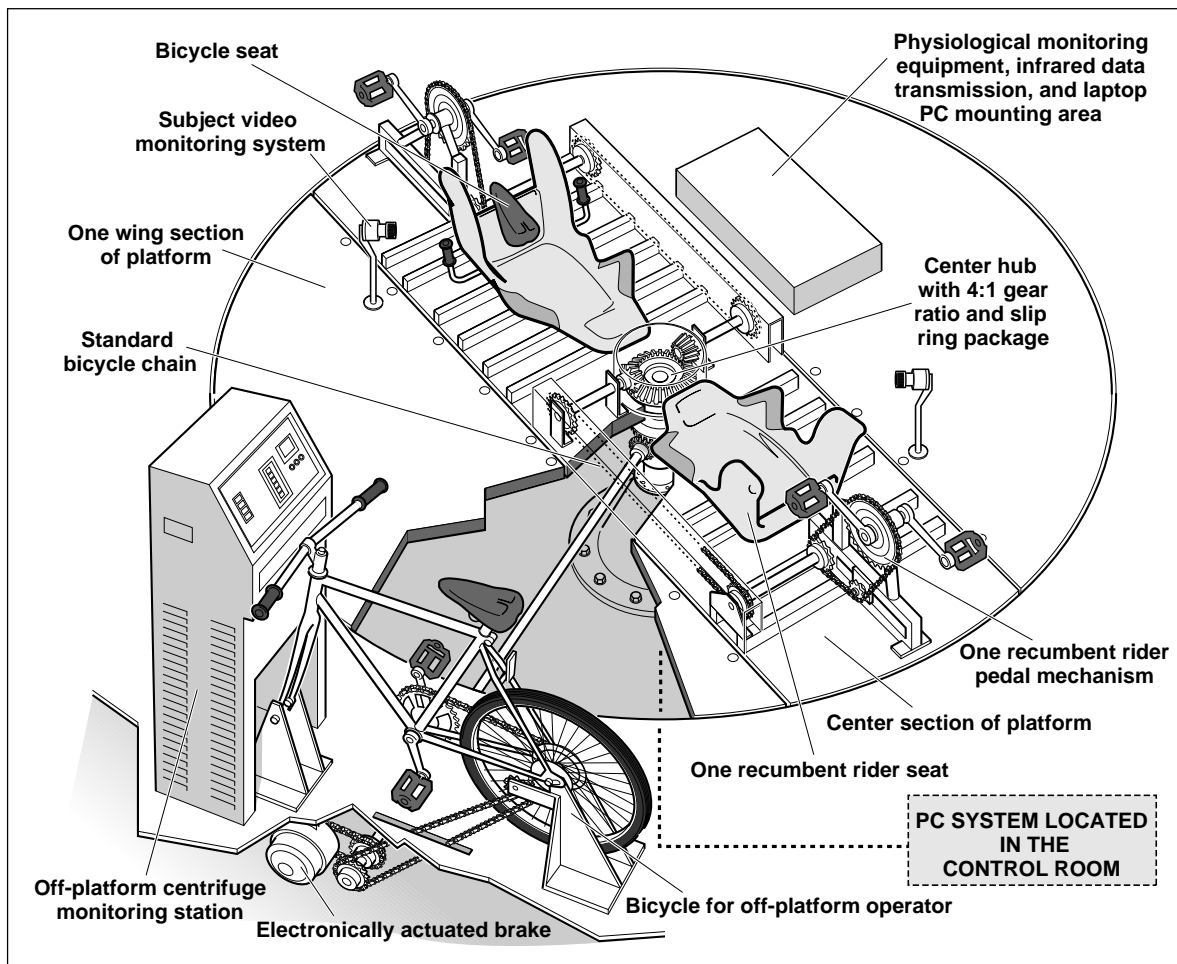


Fig. 1. Schematic of human-powered, short-arm centrifuge.

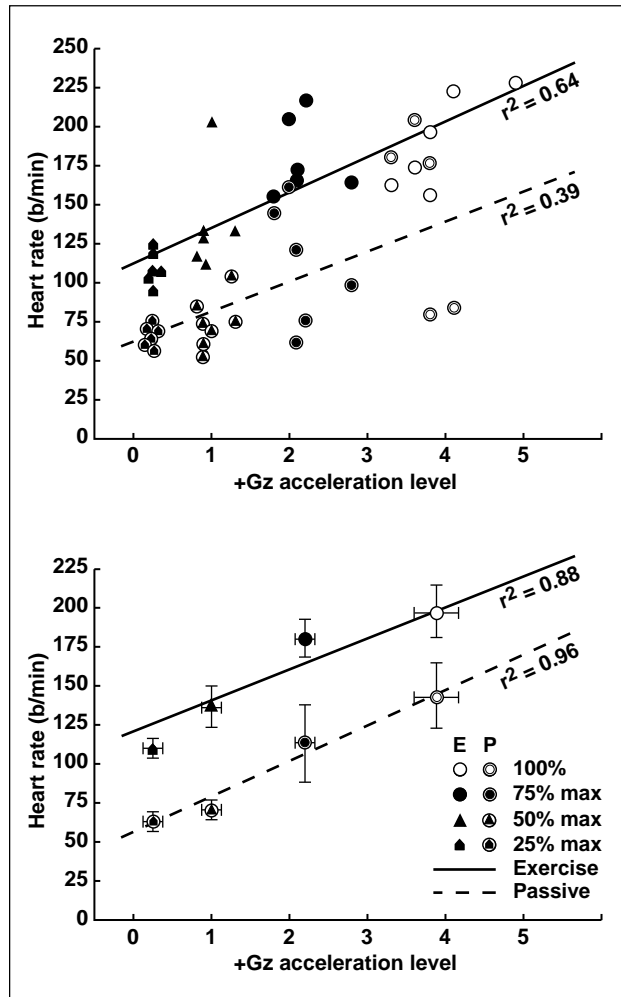


Fig. 2. Regression of heart rate on +Gz acceleration level for the 120 second submaximal (25%, 50%, 75%) and maximal (100%) exercise (E) acceleration (solid lines) and passive (P) acceleration (dash lines) runs. Individual (upper panel) and mean (lower panel) heart rates are given. r^2 = square of the correlation coefficient.

The purpose of this study was to compare heart rate response, as an indicator of body stress, in five men, 35 to 62 years of age, and two women, between 30 and 31 years of age, during exercise acceleration versus passive acceleration (by an off-board operator) at 100% maximal acceleration (Amax), and at 25%, 50%, and 75% of Amax. Mean (\pm standard error) Amax was 43.7 ± 1.3 revolutions/minute ($+3.9 \pm 0.2$ Gz). Mean heart rate at exercise Amax was 192 ± 12 beats/minute (50–70 second run time), and 142 ± 22 beats/minute at passive Amax (40–70 second run time) (second figure, upper half). Regression of mean heart rate at the various +Gz levels indicated correlations of $r^2 = 0.88$ (exercise) and $r^2 = 0.96$ (passive) (second figure, lower half). Exercise heart rate of 107 ± 4 (25%) to 192 ± 12 (100%) beats/minute were 43–50 beats/minute higher ($p < 0.05$) than comparable passive heart rate of 64 ± 2 to 142 ± 22 beats/minute. Thus, exercise adds significant physiological stress during +Gz acceleration. Inflight use of the combined exercise and passive acceleration countermeasures may maintain work capacity as well as normal orthostatic tolerance and could reduce or eliminate the general reentry syndrome.

Point of Contact: A. Hargens
(415) 604-5746

Exercise Prevents Bed-Rest Deconditioning

Donald E. Watenpugh, Richard E. Ballard, Jacqueline M. William, Andrew C. Ertl, Suzanne M. Fortney, Stuart M. C. Lee, Wanda L. Boda, Alan R. Hargens

Integrated physiological countermeasures are needed to maintain upright posture and exercise performance after spaceflight. For example, in an emergency landing of the Shuttle, astronauts may need to escape and run from the spacecraft quickly. At present, astronauts return from long-duration spaceflights in a relatively debilitated condition, in spite of the exercise countermeasures currently employed.

In two separate bed-rest studies to simulate spaceflight, it was proposed that supine exercise during lower body negative pressure (LBNP) would prevent bed-rest-induced deconditioning. Fifteen male subjects underwent five days of 6-degree head-down bed rest: five control subjects did not exercise, and 10 performed 30 minutes/day of supine interval treadmill exercise followed by five minutes of static (resting) LBNP. One body weight of footward force was generated by 55 ± 3 millimeters Mercury LBNP during supine exercise on a vertical treadmill and subsequent static LBNP at the same level. Pre- and post-bed-rest tolerance to upright posture was assessed with head-up tilt. Mean tilt tolerance was maintained in subjects who performed 30 minutes

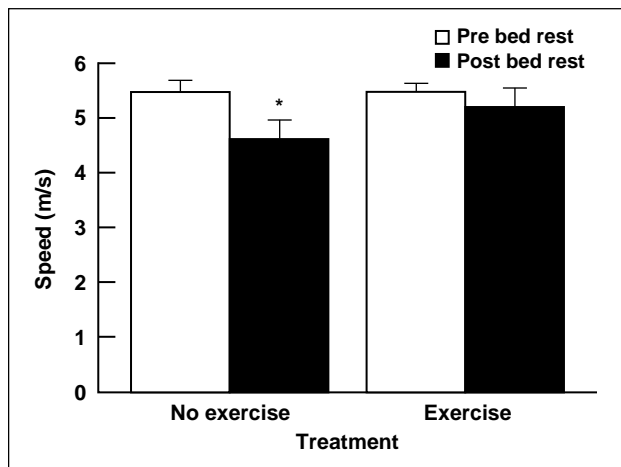


Fig. 1. Daily LBNP exercise maintained peak upright oxygen consumption at pre-bed-rest levels. Mean peak oxygen consumption decreased 14% after bed rest with no exercise (* $p < 0.05$).

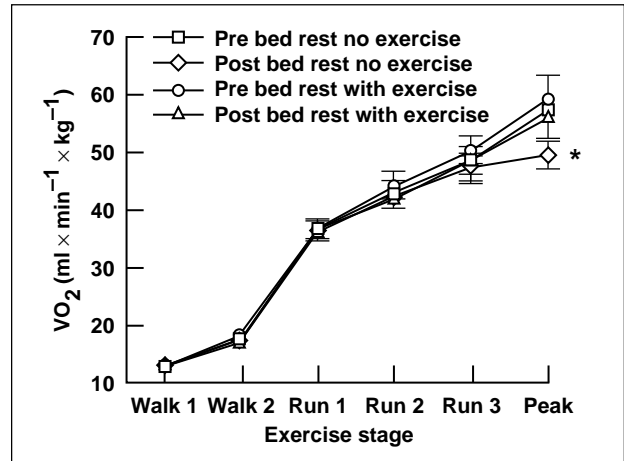


Fig. 2. Sprint speed from a standing start was maintained at pre-bed-rest levels when daily LBNP exercise accompanied bed rest. However, bed rest without daily LBNP exercise significantly reduced sprint speed (* $p < 0.05$).

per day LBNP exercise during bed rest. In contrast, tilt tolerance time in non-exercising bed-rest subjects decreased significantly by 18% ($p < 0.05$). Hematocrit increased from $41.8 \pm 1.1\%$ to $45.0 \pm 1.0\%$ in the control group during five days of bed rest, indicating substantial loss of blood volume, whereas blood volume was maintained in the group performing LBNP exercise.

These results indicate that LBNP exercise during bed rest prevents blood volume loss, which, in turn, helps maintain upright posture following bed rest. It was also proposed that daily supine exercise during LBNP maintains upright exercise responses after five days of 6 degree head-down bed rest. Neither control nor exercising subjects showed statistically significant reduction of peak oxygen uptake after bed rest. However, only the control group exhibited significant post-bed-rest increases in heart rate and ventilation during sub-maximal treadmill exercise relative to pre-bed-rest responses. This indicates that the control subjects had become deconditioned while the LBNP exercisers had not.

The promising results from the five-day bed-rest study led to the performance of a two-week bed-rest

study. LBNP exercise duration was increased to 40 minutes daily and footward force to 1.0–1.2 body weights, but the five minutes of static LBNP after each LBNP exercise session was omitted. The responses of seven male subjects to two weeks of bed rest with and without daily supine LBNP treadmill exercise were compared. Subjects' time to exhaustion during upright treadmill running decreased 10% after bed rest with no daily LBNP exercise, whereas exercise during bed rest maintained running tolerance time at pre-bed-rest levels. The first figure shows that daily LBNP exercise also maintained peak upright oxygen consumption at pre-bed-rest levels. Mean peak oxygen consumption decreased 14% after bed rest with no exercise. The second figure illustrates that sprint speed from a standing start was maintained at pre-bed-rest levels when daily LBNP exercise accompanied bed rest. However, bed rest

without daily LBNP exercise significantly reduced sprint speed.

Results from the two-week bed-rest study clearly confirm that 40 minutes per day of supine LBNP exercise maintains upright exercise function at pre-bed-rest levels. These results indicate that supine exercise during LBNP is effective in maintaining upright exercise responses during bed rest, and should be considered as a possible countermeasure to help sustain astronauts' ability to escape a spacecraft upon emergency landing. The findings strongly support continued development of LBNP exercise as a cost-effective alternative to centrifugation for periodic simulation of gravity and preservation of unit gravity function during long-term spaceflight.

Point of Contact: A. Hargens
(415) 604-5746

Finite Volume Simulation of Neuron Activity

Muriel D. Ross, Samuel W. Linton

Mesh generation is a critical step in the three-dimensional (3-D) reconstruction of objects from serial sections of biological tissues. This technique connects registered contours by polygons, producing a mesh (or grid) that describes the surfaces of the objects under reconstruction. Once the mesh is generated, the surface of even complex, branched objects such as neurons or blood vessels can be visualized as shaded solids or as semi-transparencies.

The mesh is useful for a number of other applications in the study of biological tissues. Here, a specific application is considered. This application has led to the development of a new, finite-volume method for simulating voltage changes in neurons (nerve cells) and their endings. In contrast to typical compartmental models which lump parts of a neuron together for simulation, a finite-volume method takes into account all nuances of shape and then computes electrical changes in them. A finite-volume model should, therefore, provide more accuracy.

For developmental purposes, neuronal endings in gravity sensors are used. Gravity sensors consist of

type I and type II detecting cells, specialized bottle-shaped "calyx" endings of nerve fibers that transmit information to the central nervous system and supporting cells. As shown in the figure (see Color Plate 23 in the Appendix), each calyx has an inner and an outer surface separated by cytoplasm, and the calyx typically has twig-like branches. Both type I and type II cells communicate with the neuron endings through "synapses," which are sites of chemical release that stimulate receptor sites on the neuron ending. Type I cells sit inside of a calyx and communicate with the inner surface of a calyx, while type II cells synapse with the outer membrane of a calyx or with the ends of the calyceal branches. When enough synapses are activated simultaneously, a rapid change in voltage results, and the nerve fiber extending to the central nervous system discharges. The discharge is initiated at a special region called the spike initiation zone.

The method developed for this simulation provides for a continuous mesh that describes the

nerve fiber and its spike initiation zone, each calyx (outer and inner membranes), and the little branches that extend from them to type II cells. For the simulation described here, a nerve fiber with three calyces that have branches was considered, as shown in the figure. Each component of the ending is a model representation based on averaged dimensions derived from measurements of many photographed examples (electron micrographs).

First, an integral equation is formulated, and the entire domain to be simulated is discretized into finite volumes. The finite volumes for the calyx are triangular prisms. The branches and nerve fibers, which are roughly cylindrical, are discretized into frustums; and the terminal of a calyceal branch is also treated as a frustum. The finite-volume method balances change in electrical charge within each finite volume, with the flux of the charge through the surface of each volume. The type I and type II hair cells need not be included in the simulation, only the voltage changes induced by activation of synapses at receptor sites on the calyces and nerve fiber branches. Although details are not provided here, many constraints are considered mathematically by the simulation, such as the resting state of the neuron, synapse conductance change and effective period, membrane resistivity, intracellular resistivity, membrane capacity, and electrotonic length.

An IBM parallel processing supercomputer and a Silicon Graphics Indigo workstation were used for the simulations. To visualize voltage levels, color-coding

was employed, with dark blue representing the resting state and red, depolarization and discharge. Use of color-coding permits an investigator to follow changes in voltage over time after any variety of combinations of synapse activation. In the example illustrated in the figure, a newly discovered property of neurons, back-reflection of depolarization from the spike initiation zone, is demonstrated. In the time step shown, the nerve fiber has spiked and a reflected wave of depolarization (at right, note red color) is flowing back into the nerve fiber and its calyces and calyceal branches, which are in various voltage states.

The finite-volume method of computer simulation permits the study of the effects caused by this phenomenon on near and distal parts of the ending. This is but one example of the usefulness of a finite-volume method of simulation of neurons. Eventually, it will be possible to visualize other effects using a variety of synapse activation sites in networks of neurons, and to include molecular events at synapses to discover new knowledge of how living neuronal circuits develop and are altered. Additionally, this type of simulation is readily ported into virtual reality for interactive research with investigators at remote sites.

**Point of Contact: M. Ross
(415) 604-4804**

A Pentium-Based System for Physiological Monitoring and Displays

Patricia S. Cowings

Ground-based research to study the physiological effects of microgravity is dependent upon the acquisition and processing of physiological data. In the past, the real-time processing of these data has been difficult to achieve because of the requirement for dedicated instrumentation to calculate and display derived variables such as cardiac output, vascular resistance, thoracic fluid changes, and vagus nerve activity. The dedicated instrumentation tends to be physically large (non-portable) and expensive (because of engineering input needed to design and build specific functions), and the algorithm modifications are difficult to achieve. Implementation of a digital system, based on a Pentium/90 or similar computer, serves to reduce the physical size, is less expensive, and is easier to modify since the functions are software-programmable.

In both the U.S. and Russian space programs, a great deal of effort is being spent studying the effects of long-term exposure to reduced gravitational fields. The objective is to develop effective countermeasures that will minimize the deleterious effects of microgravity on the human body. The approach used in the Psychophysiology Laboratory involves the use of Autogenic Feedback Training (AFT) to eradicate or reduce space motion sickness and the dizziness that can occur when flight crews return to the gravitational effects of a terrestrial existence. The AFT methodology requires the real-time acquisition and display of 16 input variables, 20 digitally-displayed output variables and printed averages, plus coupled audible tones, voice commands, and respiratory pacing signals. The 16 input and 20 output channels are shown in table 1.

Table 1. Listing of analog inputs and digital outputs. Displays are updated at five times per second and can be coupled to an audio-tone generator for additional feedback signals.

Analog inputs	Processed digital outputs
Blood flow detector (1)	Right finger pulse volume changes
Blood flow detector (2)	Left finger pulse volume changes
Blood flow detector (3)	Toe pulse volume changes
Blood flow detector (4)	Temporal artery flow
Respiration	Respiratory rate
Electrocardiogram	Heart rate
Skin temperature	Skin temperature
Skin conductance level	Skin conductance level
Left arm electromyograph	Left arm muscle activity
Right arm electromyograph	Right arm muscle activity
Left leg electromyograph	Left leg muscle activity
Right leg electromyograph	Right leg muscle activity
Systolic blood pressure	Systolic blood pressure
Diastolic blood pressure	Diastolic blood pressure
	Mean arterial pressure
Thoracic electrical impedance	Thoracic fluid index
Thoracic electrical impedance changes	Cardiac stroke volume
	Cardiac output
	Total vascular resistance
	Vagal nerve activity

The software for the AFT system was written for Windows-95 using Microsoft Visual BASIC. This platform was chosen because of the ease with which one can develop visual displays and user interfaces. Analog data were collected using DI-200 Data Acquisition Board and WinDaq/200 acquisition software (Dataq Instruments, Akron, Ohio). Hardware modifications included installation of an MVP4X video driver (STB Systems, Richardson, Texas) that permitted the use of four video monitors on a single computer. The four monitors were configured to provide the following: Monitors (1) and (2) – a maximum of 16 channels each of analog data available to the researcher and the subject; Monitor (3) – digital meters of all calculated variables displayed to the researcher; Monitor (4) – selected digital meter displays presented to the subject as part of the training process. Audible tones, coupled to any two of the 20 derived parameters, can be selected by the researcher and presented to the subject. The tones are generated on the PC's internal sound card using software developed in C and implemented under Visual BASIC.

Selected results of preliminary testing of the software are presented. The first figure shows the

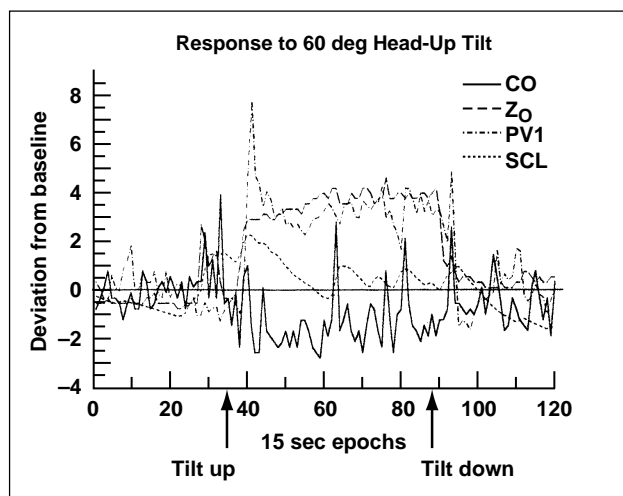


Fig. 1. Fifteen second averages (epochs) of data taken during 10 minutes supine, 10 minutes of 60 degrees head-up tilt, and a return to the supine position. The four traces show cardiac output (CO), Z_0 [an index of thoracic fluid (TFI) where $TFI = 1/Z_0^2$], pulse volume in the right foot (PV1), and skin conductance level (SCL).

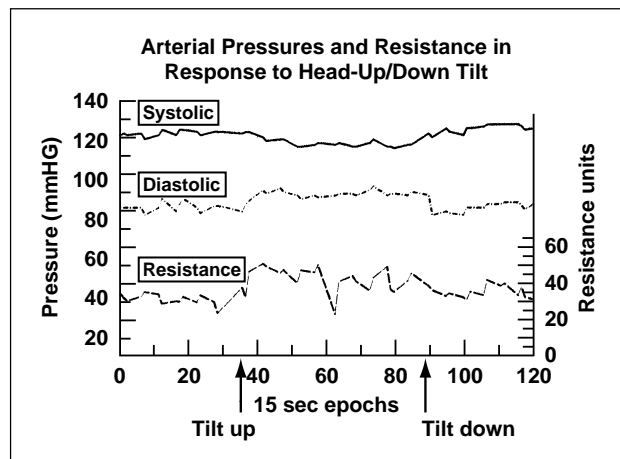


Fig. 2. (Arterial systolic and diastolic blood pressures taken during the tilt-table exercise. The resistance trace was computed to be $RESISTANCE = (Mean \text{ Arterial Pressure}) / (Cardiac \text{ Output})$. Mean arterial pressure is computed from the systolic and diastolic values. The slight increase in cardiac output shown is a compensatory response to decreased blood flow to the brain during head-up tilt.

physiological response to 60 degrees of head-up tilt from the supine position. This mild treatment results in gravity having a greater effect on the blood pool causing a fluid shift toward the feet and away from the brain. The data show increases in pulse volume at the feet (PV1), an increase in Z_0 (which is actually a decrease in thoracic fluid volume) and skin conductance level. A decrease in cardiac output is associated with the head-up tilt. The second figure shows a decrease in systolic blood pressure and an increase in diastolic blood pressure with head-up tilt. An increase in vascular resistance can also occur as a result of head-up tilt. This is a typical compensatory mechanism of the healthy individual as the body adjusts to maintain blood flow to the brain by constricting blood vessels and reducing flow in other regions of the body.

Point of Contact: P. Cowings
(415) 604-5724

CD ROMS Archive Human Biomedical Data From Space

Patricia S. Cowings

More than 300 hours of human biomedical data collected in space have been archived on CD ROMs as part of the NASA Life Sciences Archive. These CDs can be read by either a Macintosh or PC system and serve as a living archive of Space Life Sciences experiments and data. The purpose of this archive is to document, preserve, and distribute Space Life Sciences information. Data are in the form of graphs, as shown in the figure, spread sheets of one-minute means indexed by mission-elapsed time, and also raw biopotentials which may be down-loaded for analyses (for example, Fast Fourier Transforms by interested users). They represent a valuable tool and resource for Life Sciences researchers and students of space biomedicine. The efforts associated with this task included the development of a meta-data base

within the CDs that facilitates record identification and retrieval, hence making it practical for collaborative analyses of these data between remotely located parties.

This CD-ROM is a set of available data for the Autogenic Feedback Training (AFT) Experiment flown on SL-3 and SL-J. It contains the raw and processed data from six AFT subjects. These data files are in binary format and are readable from a Unix platform, with the utility OD, accessed via ftp (file transfer protocol). All processed data files can be easily retrieved from the catalog.

Point of Contact: P. Cowings
(415) 604-5724

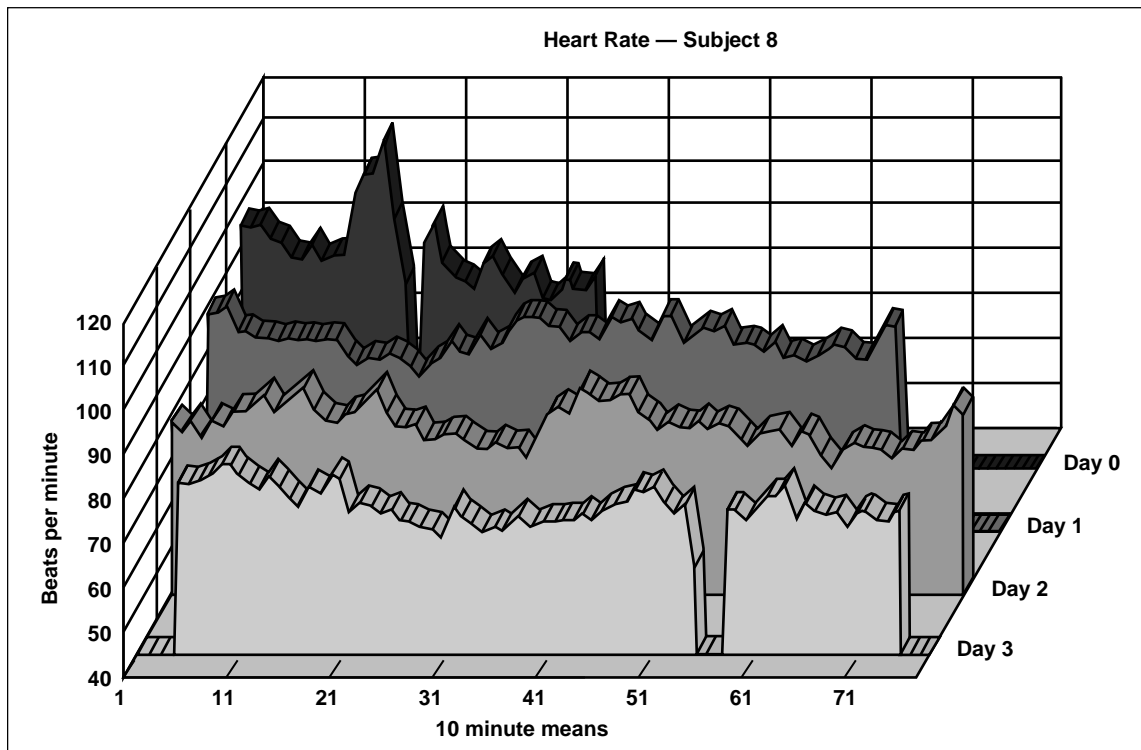


Fig. 1. Graphs of data show individual crewmember responses across days.

Center for Health Applications of Aerospace Related Technologies

Byron Wood, Louisa Beck, Sheri Dister

The Center for Health Applications of Aerospace Related Technologies (CHAART) is an outgrowth of the Global Monitoring and Human Health Program's Outreach component initiated at the beginning of FY95. CHAART's goal is to promote the application of remote sensing (RS), geographic information systems (GISs), and related technologies to issues of human health. As part of this goal, CHAART maintains ongoing collaborations with investigators from universities, research/control agencies, and private industry, as well as initiating new opportunities through Memoranda of Understanding (MOU) with other funding agencies. CHAART's objectives are to assist health investigators in achieving the goals and objectives of their research through the use of the Center's facilities, and to expand the use of RS/GIS technologies by the human health community through training, education, application projects, and direct transfer of proven technologies and knowledge to research/control agencies and universities.

The CHAART facility was established with appropriate hardware, software, furniture, and workspace to meet the needs of visiting scientists and the CHAART staff. The facility includes a Sparc20 workstation running ARC/INFO and ERDAS Imagine software; a Pentium-PC with MapInfo, ArcView, Epi-Info, and BMDP statistical software; and a Power Macintosh with Microsoft Office, Adobe Photoshop, and ArcView software.

Three investigators were assisted in the use of the CHAART facility under the Visiting Scientist Program. Ali Nasser Hassan, an Egyptian medical entomologist from Ain Shams University in Cairo, Egypt, used RS and GIS to further his research on the landscape components of filariasis transmission in the Nile River Delta. Gustavo Brêtas, a Brazilian medical doctor studying at the London School of Tropical Medicine, used image processing software and GIS capabilities

to analyze his satellite data as part of his work on malaria habitat in Rondônia. Sergey Valichko, a National Research Council Associate from the Ukraine, researched the use of radar data in human health applications.

Several MOUs were established between NASA/CHAART and Federal health agencies in the U.S. The first MOU, with the National Institutes of Health (NIH), focuses on support of basic research and technology development in the area of global monitoring and human disease. Under this MOU, a joint NASA/NIH call was issued for supplemental support for currently funded NIH research teams to employ RS/GIS in their work. The second MOU sets the stage for collaboration with scientists from the Center for Disease Control and Prevention (CDC). As part of that MOU, CHAART scientists have provided enhanced satellite data products to a CDC team studying the recent Ebola virus outbreak in Kikwit, Zaire. CDC's objectives are to use these data to map the location of exposure and residence of human victims and to accurately document the collection of vertebrate and invertebrate materials from the CDC ecological investigation, and to find correlations between these collections with underlying landscape and faunal characteristics of this emerging disease.

Another NASA/CDC collaboration during FY95 was with Dr. Durland Fish of Yale University School of Medicine. Dr. Fish used CHAART expertise and facilities to develop a map of forest patches in Rensselaer, Indiana, where Lyme disease and its tick vector were recently discovered. The forest map, generated from Landsat Multispectral Scanner data, classified forest patches into size classes. The Yale researchers used this map to design a sampling scheme that would allow them to determine if patch size is associated with tick presence or abundance.

The residential study of Lyme disease risk in two communities of Westchester County, New York, that began as a Global Monitoring and Human Health Outreach activity in collaboration with Dr. Fish, was completed in May 1995. The study showed that residential properties with high tick densities differed significantly on spectral indices derived from Landsat Thematic Mapper data, and suggested that this

method would be useful for discriminating high-risk properties for tick management and preventive education within Lyme disease-endemic communities.

Point of Contact: B. Wood
(415) 604-4187

Global Monitoring and Human Health

Louisa Beck, Sheri Dister, Mike Spanner

The Global Monitoring and Human Health Program (1985-1995) focused its last year on the conclusion of the Disease Modeling (Di-Mod) project. The overall goal of Di-Mod was to develop a landscape epidemiological approach to identifying malaria risk based on the environmental factors that determine the temporal and spatial distribution of both the vector and the disease. This research centered on the *Anopheles albimanus* mosquito which is found along the Pacific coastal plain of Chiapas, Mexico. The landscape approach integrated remote sensing and geographic information system capabilities to discriminate between villages at high and low risk for malaria transmission, as defined by the abundance of *An. albimanus*. In addition to the Ames staff, the Di-Mod team included investigators from the Centro de Investigación de Paludismo, Tapachula, Chiapas; the Uniformed Services University of the Health Sciences, Bethesda; the University of California, Davis; the California State University, Fresno; and the University of Texas Health Sciences Center, Houston.

In FY95, the goal was to use the statistical models generated in Tapachula to predict malaria transmission risk in a different area along the Chiapas coastal plain. The new area, located around the city of Huixtla, had similar landscape elements and the same malaria vector, *An. albimanus*. The discriminant analysis and regression models developed in Tapachula were applied to 40 randomly selected villages in Huixtla, using landscape information obtained from a new classification map generated

from April and October 1993 Landsat Thematic Mapper data. The study was conducted as a double-blind test in which the Huixtla predictions were not revealed to the field investigators until after the mosquito abundance data were collected, nor were the field data shared with the Ames group until after the predictions had been made and the mosquito data collected.

Of the 40 villages selected for the test, the discriminant model equations predicted that 28 would have high mosquito abundance and 12 would be low. While the landscape classification and predictions were being made, mosquito abundance was sampled in the 40 villages on an 8-day basis. At the end of the six-month sampling period, the mosquito abundance data were used to rank the villages. Of the 28 predicted as high by the discriminant model, 22 were among the top 28, based on the village ranking for an accuracy of 79%. The discriminant model correctly predicted six of the 12 lowest-ranking villages. The combined accuracy for predicting high and low villages was 70%. The mosquito abundance data used to rank the villages naturally placed the top 10 villages into a "very high" group. When this set was compared with the predicted top 10 using the regression model, the model predictions had an accuracy of 70%.

Point of Contact: L. Beck
(415) 604-5896

Patented Training Process Enables Technology Transfer— Ames Autogenic-Feedback Training System

Patricia Cowings

The Ames Autogenic-Feedback Training System (AAFTS) was originally developed by NASA to facilitate astronaut adaptation to space. The AAFTS has three components:

(1) Autogenic-Feedback Training Exercise (AFTE): A six-hour training program, a highly efficient and effective method of enabling people to voluntarily control several of their own physiological responses to a variety of environmental stressors.

(2) Autogenic-Feedback System-2 (AFS-2): An ambulatory physiological monitoring and feedback system that includes a garment, transducers, signal conditioning amplifiers, a microcontroller, a wrist-worn feedback display, and a cassette tape recorder, as shown in the first figure.

(3) Autogenic Clinical/Lab System (ACLS): A PC-based physiological monitoring and training system that includes an i586 processor with a 16-bit analog-to-digital converter and a multiple video-display adapter (four monitors) that utilizes software applications in the Windows 95 operating system environment. The user-interactive software can directly measure and display physiological responses in real time. Further, real-time calculations enable non-invasive measures of cardiovascular dynamics (for example, cardiac output, blood pressure, vagal tone, and total peripheral resistance).

The AAFTS offers numerous potential commercial applications. AFTE can be used in the treatment of hypertension, dysautonomia, autonomic neuropathy, and nausea associated with chemotherapy. The training is also useful for alleviating low blood pressure in patients with diabetes, spinal cord lesions, or generalized somatic paralysis. Training can be used to modify central nervous system activity in the treatment of neuropathological disorders such as epilepsy, Attention Deficit Disorder, and mild head trauma.

Military, commercial, and private pilots can use AFTE to reduce the risk of human-error accidents by helping to control the physiological arousal associ-

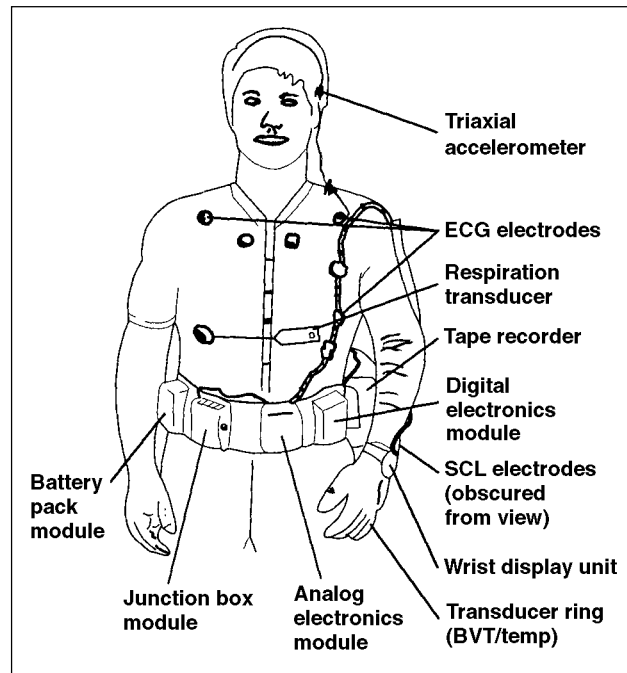


Fig. 1. The Ambulatory Monitoring System (ASF-2) as worn by crewmembers.

ated with emergency flying conditions that can negatively impact crew performance and safety. Ambulatory monitoring allows users to determine the impact of motion sickness, fatigue, and sleep deprivation in military and civilian operators of land, air, and sea vehicles, and evaluate corrective countermeasures.

AFTE can be used to alter brain activity, resulting in the ability to modify the effects of sleep deprivation on cognitive performance and to facilitate sleep, thereby reducing disturbances in circadian rhythmicity. Similarly, individuals subject to fatigue, jet lag, insomnia, high-stress work environments, and motion sickness can use AFTE to alleviate their symptoms.

The patented training process offers the following benefits:

(1) High success rate: Training is effective within four to six hours in 85% of subjects tested as a treatment for motion sickness and in high-performance military aircraft for airsickness.

(2) Multipurpose training method: AFTE can be used to reduce physiological arousal and to improve psychomotor performance, crew coordination, and communication.

(3) Nonpharmacological treatment: Training in both the recognition and control of changes in physiological responses provides an alternative, nonpharmacological method of treating a variety of disorders without side effects often seen with medication.

(4) Multiparameter PC-based system: This system is more sophisticated than commercially available

equipment by allowing the utilization of more information, making calculations in real time, and utilizing multiple digital, waveform, and audio displays simultaneously as controlled by the operator.

(5) Highly regarded ambulatory monitoring-feedback system: The AFS-2 has been rated by members of NASA's Astronaut Office as the best instrument of its kind because of its high data quality, ease of operation, and minimal time for setup and operation. The small size of the system allows for greater comfort and mobility.

**Point of Contact: P. Cowings
(415) 604-5724**

Portable Computer Technology Project

Richard Alena, Kim Hubbard

The Portable Computer Technology Project completed a flight experiment aboard both the U.S. Shuttle and the Russian Mir space station. The Wireless Network Experiment (WNE) was one of several Risk Mitigation Experiments performed during joint Shuttle-Mir docking missions that were intended to evaluate advanced technology for use in constructing and operating the International Space Station. The WNE successfully demonstrated the feasibility of wireless mobile computing for space use, and the effective use of commercial computer hardware and software for non-critical applications in space.

The experiment hardware consisted of three computers linked by radio frequency network adapters that measured the rate of network communications as the distance between the computers was increased. The WNE was launched aboard STS-74 and stored aboard Mir until it was performed by

astronauts Kevin Chilton and Rick Searfoss during the STS-76 mission. The experiment demonstrated network coverage for the entire Orbiter habitable volume.

The figure illustrates the flight configuration. The Wireless Network Server, the Advanced Portable Workstation (APW-II) prototype developed by Scientific Applications International Corporation, incorporated rugged packaging, power conditioning, and a Pentium processor with error-correcting memory to enhance reliability for space use. The two mobile computers were commercial-off-the-shelf items powered by batteries. The Subnotebook computer was an HP Omnibook 600C with a keyboard, mouse, and color display; and the Personal Digital Assistant was a Norand PenKey hand-held computer. The wireless network adapters were the RangeLAN2 product from Proxim Corporation.

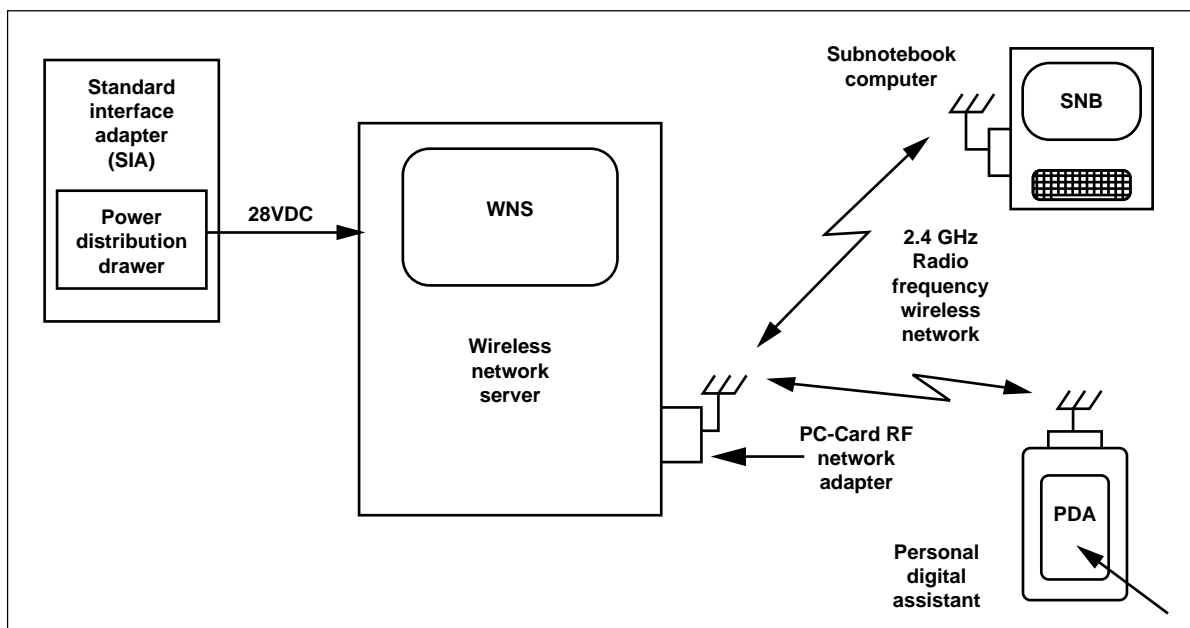


Fig. 1. Wireless Network Experiment Flight Configuration.

Flight certification tests were conducted to ensure reliability after launch. Safety reviews were conducted for operation aboard both Mir and the Shuttle. The Subnotebook computer and the Personal Digital Assistant were modified slightly to meet space flight requirements. In addition, an integration test was conducted in the Mir Core Mockup in Moscow to prove that WNE produced no electromagnetic interference to vital spacecraft systems and payloads.

The server was installed at a fixed location and powered from Orbiter or Mir power systems during the experiment. The handheld units were battery-operated. All three computers communicated through

the network operating system and frequency-hopping radio system at data rates exceeding 500 kilobits per second, which is over ten times faster than a 28.8 kilobytes per second modem. A sophisticated network analyzer running on the server captured the data packets and produced a graph of network throughput in real-time. Ground tests indicated adequate coverage of at least two space station modules at this rate.

Point of Contact: R. Alena
(415) 604-0262

Just-In-Time-Training

Nicolas Groleau, Leo Yu, Kim Hubbard

In collaboration with Johnson Space Center's (JSC) Mission Operations Directorate, Just-In-Time-Training (JITT) is a project that provides Field Deployable Trainers in the form of a laptop computer. The project's long-term objective is to define software and hardware requirements for Space Station JITT tools. To develop these requirements, operational systems are built to provide astronauts and flight operators with intelligent feedback training for shuttle systems during prolonged missions away from JSC.

The first system was developed to help astronauts learn an In-Flight Maintenance procedure to replace one of four General Purpose Computers. The procedure is essentially mechanical and must be performed rapidly as the cooling system is shared by all the computers and is inoperable during the procedure. This lesson is a hypermedia browsing lesson. The trainee is shown a series of screens. Each screen contains one of the sixty detailed procedural steps together with additional explanations in the form of text, graphics, and short videos. Related pieces of information are graphically linked. They appear as blue text or blue outlined images. The trainee can navigate from page to page by clicking on these links using the mouse.

The project combines high-paced, cutting-edge software development and rigorous testing to take advantage of flight opportunities. The HTML language was used to develop pages available on the World Wide Web (WWW). The use of this modern software environment allowed the development of the first hypermedia lesson twice as fast as veteran curriculum developers. Moreover, the lesson can be used on many types of computers supporting the Netscape WWW browser (using the Macintosh, PCs, and Suns) or over the Internet. The software was delivered to JSC to be tested by astronaut Shannon Lucid during her stay on the Russian Mir space station.

Work has begun on the second phase of the project to extend the first prototype with a simulation environment (the space shuttle cockpit). The trainee must indicate which control panels to display, switches to flip, and screens to monitor. Specifically, the project now focuses on demonstrating the use of rule-based techniques (using the NASA-developed CLIPS tool) to provide intelligent feedback to the trainee.

**Point of Contact: N. Groleau
(415) 604-0611**

Biological System Dynamics

Harry Jones

People living on the Moon and Mars for long periods of time will require biological life-support systems that provide food, water, and air, while minimizing the amount of materials that must be supplied from Earth. A fully regenerative biological life-support system will be able to recycle the solid, liquid, and gaseous wastes produced by the crew into food, drinkable water, and breathable atmosphere.

Developing and operating a biological life-support system that is robust and efficient for several years is a formidable task. Although some relatively short-term tests have established a proof of concept, long-term system performance is not well understood. A biological life-support system is a complex, dynamic system made up of many nonlinear components. Perturbations, even small ones, can have serious consequences at a later date. Preliminary simulations have shown that although a system may recover in the short term from some component failures, these disturbances can have serious, even catastrophic, long-term consequences.

The goal of the Biological System Dynamics Project is to provide the knowledge and understanding that is needed to develop biological life-support systems for use in long duration Lunar and Mars missions. The Project studies the fundamental principals that govern the stability of dynamics within fully regenerative life-support systems operating for durations greater than one year.

A small, compact, and relatively uncomplicated biological life-support system has been developed.



Fig. 1. Crop growth chamber.

This system includes a crop growth chamber shown in the figure, an incinerator waste processor, and a set of buffer tanks. This system has been used to grow a wheat crop, using bottled carbon dioxide instead of incinerator gas. The primary reason for the assembly of this hardware testbed is to validate mathematical models and results predicted by computer simulations, and the secondary reason is to study the response of closed systems to individual processor failure or off-nominal conditions.

Point of Contact: H. Jones
(415) 604-5518

Systems Control

Charles C. Blackwell

In FY95, the principle systems control research thrust of the Flight Projects Integrated Project was to develop new methods and adapt the results of recent research to make space exploration life-support systems development and automatic operation maximally effective and as simple as possible. The results will be useful in virtually all cases of development and operation of complicated systems. Although these results were obtained in addressing the NASA Strategic Enterprise of Human Exploration and Development of Space, they also are applicable to the Aeronautics and Space Transportation Enterprise.

The goal of the research was to make the means available to take advantage of every opportunity to minimize cost of the development of space exploration life-support systems. These costs are incurred in the design phase, the physical system fabrication phase, and the operation phase. This work was an in-house follow-on to work which began as a collaboration with the University of Santa Clara. This research is appropriate because even today one finds a great deal of "trial and error" in system development and operation, and much of it is done because

appropriate, advanced methods are not, in fact, practically available for use.

Elements of advanced perturbation theory and advanced stability theory were combined to achieve the goal. However, efforts have not produced the desired theory and methods that can indicate how to obtain the desired controller system. Topological analysis via linear graphs is not compatible numerical computation.

The means of systematically achieving maximal simplicity while assuring required system performance have been established. An unexpected bonus is that the procedure can be used to advantage in the development of any system, whether the environment is a very large institution or a very small business in the start-up phase. In fact, the availability of these results will reduce the uncertainty and risk for the small enterprises with limited resources.

**Point of Contact: C. Blackwell
(415) 604-3208**

Mission to Planet Earth Enterprise



Overview

NASA's Mission to Planet Earth (MTPE) studies the total Earth environment—atmosphere, ice, oceans, land, biota, and their interactions—to understand the effects of natural and human-induced, near-term changes on the global environment and to lay the foundation for long-term environment and climate monitoring and prediction. Ames Research Center supports the MTPE Enterprise by conducting research and by developing technology with the objective of expanding the knowledge of Earth's atmosphere and ecosystems. This is also one of the goals of the Agency's astrobiology research and technology efforts, which are led by Ames. A complementary objective is to apply the knowledge gained to practical, everyday problems and to transfer the technology and knowledge to users outside NASA. During FY95, numerous research and technology efforts were accomplished, and the results address the following goals of the MTPE Enterprise:

- Expand scientific knowledge of the Earth's environmental system.
- Enable the productive use of MTPE science and technology.
- Disseminate information about the Earth system.

The research is particularly concerned with atmospheric and ecosystem science and with biosphere/atmosphere interaction. Key components of the research include the study of physical and chemical processes of biogeochemical cycling; dynamics of terrestrial and aquatic ecosystems; the chemical and transport processes that determine atmospheric composition, dynamics, and climate; and the physical processes that determine the behavior of the atmosphere on the Earth and other solar system bodies. Of special interest are the development and application of new technologies required to bring insight to these science topics. Significant contributions were made in three areas: analysis of critical gaseous emissions, development of models and instruments, and radiation research.

Research highlighted in this report include focus on important environmental concerns related to stratospheric ozone depletion, perturbations in the chemical composition of the atmosphere, and

climatic changes from clouds, aerosols, and greenhouse gases. Numerous state-of-the-art instruments were flown successfully, and significant data were collected for stratospheric and tropospheric research. For stratospheric experiments, the following are included: the Airborne Tunable Laser Absorption Spectrometer to measure nitrous oxide and carbon monoxide; the Meteorological Measurement System (MMS), which measures pressure, temperature, and the wind vector; the Ultraviolet Ozone Photometer for measuring ozone; and the Whole Air Sampler to obtain samples of long-lived gases.

These instruments were flown on the ER-2 aircraft for the Airborne Southern Hemisphere Ozone Experiment and for the Measurements for Assessing the Effects of Stratospheric Aircraft (ASHOE/MAESA) and the Stratospheric Tracers Atmospheric Transport studies. The ASHOE/MAESA study conclusively confirmed that chlorine and bromine dominate ozone destruction in the lower stratosphere. For tropospheric experiments, instruments were flown on several aircraft to measure carbon monoxide, nonmethane hydrocarbons, carbonyls, and reactive nitrogen species. Specifically, fluxes of important biogenic gases from terrestrial ecosystems were quantified.

Ames was one of seven organizations participating in the Arizona program for advancing the understanding of winter storm development, morphology, and precipitation in a mountainous region. Ames scientists conducted cloud remote sensing analysis for determining cloud water thermodynamics phase, cloud thickness, and liquid water content. Using the Airborne Visible-Infrared Imaging Spectrometer, another study characterized the population composition and dynamics of coastal phytoplankton blooms in Florida Bay.

Technology developments were realized on two fronts—modeling and instruments. Model development efforts or simulations based on developed models are presented for the following phenomena: the impact of gravity waves generated by convection or stratospheric circulation; the effects of climate and landcover interactions in the boreal biome; soil/atmosphere exchange of key trace gas species; biomass combustion and pyrogenic trace gas emissions; seasonal differentiation of microbial methane sources; estimation of global biogenic isoprene emissions; and paleoenvironment studies using

pollen data and leaf area development. Newly developed instruments include: a miniaturized, lightweight, tunable diode laser spectrometer; an MMS on the NASA DC-8 aircraft to provide science-quality state variables and wind data; and a fully automated, 14-channel sunphotometer to fly on remotely piloted aircraft and other platforms.

Radiation research focuses on phenomena associated with the interaction of solar and planetary radiation with atmospheres and solar system bodies. The high-resolution infrared spectroscopy is devoted to basic experimental and theoretical research into the absorption of radiation by gases. The purpose is to determine the molecular spectroscopic parameters needed for the design and interpretation of field measurement programs related to the environment of Earth's and other planetary and stellar atmospheres. This report highlights experiments conducted with the Radiation Measurement System and with a new within-leaf radiative transfer model.

Using MTPE data and technology, commercial firms can expand their businesses and public-sector managers can exercise stewardship of our natural resources. The enabling, productive use of MTPE science and technology is exemplified by the following accomplishments: the effects of land-use change on the methods and assumptions currently in use to estimate the impact of land cover in Earth's carbon system in Oregon; and the use of Synthetic Aperture Radar for monitoring fisheries in the Pacific Northwest and North Atlantic U.S. coastal waters. Other reported data, analyses, and technologies can be used by researchers seeking answers to key Earth science questions and by educators teaching Earth sciences.

Broadcast and multicast protocols and corresponding reliable (verified and validated) complex software systems are required to gather large-scale data and to disseminate information. Such protocols are needed to maintain coherent copies of data at multiple sites efficiently. Also a difficult task in any software project is the collection of metrics and adherence to a disciplined development process. Assessment of the status of a project is critical to the reassignment of resources, adjustment of schedules, and measurement of product quality. Both of these research efforts are highlighted. In addition to the MTPE Enterprise, these efforts support the other Enterprises.

Airborne Southern Hemisphere Ozone Experiment/ Measurements for Assessing the Effects of Stratospheric Aircraft

Steve Hipskind, Duane Allen, Quincy Allison, Stu Bowen, Paul Bui, Roland Chan, Estelle Condon, Michael Craig, Guy Ferry, Steve Gaines, Jeff Grose, Patti Hathaway, Max Loewenstein, Jim Podolske, Rudi Pueschel, Tony Trias

The Airborne Southern Hemisphere Ozone Experiment/Measurements for Assessing the Effects of Stratospheric Aircraft (ASHOE/MAESA) programs were sponsored by NASA's Upper Atmosphere Research Program and High Speed Research Program. The National Oceanic and Atmospheric Administration and the National Science Foundation also contributed substantially, as did the meteorological services of New Zealand, Australia, United Kingdom, and those who signed the agreement governing the European Centre for Medium-Range Weather Forecasts (ECMWF). The mission was designed to address questions about the causes of the year-round, mid-latitude ozone loss observed in the Southern Hemisphere during the last 15 years—in particular, the relative roles of vortex air transported to mid-latitudes and in situ loss induced by heterogeneous chemistry on sulfuric acid aerosols. These questions are important for the general understanding of the composition of the lower stratosphere and its consequent effects on the radiative balance of the atmosphere, and hence, for the assessment of the potential environmental effects of stratospheric aircraft upon this balance (a goal also served by the flights studying the exchange of air between the tropics and mid-latitudes of both hemispheres).

Flights of the NASA ER-2 high-altitude aircraft, carrying as many as 16 instruments, provided new observations to diagnose the chemistry, physics, and fluid motion of air in the lower stratosphere. Measurements spanned February to November, 1994, and from the edge of Antarctica at 70°S to upper Canada at 60°N, in conjunction with observations from the ground, balloons, and satellites. Most measurements were in the southern hemisphere and in the tropics; the former was studied using in situ techniques over the entire evolution of the winter vortex, while the latter was investigated for the first time.

The observations are based primarily on 45 flights of the ER-2. For most flights, the ER-2 carried 16 instruments to measure the abundance of reactive and inert trace gases, aerosols, temperature, pressure, winds, ultraviolet light, and temperature profiles. For flights specifically to study dynamics and radiation, some of the trace gas instruments were removed and an instrument that measures infrared radiation was added. Among the 45 flights, 26 were from Christchurch, New Zealand; 5 were from Barber's Point, Hawaii; and 6 were transits between New Zealand, Fiji, Hawaii, and California. Also included were two full duration (8-hour) test flights north from Moffett Field in February, five short (2+ hours) test flights from Moffett Field between January and March, and a northbound flight from Moffett Field in November, 1994. Thirty-two flights had the full payload, eleven had the dynamics and radiation configuration, and two were test flights for individual instruments.

Observations from balloons, satellites, and ground instruments provided valuable contributions to ASHOE/MAESA. Analyses of weather observations by United Kingdom Meteorological Office, ECMWF, United Kingdom Universities Global Atmospheric Modeling Program, National Meteorological Center, and Goddard Space Flight Center (GSFC) aided flight planning and dynamical analyses. Satellite data from the Microwave Landing System, Halogen Occultation Experiment on Upper Atmosphere Research Satellite, and the Total Ozone Mapping Spectrometer on Meteor-3 give a global context for the local measurements of the ER-2. The GSFC Lidar and National Institute of Water and Atmospheric Research column measurements from Lauder, New Zealand, and the MacQuarie Island ozonsondes provided valuable intercomparisons for aerosol and ozone measurements on the aircraft.

The observations were extended well above and below the aircraft.

Mission highlights and milestones include: (1) the first Southern Hemisphere stratospheric measurements of a complete suite of hydrogen, nitrogen, chlorine and bromine chemical radicals, as well as many long-lived tracer species using the NASA ER-2 aircraft; (2) conclusive confirmation that chlorine and bromine dominate ozone destruction in the lower stratosphere to roughly 20 kilometers; (3) the first measurements of air almost depleted of ozone obtained at roughly 16 kilometers altitude on two occasions in early October; and (4) the first

sampling in the stratosphere of the exhaust plume of a commercial airliner at supersonic speeds. NASA ER-2 aircraft made measurements of carbon dioxide, water vapor, particles, and nitrogen compounds in the exhaust plume of an Air France Concorde flying at Mach 2 off the coast of New Zealand. Amounts of chemicals in the plume were consistent with previous laboratory tests of the Concorde engines.

**Point of Contact: S. Hipkind
(415) 604-5076**

Ecosystem Trace Gas Fluxes

Christopher S. Potter, Steven A. Klooster

Studies have been completed to quantify fluxes of important biogenic gases from terrestrial ecosystems, and to understand the sources, sinks, and processes that control exchange with the atmosphere at several scales. The long-term goal of the project was to establish a geographic perspective on trace gas fluxes and biogeochemical processes in terrestrial environments. This includes comparisons of measured gas fluxes from soils with predicted fluxes from ecosystem simulation models.

The CASA (Carnegie-Ames-Stanford Approach) model is designed to capture much of the current understanding of localized interactions between nitrogen (N) mineralization, soil moisture, and the resulting variation in nitrous oxide (N₂O) and nitric oxide (NO) emissions, and to extend these relationships over broad geographic regions using remotely sensed drivers. Estimation of ecosystem production comes from the vegetation index derived from the National Oceanographic and Atmospheric Administration's Advanced Very High Resolution Radiometer at monthly intervals. CASA model estimates for global emission at the soil surface are 6.1 terragrams nitrogen and 9.7 terragrams nitrogen per year for N₂O and NO, respectively. Using this formulation, tropical dry forests and savannas are identified as important source areas for nitrogen

trace gas emissions and target areas for more field measurements.

A comprehensive modeling study of global patterns of carbon dioxide emissions from soils was conducted. For this analysis, empirically based statistical models were used to predict the spatial and temporal patterns of global carbon dioxide (CO₂) emissions from soils. Historical land cover changes are estimated to have reduced current annual soil CO₂ emissions by up to 2 petagrams carbon per year in comparison with undisturbed vegetation cover. This study presents the most comprehensive and best resolved estimate to date of global soil CO₂ fluxes.

A geographic information system (including digital elevation, climate, land use, and satellite imagery) was built to support site and gradient comparison studies for the island of Hawaii. An agreement has also been established with the Forest Service of the U.S. Department of Agriculture to validate CASA nitrogen gas algorithms using forest-to-pasture chronosequence data sets from sites in Costa Rica.

**Point of Contact: C. Potter
(415) 604-6164**

The Arizona Program

Peter Pilewskie, Warren J. Gore

The 1995 Arizona Program was a multi-investigator field experiment focused on advancing the understanding of winter storm development, morphology, and precipitation in a mountainous region of central Arizona. From 15 January through 15 March, 1995, a wide range of instrumentation was operated in and around the Verde Valley southwest of Flagstaff, Arizona. Ames Research Center's visible and near-infrared spectroradiometers, two Doppler radars, an instrumented aircraft, a lidar, microwave radiometers, and other surface-based instrumentation focused on the analysis of wintertime storms in this geographically diverse area. Over twenty-five scientists from seven institutions participated in the Program. Of special interest to the Arizona Program is the interaction of topographically induced gravity waves with the ambient upslope flow. It is hypothesized that these waves may serve to augment the upslope-forced precipitation that falls downwind of this feature onto the Mogollon Rim. A major objective of the program was to compare the observations of these and other aspects of winter storms with those predicted with a numerical model.

The primary role of the Ames research effort was to provide cloud remote-sensing analysis for determining cloud water thermodynamic phase, cloud thickness, and liquid water content (LWC). The unique collection of surface and in situ sensors provided valuable data for future efforts to determine the relationships between cloud radiative properties and microphysics and investigations into the role of clouds in climate. Understanding the role of clouds in climate is based not only on determining the complex manner in which radiative energy is redistributed by clouds but also on the hydrological processes that regulate the distribution of condensed water and water vapor in the atmosphere. In the present understanding of the hydrological cycle, there are fundamental gaps that limit our ability to assess the present climate, let alone predict future climate, or climate response in the presence of

increased greenhouse gases. Because the removal rate of condensed water depends strongly on cloud LWC, determining its distribution and dependence on temperature are crucial to understanding cloud-climate feedback.

During the Arizona program, a spectro-radiometer system consisting of three independent monochromator-detector units (spectral coverage from 0.4 to 2.5 millimeters, 10 nanometer resolution, and 1 milliradian field of view) was deployed at a surface site in a zenith-pointing configuration. Over 200 hours of transmission data were obtained under a variety of meteorological and cloud-type conditions, with roughly 10% direct overhead aircraft coverage and another 40% coverage within 100 kilometers. These data were readily used to infer cloud water phase (liquid or ice—the most crucial parameter for determining a cloud's likelihood to precipitate). Multiwavelength analysis was necessary to separate the information content on particle size, cloud thickness, and water phase; the methodology was similar to current aircraft and satellite cloud retrieval algorithms. Particle size and optical depth were sufficient to determine the *integrated* cloud water path.

Asymptotic formulae provided an effective means to closely approximate the qualitative and quantitative behavior of transmission (and reflection) computed by more laborious, detailed methods. Relationships derived from asymptotic formulae were applied to measured transmission spectra to test objectively the internal consistency of data sets acquired during the field program, and they confirmed, rather dramatically, the quality of the measurements. However, these relationships appear to be very useful in themselves, not merely as a quality control measure, but also as a potentially valuable remote-sensing technique in its own right. Another benefit of this analysis was the separation of condensed water (cloud) and water vapor transmission.

The capability of tracing this additional water vapor path within a cloud as a function of cloud height and geometric depth will determine the ability to derive LWC. The integrated cloud water path can be derived by retrieving cloud optical thickness and particle size; the additional height information will facilitate

the retrieval of LWC. The Arizona Program data set will provide ground-truth verification.

Point of Contact: P. Pilewski
(415) 604-0746

Remote Sensing of Phytoplankton Dynamics Using AVIRIS Derived Spectral and Image Data

Vincent G. Ambrosia, Laurie L. Richardson

The objectives of this project, initiated in late FY95, are to test the use of the Airborne Visible-Infrared Imaging Spectrometer (AVIRIS) to characterize population composition and dynamics of coastal phytoplankton blooms based on detection of algal accessory pigments. Specific objectives are to monitor the composition and dynamics (spatial and temporal) of the algal blooms in Florida Bay by identification and quantification of taxonomically significant algal accessory pigments using high performance liquid chromatography; to analyze field spectroradiometer data (surface reflectance) acquired during sampling for pigment analysis in terms of pigments present; to create a spectral library of the above field spectra, algal spectral signatures and pigment signatures; and to analyze AVIRIS data sets using both the spectral library and image-derived spectra using ERDAS and ENVI software.

This project extends the earlier research, conducted in highly colored, hypersaline aquatic ecosystems, to a natural, coastal ecosystem that has a more dilute optical signal due to less algal/photosynthetic bacteria biomass. Florida Bay was selected as the

research site because of the vast phytoplankton bloom that occurs there year-round. Monitoring that bloom has profound implications on the health and ecological viability of the Florida Everglades. Characterization of various pigments will allow the analysis of the distribution and extent of the bloom.

Presently, specific accessory pigments have been detected (as opposed to strongly varying reflectance properties) with AVIRIS data. Isolated pigment absorption features such as the 620-nanometer absorbance by phycocyanin and the red absorbance features of chlorophylls were directly discerned in reflectance spectra. Successful discrimination of specific pigment features in areas of the spectrum with overlapping absorbance, however, was achieved by using fourth derivative spectral analysis. In this manner, the 508-nanometer absorbance feature of the cyanobacterial-specific pigment myxoxanthophyll could be discriminated.

Point of Contact: V. Ambrosia
(415) 604-6565

Convectively Generated Gravity Waves

Leonhard Pfister

This work evaluates the impact of gravity waves generated by convection on the stratospheric circulation in the tropics. Each convective event emits a spectrum of gravity waves with a broad variation of phase speeds. Each component of that spectrum carries an upward flux of momentum. These waves will break at a variety of altitudes corresponding to their phase speeds; and when they do, they will exert a force at that altitude that can affect the overall circulation of the tropical stratosphere. The assessment of the importance of these convectively generated gravity waves has two steps. First, measurements from ER-2 high altitude aircraft overflights of convective systems are used to evaluate the spectral characteristics of gravity waves emitted by convective systems. Second, global meteorological satellite data sets are used to extrapolate from individual convective systems, thus deriving global budgets of upward momentum flux.

Previous work has shown that amplitudes of mesoscale gravity waves (≈ 100 kilometer wavelengths) emitted by convective systems in the tropics can make significant contributions to the overall circulation in the tropical stratosphere, specifically the westerly phase of the semiannual oscillation at the stratopause (50 kilometer altitude) and the

easterly phase of the quasi-biennial oscillation between 20 and 30 kilometer altitude.

These calculations considered only fall conditions. Given the strong variations in convection throughout the year in the tropics, seasonal variations need to be considered to properly assess the impact of convectively generated gravity waves on the tropical stratosphere circulation. Calculations for all seasons were performed this year, and the effect of spatially variable tropopause winds on the spectral distribution of momentum flux was evaluated.

There are two basic conclusions. First, seasonal variations in momentum flux are fairly small, with no more than a 15% effect. Second, spatially varying tropopause winds have a significant effect on the spectral distribution of momentum flux, reducing the momentum flux at all phase speeds by 30–50%. These results indicate that the next step in the investigation is to examine the effect of the speeds of individual convective systems (so far assumed to be zero) on the total budget of momentum flux.

**Point of Contact: L. Pfister
(415) 604-3183**

BOREAS Modeling

Joseph Coughlan

In collaboration with Steven W. Running (University of Montana) and Lawrence E. Band (University of Toronto), this study investigates the effects of climate and landcover interactions in the boreal biome and is part of the Boreal Ecosystem–Atmosphere Study (BOREAS). The Regional Hydro-ecological Simulation System (RHESSys) was used to explore the hydrology and hydrologic controls on the biome. Previously, RHESSys was used in water-limited areas to quantify the influence of water stress (drought) on vegetation. In the boreal biome, the water controls are the opposite—too much water limits growth. A second issue is the role water plays in the natural fire cycle of this biome. Increased warming has been hypothesized to play a significant role in the fire cycle, causing more intense and more frequent fires.

A preliminary data set defining five boreal cover types was constructed to identify field data gaps and communicate model needs to the BOREAS field scientists. Site definitions were made for wet and dry conifer, deciduous, disturbed (burned) dry conifer, and fen. Ecosystem simulation results show that a

one-dimensional (1-D) representation of site hydrology appears inadequate for defining the mesic boreal cover types: deciduous, wet conifer, and fen. For example, when placed in a closed, 1-D framework, the wet conifer site generated chronic water stress (1.4 megapascals) that reduced simulated carbon and water fluxes. It is hypothesized that the wet conifer and fen sites are naturally irrigated by groundwater moving into the upper soil layers. One hypothesized source of groundwater recharge would be from disturbed dry conifer sites. The simulated disturbed site produced the largest amount of outflow (215 millimeters/year) because of the reduction in leaf area index, while the undisturbed dry conifer site produced no outflow (0.0 millimeter/year). Results suggest that disturbance (burn frequency and burn extents) can be an important factor in determining the hydrology at the wetter boreal sites, a heretofore unrecognized negative feedback.

Point of Contact: J. Coughlan
(415) 604-5689

Trace Gas Flux Measurements

Gerald P. Livingston, Gordon L. Hutchinson, William H. Anthony, James Podolske, Leslie A. Morrissey, David J. DesMarais, Richard W. Healy, Rob G. Striegl

Dramatic changes in the atmospheric concentrations of various trace gas species over the past century demonstrate that mankind's influence on his environment is global in scale. It is also well known that many of these trace gas species are key components in the Earth's atmospheric chemistry and radiative balance. Complicating credible efforts to predict the global budgets of these species is the uncertainty in the global distribution and diversity of their sources and sinks. In particular, many gas species have both anthropogenic and natural, for example, microbial, sources and sinks. Quantifying the respective contributions of natural and anthropogenic sources and sinks is necessary, however, to understand observed atmospheric changes, to predict the impact of these changes, or to suggest possible mitigating actions. Uncertainties in measurements of soil-atmosphere exchange of key trace gas species produced as a result of microbial decomposition processes are currently a key factor limiting the certainty with which the magnitude and timing of climate change can be predicted.

These issues have been addressed by evaluating measurement techniques commonly employed in making soil-atmosphere exchange, and by developing new analytical approaches. Two efforts are described below:

(1) Chambers play a critical role in many aspects of research concerning surface-atmosphere trace gas exchange, and much literature is devoted to observations based on this technique. The chambers function by enclosing a volume of air above a known area of the surface and monitoring the concentration changes in that volume of air over time. A model is then fit to the observed data to predict the rate of gas exchange immediately prior to the placement of the chamber. It is widely assumed that over short deployment intervals this approach yields reasonably accurate estimates of the true exchange rate, although it is also widely recognized that a change in the concentration of any trace gas in the chamber headspace will alter the gradients driving diffusion

of that gas through the underlying substrate and thus effect its rate of exchange across the surface-atmosphere boundary. In collaboration with the Agricultural Research Service of the U.S. Department of Agriculture and the U.S. Geological Survey, efforts were focused on examining chamber approaches in detail, evaluating potential sources of error, and modeling the soil-atmosphere diffusion processes beneath a chamber. Numerical simulations were performed to evaluate the accuracy of chamber measurements in relation to natural (surface-atmosphere interfacial layer and soil characteristics, and the magnitude and distribution of trace gas sources and sinks within the soil horizon) and deployment (forced mixing within the chamber, etc.) factors. While potential biases in chamber-based measures of surface-atmosphere exchange are significant, most sources of error can be controlled by careful deployment practices and adoption of improved analyses techniques over those presently available.

(2) Measurement of stable isotope ratios in atmospheric samples is but one of very few approaches available to estimate surface-atmosphere exchange rates on regional scales. The logistical difficulties and cost of applying this approach to trace gas species with low atmospheric concentrations, however, has severely limited its application. The efforts to estimate methane (CH_4) exchange from northern ecosystems led to the development of a technique that combines gas chromatography and isotope ratio-monitoring mass spectroscopy, and allows rapid analysis of low volume (<20 milliliter) samples of trace gas species at ambient atmospheric concentrations (~1–10 parts per million by volume). This technique promises to make regional CH_4 analyses by isotope ratio-monitoring techniques feasible for the first time.

**Point of Contact: J. Podolske
(415) 604-4853**

Spatial and Temporal Distribution of Biomass Combustion and Pyrogenic Trace Gas Emissions

James Brass, Christine Hlavka, Robert Chatfield, Pamela Matson, Liane Guild, Vincent Ambrosia

The goal of this project was to develop methods for estimating the extent of biomass burning and pyrogenic trace gas emissions in tropical regions and to test them in the cerrado (tropical savanna) of central Brazil. The approach included the following components: geographic stratification to define ecozones, analysis of satellite imagery, and use of trace gas emissions data from other researchers.

A geographic information system (GIS) database was developed for stratification of the Brazilian cerrado by type of cerrado vegetation. The data sets in the GIS include a digitized version of a vegetation map developed by the Brazilian Institute of Environment and Natural Resources (Instituto Brasileiro de Meio Ambiente e dos Recursos Naturais Renováveis (IBAMA)). The data sets also provided global data on soils, land use, and geographic features such as roads and rivers developed by other researchers and commercial sources.

During three weeks in September 1992, estimates of trace gas emissions from fires were produced to test this approach for estimating pyrogenic gas emissions by combining geographic data and information from satellite imagery with other data. The geographic stratification was based on the types of cerrado vegetation as delineated on the IBAMA map, and was used to estimate the amount of vegetation burned per unit area in fires as a function of geographic location. A weekly fire product provided by the Brazilian Space Institute (Instituto Nacional de Pesquisas Espaciais (INPE)) was developed from analysis of weather satellite Advanced Very High Resolution Radiometer (AVHRR) imagery, and was used to estimate the occurrence of fires (area per week) as a function of geographic location. These data were combined with data on emission rates per unit of biomass burned to provide weekly estimates

of total trace gas emissions by type of cerrado vegetation, and for the Brazilian cerrado as a whole.

The INPE fire product was based on detection of active fires with AVHRR imagery. Active fires that are obscured by clouds may go undetected during the satellite overpass, or the burn area may be underestimated because only the fire front during the time of overpass is observed. To address these problems, two methods were developed and tested for mapping burn scars because of recent fires with AVHRR imagery. One method involved analysis of AVHRR bands 1 (red in the visible spectrum) and 3 (a thermal infrared band) to detect warm areas without green vegetation. The second method involved analysis of AVHRR bands 2 (near infrared) and 3 to detect areas on land darkened in the near infrared by the presence of an ash layer.

Comparison of the processed AVHRR with Landsat imagery of two test sites validated the presence of many of the burn scars, but accuracy varied from one area to another because of effects from atmospheric haze on the imagery. The practical use of AVHRR for mapping burn scars over large areas will therefore depend on developing methods for correcting for atmospheric effects on AVHRR imagery and/or selection of imagery under clear sky conditions. The coarse spatial resolution of AVHRR tended to distort the extents of small burns, leading to overestimation of burn area by a factor of 0.3. Analysis of the distribution of sizes of the small scars with the Landsat imagery indicated that this effect may be correctable using statistical modeling techniques.

Point of Contact: J. Brass
(415) 604-5232

Mapping Northern Ecosystems Using Synthetic Aperture Radar

Leslie A. Morrissey, Gerald P. Livingston, Joel Stearn, Stephen Durden

Climate models predict that increasing atmospheric concentrations of greenhouse gases, such as carbon dioxide (CO₂) and methane (CH₄), will result in significant global warming within the next century and that climate change will be most dramatic in northern high latitudes. Uncertainties in the current understanding of the role of microbial decomposition processes in the soils of northern ecosystems, however, remain an unresolved but key factor limiting the certainty with which the magnitude and timing of climate change can be predicted. Since the organic carbon stored in the peat and soil beneath these ecosystems exceeds that of any other biome on Earth, climatic changes that will increase microbial decomposition of these vast carbon stores will almost certainly lead to increased atmospheric loading of CO₂ and CH₄ and to enhancement of the greenhouse phenomenon.

Boreal wetlands are a globally significant source of atmospheric CH₄, yet the magnitude and seasonal dynamics of their contribution remains poorly understood. Over the past decade, numerous studies have provided estimates of the rate of CH₄ surface-atmosphere exchange from these ecosystems. In contrast, little information is available on the areal and temporal extents over which these exchange rates apply. Available estimates of the areal extent of northern wetlands have been derived from varied sources which differ greatly in their classification accuracy and spatial resolution, having often been derived from 1:1,000,000 or coarser scale navigational maps. Furthermore, information on seasonal variability is virtually nonexistent. Uncertainties in both the areal extent and seasonal dynamics of northern wetlands, therefore, must be reduced if insight is to be gained into the role of northern

ecosystems in the present or projected global carbon budget as it relates to climate change.

Present efforts have focused on the development of multitemporal algorithms which, when applied to European Radar Satellite (ERS-1/2) Synthetic Aperture Radar (SAR) data, allow for seasonally differentiating microbial CH₄ sources in circumpolar ecosystems. Unlike optical data, SAR data can be acquired regardless of cloud cover or solar elevation. These algorithms were developed from an understanding of seasonal radar backscatter observed over study sites in northern Alaska and from physical-based models of radar-surface interactions derived from NASA AIRSAR multiparameter data collected over rice growing regions in central California. Specifically, these algorithms made it possible to differentiate open surface waters (low magnitude CH₄ source areas), inundated and herbaceous wetlands (high magnitude CH₄ source areas), and uplands (CH₄ non-source areas).

The backscatter modeling results indicate that observed differences in ERS-1/2 SAR backscatter are the result of inherent differences in the dielectric properties and scattering mechanisms of the respective classes. Moreover, the importance of selecting SAR acquisitions under freezing conditions to optimize the separation of the classes of interest has been demonstrated. The results also demonstrate some of the first applications of multitemporal SAR to land cover analyses and the necessity of this approach to both increase the robustness of the algorithms and provide seasonal information.

**Point of Contact: J. Stearn
(415) 604-0636**

Non-Methane Hydrocarbon Emissions

Susan E. Alexander, Christopher S. Potter, Steven A. Klooster, Joseph C. Coughlan, Robert B. Chatfield

Isoprene, a volatile organic compound emitted from natural sources, has an important impact on atmospheric chemistry and global air quality. Global emission of isoprene from vegetation is the primary source of photochemically reactive reduced trace gases in the troposphere. Isoprene plays an important role in regulating the oxidative capacity of the lower atmosphere. It reacts rapidly with the hydroxyl radical (OH), the principal oxidizing compound of the troposphere, and indirectly affects climate forcing by influencing the concentrations of carbon monoxide, ozone, and methane. The timely quantification of global isoprene emission is very important given isoprene's potential for controlling the concentration of greenhouse gases and modifying the chemistry of Earth's atmosphere.

The present modeling effort explores approaches to estimating global biogenic isoprene emissions. Current regional and global models of isoprene emission are based on ecosystem specific biomass and emission factor estimates and algorithms describing the relationship between light, temperature, and isoprene emission. Uncertainties exist, however, in the data and the driving variables of the model. A link was developed between an isoprene emission model and a process-based computer simulation model of trace gas fluxes, the Carnegie-Ames-Stanford Approach, that operates on scales that link regional and global data sets and ecosystem nutrient transformations. The issue is the effect and sensitivity of new model drivers in this coupled biogenic isoprene emission/terrestrial ecosystem production framework. The resulting emission products from the

global 1 degree \times 1 degree coverage provided by the satellite data sets and the process model allow flux estimations across large spatial scales and enable direct linkage to atmospheric models of trace-gas transport.

Preliminary results suggest that land classification and associated base emission estimates are important controls of isoprene emission rate estimates from models. An annual global isoprene flux of 513 terragrams carbon is estimated, slightly higher than previous estimates. Two vegetation cover types, broadleaf evergreen forest and wooded grassland, are responsible for approximately three-quarters of global total isoprene emissions. Emissions are highest in the tropics and lowest in the polar regions. In the high latitudes, emissions vary over months by several orders of magnitude because of fluctuations in temperature and solar radiation. Emissions peak during the warmest months. Tropical regions remain fairly constant between months.

The isoprene emission estimates described in this modeling effort represent a first step in linking an isoprene flux model to an ecosystem production model. Large uncertainties exist in estimating global emission rates. In addition to accurate estimates of vegetation source types and densities, improvements in emission factors and a better understanding of the influence of climate drivers are necessary.

Point of Contact: S. Alexander
(415) 604-3620

Paleoenvironmental Studies

Hector D'Antoni

Predictions of the future evolution of the atmosphere's chemistry and its impact on global circulation patterns are based on models that integrate the complex interactions of the biosphere, atmosphere, and the oceans. These models must be tested beyond the short-term climate record we currently have. An appropriate timeframe extends over the Holocene period (the last 10,000 years). Pollen analysis has successfully reconstructed the paleoecology of the last 10,000 years, thus providing a powerful time-link between short- and long-term processes in the biosphere.

However, these paleoecological findings cannot be directly linked to these complex models. Instead, modern pollen data may be linked to climate-driven biosphere properties, such as leaf area development, a parameter that is measured by remote-sensing means. Leaf area is one of the main variables used in ecophysiological models relating climate variation to canopy processes and development. Thus, both the pollen/remote-sensing relationship and the ecophysiological model can be used to construct relations between short-term and long-term climate and vegetation processes. These new methods open new dimensions in paleoenvironmental research.

At the southern tip of South America, the island of Tierra del Fuego is closer to Antarctica than any other continental landmass in the Southern Hemisphere. It is covered by four main types of vegetation: (a) Patagonian steppe (grassland, scrub, and heath), (b) deciduous forest dominated by *Nothofagus antarctica* and *N. pumilio* (with spots of scrub, heath, grassland, and bogs), (c) evergreen forest with *Nothofagus betuloides*, and (d) Magellanic moorland (with bog communities).

Estancia Rio Claro (54°22'S, 68°W) is located within the deciduous forest in Tierra del Fuego. Pollen analysis was performed from this location with a prototype imaging microscope (Zeiss Photomat fitted with a Pulnix TMC-7, CCD camera connected to a high resolution monitor and to a PC computer fitted with a Targa+ frame grabber). Pollen counts were larger than 300 for a safe application of statistical analysis. Profile zonation was performed by cluster analysis of the data matrix. Four zones that describe the vegetation process through the last 4,500 years were obtained. Without calibration for temperature estimates, temperature trends were determined. Thus, Zone I and II had a stable temperature similar to the present with a period of lower temperature around 1,700 BP. Zone III was apparently warmer and Zone IV was the coldest in the profile. Prediction of 'Paleo' Normalized Difference Vegetation Index (NDVI) and simple ratio index is being linked to this extensive pollen record.

The Oregon Pollen Transect is another application of this methodology. It includes 40 surface samples taken along an East to West transect from Dayville to Newport, Oregon. Remote-sensing data were obtained for Oregon from the OTTER CD-ROMs. These data were used to build a time series of NDVI data for the year 1990 for each sampling site along this 250-mile transect.

Point of Contact: H. D'Antoni
(415) 604-5149

Radiation Measurement System for Atmospheric Research

Warren J. Gore, Francisco P. J. Valero, Larry Pezzolo, Neil Heather

The Radiation Measurement System (RAMS) contributed valuable data to two recently completed atmospheric research missions, the NASA-sponsored Smoke, Clouds, and Radiation-Brazil (SCAR-B) and the International Global Atmospheric Chemistry Southern Hemisphere Marine Aerosol Characterization Experiment (ACE-1). RAMS consisted of an upward-looking total-direct-diffuse multichannel narrow spectral bandpass radiometer for optical depth measurement and a downward-looking multichannel narrow spectral bandpass radiometer for spectral flux measurement. Both radiometers have identical detectors making measurements at 380 nanometers (nm), 412 nm, 500 nm, 675 nm, 862 nm, 1064 nm, and 1640 nm.

SCAR-B made simultaneous in situ and remote measurements of the physical and chemical properties of the smoke produced by biomass burning in

Brazil. The mission goal was to determine the effects of the smoke on the Earth's radiation balance and climate. RAMS was integrated on the University of Washington Convair C131A aircraft, which made numerous flights, some in coordination with the NASA ER-2.

The goal of ACE-1 was to determine and understand the properties and controlling factors of the aerosol in the remote marine atmosphere that are relevant to radiative forcing and climate. The experiment was conducted in the midlatitude Southern Hemisphere marine site near Tasmania. For this mission, RAMS was flown on the National Center for Atmospheric Research C-130 aircraft.

Point of Contact: W. Gore
(415) 604-5533

A New Within-Leaf Radiative Transfer Model

David Peterson, Barry Ganapol, Lee Johnson, Christine Hlavka, Phillip Hammer

Researchers at Ames Research Center and the Agricultural Research Service of the U.S. Department of Agriculture, Athens, Georgia, have developed a new model to describe the interaction of energy with plant leaves. Unlike previous models which are based on the Kubelka-Munk theory, the Leaf Experimental Absorptivity Feasibility Model (LEAFMOD) is based on a radiative transfer formulation and on the assumption of the separation of the origins of the scattering and absorption transport effects. By explicitly accounting for photon deflection, the model captures the essence of scattering without introducing undue complexity into the computation. The model runs in forward mode to simulate observed leaf reflectance spectra with a high degree of success, and in inverse mode to generate

scattering and absorption profiles throughout the visible and near infrared spectral regions (400–2500 nanometers) from input spectra. By removing the confounding influence of scatter, LEAFMOD presents a potentially superior accounting for biochemical absorption and hence for estimation of foliar biochemical concentration. Decomposition analysis of composite absorption in several leaf reflectance studies by other investigators are revealing good relative absorption profiles; use of the model will remove the scattering effects to achieve specific absorptivities.

Point of Contact: D. Peterson
(415) 604-5899

Impact of Land Use and Land Surface Aggregation on Estimating Temperate Coniferous Forest Net Primary Productivity, Dry Matter Yield, and Carbon Budgets

Joseph Coughlan, Jennifer Dungan

This project investigates the effects that land-use change has on the methods and assumptions currently used to estimate the role and significance of land cover in Earth's carbon system. Process-based models are used to estimate regional water and carbon flux. Input data sets are derived from different spatial supports (scales) and with different land-cover assumptions (disturbed and potential vegetation). The use of data at different supports represents a mix of top-down (macro-support) and bottom-up (micro-support) approaches. The inclusion of land-use effects on regional estimates made at micro-support can be aggregated and compared to top-down methods using larger-scale support methods that omit or simplify land-use changes.

Inconsistencies between data-set support are a significant source of error for simulation model experiments. One significant contribution to this research is the use of remote-sensing data to change the support of critical yet highly variable data sets at the finer support scales (1.1 kilometers). Using ecological knowledge, remotely sensed vegetation amounts can be used to modify the support of soils data to reduce these errors. In this example, the soils data have known variability, but the location of that variability is blurred into soils classes that are mapped as polygons at a support far larger than the vegetation data (1.1 kilometers). Within these classes, the geographic location of the soil variability is not known but can be inferred by reference to the vegetation. Vegetation constrains the corresponding

soil variables to be at a value at least large enough to maintain the health of the observed vegetation.

An Oregon-statewide application of this method has been executed using vegetation estimated from Advanced Very High Resolution Radiometer (AVHRR) data and the U.S. Geological Survey's State Soil Geographic (STATSGO) database. STATSGO uses larger sized (10–100 kilometer) land units than the AVHRR (1.1 kilometers), and it maps the type and fraction of soil properties found within each soil polygon-class using statistics. These distributions of soil properties are not mapped to an exact location within the class, so any point can have one of several probable values. Using vegetation estimates, researchers generated a set of maps representing the probable locations of soil water holding capacities, providing critical information for regional simulation models. The relationship between the vegetation and soil that guides the map generation process is constructed with our Regional Hydroecological Simulation System. The new soil maps are constructed using the amount of vegetation as a guide for the amount of water present at each 1.1 kilometer location within each 10–100 kilometer polygon. The new soil maps represent the soil at the same 11.1 kilometer resolution as the vegetation data, improving the quality of the original soil map.

**Point of Contact: J. Coughlan
(415) 604-5689**

Monitoring and Enforcement of Fisheries Aided by Synthetic Aperture Radar

Robert Wrigley, Don Sullivan

Recent evidence suggests that the Pacific Northwest and North Atlantic U.S. Coastal waters are being overfished. This evidence also suggests that it is not only U.S. fishermen who are involved. This overfishing situation emphasizes the inadequacy of the present observation system of two ships and one aircraft monitoring over one million square miles of the Pacific Northwest fishing grounds. The synoptic capabilities of remote sensing offers a sophisticated monitoring and enforcement capability for fisheries internationally. Independent spot checks using satellite imagery enables detection, deters cheating, and encourages legal vessel participation.

Under NASA's Earth Observation Commercial Applications Program, Natural Resources Consultants, Inc. and Ames Research Center have developed a commercial workstation, OmniVision, to use synthetic aperture radar (SAR) data to detect vessels larger than 50-100 meters. In an operational scenario, vessels would be checked against a data

base of known (legal) ships, and, failing a match, could be interdicted.

In cooperation with NASA's Alaska SAR Facility, algorithms were developed that allow interactive geolocation of potential ship targets to within 125 meters. Work was done to reduce inhomogeneities in background features as an adjunct to improve target acquisition. OmniVision algorithms for edge detection, land masking, and ship detection were investigated and developed, along with an operating system independent high-speed vector graphics library. An equipment evaluation was undertaken to determine current capabilities and prices of PCs and workstations for implementing this system.

Point of Contact: R. Wrigley
(415) 604-6060

The Reliable Multicasting Protocol

John Callahan

Reliable Multicasting Protocol (RMP) is a high-performance transport protocol, designed to provide reliable, fault tolerant, and ordered delivery of messages between multiple senders and multiple destinations in LAN and WAN environments. RMP provides message delivery semantic selection on a per message basis as well as message resiliency and fault tolerance selection on a group basis. The fault recovery process of RMP is totally transparent to the application.

Reliable broadcast and multicast protocols will play major roles in the development of future large-scale data systems. For example, such protocols will be needed to maintain coherent copies of data at multiple sites in an efficient manner. Due to the complexity and criticality of such protocols, it is important that they be developed and researched in an atmosphere where correctness and verification are integral parts of the process.

RMP is based on an algorithm that was originally developed by Chang and Maxemchuk for reliable delivery of data in broadcast-capable, packet-switching networks. The original algorithm, which is called the Token Ring Protocol, allows sites in a packet-switching network to establish a token ring for distributing responsibility for acknowledgments. A single token is passed from site to site around the ring and only the holder of the token (called the current token site) can acknowledge certain data packets. RMP has high-performance characteristics because acknowledgments themselves are multicast to all other token ring sites. When a site gets the token (that is, it becomes the current token site), it multicasts an acknowledgment only if it has seen all data packets

since its receipt of the last acknowledgment. The token is passed in the multicast acknowledgment packet. The acknowledgment packet includes the source and sequence numbers of the data packets it is acknowledging. This allows each site to detect any missing packets. A site will use negative acknowledgments to request retransmission of any missing packets. When all packets (since the last acknowledgment received) have been received by the current token site, then that site can multicast its acknowledgment and thus pass the token to the next site on the ring. When a token site sends an acknowledgment, it is assumed that all data packets since it last held the token have been received by all sites.

To ensure the correct operation of the protocol and its implementation, a strategy and development process were created that enhanced the evolution of RMP by testing and verification. The protocol was specified as a set of mode tables that helped to organize and structure tests while developing implementation prototypes. The approach has been to study the problems that have occurred during development, testing, and operation of RMP. Through an analysis of such problems during software development, efforts were made to find methods that disclose problems earlier in the development life-cycle. The development of RMP provided useful incite into a real-world project that has commercial, academic, and social impact.

**Point of Contact: G. Sabolish
(415) 604-8215**

Web Integrated Software Environment

John Callahan

Collection of metrics and adherence to a disciplined development process are difficult tasks in any software project. Yet, project developers and managers need to understand their processes in order to coordinate assigned tasks effectively. To understand their own work processes and assess the status of an ongoing project, they must be able to measure various aspects of the project tasks, people, and products. An assessment of a project's status is critical to the reassignment of resources, adjustment of schedules, and measurement of product quality.

Change activity is a powerful indicator of a project's status. Automated systems that can handle change requests, track issues, and process electronic forms provide an excellent platform for tracking the status of the project.

The development of a World-Wide-Web-based approach called the Web Integrated Software Environment (WISE) supports the measurement of change activity as an implicit part of the software process. WISE provides a forms-based, workflow management system that helps members of a software development team overcome geographical barriers to collaboration. WISE allows for the improvement of the software process in a realistic environment based on dynamic analysis of changes to information and communication in the workflow. WISE tracks issues in the software development process, provides informal communication between users with different roles, supports to-do lists, and helps in software process improvement. Projects have used Java-based data visualization tools in WISE to create graphs of effort levels, defect rates, and other dynamic properties of their organizations. Such information is

available through audits of the backend WISE database that is transparent to users. In this fashion, WISE focuses attention on issue tracking and minimizes the time devoted to metrics collection, analysis, and reporting tasks not related directly to project activities. Automated tools like WISE focus on understanding and management of a software process rather than the bureaucracy of an organization.

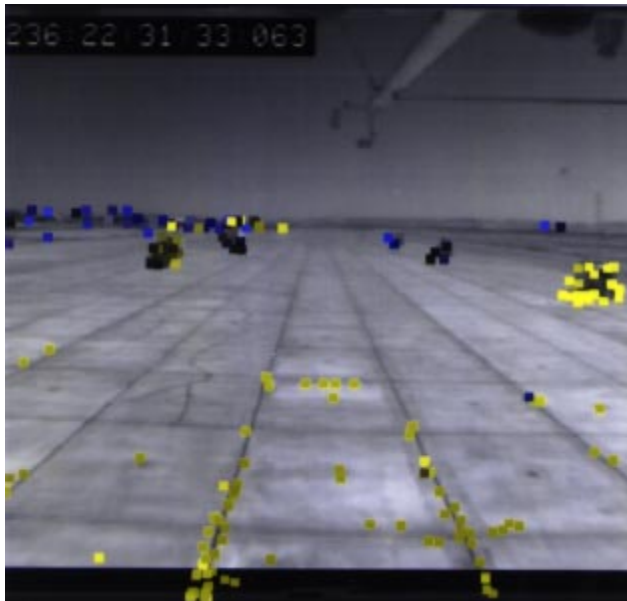
WISE has been used on several projects within NASA and the private sector to coordinate and monitor software verification and validation activities. WISE can be installed and made available at a specific URL (Universe Resource Locator) on the Internet or within a corporate network. Using an appropriate browser, each user connects into the WISE home page to view their personal "to-do lists" (TDLs) available on several projects. Each person in an organization may be assigned to one or more projects and, therefore, may have one or more TDLs under WISE.

The issue-based approach used in WISE is dominant not only in problem tracking, but is critical in capturing design rationale, informal information, requirements, and change requests. Design dependencies can be represented in an issue-based style and tracked throughout the life cycle of a project. In all cases, participants in an issue-based discussion contribute their expertise and viewpoints to discover and resolve issues. Each issue is followed by one or more positions that respond to an issue.

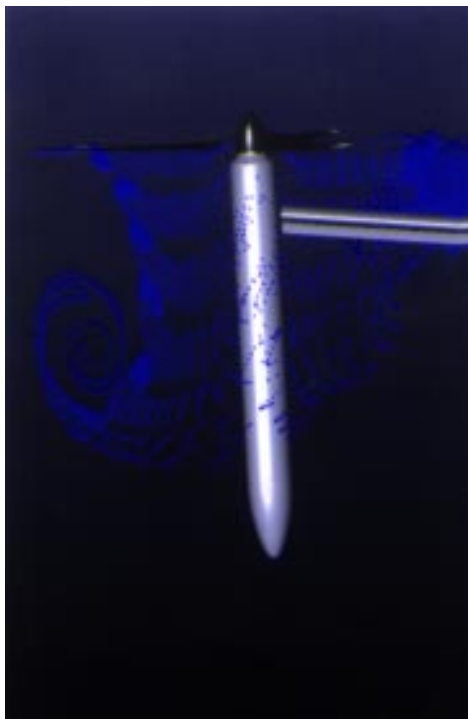
**Point of Contact: G. Sabolish
(415) 604-8215**

Appendix

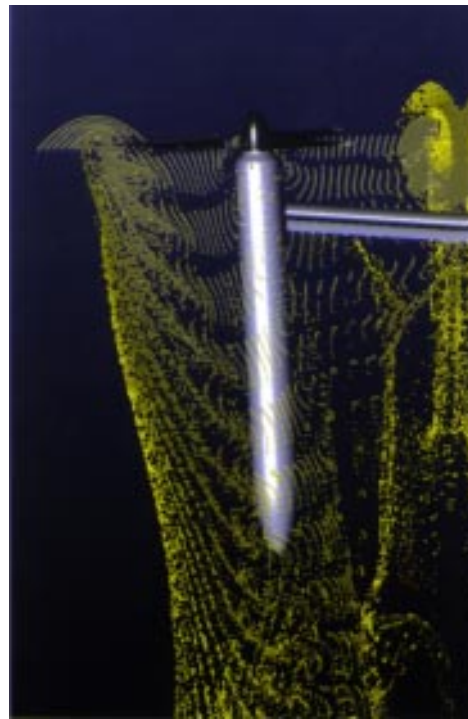
The color plates in this appendix correspond to figure citations that appear in the text. Each caption also provides the location of the figure citation.



Color Plate 1. Color-coded range results. (Smith, p. 14)

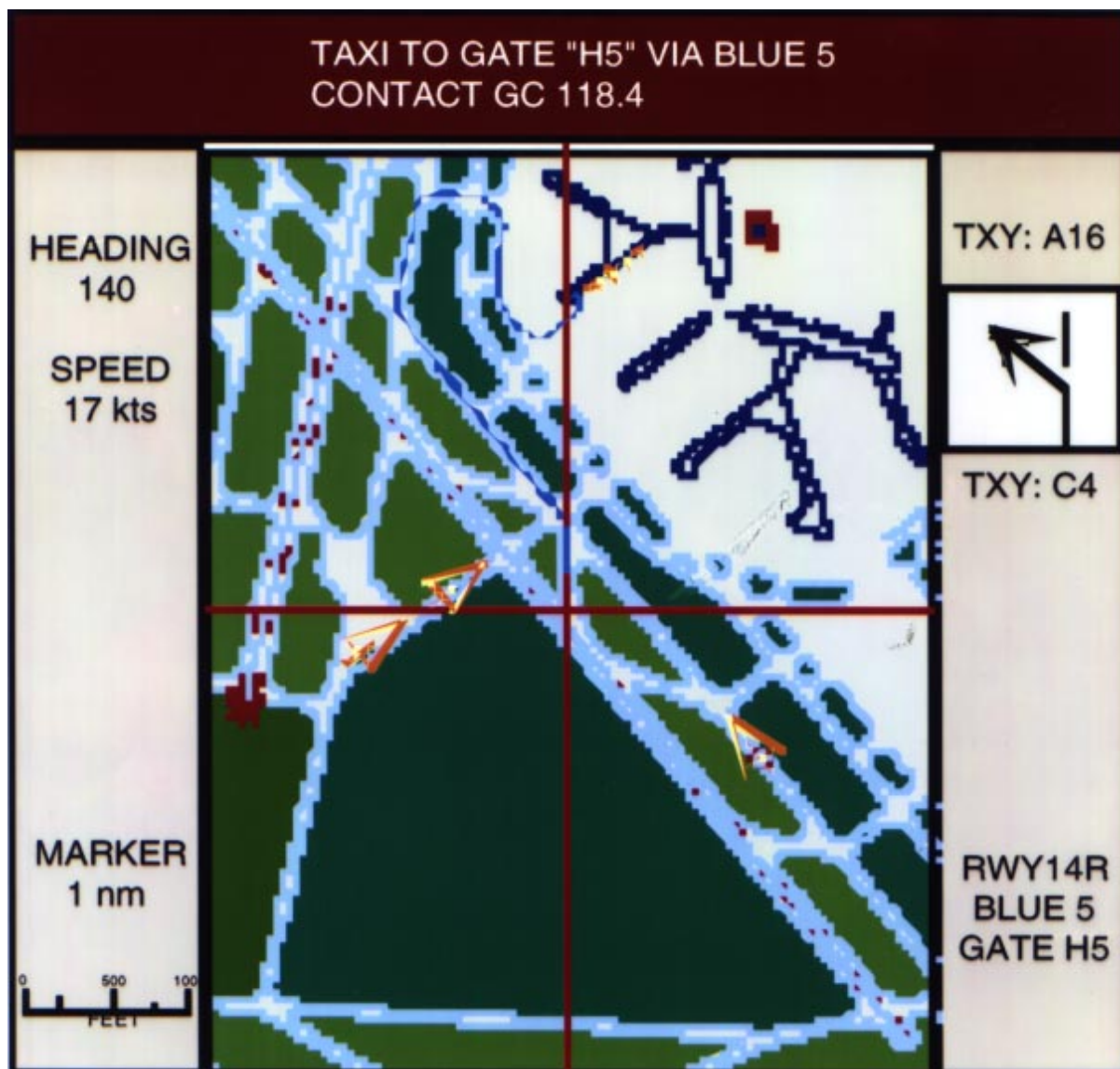


(2a)

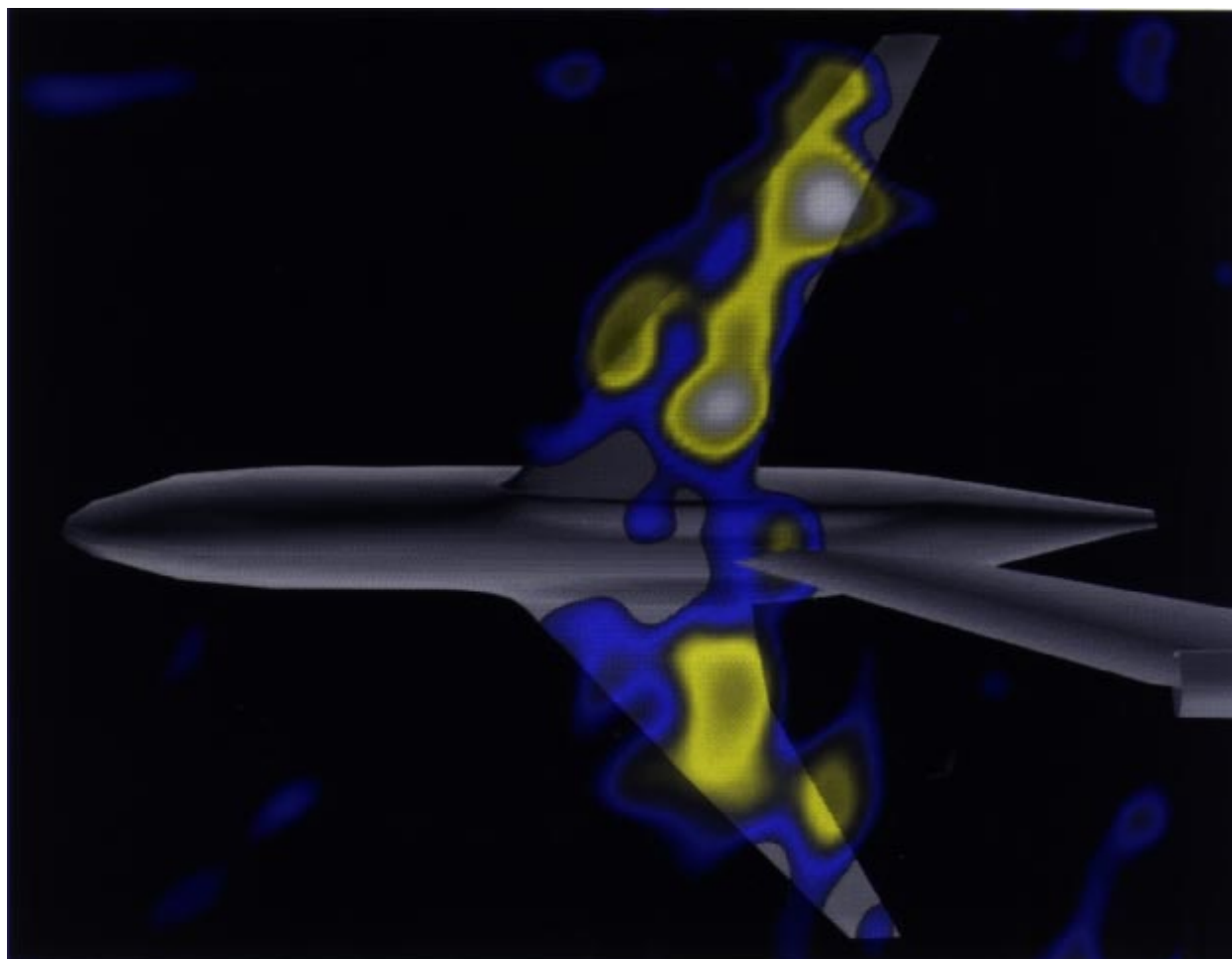


(2b)

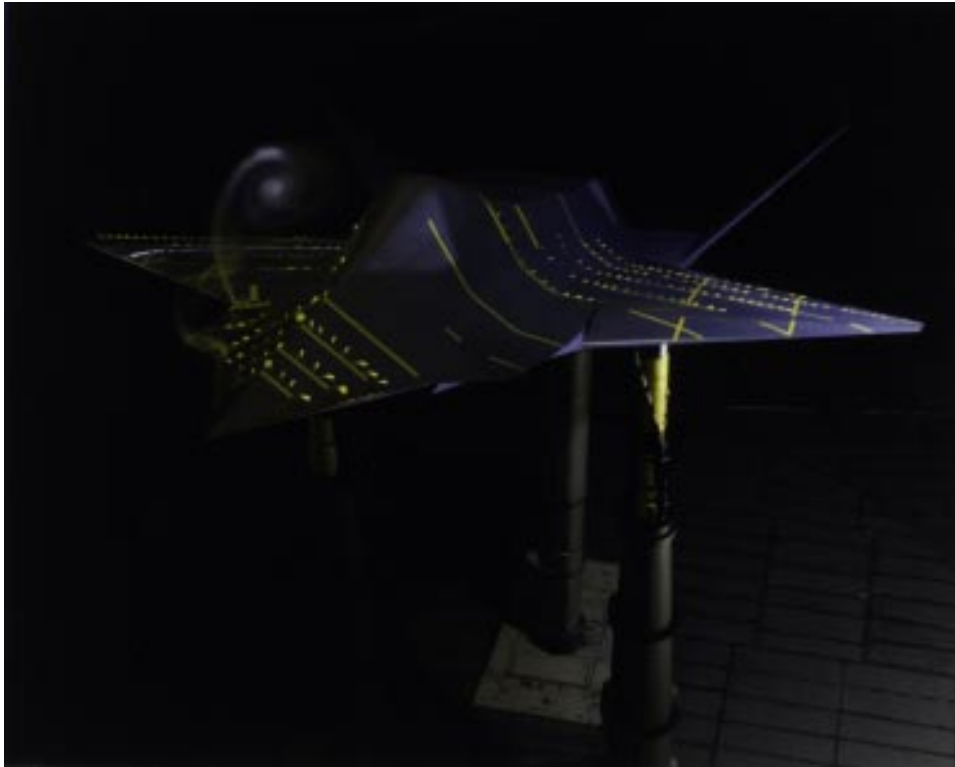
Color Plate 2. Traces of particles that have been released from seed locations along a line in the plane of the rotor every 50 time-steps; (a). Particles after about 5 revolutions; (b). Particles after about 15 revolutions. (Meakin, p. 22; Kao, p. 78)



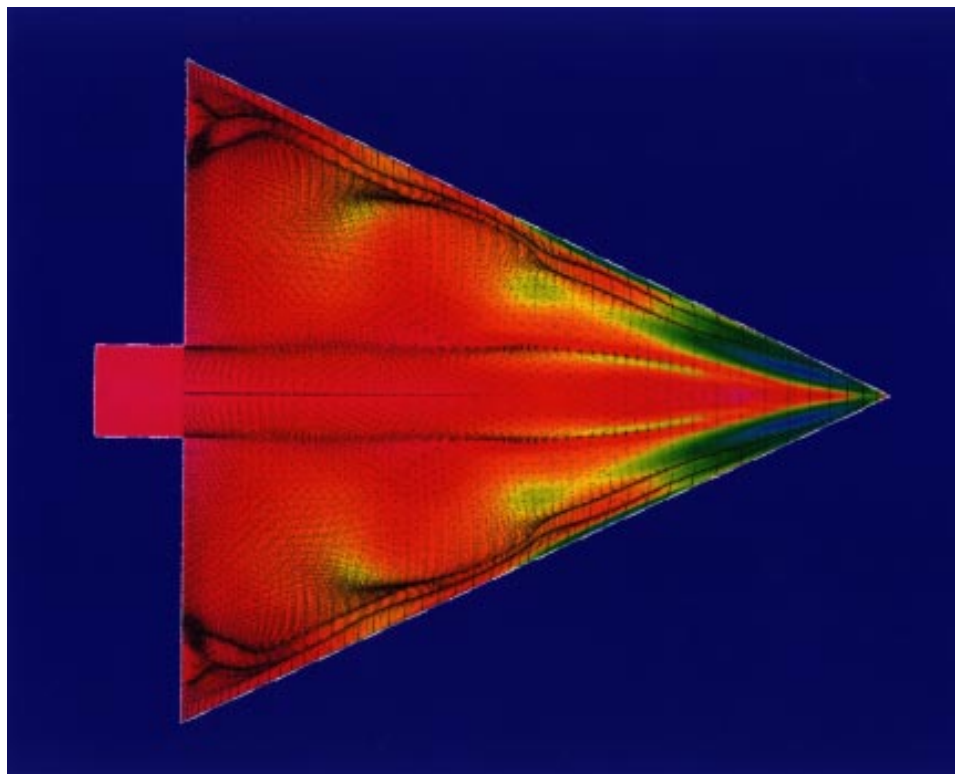
Color Plate 3. Prototype Advanced Navigation Display System. (Battiste, p. 29)



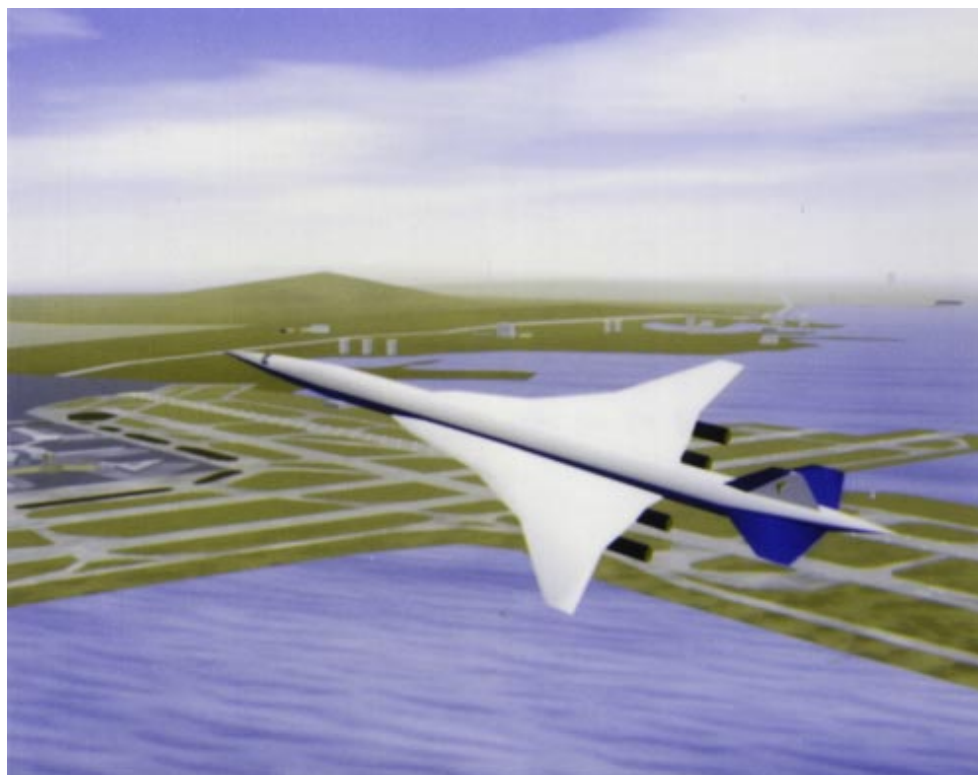
Color Plate 4. Noise map for 10 kilohertz. (Hayes, p. 36)



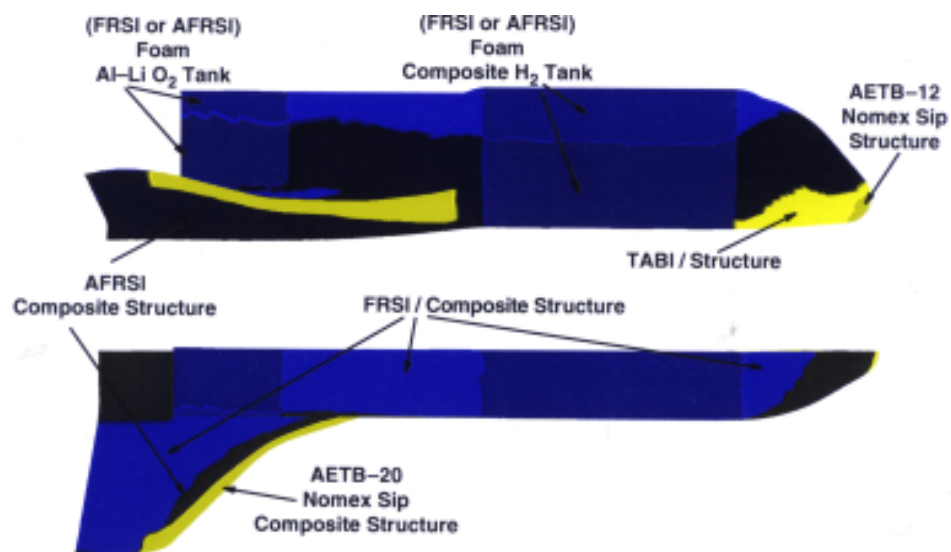
Color Plate 5. Flow visualization of forebody vortex. (Samuels, p. 43)



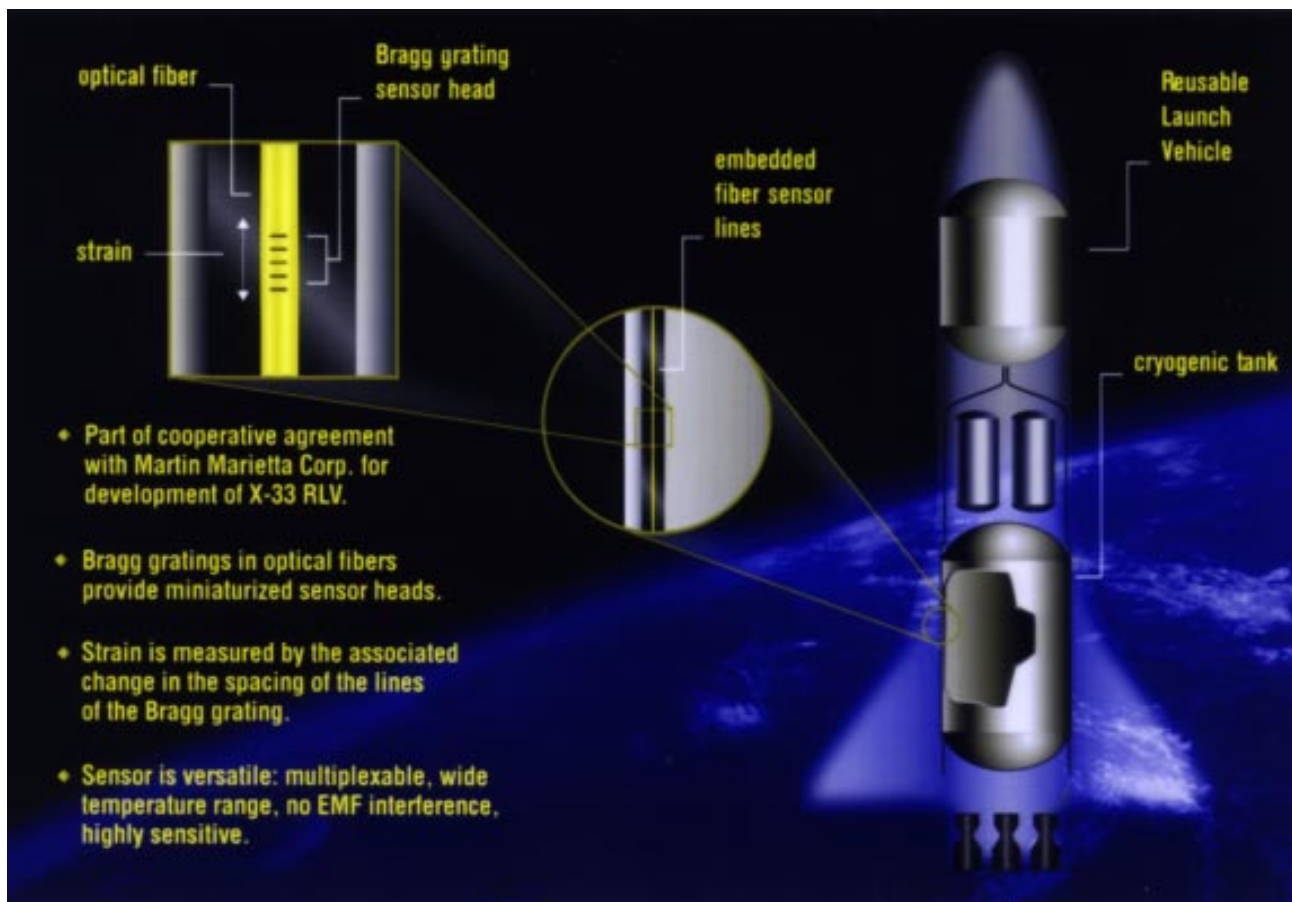
Color Plate 6. Numerical flow visualization of nonsteady surface pressures and surface-flow patterns. (Chaderjian, p. 47; Kao, p. 78)



Color Plate 7. High-speed civil transport aircraft. (Schroeder, p. 53)



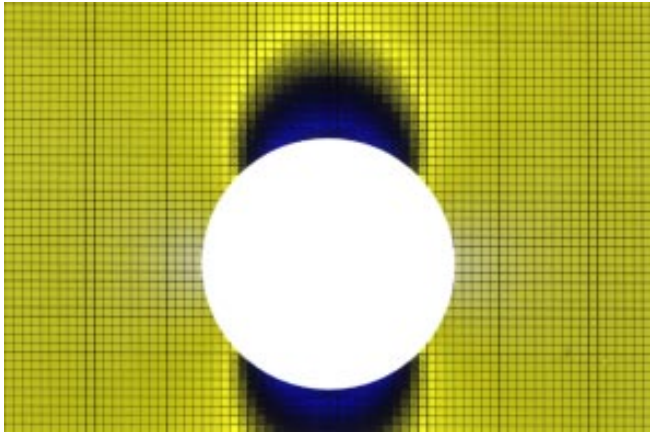
Color Plate 8. TPS material map and underlying tank structure for the Rockwell winged-body vehicle. (Henline, p. 55)



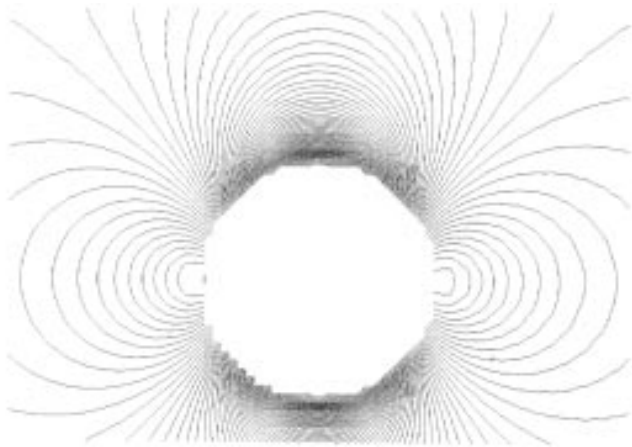
Color Plate 9. One application of fiber strain sensors monitors the condition of the fuel tanks for the Reusable Launch Vehicle as shown above. In this case, Bragg grating sensors are used. (Gary, p. 56)



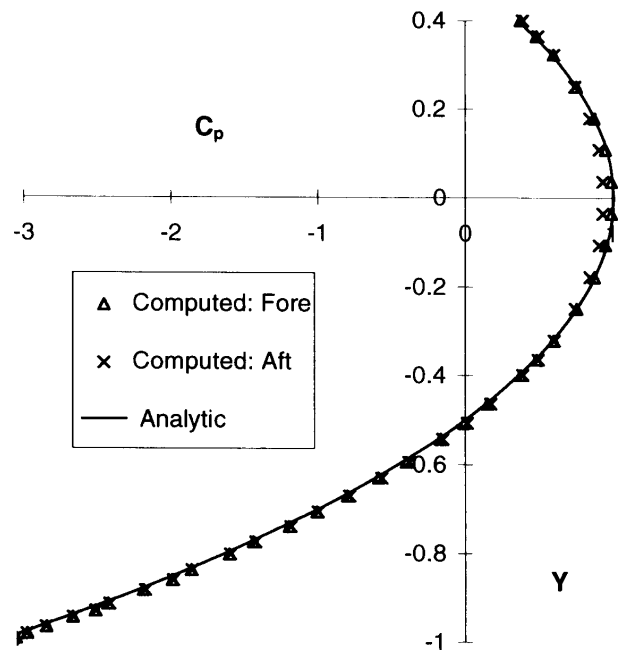
Color Plate 10. Surface pressure distribution for Apache helicopter. (Melton, p. 75)



(11a)

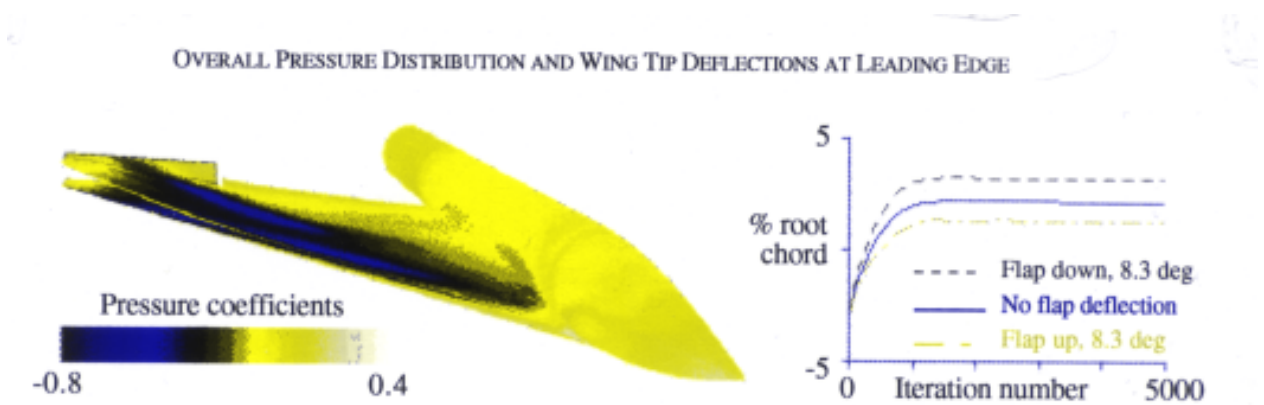


(11b)

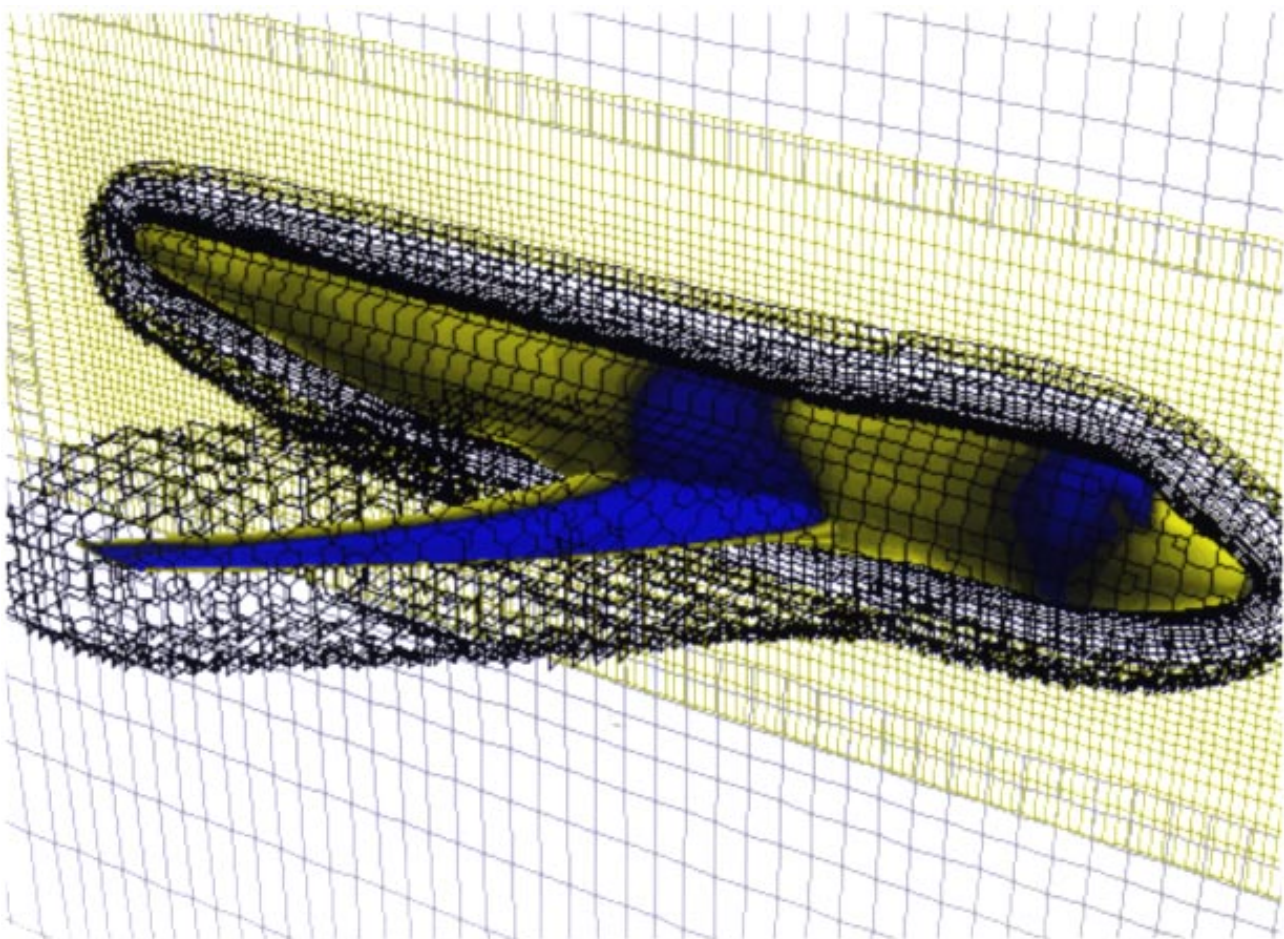


(11c)

Color Plate 11(a). Cartesian grid painted by pressure for circular cylinder; (b). Pressure contours for circular cylinder; (c). Surface pressure distributions for circular cylinder. (Melton, p. 75)



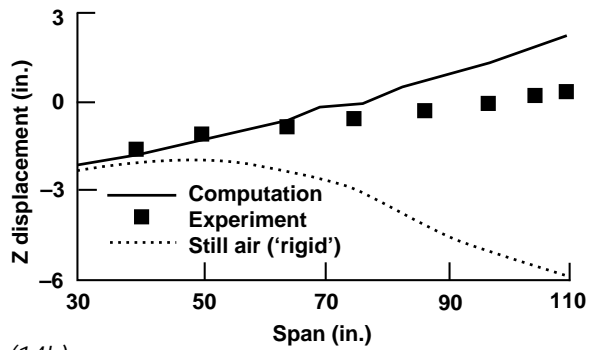
Color Plate 12. Aeroelastic computations on wing-body-control configurations. (Guruswamy, p. 76)



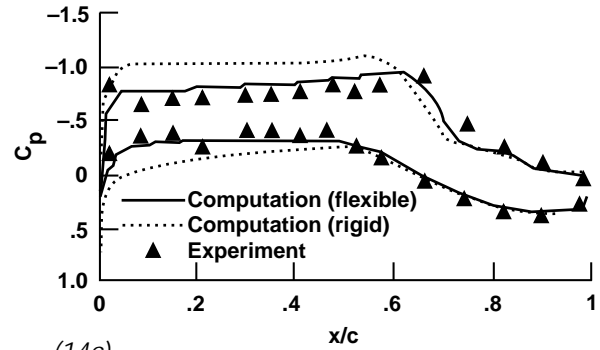
Color Plate 13. Boeing 747 surface pressure and volume grids generated by the automated wing/body CFD script. (Nash, p. 76)



(14a)

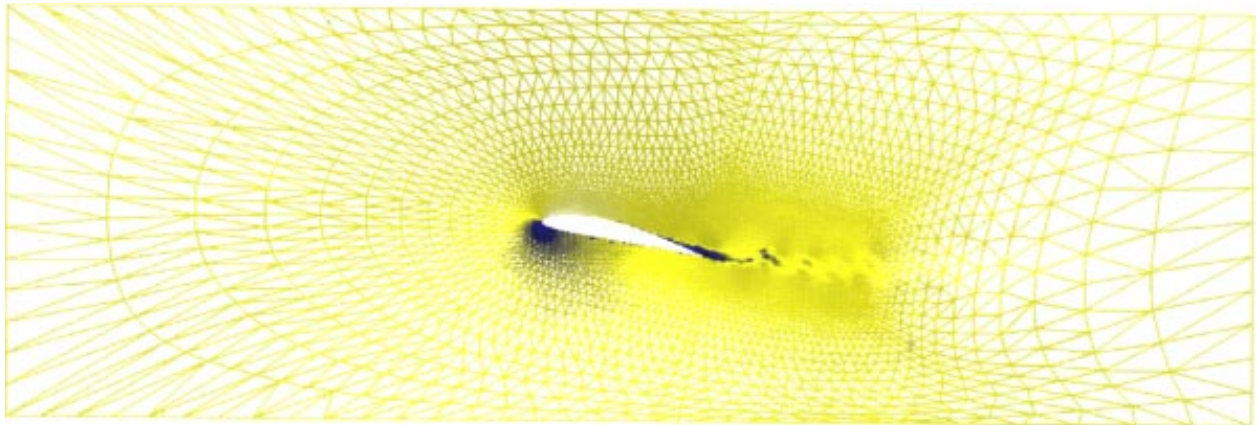


(14b)

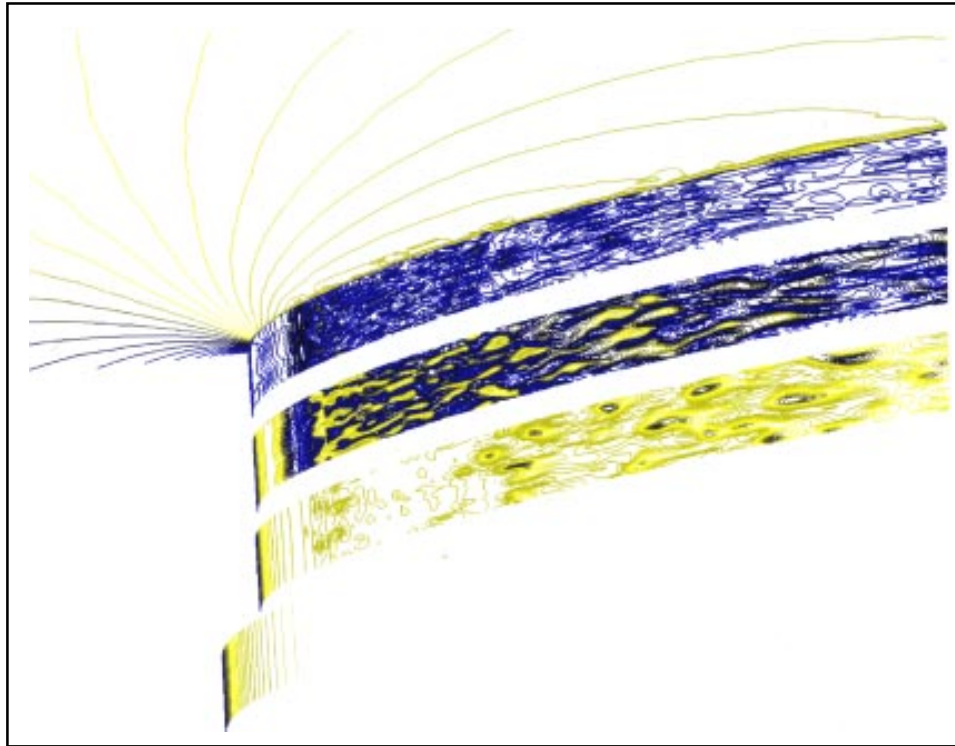


(14c)

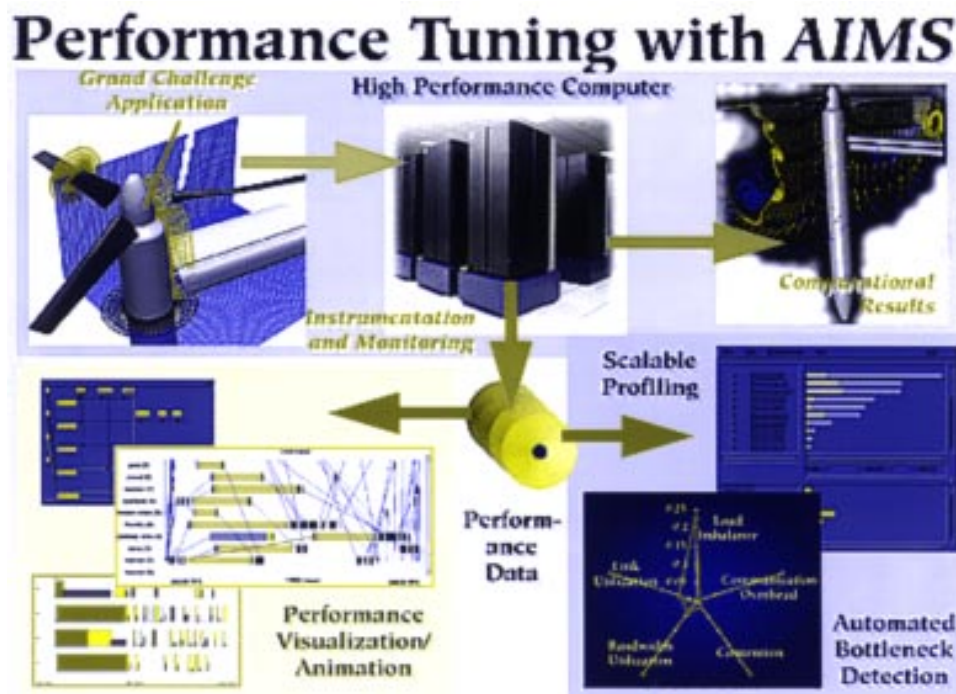
Color Plate 14(a). Pressure on rigid and flexible configurations; (b). Static aeroelastic deflection along the rear spar, $0.62c$: $M = 0.85$, $\alpha = 1^\circ$, $Re = 7.56 \times 10^6$; (c). Pressure coefficient comparison at 71% span: $M = 0.85$, $\alpha = 1^\circ$, $Re = 7.56 \times 10^6$. (Guruswamy, p. 77)



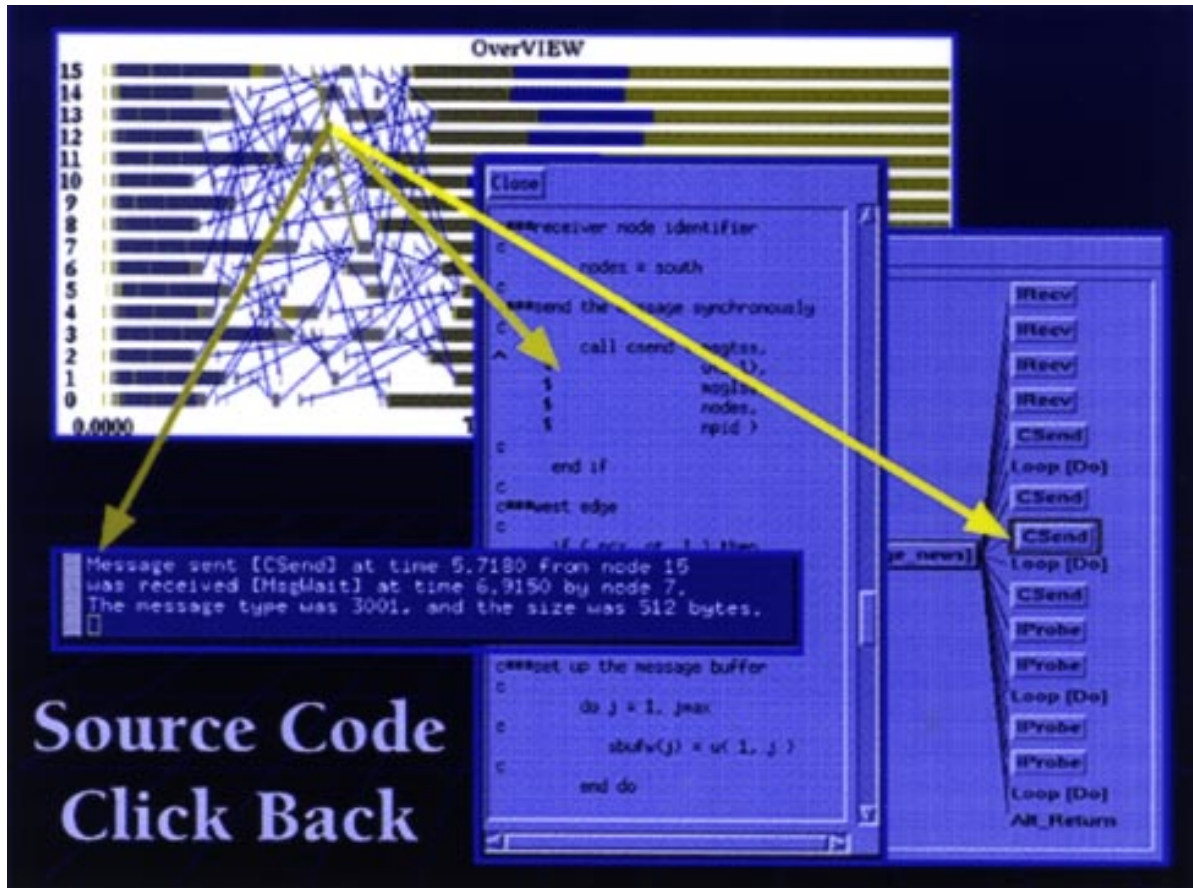
Color Plate 15. Large-eddy simulation of an airfoil at maximum lift using the unstructured mesh technique. Streamwise velocity contours superimposed on a mesh cross section (the simulation is three-dimensional). (Moin, p. 80)



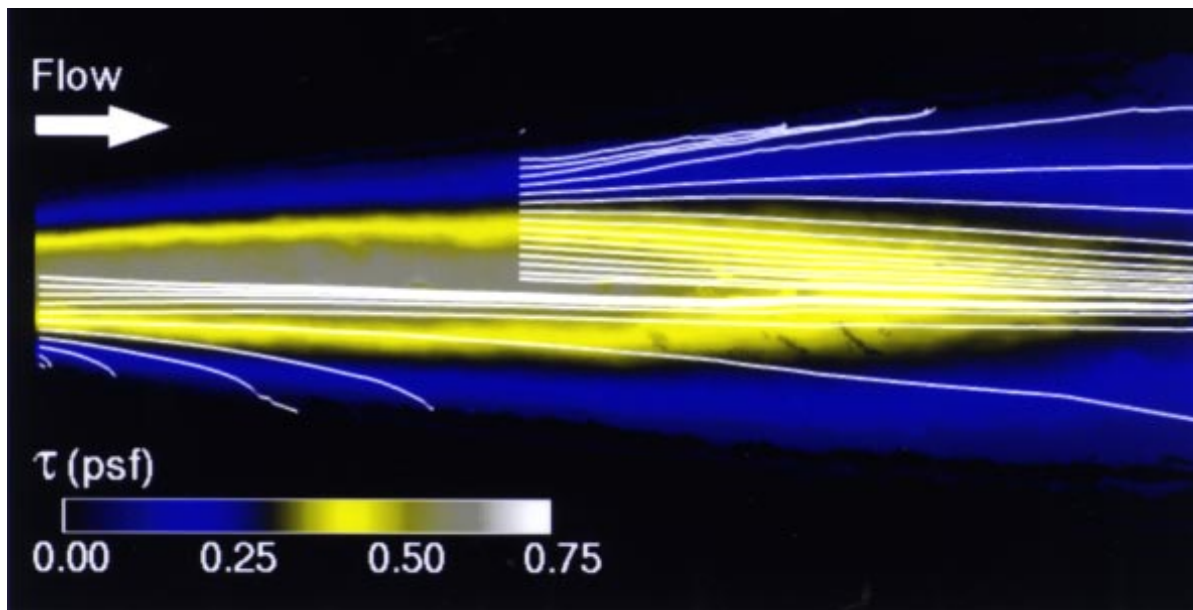
Color Plate 16. Contours of tangential velocity showing transition to turbulence on the airfoil upper surface. From top to bottom the contours are plotted on surfaces with increasing distance from the airfoil. (Moin, p. 80)



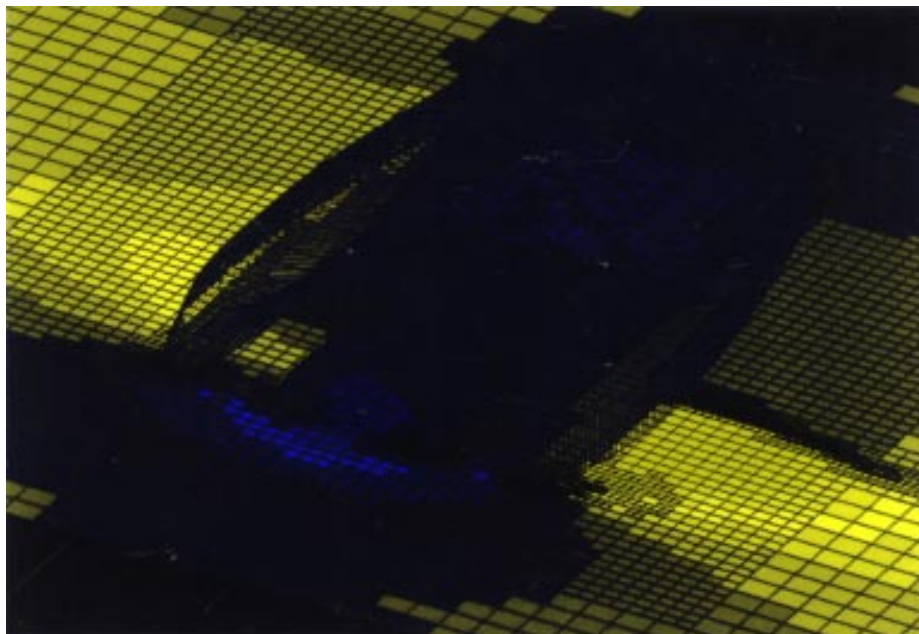
Color Plate 17. An automated instrumentation and monitoring system. (Yan, p. 83)



Color Plate 18. Parallel programmers can interact with AIMS' displays via point and click protocols to reveal parallel program behavior in incremental levels of detail. (Yan, p. 83)



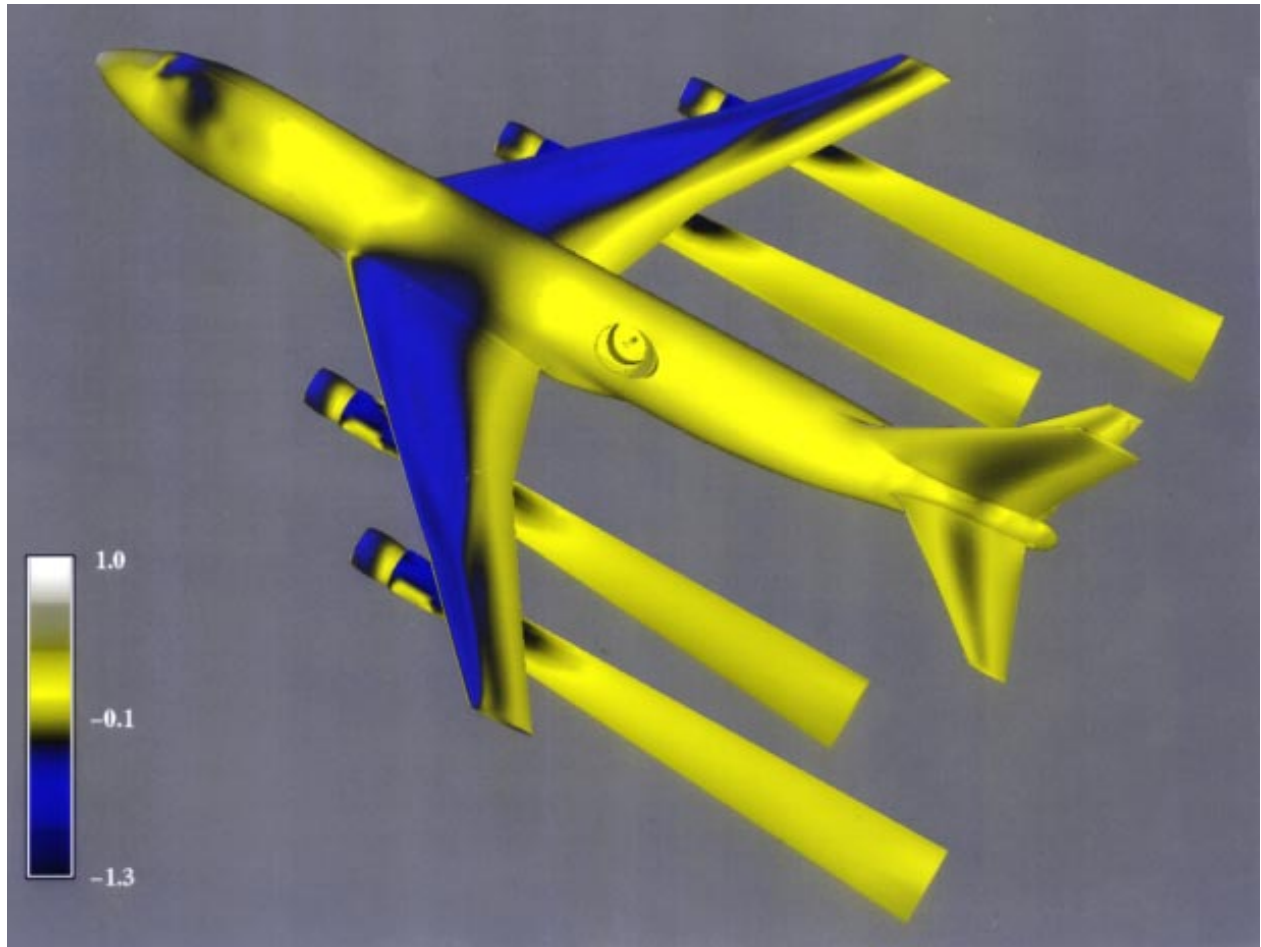
Color Plate 19. Surface shear-stress vector fields; color contours of magnitude and streaklines originating from $x/D = 5$ and 10. (Reda, p. 96)



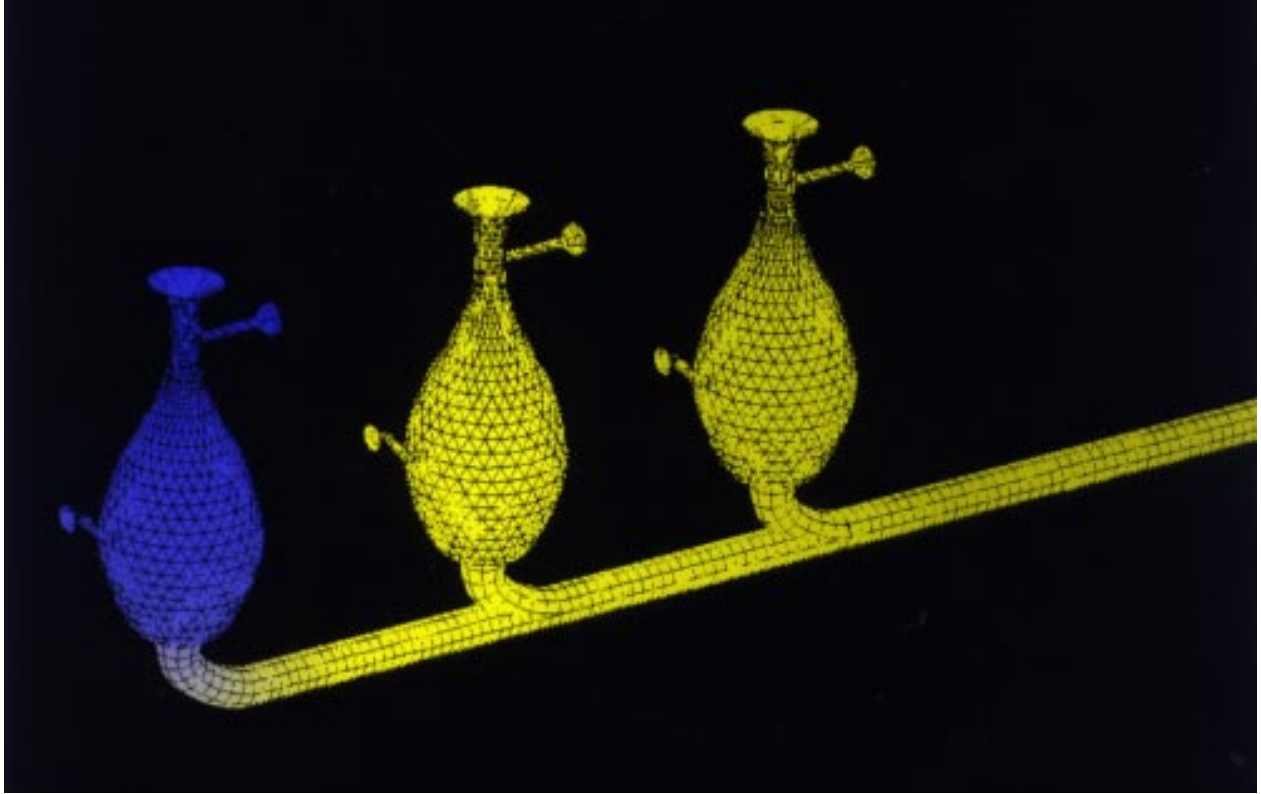
Color Plate 20. Mach distribution on Tranair Model. (James, p. 97)



Color Plate 21. Atmospheric sampler on Ames DC-8. (James, p. 97)



Color Plate 22. Instantaneous surface-pressure coefficient distribution at free-flight conditions for the full configuration aircraft with cavity and with powered engines. (Roth, p. 151)



Color Plate 23. The nerve fiber has three calyces (bottle-shaped objects) that have small branches. Synapses were activated at the ends of the calyceal branches and at the inner and outer surfaces of the calyx. This discharged the spike initiation zone at far right (color-coded in red). A back reflection of depolarization has reached the calyces and their branches in this time-step caught photographically. Voltage changes are taking place directionally, from right to left as shown by color coding: orange (far right) most change; yellow (center) some change; blue (far left) least change. (Ross, p. 199)

REPORT DOCUMENTATION PAGE			Form Approved OMB No. 0704-0188	
Public reporting burden for this collection of information is estimated to average 1 hour per response, including the time for reviewing instructions, searching existing data sources, gathering and maintaining the data needed, and completing and reviewing the collection of information. Send comments regarding this burden estimate or any other aspect of this collection of information, including suggestions for reducing this burden, to Washington Headquarters Services, Directorate for Information Operations and Reports, 1215 Jefferson Davis Highway, Suite 1204, Arlington, VA 22202-4302, and to the Office of Management and Budget, Paperwork Reduction Project (0704-0188), Washington, DC 20503.				
1. AGENCY USE ONLY (Leave blank)		2. REPORT DATE December 1996		3. REPORT TYPE AND DATES COVERED Technical Memorandum
4. TITLE AND SUBTITLE Research and Technology 1995			5. FUNDING NUMBERS	
6. AUTHOR(S) Ames Investigators				
7. PERFORMING ORGANIZATION NAME(S) AND ADDRESS(ES) Ames Research Center Moffett Field, CA 94035-1000			8. PERFORMING ORGANIZATION REPORT NUMBER A-975413	
9. SPONSORING/MONITORING AGENCY NAME(S) AND ADDRESS(ES) National Aeronautics and Space Administration Washington, DC 20546-0001			10. SPONSORING/MONITORING AGENCY REPORT NUMBER NASA TM-110419	
11. SUPPLEMENTARY NOTES Point of Contact: John T. Howe, Chief Scientist, Ames Research Center, MS 200-16, Moffett Field, CA 94035-1000 (415) 604-5500 or contact person(s) at the end of each article				
12a. DISTRIBUTION/AVAILABILITY STATEMENT Unclassified — Unlimited Subject Category 99			12b. DISTRIBUTION CODE	
13. ABSTRACT (Maximum 200 words) This report presents some of the challenging research and technology accomplished at NASA Ames Research Center during FY95. The accomplishments address almost all goals of NASA's four Strategic Enterprises: Aeronautics and Space Transportation Technology, Space Sciences, Human Exploration and Development of Space, and Mission to Planet Earth. The report's primary purpose is to inform stakeholders, customers, partners, colleagues, contractors, employees, and the American people in general about the scope and diversity of the research and technology activities. Additionally, the report will enable the reader to know how these goals are being addressed.				
14. SUBJECT TERMS Aeronautics, Space transportation, Space sciences, Earth sciences, Life sciences, Information technology, Research and technology			15. NUMBER OF PAGES 262	
			16. PRICE CODE A12	
17. SECURITY CLASSIFICATION OF REPORT Unclassified	18. SECURITY CLASSIFICATION OF THIS PAGE Unclassified	19. SECURITY CLASSIFICATION OF ABSTRACT	20. LIMITATION OF ABSTRACT	